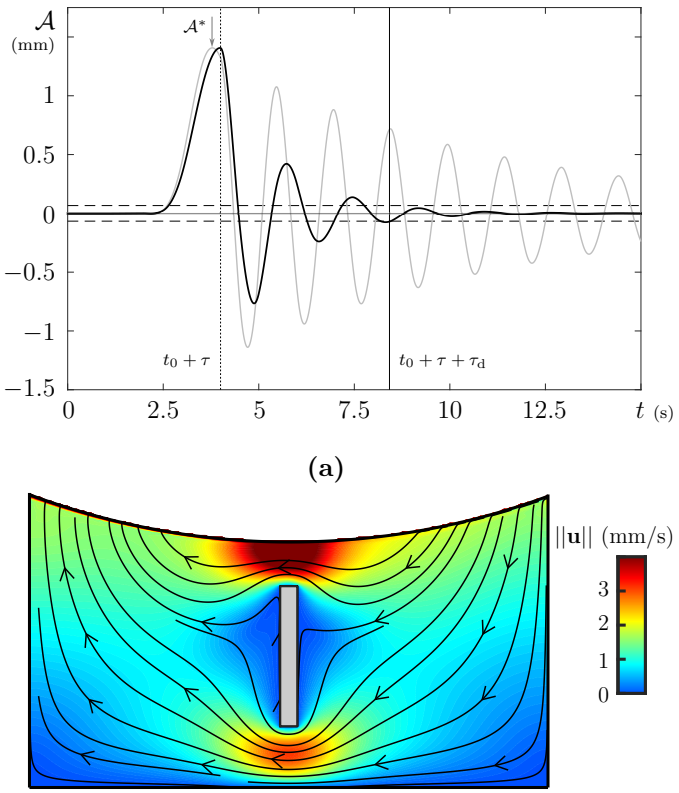


Figure 9.3: (a) Time evolution of the asymmetry $\mathcal{A}$ for the reference case without baffle (gray) and the case with a vertical centered baffle of dimensions 1 mm × 8 mm (black). (b) Instantaneous streamlines and velocity magnitude $||\mathbf{u}||$ at the first $\mathcal{A} \simeq 0$ lapse of the sloshing cycles with the 1 mm × 8 mm vertical centered baffle.

where k is the wavenumber, and g is the gravity acceleration. For a $L \times H = 30$ mm × 15 mm container in microgravity conditions ($g = 0$), the first sloshing mode is associated to $k = \pi/L$ with a sloshing frequency $\varpi/(2\pi) \simeq 0.731$ Hz.

This prediction can be compared to the results of Fig. 9.3(a), where the natural, uncontrolled sloshing response (i.e., without baffle) of the system is shown via the time evolution of $\mathcal{A}$ (gray curve). The calculated sloshing frequency is $\omega_0/(2\pi) \simeq 0.667$ Hz, which is in good agreement with that predicted by Eq. (9.13). In this scenario, the decay time is $\tau_{d0} \simeq 21.09$ s and the calculated damping $\xi_0 \simeq 0.0326$ is relatively small, suggesting a great margin for improvement with the addition of passive baffles. These values, marked with the subscript '0', are used as reference in the remainder of this manuscript.

Even in the absence of baffles and the restoring effect of gravity, the fluid naturally reverts to its original symmetric state over time. This evolution can be understood from an energetic standpoint, considering the role of surface tension. Surface tension is a force that tends to minimize the size of the free surface. When the microgravity disturbance is introduced, the fluid moves and the free surface deforms, placing it in a more energetic configuration than its initial equilibrium. As the applied acceleration vanishes, the influence of surface tension

guides the system towards its symmetric equilibrium. Nevertheless, owing to inertia, the liquid initiates a back-and-forth oscillation. Throughout these oscillations, viscosity dissipates momentum and attenuates fluid motion, ultimately leading to the initial symmetric state with $\mathcal{A} = 0$. On ground, gravity acts as a supplemental restoring force that helps resetting the original stable configuration.

The addition of passive baffles favours the natural tendency of the system to return to its original symmetric state via various interconnected mechanisms.

By intersecting the streamlines:

This is one of the most natural solutions when trying to control sloshing. The idea is that, if a baffle is placed perpendicular to the streamlines, these will have to reorder themselves in more complex paths that cause pressure differences in the fluid, difficult the transfer of fluid from one side of the baffle to the other, and, eventually, increase friction inside the fluid.

The reorganization of the flow appears to be the most relevant effect within this operating mechanism, as it also affects the sloshing frequency. This can be explained as follows: since the baffle obstructs the streamlines, the fluid must travel a longer path for sloshing to occur; see Fig. 9.3(b). This not only reduces sloshing motion, but also slows down the response. To justify somewhat this discussion, Fig. 9.4 illustrates the time evolution of the flow $\mathcal{Q}$ across the mid-plane of the container:

$$\mathcal{Q} = \int_S \mathbf{u} \cdot \mathbf{i}\, dS, \tag{9.14}$$

$S \equiv \{\mathbf{x} \in \{0\} \times [0,\ f(0,\ t)]\}$, for three vertical centered baffles of increasing heights $H_b = 2,\ 4,\ 8$ mm; these values are made nondimensional with the flow $\tilde{\mathcal{Q}}$ for the reference case without baffle. As evidenced in this panel, the presence of the baffle reduces $\mathcal{Q}$. The reduction is greater with larger baffle dimensions. Besides this, the overall system response is delayed, with a slight decrease of the sloshing frequency. Later on, it will be observed that almost all the baffles explored reduce the sloshing frequency due to this effect.

By increasing viscous dissipation:

The presence of baffles enforces a vanishing fluid velocity on their walls, with an increased local relevance of viscous dissipation.

In close connection with the previous mechanism, we provide here an example of the increased friction caused by the reorganization of the flow pattern. If the baffle constrains fluid motion and enforces the liquid to pass through specific regions of the container, the local velocity will increase significantly in these areas, which results in higher viscous forces. In the right panels of Fig. 9.4, profiles of the horizontal velocity u_x are illustrated at two selected times. Note that viscous forces can be estimated as $\nabla \cdot \tau \sim \rho\nu\Delta u/\Delta s^2$, where s is a coordinate perpendicular to u. Therefore, steepest profiles with large velocity variations favour viscous dissipation. Looking at these panels, one can estimate a viscous force opposing fluid motion of

$$\nabla \cdot \tau_0 \sim \rho\nu \frac{\Delta u_x}{\Delta s^2} \sim \rho\nu \frac{\max(u_x)}{H^2} \sim \mathcal{O}(10^{-2})\,\mathrm{N/m^3}$$

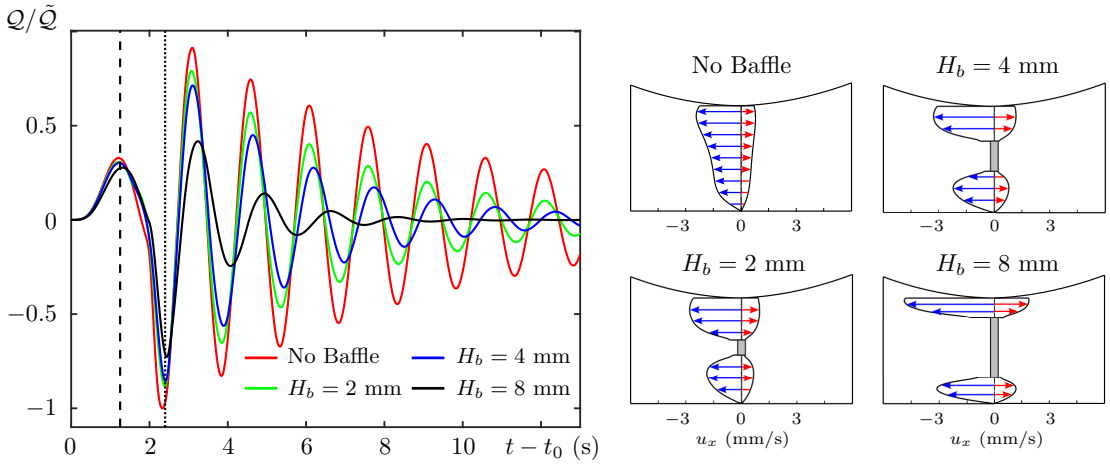


Figure 9.4: Time evolution of the flow $\mathcal{Q}$ across the mid-plane of the container, $x = 0$, for three vertical centered baffles of dimensions $L_b = 1$ mm and $H_b = 2, 4, 8$ mm; the values are made nondimensional with the flow $\tilde{\mathcal{Q}}$ for the reference case without baffle. The associated profiles of the horizontal velocity u_x are illustrated in the right panels of the figure at two selected times (marked by vertical lines).

in the reference case, two orders of magnitude smaller than the same estimate

$$\nabla \cdot \tau \sim \rho\nu \frac{\Delta u}{\Delta s^2} \sim \rho\nu \frac{\max(u_x)}{(H/4)^2} \sim \mathcal{O}(10^0)\,\mathrm{N/m^3}$$

for the vertical baffle with $H_b = 8$ mm.

By stagnating a large amount of fluid around:

The idea behind this approach is for the baffles to encompass a large amount of fluid and protect it from sloshing motion, creating partially enclosed zones that have limited freedom to move.

Usually, this strategy involves the use of large, thin baffles that guide the fluid motion around them, effectively confining the fluid within their boundaries. Examples are found with baffles that almost enclose the liquid at a certain height and leave the free surface as a small thin layer over them, or in relatively complex structures that trap the fluid inside them such as cross-shaped baffles.

Despite the efficacy of this mechanism and associated designs, one must be careful when trying to exploit it, as big baffles might be needed, potentially increasing the mass and complexity of the system, while reducing the available volume in the tank.

By modifying the geometry of the tank:

The presence of the baffle can also be understood as an additional wall to the tank. This ultimately modifies the geometry, affecting its effective shape or dimensions. We find it

important to mention that, for this effect to be dominant, baffles must closely resemble the walls of the geometry being imitated, greatly limiting the connection between the fluid regions on either side of them.

A common natural example is placing a vertical baffle in the center of a tank of length L, thus trying to divide the container into two separate compartments of half the original length $L' = L/2$. Reality is that, if we want to consider it a baffle (and not a "separator"), one must leave some small space where the two regions of fluid connect.

Using Eq. (9.13), the first sloshing frequency of the new container ϖ' is modified by a factor:

$$\frac{\varpi'}{\varpi} = \left(\frac{k'}{k}\right)^{\frac{3}{2}} \sqrt{\frac{\tanh(k'H)}{\tanh(kH)}} = 2^{\frac{3}{2}} \sqrt{\frac{\tanh(2\pi/\Gamma)}{\tanh(\pi/\Gamma)}} \geq 2^{\frac{3}{2}} \simeq 2.83,$$

where $\Gamma = L/H$ quantifies the slenderness of the liquid system considered. This provides us with a lower bound for the frequency increase that can be achieved by reducing the container length by half. Increasing the sloshing frequency is a very helpful strategy because, usually, higher frequencies need to be excited by higher energy perturbations, except in the case where the disturbance spectrum coincides with the excitation of the new —and higher— sloshing frequency.

Besides using baffles, the geometry of the tank can be modified initially to reduce the natural sloshing response of the system. In Ref. [49], a V-shaped tank, where its walls form a semi-angle of 45° and has a free surface of length L, is analyzed. The associated dispersion relation for this type of container is derived, predicting a first sloshing frequency about twice that of a rectangular tank with the same free surface. Note that, despite we focus here on rectangular containers, baffles can be placed inside so that the sloshing response resembles that of a V-shaped container, thereby doubling the first sloshing frequency.

Hereafter, the first part of the analysis is presented, focusing on rectangular baffles for their simplicity and good performance. Then, more complex designs are analyzed, together with complementary strategies for active sloshing control.

9.4 Design and performance of simple baffles

We analyze here the performance of simple baffles. The purpose of this analysis is to determine which design parameters defining the geometry and position of the baffle are most relevant, and explore qualitatively the sloshing response sensitivity to their variation.

9.4.1 Design parameters

As illustrated in Fig. 9.5, rectangular baffles can be defined by the following parameters:

– Baffle length L_b and height H_b, selecting the baffle dimensions $L_b \times H_b$. Below, these values are often referred to the liquid volume $L \times H$, giving a qualitative idea of how

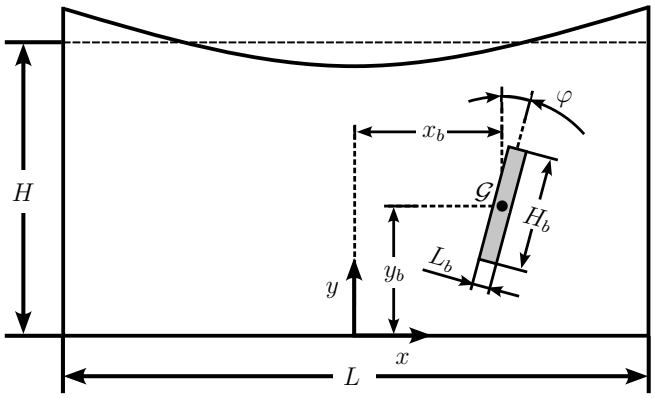


Figure 9.5: Sketch illustrating the design parameters considered for simple rectangular baffles: baffle length L_b and height H_b, position (x_b, y_b) of the baffle center of mass $\mathcal{G}$, and baffle orientation φ.

much space the baffle occupies with respect to the liquid in both horizontal and vertical directions.

- Relative position (x_b, y_b) of the baffle center $\mathcal{G}$, with respect to the container frame. Again, these values are often referred to L and H, providing a direct idea of the baffle position as fractions of the container dimensions.
- Baffle orientation φ with respect to the local y-axis of the container; φ is considered positive in a clock-wise sense, as sketched in Fig. 9.5.

Note that, to avoid topological changes during simulations (i.e., free surface break-up by the baffle), there exists certain constraints in the admissible values for these parameters. These are mentioned below, when applicable.

We consider initially a point-like baffle of $L_b \times H_b = 1$ mm $\times$ 1 mm placed in the center $(x_b, y_b) = (0, 7.5)$ mm of the initial fluid domain. Then, we explore how the sloshing response is affected by each design parameter.

9.4.2 Performance analysis

Effect of baffle length and height, L_b and H_b

The effect of L_b is analyzed first. We consider four horizontal baffles with increasing values $L_b = 1$, 2, 4 and 8 mm and fixed $H_b = 1$ mm. The center $\mathcal{G}$ is placed at $(x_b, y_b) = (0, 7.5)$ mm. In Fig. 9.6(a), the sloshing frequency ω, decay time τ_{d}, and damping ratio ξ are illustrated as functions of L_b/L. These values are made dimensionless with the reference values $\omega_0/(2\pi) \simeq 0.667$ Hz, $\tau_{\mathrm{d}0} \simeq 21.09$ s and $\xi_0 \simeq 0.0326$ associated to the sloshing response without baffle.

Looking at ω, the influence of L_b is weak within the interval explored $L_b \in (0, 8]$ mm. Note, however, that in the limit $L_b \to L$, the baffle would effectively divide the liquid volume into two volumes with characteristic heights $H' \sim H/2$. As predicted by Eq. (9.13), this would

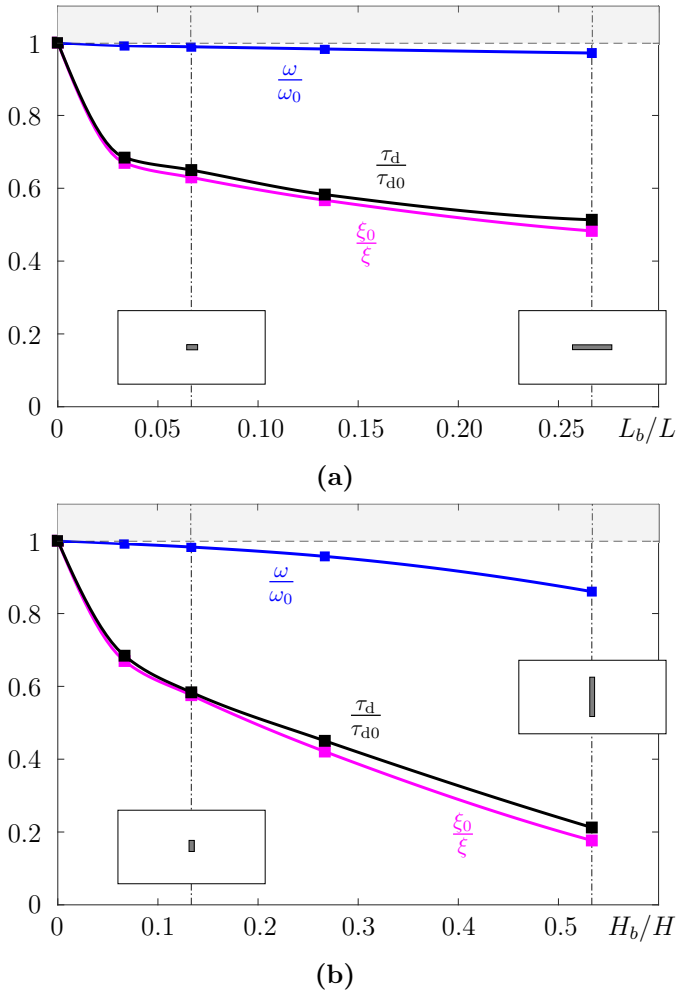


Figure 9.6: Effect of L_b (a) and H_b (b) on the sloshing frequency ω, decay time τ_d, and damping ratio ξ. The baffle dimensions are referenced to L and H, respectively, while ω, τ_d and ξ are made dimensionless with the reference values $\omega_0/(2\pi) \simeq 0.667$ Hz, $\tau_{d0} \simeq 21.09$ s and $\xi_0 \simeq 0.0326$ associated to the sloshing response without baffle.

modify the sloshing frequency if $kH' \ll 1$, i.e., in the limit of shallow layers. For sufficiently deep containers with $kH' \gg 1$, this has a negligible effect.

The values of τ_d and ξ, however, are more sensitive to L_b. For the point-like baffle, both values are improved by more than a 30% with respect to the reference case without baffle. By increasing L_b, this improvement increases in a nearly linear fashion up to a 50%. This trend can be explained in terms of viscous dissipation. Sloshing motion is characterized by horizontal streamlines in the central region of the container. The presence of horizontal baffles creates viscous boundary layers parallel to this flow stream that act all along the baffle length. The associated dissipation, therefore, is expected to increase with L_b.

Following the same approach, we analyze now the effect of H_b. Four vertical baffles with increasing $H_b = 1$, 2, 4 and 8 mm and fixed $L_b = 1$ mm are considered. Again, $\mathcal{G}$ is located at $(x_b, y_b) = (0, 7.5)$ mm. In Fig. 9.6(b), ω, τ_d and ξ are illustrated as functions of H_b/H.

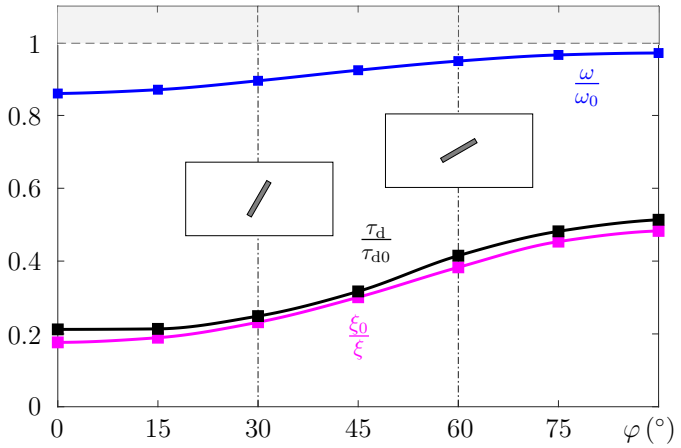


Figure 9.7: Effect of φ on ω, τ_d and ξ; these are made dimensionless with $\omega_0/(2\pi) \simeq 0.667$ Hz, $\tau_{\mathrm{d}0} \simeq 21.09$ s and $\xi_0 \simeq 0.0326$ associated to the sloshing response without baffle.

Vertical baffles are shown to have larger influence on ω. Surprisingly, there is a 15% decrease with respect to the reference case within the interval explored $H_b \in (0,\, 8]$ mm. This behavior is contrary to the frequency increase predicted by Eq. (9.13). This prediction, however, is only valid in the limit of a long vertical baffle that effectively acts like a wall; the largest vertical baffle of 1 mm $\times$ 8 mm considered here is not large enough to reflect this effect. Recall that there is a practical limitation on the maximum value of H_b for the present simulations to avoid the break-up of the free surface. To check this in more detail, refined meshes have been implemented to allow for larger vertical baffles. These simulations were characterized by a sloshing frequency $\omega/(2\pi) \simeq 1.818$ Hz, consistent with the increase by a 2.83 factor expected from the inviscid dispersion relation; see Sec. 9.3.

Looking now at τ_d and ξ, a strong enhancement of the response is evident, up to an 80% for the 1 mm $\times$ 8 mm vertical baffle. Besides the viscous effect discussed above, vertical baffles enforce a complete reconfiguration of the streamlines, intersecting them; see Fig. 9.3(b). This type of baffles restricts the horizontal transfer of fluid in the liquid bulk, and redirects the fluid towards the bottom wall and the free surface. As illustrated in the right panels of Fig. 9.4, these regions display larger horizontal velocities and locally increase viscous dissipation too.

From these results, one can highlight the 1 mm $\times$ 8 mm vertical centered baffle for its simplicity and good performance. Below, most of the explored baffles will be sequential modifications of this simple design.

Effect of baffle orientation, φ

The effect of φ is analyzed now. We consider 1 mm $\times$ 8 mm baffles centered at $(x_b,\, y_b) = (0,\, 7.5)$ mm with increasing values of $\varphi \in [0°,\, 90°]$; the analysis is restricted to this interval, considering the (approximate) time-averaged left-right reflection symmetry of the sloshing response. In Fig. 9.7, ω, τ_d and ξ are illustrated as functions of φ.

First, note that the cases $\varphi = 0°,\, 90°$ coincide with the largest vertical and horizontal designs

discussed above, respectively. Having this in mind, the obtained results are somewhat intuitive. For intermediate φ, the sloshing response is intermediate with respect to these cases. The baffle performance is thus deteriorated progressively as it is inclined.

This can be explained by looking at the projected dimensions of the baffle $(L_b', H_b') \approx H_b\,(\sin\varphi, \cos\varphi)$. As φ increases, H_b' decreases, as it does the baffle efficacy to intersect the streamlines, while L_b' increases, favouring viscous effects. Note that the curves of Fig. 9.7 resemble this sinusoidal dependence in both limits, with small derivatives near $\varphi = 0°, 90°$.

Considering this, two special baffles are evaluated. These designs are based on modifying H_b to preserve its projected height as the baffle is tilted. For the maximum projected height $H_b' = H_b \cos\varphi = 8$ mm considered in this work, the baffle dimensions are constrained by the container length: $H_b \sin\varphi < L$. Therefore, the maximum φ is given by $\varphi < \tan^{-1}(L/H_b') \simeq 75°$. In a more general scenario, one can consider the maximum projected height as H. This approach provides the upper bound $\varphi < \tan^{-1}\Gamma \simeq 63.4°$.

Baffle with $\varphi = 45°$ and $H_b' = \sqrt{2}\,H_b$. The sloshing response is characterized by $\omega/\omega_0 \simeq 0.865$, $\tau_\mathrm{d}/\tau_{\mathrm{d}0} \simeq 0.211$, and $\xi_0/\xi \simeq 0.177$.

Baffle with $\varphi = 60°$ and $H_b' = 2\,H_b$. The sloshing response is characterized by $\omega/\omega_0 \simeq 0.873$, $\tau_\mathrm{d}/\tau_{\mathrm{d}0} \simeq 0.214$, and $\xi_0/\xi \simeq 0.194$.

In both cases, the sloshing response is improved with respect to the simply rotated counterparts. Additionally, it can be observed that the improvement by lengthening the baffle is more beneficial for the case of $\varphi = 60°$. This can be explained by the fact that, at equal projected height, the extent to which streamlines are reorganized is similar, while the increased length of the baffle for $\varphi = 60°$ provides larger viscous dissipation. Indeed, the associated improvements can be quantified, for example, comparing the relative decrease in τ_d with respect to the inclined cases: $\Delta\tau_\mathrm{d} \simeq -33, -48\%$ for $\varphi = 45°, 60°$. Note that, in general, the reduced performance observed in Fig. 9.7 as φ increases is somewhat compensated by the augmented baffle dimensions and the associated viscous damping.

Furthermore, this idea of creating evolutionary designs based on previous results paves the way to the second part of this work, where complex baffles are proposed and assessed, identifying the sloshing mitigation mechanisms that come into play in each design. This will be discussed in detail in Sec. 9.5.

Effect of baffle position, (x_b, y_b)

Here, the effect of (x_b, y_b) is explored. Again, we consider the 1 mm × 8 mm vertical baffle and evaluate its performance when placed at different locations of the container.

We begin exploring the influence of its position along the x-axis. Four different x_b values are evaluated: $x_b = -1$, -3.75, -7.5 and -11.25 mm, with the last three values evenly spaced from the container midplane. Note that we restrict the analysis to $x_b < 0$, considering again the approximate reflection symmetry. In Fig. 9.8(a), ω, τ_d and ξ are illustrated as functions of x_b/L.

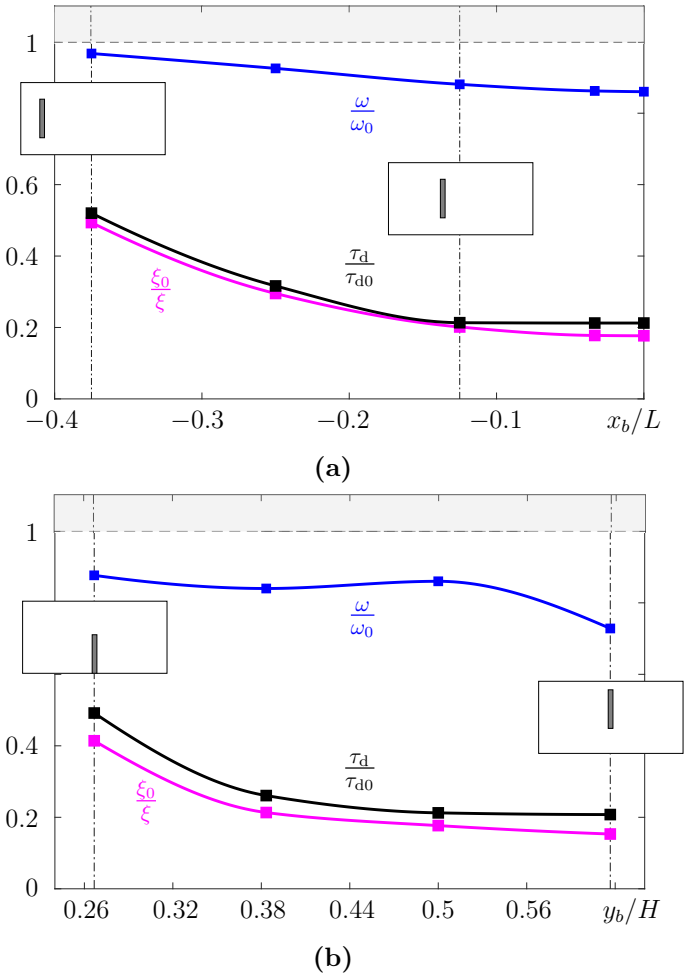


Figure 9.8: Effect of x_b (a) and y_b (b) on ω, τ_d and ξ. The coordinates (x_b, y_b) are referenced to H and L, respectively, while ω, τ_d and ξ are made dimensionless with $\omega_0/(2\pi) \simeq 0.667$ Hz, $\tau_{d0} \simeq 21.09$ s and $\xi_0 \simeq 0.0326$ associated to the sloshing response without baffle.

These results suggest a degraded sloshing mitigation — yet better that in the reference case — as soon as the baffle is placed with an offset respect to the central plane of the container, $x = 0$. When the baffle is centered, it divides the liquid domain into two equally-sized regions that shield the fluid motion evenly; see Fig. 9.3(b). By offsetting the x-position, as illustrated in Fig. 9.9, one of these regions grows (region B) while the other shrinks (region A). Although the behavior in the smaller region seems desirable with more complicated streamline paths and a narrower passage for the fluid, the larger region increasingly resembles the reference case without baffle. The net effect results in a worse performance than in the centered case. Put in other words, the centered baffle position is the most favorable for mitigating sloshing.

The effect of the baffle position along the y-axis is analyzed in a similar manner. Four different positions are evaluated: $y_b = 9.25$, 7.5, 5.75 and 4 mm. This last value is selected to explore the dynamics of a baffle that is in contact with the bottom wall, as in Ref. [53]. Note that this case is somewhat special, as it significantly modifies the flow pattern, with a characteristic transfer of fluid that is concentrated between the upper wall of the baffle and the free surface.

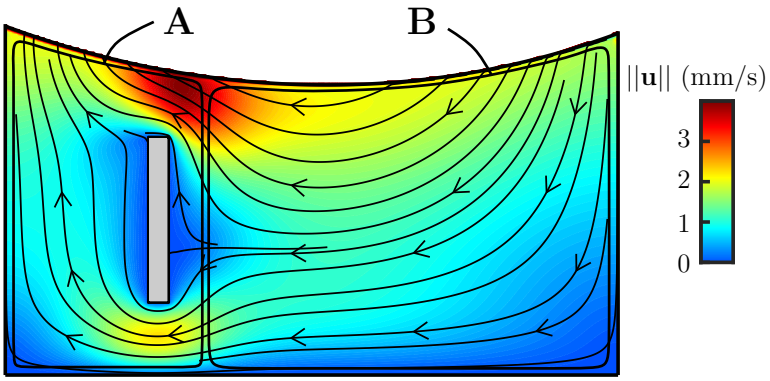


Figure 9.9: Instantaneous streamlines and velocity magnitude $||\mathbf{u}||$ at the $\mathcal{A} \simeq 0$ lapse of the oscillation with the 1 mm $\times$ 8 mm vertical baffle placed at $x_b = -7.5$ mm.

In Fig. 9.8(b), ω, τ_d, and ξ are illustrated as functions of y_b/H. An overall improvement is observed as the baffle gets closer to the free surface. However, we find it important to recall the limitation of the present numerical model associated with the free surface break-up.

To overcome this limitation, we have evaluated two cases where the baffle is placed high enough to intersect the free surface. Two different scenarios can be discussed.

The first one considers the baffle attached to the upper wall of a partially filled container. The baffle is then submerged into the liquid, dividing the free surface and leaving an encapsulated air pocket on each side. In this case, sloshing motion behaves similarly to two separated containers of length $L/2$. Besides this, since $\mathbf{a}(t)$ is positive along the x-axis, the fluid level on the right side of the container rises. The air volume on the right (left) side slightly compresses (expands) as the perturbation is applied, generating a pressure difference between both free surfaces. This pressure difference tends to push the fluid back to its initial equilibrium, driving a damped back-and-forth fluid motion.

The second case also involves a baffle partially submerged in the fluid, but not connected to the upper wall. Instead, the air above the liquid is not divided in two volumes and is at the same pressure during the process. After applying $\mathbf{a}(t)$, surface tension acts maintaining the shape of the free surfaces on both sides of the baffle. In this case, the fluid transfers from one side to the other of the baffle, while the air pressure is maintained during the process. This means that there is no restoring force that tends to bring the liquid back to its initial equilibrium and, if the perturbation is sufficiently large, the fluid would start to rotate around the baffle [220]. This motion is just damped by viscous effects.

This case highlights an important limitation of baffles: if the baffle divides the surface into two parts, connecting the air above it (as in the case of a partially submerged baffle), the desired behaviour is lost. In practice, this situation can be easily avoided as soon as three-dimensional containers are considered. For example, one could easily allow the liquid to connect close to the lateral walls of the container along that third dimension. This way, surface tension would act as a restoring force, bringing the free surface back to its original position. Another possible solution could be to add small holes or perforations to the baffle, that connect both sides of the container in various points at different heights, in order to preserve the desired

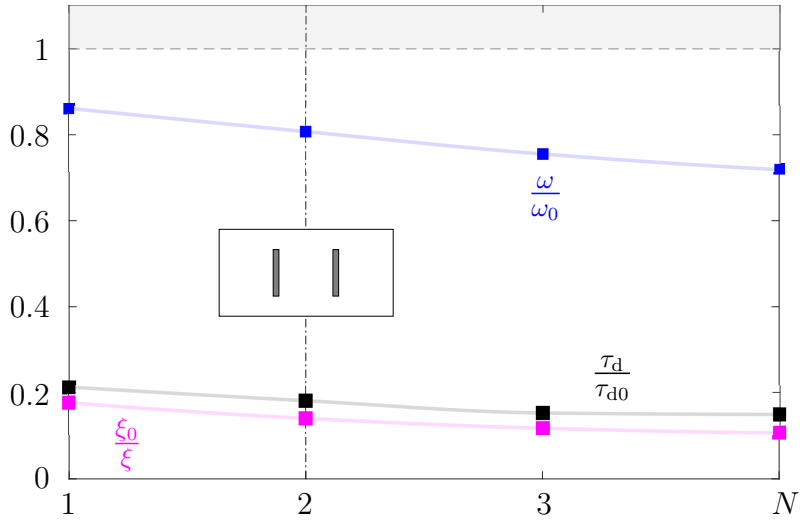


Figure 9.10: Effect of N on ω, τ_d and ξ; N vertical baffles equispaced along the container length L are considered. Values are made dimensionless with $\omega_0/(2\pi) \simeq 0.667$ Hz, $\tau_{d0} \simeq 21.09$ s and $\xi_0 \simeq 0.0326$ associated to the case without baffle.

behaviour at different tank fill levels (like a narrow grid).

As a final conclusion of this parametric study, no other parameter improves the sloshing response as much as H_b does. In accord to this, the 1 mm $\times$ 8 mm vertical centered baffle can be easily identified as the optimal design, since it outperforms any of the other explored designs.

Number of baffles

To complete this analysis, we explore the influence of having multiple vertical baffles. We consider a design of N baffles evenly spaced along the container length, so that it is effectively divided into $N + 1$ regions of equal length. Each baffle has dimensions 1 mm $\times$ 8 mm and are all located at $y_b = 7.5$ mm, so that they are completely surrounded by liquid. The results are presented in Fig. 9.10, where the sloshing response is presented as a function of N for $N = 1$, 2, 3 and 4.

The straightforward conclusion is the positive effect of additional baffles on the sloshing response, increasing ξ and reducing τ_d. With each additional baffle, however, the relative improvement is less pronounced and the available liquid volume is penalized, making this design alternative less attractive.

With $N = 2$, the reason behind the observed improvement is the flow configuration. The baffles localize the fluid motion around them, pushing the liquid towards the bottom wall and the free surface, and preventing the formation of horizontal streamlines in the center of the tank, where they would naturally occur in their absence. As additional baffles are included, the relative improvement diminishes to the point that placing four baffles becomes practically insignificant. For $N = 4$, in particular, we observe that the most effective baffles are those located near the center of the tank, while the other two outer baffles have less impact on the

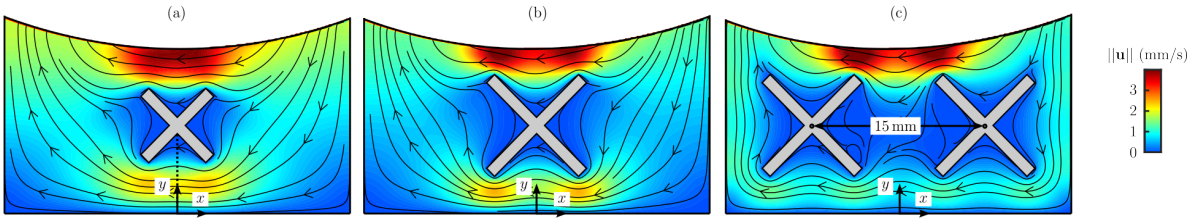


Figure 9.11: Four-arm cross-shaped baffles: (a) nominal arm length – Cross-4-1, (b) extended arm length – Cross-4-1-extended, (c) two extended arm length baffles – Cross-4-2-extended. Instantaneous streamlines and velocity magnitude $||\mathbf{u}||$ close to the first $\mathcal{A} \simeq 0$ of the sloshing response.

flow pattern. This helps explain why the improvement, if any, is minimal for $N > 3$.

In terms of ω, no significant variation or, at least, not as pronounced as Eq. (9.13) anticipates, is observed. As discussed above, this is attributed to the fact that baffles are not long enough to divide the liquid volume into $N + 1$ compartments of length $L' \sim L/N$, and observe such frequency variation. For large N, in contrast, the set of baffles would not affect the effective container length but its height H', leaving a long shallow layer of liquid above them, and making the system sensitive to H', if $kH' \ll 1$. Note, however, that this scenario lacks of practical interest, since the available liquid volume would be significantly reduced.

9.5 Complex baffle designs and complementary strategies

As anticipated above, the results of Sec. 9.4 suggest themselves for further investigation. In this section, we explore more complex designs, including cross-shaped baffles, as a natural extension of oblique baffles, and free surface baffles, characterized by a stronger interaction with the free surface. To extend the analysis, we also explore the novel sloshing reduction strategy proposed in Ref. [225], combining active thermocapillary-based control with passive baffles.

9.5.1 Cross-shaped baffles

In this section, we focus on a specific type of baffles: the cross-shaped baffles. Designs with four and three arms, and variable lengths are explored.

In general, this baffle design helps reduce τ_d by trapping a large amount of fluid between their arms and stagnating it. The remaining liquid flows around this quiescent region. The length of the arms has the intuitive effect of enlarging this quiescent zone, forcing a more pronounced reorganization of the flow pattern around.

Four-arm cross-shaped baffles

The starting baffle for this subsection is formed by combining two centered baffles of dimensions 1 mm × 8 mm oriented obliquely at $\varphi = \pm 45°$, forming a cross. Then, we explore a baffle with an arm length extended by a factor of $\sqrt{2}$, as discussed in Sec. 9.4.2. Finally, an additional

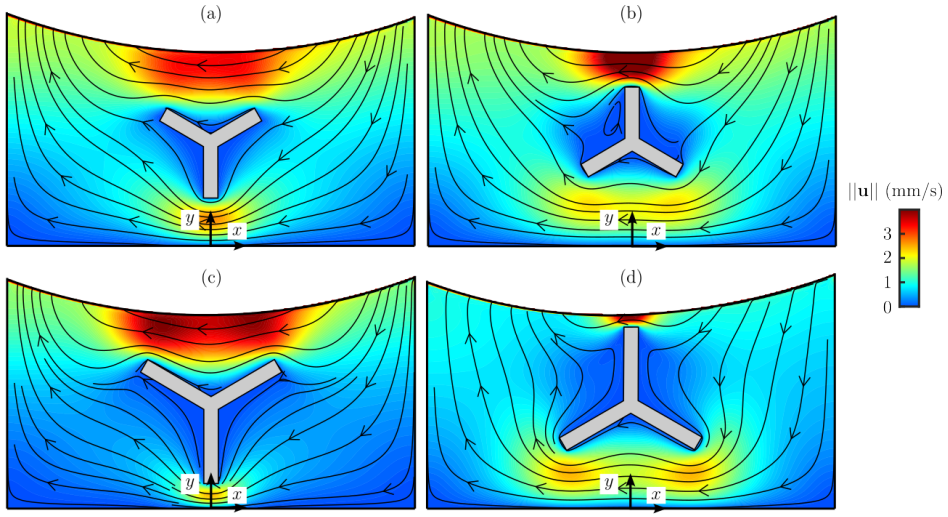


Figure 9.12: Three-arm cross-shaped baffles: (a) downright nominal arm length – Cross-3-D, (b) upright nominal arm length – Cross-3-U, (c) downright extended arm length – Cross-3-D-extended, (d) upright extended arm length – Cross-3-U-extended. Instantaneous streamlines and velocity magnitude $||\mathbf{u}||$ close to the first $\mathcal{A} \simeq 0$ of the sloshing response.

scenario with two identical cross-shaped baffles with extended arm length located at $x_b = \pm 7.5$ mm is considered. These designs are illustrated in Fig 9.11. For the sake of clarity, we refer to these baffles as 'Cross-4-1', 'Cross-4-1-extended' and 'Cross-4-2-extended' following the same order. Here, the reference 'Cross' denotes the baffle shape, the digits 4 and 1/2 refer to the number of arms and the number of baffles in the design, and the increased arm length is denoted by the suffix 'extended'.

The sloshing response is characterized by:

- Cross-4-1: $\omega/(2\pi) \simeq 0.582$ Hz, $\tau_\mathrm{d} \simeq 5.33$ s and $\xi \simeq 0.1493$.
- Cross-4-1-extended: $\omega/(2\pi) \simeq 0.511$ Hz, $\tau_\mathrm{d} \simeq 3.18$ s and $\xi \simeq 0.2806$.
- Cross-4-2-extended: $\omega/(2\pi) \simeq 0.450$ Hz, $\tau_\mathrm{d} \simeq 2.68$ s and $\xi \simeq 0.5045$.

The performance is better for the multiple (cross-shaped) baffle case. This design, however, can penalize substantially the amount of available liquid volume within the tank. For instance, the relative improvement between cases 'Cross-4-1-extended' and 'Cross-4-2-extended', doubles the baffle mass and reduces the fluid volume accordingly.

In any case, this design constraint can be likely alleviated by optimizing the baffle design in a more detailed analysis. This can be achieved by reducing the baffle thickness, using lighter materials like composite structures, or allowing the baffle to be filled with fluid.

Three-arm cross-shaped baffles

The architecture of these baffles is similar to the previous ones, consisting of 1 mm thick arms with a 4 mm length. Here, three arms configurations are considered, separated by 120°. Two interesting positions are found for this type of baffles, as illustrated in Fig. 9.12(a, b).

Similarly to the previous cases, additional designs with an arm length scaled by a factor $\sqrt{2}$ are considered; see Fig. 9.12(c, d). Note that, given the relative semi-angle of 60° between each arm, a scale factor of 2 should have been considered instead. This configuration, however, provides an excessively large projected height, getting too close to the free surface or the bottom wall.

Again, the reference for these baffles is as follows: 'Cross-3-D', 'Cross-3-D-extended', 'Cross-3-U' and 'Cross-3-U-extended', where the digit '3' refers to the number of arms, 'D/U' to its downright/upright orientation, and the suffix 'extended' denotes an extended arm length.

The sloshing response is characterized by:

- Cross-3-D: $\omega/(2\pi) \simeq 0.603$ Hz, $\tau_{\mathrm{d}} \simeq 5.92$ s and $\xi \simeq 0.1320$.
- Cross-3-U: $\omega/(2\pi) \simeq 0.577$ Hz, $\tau_{\mathrm{d}} \simeq 5.20$ s and $\xi \simeq 0.1615$.
- Cross-3-D-extended: $\omega/(2\pi) \simeq 0.511$ Hz, $\tau_{\mathrm{d}} \simeq 3.26$ s and $\xi \simeq 0.2439$.
- Cross-3-U-extended: $\omega/(2\pi) \simeq 0.392$ Hz, $\tau_{\mathrm{d}} \simeq 2.83$ s and $\xi \simeq 0.3947$.

The improved performance of the extended arm cases is attributed to the supplemental effects of a larger vertical arm and the increased amount of stagnated liquid around the baffle. Note that the 'Cross-3-U-...' cases outperform the four-arm counterparts 'Cross-4-1-...'. This means that, for a three-arm baffle with the same arm length, the response is better, but with the additional consideration of placing the baffle in an upright orientation. In this scenario, three-arm baffles present the additional advantage of providing a large available liquid volume in the container, while requiring less baffle material.

9.5.2 Free surface baffles

Free surface baffles, also referred here as interfacial baffles, are the culmination of this evolutionary design process. Six different classes are tested, all inspired by the horizontal baffle designs found in the literature, where the baffle is typically attached to the lateral walls of the container [266], combined with some of the lessons learned from previous sections.

These surface baffles are expected to interfere to a greater extent with the fluid flow underneath the free surface. As a consequence, we expect these baffles to achieve their peak performance when sufficiently close to the free surface.

If considerable variations in the container filling ratio are expected, two problems may arise: for reduced filling ratios, the liquid response would resemble that of the reference case and the baffles just act as lower tank "ceiling" in some cases; for increasing filling ratios, the baffles may be partially submerged. The latter case involves a complexity that cannot be analyzed properly with the moving-mesh approach used here, as the free surface would be segmented and any perturbation may give rise to free surface break-up. Contact properties as well as the fragmented free surface shape are expected to play a key role in the sloshing behavior of such systems, which lie beyond the scope of the present study.

Based on the previous discussion, we could assume that surface baffles optimize the fluid sloshing response over a certain range of filling ratios. This consideration opens the possibility

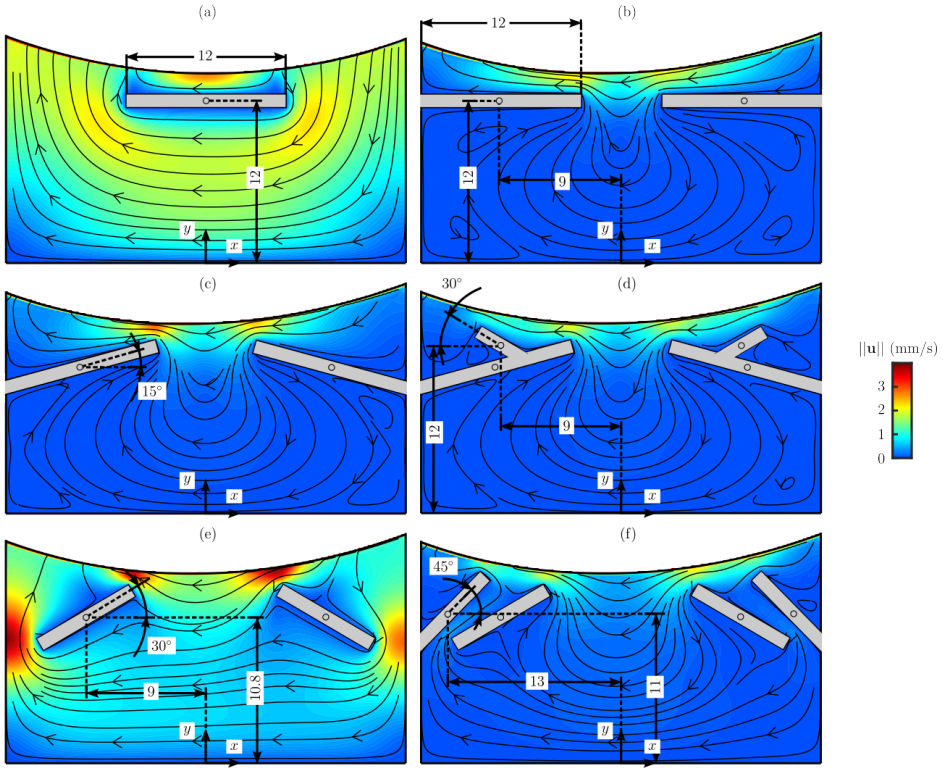


Figure 9.13: Free surface baffles: (a–f) type 1–6. Instantaneous streamlines and velocity magnitude $||\mathbf{u}||$ close to the first $\mathcal{A} \simeq 0$ of the sloshing response.

of another typical strategy: placing these surface baffles repeatedly along the lateral walls of the container, hence acting effectively at different fluid levels. Note that this design alternative is associated with increased structural mass and reduced tank capacity. Another limitation is that the baffle geometry should avoid highly complex geometries, as some liquid could get trapped, leaving residues inside the tank.

The six different types of free surface baffles, numbered 1 to 6, are grouped, for practical reasons, into three groups. Their geometric definition and performance is presented hereafter. At a numerical level, the analysis of these baffles is limited due to their proximity to the free surface. For all cases, the criterion of maintaining a distance of approximately $0.1\,H$ from the surface after the contact angle is settled is respected.

Type 1 and 2

These designs are illustrated in Fig. 9.13(a, b). The type 1 baffle is a horizontal baffle with dimensions $L_b \times H_b = 12$ mm $\times$ 1 mm located at $(x_b, y_b) = (0, 12)$ mm, i.e., centered along the x-axis and displaced toward the free surface. The type 2 design consists of two baffles of the same dimensions as the previous one, at the same height, but placed in such a way that they are attached to the side walls, i.e., $x_b = \pm 9$ mm.

For the type 1 baffle, the performance is similar to that observed for horizontal baffles in Sec. 9.4.2 with a sloshing frequency $\omega/(2\pi) \simeq 0.567$ Hz. The streamlines easily surround the

baffle, without a strong reorganization of the flow. The increased length, however, favours viscous dissipation and drives a fast mitigation of the sloshing response. Compared to the reference case without baffle, the decay time is $\tau_\mathrm{d} \simeq 4.62$ s, reduced by a 79% factor.

The type 2 design behaves differently. Two mechanisms come into play for an improved performance. First, each baffle isolates the fluid underneath, which remains quiescent during the sloshing oscillation; sloshing is reduced by stagnating a large amount of fluid. Second, the layers of liquid above, where the sloshing motion is concentrated, behave as if it was a large aspect ratio container; sloshing is reduced by the effective modification of the geometry of the tank. Associated to this effect, a significant decrease in the sloshing frequency to $\omega/(2\pi) \simeq 0.188$ Hz is observed, as predicted by Eq. (9.13). Regarding τ_d, it is reduced by a 92% factor to 1.73 s, while damping increases to $\xi \simeq 0.8002$, since viscous dissipation becomes dominant over the entire height of the upper layer of liquid. In line with this, the maximum $\mathcal{A}$ reached is significantly reduced as well, as less mass of the fluid is set in motion due to the aforementioned effect of the fluid stagnation below the baffles.

Type 3 and 4

The type 3 design is derived from the previous configuration by tilting both baffles symmetrically, targeting to reproduce the shape of a V-shaped container. Recall that this type of containers were shown to double the sloshing frequency compared to their rectangular counterparts [49].

The left baffle had the same dimensions as the previous ones (12 mm $\times$ 1 mm) and forms a 15° angle with respect to the x-axis, with its center at $(x_b, y_b) = (-9.45, 10.8)$ mm. As anticipated above, the right baffle is symmetric with respect to the midplane of the container. A sketch of this design is provided in Fig. 9.13(c).

The performance is characterized by $\omega/(2\pi) \simeq 0.194$ Hz, $\tau_\mathrm{d} \simeq 1.66$ s and $\xi \simeq 0.7881$. First, note that the frequency decreases, indicating that, to emulate the response of a V-shaped container, both baffles need to be much longer than the 12 mm length considered here.

In terms of response parameters, this baffle seems to be an upgrade of the type 2. While the same underlying mechanisms are still working — the liquid below these baffles remains quiet and encapsulated, and the fluid motion is concentrated in the vicinity of the free surface —, there seems to be an additional effect that involves the bulk of fluid at each sides of the tank. The result of tilting the baffles constrains the stream even more to the surface, and creates at each sides of the tank a large bulk of fluid that remains with much less velocity than the coming stream, having a greater slowing effect.

Based on the previous design, baffle type 4 aims to improve its performance by including a protrusion of 1 mm $\times$ 4 mm to each baffle, forming a 30° angle with the horizontal and centered at $(x_b,\, y_b) = (-9, 12.4)$ mm. A sketch of this design is provided in Fig. 9.13(d). The results are characterized by $\omega/(2\pi) \simeq 0.110$ Hz, $\tau_\mathrm{d} \simeq 2.01$ s and $\xi \simeq 0.9347$. These baffles achieve an improvement in comparison to the previous regarding ξ, but, on the other hand, ω and τ_d are worse. This is because when trying to further optimize baffles that already have a damping of around $\xi \sim 0.7 - 0.8$, the system has an enhanced damping but paying the price of having a slower response. This follows the typical criterion for a desirable damping

in second order systems $\xi \sim 0.7 - 0.8$, as more damping would slow down the response too much.

The main effect of the protrusions is enhancing the viscous effects on the previous baffle. As a direct consequence, the fluid near the side walls barely moves, creating small pockets where it becomes almost steady and helps slowing down the currents of sloshing when they are about to reach the walls. Furthermore, it concentrates the motion even more at the free surface, isolating the rest of the fluid, and due to its angular shape, the streamline paths zigzag as they pass over these protrusions.

Type 5 and 6

The type 5 results from the idea of trying to maximize the protection of the areas in contact with the wall by positioning the baffles perpendicular to the local streamlines; the idea is similar to that of the vertical centered baffle, which was also positioned perpendicular to the streamlines in the center of the tank. Additionally, it has the advantage of not being very vertical, its design is simple, and it is not attached to the wall, which avoids all the potential difficulties mentioned earlier.

A sketch of this design is provided in Fig. 9.13(e). Geometrically, it is defined as follows: the left baffle has dimensions 8 mm $\times$ 1 mm, forms a 30° angle with the horizontal, and its center is located at $(x_b, y_b) = (-9, 10.8)$ mm. The right baffle is a left-right reflection with respect to the midplane of the container.

The sloshing response for baffle 5 is characterized by $\omega/(2\pi) \simeq 0.433$ Hz, $\tau_{\mathrm{d}} \simeq 2.70$ s and $\xi \simeq 0.3537$. The performance is improved with respect to the centered vertical baffle. Here, the streamlines on both sides of the container surround each baffle, causing local velocity increases in the vicinity of the baffle ends. These results suggest a family of designs with multiple baffles that progressively separate from the center of the container while keeping a local perpendicular orientation with respect to the streamlines of the reference case.

Finally, the type 6 design arises from an attempt to "fine-tune" type 5 baffles. The geometry of this design is the same as the former, with extra wall protrusions. The left protrusion has dimensions 8 mm $\times$ 1 mm, an angle of $\varphi = 45°$, and its center position is $(x_b,\, y_b) = (-13, 11)$ mm. The right protrusion is its symmetric counterpart with respect to the y-axis. A sketch of this design is provided in Fig. 9.13(f).

In the type 5 design, there is a strong flow along the side walls that significantly contributes to the variation in asymmetry. When the fluid moves towards the left, two currents can be observed: one near the free surface (as the baffle restricts the movement in that area) and another upward and parallel to the left wall, which contributes to raising that contact point too. The purpose of the type 6 design is to redirect this flow through protrusions and direct it opposed to the surface flow, eliminating not only the upward flow by redirecting it to another point but also slowing down the surface flow, as an opposed current is impacting it.

The associated sloshing response is characterized by $\omega/(2\pi) \simeq 0.005$ Hz, $\tau_{\mathrm{d}} \simeq 2.05$ s and $\xi \simeq 0.9999$. It is worth noting that this design displays the highest damping coefficient within the scope of this work. Again, it is not surprising that despite having the highest damping,

its decay time is somewhat worse than for other baffles, as it occurred with baffle type 4.

9.5.3 Passive baffles and thermocapillary-based control

As discussed in the work of Peromingo et al. [225], thermocapillary control is an effective alternative to actively reduce sloshing in microgravity. In particular, these authors showed that this active strategy is generally able to reduce the natural τ_{d} of sloshing by a 50% with reasonable cost; the required thermal performance is found within the envelope of comercially available Peltier element devices. Furthermore, a novel strategy combining thermocapillary controllers with a centered vertical passive baffle was analyzed. On its own, the baffle reduced τ_{d} by an 80% factor with respect to the uncontrolled case at zero cost, consistent with the results of Fig. 9.6(b). Besides this, the thermal output demanded by the thermocapillary controller was significantly alleviated.

Here, we extend these efforts and analyze the combined performance of different types of passive baffles with active thermocapillary controllers. The same standard proportional-derivative (PD) control, characterized by its proportional K_P and derivative K_D gains, is considered. The controller produces the signal ΔT following the law:

$$\Delta T = -K_P \mathcal{A} - K_D \frac{d\mathcal{A}}{dt}. \tag{9.15}$$

This signal is applied (anti-symmetrically) at the lateral walls of the container to reduce $\mathcal{A}$. For further details on the complete mathematical formulation, boundary conditions including the thermocapillary effect, and numerical implementation, the reader is referred to Refs. [201, 225].

To provide an example of application, we investigate first the combined performance of two vertical baffles and an intermediate controller with $K_P = 250$ K/m and $K_D = 1000$ K s/m. This type of controller provides a good compromise between reduced decay time and reasonable thermal output [225]. In Fig. 9.14, the time evolution of the asymmetry $\mathcal{A}$ is shown in panel (a), together with the required controller output, characterized by ΔT and its time derivative ΔT_t, in panel (b). The associated decay times are indicated with vertical lines in (a). Results for the case with baffles (light red) and combined with thermocapillary control (red) are included for visual comparison. The associated performance of the thermocapillary controller alone is shown in gray.

As discussed in Sec. 9.4.2, the design including two vertical baffles already provides a good sloshing response, characterized by $\omega/(2\pi) \simeq 0.539$ Hz, $\tau_{\mathrm{d}} \simeq 3.82$ s and $\xi \simeq 0.2318$. The supplemental contribution of the thermocapillary controller reduces the decay time to 2.98 s, by a 22% compared to the performance of the baffle design alone. The presence of baffles, on the other hand, alleviates the thermal requirement on the controller output by a 30%, reducing the maximum ΔT from -4.09 K to -2.79 K, and the maximum time derivative ΔT_t from -19.64 K/s to -13.73 K/s. Consistent with Ref. [225], note that this required thermal envelope can be achieved by commercial Peltier elements.

To provide other examples, we further evaluate this intermediate controller combined with selected baffle designs. The performance, in each case, is as follows:

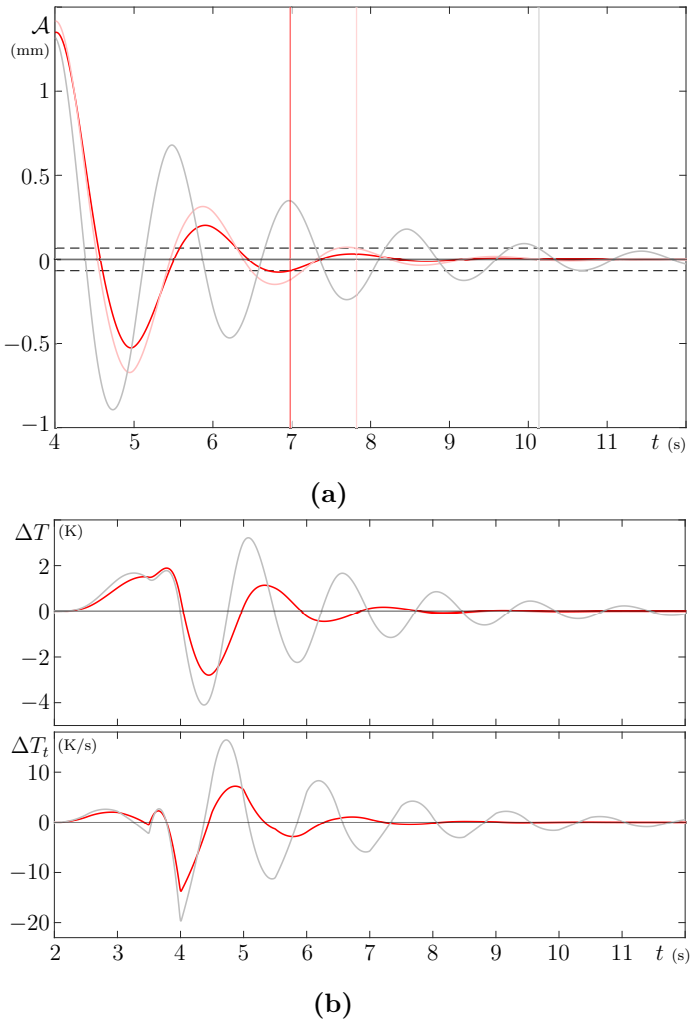


Figure 9.14: Performance of an intermediate thermocapillary controller with $(K_P, K_D) = (250, 1000)$ combined with two vertical passive baffles (red) and without them (light red). Time evolution of the asymmetry $\mathcal{A}$ (a) and controller output ΔT, ΔT_t (b). The associated performance of the thermocapillary controller alone is shown in gray for comparison.

- Vertical centered baffle: $\omega/(2\pi) \simeq 0.568$ Hz, $\tau_{\mathrm{d}} \simeq 2.94$ s and $\xi \simeq 0.2488$.
- Three vertical baffles: $\omega/(2\pi) \simeq 0.496$ Hz, $\tau_{\mathrm{d}} \simeq 2.98$ s and $\xi \simeq 0.2898$.
- 'Cross-4-1': $\omega/(2\pi) \simeq 0.578$ Hz, $\tau_{\mathrm{d}} \simeq 3.68$ s and $\xi \simeq 0.2139$.
- 'Cross-4-1-extended': $\omega/(2\pi) \simeq 0.502$ Hz, $\tau_{\mathrm{d}} \simeq 2.38$ s and $\xi \simeq 0.3360$.
- 'Cross-3-D': $\omega/(2\pi) \simeq 0.599$ Hz, $\tau_{\mathrm{d}} \simeq 3.60$ s and $\xi \simeq 0.1986$.
- 'Cross-3-U': $\omega/(2\pi) \simeq 0.573$ Hz, $\tau_{\mathrm{d}} \simeq 3.65$ s and $\xi \simeq 0.2250$.
- 'Cross-3-D-extended': $\omega/(2\pi) \simeq 0.5016$ Hz, $\tau_{\mathrm{d}} \simeq 2.41$ s and $\xi \simeq 0.2985$.
- 'Cross-3-U-extended': $\omega/(2\pi) \simeq 0.384$ Hz, $\tau_{\mathrm{d}} \simeq 1.95$ s and $\xi \simeq 0.4365$.
- Type 2 free surface baffle: $\omega/(2\pi) \simeq 0.187$ Hz, $\tau_{\mathrm{d}} \simeq 1.69$ s and $\xi \simeq 0.8001$.

- Type 3 free surface baffle: $\omega/(2\pi) \simeq 0.191$ Hz, $\tau_{\mathrm{d}} \simeq 1.65$ s and $\xi \simeq 0.8035$.
- Type 4 free surface baffle: $\omega/(2\pi) \simeq 0.103$ Hz, $\tau_{\mathrm{d}} \simeq 2.02$ s and $\xi \simeq 0.9431$.
- Type 5 free surface baffle: $\omega/(2\pi) \simeq 0.4281$ Hz, $\tau_{\mathrm{d}} \simeq 2.60$ s and $\xi \simeq 0.3864$.

Overall, thermocapillary control improves the performance of each baffle design, reducing τ_{d} and increasing ξ. The associated improvement is, however, different in each case, fact that can be explained in terms of the baffle performance without control and the controller gains. On the one hand, note that the improvement is more pronounced for baffle designs with a moderate performance. Free surface baffles, for instance, already provide the largest reductions in τ_{d} and are thus less sensitive to the thermocapillary control. The controller gains, on the other hand, can be selected to optimize the system response in terms of τ_{d}, cost or a trade-off between both. The values used here are reproduced from Ref. [225], where they were shown to provide an intermediate performance without baffles, and are not optimized for any particular baffle design. In this sense, the present results can be improved case-by-case following the approach of Ref. [225]. This tailored selection of controller gains is not considered in this work and will be undertaken elsewhere.

9.6 Overview and summary of results

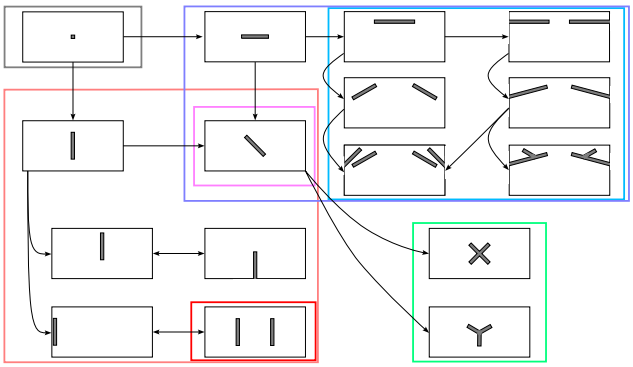
For the sake of clarity, a summary of the obtained results is given in this section. Figure 9.15(a) illustrates the roadmap followed to explore the different baffle designs, from the initial point-like baffle, to the more complex cross-shaped and free surface baffles. Panel (b) summarizes the performance (square markers) of each type of baffle design in terms of (ω/ω_0) and $(\tau_{\mathrm{d}}/\tau_{\mathrm{d0}})$. The associated performance envelope of selected baffles combined with thermocapillary control is denoted with solid lines and circular markers. Table 9.3 outlines the sloshing response of the most representative designs explored, and that of the novel strategy based on supplementary thermocapillary control. Recall that the reference case without baffle is characterized by $\omega_0/(2\pi) \simeq 0.667$ Hz, $\tau_{\mathrm{d0}} \simeq 21.09$ s and $\xi_0 \simeq 0.0326$.

The effectiveness of passive baffles is evident from the very beginning of the present analysis, since the addition of a centered point-like baffle of 1 mm $\times$ 1 mm already provides a 30% reduction (increase) in τ_{d} (ξ) to 14.13 s. From this simple baffle, the effect of the baffle length L_b, height H_b, position, and orientation φ is revised:

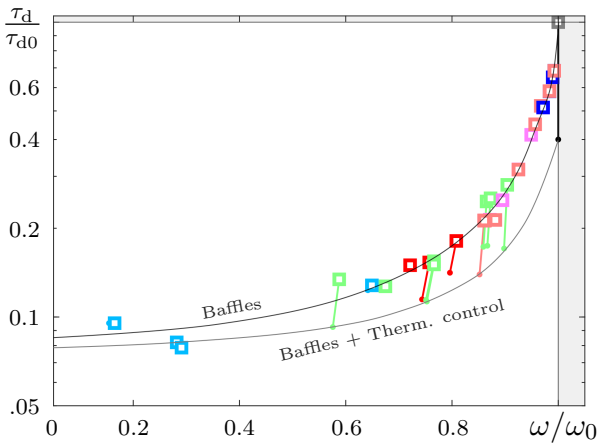
— By increasing L_b, one can explore a wide variety of horizontal baffles (marked in blue in Fig. 9.15). This family of baffles shows a relatively small reduction in τ_{d} up to a 49%, supported by the increased viscous dissipation associated to the baffle dimension.

— By increasing H_b, vertical baffles are investigated (marked in light red in Fig. 9.15). Besides increasing viscous damping, this type of baffles also acts intersecting the streamlines and re-organizing the flow around them. Various designs are explored varying H_b and its position $(x_b,\, y_b)$. The optimal response is found for the 1 mm $\times$ 8 mm centered vertical baffle. With this simple design, τ_{d} is reduced by a 79% to 4.48 s. This can be further improved by offsetting its vertical position towards the free surface.

— As an intermediate type of baffles, oblique baffles (marked in pink in Fig. 9.15) resulting



(a)



(b)

Figure 9.15: (a) Roadmap of the baffle designs considered in this work. (b) Summary of the baffles performance (square markers) in terms of ω/ω_0 and τ_d/τ_{d0}. Each marker is color-coded according to the type of baffle: reference case (gray), horizontal baffles (blue), vertical baffles (light red), oblique baffles (pink), multiple vertical baffles (red), cross-shaped baffles (green) and free surface baffles (light blue). The associated performance envelope combined with thermocapillary control is denoted with solid lines and circular markers in selected cases.

from varying φ, are analyzed. As one would expect, the sloshing response is found midway that of horizontal and vertical baffles. Special cases with extended baffle dimensions that preserve the projected height of the baffle are also tested, showing a better performance compared to their "nominal" length counterparts.

As a natural extension of the simple vertical baffle, we check the effect of having multiple vertical baffles (marked in red in Fig. 9.15) equi-spaced within in the container length. Compared to a single-baffle design, these multiple-baffle solutions further enhance the sloshing response by reducing τ_d up to 3.23 s, that is, by an additional 28%.

In addition to simple baffles, we also investigate:

— Cross-shaped baffles (marked in green in Fig. 9.15). This design family is motivated by the results of oblique baffles. They improve the overall performance of oblique baffles, reducing the decay time up to 85%. Different designs, including four or three arms,

variable lengths, and single-baffle or multiple-baffle arrangements are considered.

— Free surface baffles (marked in light blue in Fig. 9.15). These result from progressive modifications of horizontal baffles and previous works found in the literature. Six different types of surface baffles are tested, showing the best performances in terms of τ_d.

Motivated by recent work [225], we also evaluate the sloshing reduction strategy based on combining passive baffles and active thermocapillary control. On their own, thermocapillary controllers are able to reduce τ_d up to a 50–60% with reasonable controller output. This performance envelope is marked in Fig. 9.15(b) by a solid vertical black line; note that ω is almost insensitive to the thermal control.

The other cases explored in this work are similarly marked by colored solid lines (and circular markers) in panel (b). In these cases, the performance is calculated for an intermediate controller, requiring a thermal output achievable by commercial Peltier elements. These results suggest a lower bound in τ_d that delimits the operational envelope of the combined strategy. In this sense, note that the thermocapillary control is more effective for baffle designs with intermediate values of τ_d. When applied in combination with free surface baffles, for which a significant reduction in τ_d is already achieved, the supplemental effect of the thermal control is almost imperceptible. In line with this, results also suggest a maximum reduction in τ_d by an approximate 93% factor.

9.7 Conclusions

Throughout this manuscript, we analyzed in detail the design and performance of passive baffles for sloshing reduction in microgravity. Sloshing dynamics were investigated for a rectangular container holding a volume $L \times H = 30$ mm $\times$ 15 mm of liquid with properties similar to a 5 cSt silicone oil, and for a static contact angle of 70°. The sloshing response to a pulse-like perturbation was characterized in terms of the sloshing frequency ω, the decay time τ_d, and damping ratio ξ.

The analysis focused first on simple rectangular baffles, parameterized in terms of their length and height, position of its center, and orientation. The sensitivity of the sloshing response to variations in these parameters was carefully investigated. From these results, the vertical 1 mm $\times$ 8 mm centered baffle highlighted for its design simplicity and good performance. Compared to the natural response of the system, this baffle design was shown to achieve an 80% reduction in τ_d.

Motivated by these results, we extended the analysis to other baffle designs of higher complexity, including cross-shaped baffles of four and three arms, and free surface baffles, characterized by an increased interaction with the fluid flow in the vicinity of the free surface.

Overall, the associated designs suggest a trade-off between design simplicity and performance. This performance was shown to be tightly related with the existing interaction between the baffles and the fluid flow. In this regard, the obtained results can be classified as follows:

Free surface baffles effectively divide the container into two regions: a shallow layer of fluid

near the free surface, and the region beneath them, which contains the majority of the fluid and remain relatively quiescent. The sloshing motion concentrates within the liquid layer near the free surface, resembling the behavior observed in large aspect ratio containers. Thus, the sloshing frequency decreases, consistent with the dispersion relation (9.13).

The remaining types of baffles act as obstacles for the bulk flow. If we focus on the vertical baffles, we observe a significant decrease in ω. Placing an obstacle in the middle of the container complicates the transfer of liquid from one half to the other (from the left side to the right, and vice-versa). As a result, the sloshing motion is slower, leading to a decrease in the associated frequency. This observation helps explain the decrease in the sloshing frequency detected, and can be extended to the other types of baffles considered.

Motivated by the recent work of Peromingo et al. [225], we also explored the performance of passive baffles combined with active thermocapillary controllers. We showed that thermocapillary control is more effective for baffle designs with intermediate values of τ_{d}. Furthermore, the present results also suggested a performance envelope for this combined strategy, and that the maximum achievable reduction in τ_{d} is limited to approximately a 90%.

Finally, directions for future work may include the consideration of other fluids and containers [220], exploration of more advanced control schemes or mixed strategies that combine these approaches with, for example, active or moving baffles or magnetic control, and experiments in reduced gravity.

Acknowledgments This work was supported by the Ministerio de Ciencia e Innovación under Project No. PID2020-115086GB-C31, and by the Spanish User Support and Operations Centre (E-USOC), Center for Computational Simulation (CCS).

Author declarations

Conflict of interest The authors have no conflict of interest to disclose.

Data Availability Statement The data that supports the findings of this study are available within the article.

Baffle type	x_b/L	y_b/H	L_b (mm) × H_b (mm)	φ (°)	$\omega/(2\pi)$ (Hz)	τ_d (s)	ξ ($\times 10^{-1}$)
None	—	—	—	—	0.667	21.09	0.326
Simple baffles							
Point	0	1/2	1 × 1	0	0.662	14.43	0.487
Horizontal short	0	1/2	2 × 1	0	0.660	13.71	0.518
Horizontal medium	0	1/2	4 × 1	0	0.656	12.29	0.575
Horizontal	0	1/2	8 × 1	0	0.648	10.83	0.676
Vertical short	0	1/2	1 × 2	0	0.656	12.31	0.567
Vertical medium	0	1/2	1 × 4	0	0.638	9.50	0.775
Vertical (optimal)	0	1/2	1 × 8	0	0.574	4.48	1.846
Vertical x-offset	−1/4	1/2	1 × 8	0	0.617	6.67	1.106
Vertical y-offset	0	7/60	1 × 8	0	0.486	4.38	2.130
Inclined	0	1/2	1 × 8	30	0.597	5.25	1.406
Inclined	0	1/2	1 × 8	45	0.617	6.68	1.086
Inclined	0	1/2	1 × 8	60	0.633	8.75	0.853
Inclined extended	0	1/2	1 × 11.31	45	0.577	4.44	1.845
Two vertical	±1/6	1/2	1 × 8	0	0.539	3.82	2.318
Three vertical	±1/4, 0	1/2	1 × 8	0	0.505	3.23	2.762
Cross-shaped baffles							
Four-arm	0	1/2	—	0	0.582	5.33	1.493
Four-arm extended	0	1/2	—	0	0.511	3.18	2.806
Two four-arm extended	0	1/2	—	0	0.450	2.68	5.045
Three-arm downright	0	1/2	—	0	0.603	5.92	1.320
Three-arm upright	0	1/2	—	0	0.577	5.20	1.615
Three-arm upright extended	0	1/2	—	0	0.392	2.83	3.947
Free surface baffles							
Type 2	—	—	—	—	0.188	1.73	8.002
Type 3	—	—	—	—	0.194	1.66	7.881
Type 4	—	—	—	—	0.110	2.01	9.347
Type 5	—	—	—	—	0.433	2.70	3.537
Baffle(s) + thermocapillary control							
Vertical baffle	0	1/2	1 × 8	0	0.568	2.94	2.488
Two vertical baffles	±1/6	1/2	1 × 8	0	0.531	2.98	2.898
Three vertical baffles	±1/4, 0	1/2	1 × 8	0	0.496	2.42	3.285
Four-arm extended	0	1/2	—	0	0.502	2.38	3.360
Three-arm upright extended	0	1/2	—	0	0.394	1.95	4.365

Table 9.3: Summary of the sloshing reduction performance of representative baffle designs considered in this work. The associated performance of selected designs when combined with thermocapillary control is also included.

Chapter 10

Sloshing mitigation in microgravity with moving baffles

D. Gligor, C. Peromingo, P. Salgado Sánchez, J. Porter, J. Fernández and M. A. Méndez

Acta Astronautica **219**, 639-652 (2024)

https://doi.org/10.1016/j.actaastro.2024.03.047

We numerically investigate the effect on sloshing in microgravity of systems with passive, moving baffles whose motion is restricted by linear springs. The liquid is assumed to have physical properties similar to those of 5 cSt silicone oil while the baffle is made of aluminium. Two kinds of numerical models are developed depending on whether the allowed baffle motion is translational or rotational. Simulations show that moving baffles significantly improve sloshing mitigation compared to fixed baffles, with decreases of up to 48% in the decay time and 23% in the fluid kinetic energy following excitation by a certain pulse-like acceleration. In all configurations considered, there exists an optimal spring stiffness that minimises the kinetic energy or decay time. Frequency analysis reveals two peaks in the range of 0.1–2 Hz whose amplitudes vary as a function of spring stiffness, analogous to the behaviour of Tuned Mass Dampers (TMDs). The effectiveness of the moving baffle system is then assessed using a real microgravity perturbation measured during a reboosting manoeuvre of the International Space Station (ISS) and a significant reduction in decay time relative to the fixed baffle case is found: to 1.3 s from 4 s.

10.1 Introduction

The manipulation of fluid behaviour and the control of instabilities is of crucial interest in numerous applications. This control is particularly challenging in microgravity environments due the fact that many common instabilities are moderated by gravity which, among other things, helps limit the growth of unstable modes. For example, the frozen wave instability, which arises when two (or more) distinct fluids are vibrated parallel to the interface separating them, initially produces small-amplitude sinusoidal waves on Earth [4, 181, 267]. In the

absence of gravity, however, these waves immediately grow into large columnar patterns spanning the entire domain [5–11]. Controlling instabilities such as this may simply involve an appropriate selection of parameters and container design or the application of external forcing; see the work of Porter et al. [144] for a review of fluid control strategies.

In some cases, one type of fluid dynamics or phenomenon is deliberately introduced in order to suppress another, or simply to enhance a desired effect. For example, Phase Change Materials (PCMs) are widely used to control temperatures and improve efficiency in thermally sensitive systems [174–176, 254]. The performance of popular organic PCMs, however, suffers due to their low thermal conductivity. Thus, various strategies have been explored to enhance heat transport during the phase change, including designs that promote natural convection [177]. In microgravity environments, buoyancy-driven convection cannot be used so thermocapillary convection has been investigated as an alternative. During PCM melting, the dependence of surface tension on the temperature gradient naturally draws fluid from warmer (lower surface tension) to colder (higher surface tension) regions, generating convective cells and accelerating the phase change. Recent parabolic flight experiments [122, 123, 152] with n-octadecane and related numerical work [124–127, 138, 139, 210, 211, 253, 261, 268] have demonstrated the potential for significant performance enhancement from this effect while the upcoming ISS experiment "Effect of Marangoni convection on heat transfer in Phase Change Materials" [111, 214] will more definitively test the benefits of thermocapillary-based PCM design strategies.

Sloshing motion is a prominent concern in many fluid systems with a free surface and even more so in microgravity where the fluid motion is far less constrained [9]. Indeed, the same thermocapillary flow that can be used to enhance heat transfer in PCMs can excite sloshing modes if the thermocapillary forcing varies in time, as explored in the recent work of Gligor et al. [178]. On the other hand, this coupling can be exploited to *suppress* sloshing through the deliberate application of periodic thermal forcing with appropriate phase, either separately [201, 220] or in combination with passive baffles, as in the recent work of Peromingo et al. [224, 225]. More commonly, sloshing is excited by inertial forcing such as vibrations, which can be particularly problematic in space missions [39, 42, 48, 183].

The dynamics of sloshing have attracted sustained attention for many decades, drawing from the seminal work of Abramson [39]; for a review of more recent developments, see Refs. [40, 41]. Much effort has been dedicated both to the modelling of liquid sloshing (see, e.g., Ref. [42]) and to the development of strategies for mitigating its undesired effects. The most studied approaches to reduce sloshing are based on enhancing viscous effects [49] or the introduction of material devices, like baffles, that interfere with the bulk flow. Utsumi [50], for example, analysed the damping caused by contact angle hysteresis and showed its importance in reduced gravity environments. There are many publications examining the use of passive baffles for sloshing mitigation in normal gravity conditions [51–56]. Active strategies relying on controlled baffles have also been explored, with Xie and Zhao [57] achieving an 80% reduction using reinforcement learning, for example. Other strategies, such as the use of actively controlled magnetic fields, have been proposed but remain largely unexplored in practical applications [43, 44].

In the present study, we investigate the use of moving baffles attached by springs. This design is analogous to that of Tuned Mass Dampers (TMDs) [68] — mounted devices that

can stabilise the response of a structure to excitation near its resonant frequency. In typical applications, the TMD mass, which is smaller than that of the original structure, is mounted on one or more damped springs and has the effect of splitting the main resonance peak into two smaller peaks at slightly different frequencies [69, 70]. The use of TMDs is widespread in structural engineering where these relatively simple systems, when properly tuned to the natural frequency of the structure being controlled, help reduce earthquake motion [71], dampen wind disturbances [72], and stabilise industrial machinery [73].

In the case of liquid sloshing, moving baffles have only recently been investigated and their effect on sloshing motion, as well as the dependence on key parameters like the spring constant, is still not well understood. While most baffle designs are fixed, Idelsohn et al. [62] used a configuration with flexible baffles, either clamped or hanging, to validate numerical simulations based on the Particle Finite Element Method (PFEM). Hwang et al. [63] conducted additional numerical simulations of sloshing in the presence of the same two types of elastic baffles. Kim et al. [64] performed experiments in a tank of water with horizontally oriented baffles attached by springs above the equilibrium surface. When large-amplitude sloshing motion was excited, the water impacted these baffles and the sloshing motion was significantly reduced compared to the no-baffle case. The impact force was found to be lower in the case of low spring stiffness. The same setup was numerically investigated by Iranmanesh and Nikbakhti [65] who found that the moving baffles reduced sloshing both by absorbing kinetic energy and by dissipating energy through recirculation zones. The spring constant was found to have only a minor effect. Wang et al. [67] then analysed a submerged baffle attached by springs and moving along the bottom of the container. Their results showed that sloshing can be reduced with respect to the fixed baffle case. A minimum of the peak pressure, maximum wave elevation and maximum load was observed for a certain (optimal) spring stiffness, which increased with the filling ratio.

In this work, we investigate submerged moving baffles in microgravity in several configurations, including a vertically-oriented baffle like that considered in Ref. [67] but raised above the bottom of the container, and rotating baffles with one or three arms [224]. The splitting of the fixed-baffle sloshing resonance peak into two separate peaks and their associated fluid dynamics are investigated and the problem of selecting an appropriately tuned spring constant is considered from the point of view of minimising damping time as well as integrated kinetic energy. Finally, we test the translating baffle configuration by subjecting it to an acceleration signal measured on board the ISS during a reboosting manoeuvre.

The manuscript is organised as follows. In Sec. 10.2, the mathematical and numerical models are summarised and validated. Results for a baffle moving along the x-axis are presented in Sec. 10.3 by applying a pulse-like acceleration and performing a frequency analysis of the full system. Section 10.4 contains results for the same baffle under rotational rather than translational motion and for a more complicated three-armed baffle. A practical application based on a reboosting acceleration profile is considered in Sec. 10.5 while conclusions are drawn in Sec. 10.6.

10.2 Mathematical formulation

We consider laminar and incompressible flow so that the conservation of mass and momentum can be described by the Navier-Stokes equations [75]:

$$\nabla \cdot \mathbf{u} = 0, \tag{10.1a}$$

$$\rho \left(\frac{\partial \mathbf{u}}{\partial t} + (\mathbf{u} \cdot \nabla)\mathbf{u} \right) = -\nabla p + \mu \nabla^2 \mathbf{u} + \rho \, \mathbf{a}(t), \tag{10.1b}$$

where $\mathbf{u}$ and p are the velocity and pressure fields, and ρ and μ refer to the density and dynamic viscosity. The term $\rho \, \mathbf{a}(t)$ in equation (10.1b) captures the effect of the applied acceleration (perturbation). A two-dimensional (2D) approximation is assumed, with the problem depending only on the horizontal (x) and vertical (y) coordinates.

At the free surface, $F = y - f(x,t) = 0$, the balance between pressure, viscous stresses and surface tension σ is expressed by

$$-\mathbf{n} \cdot (-p \, \mathbf{I} + \boldsymbol{\tau}) = \sigma (\nabla \cdot \mathbf{n}) \, \mathbf{n}, \tag{10.2}$$

where $\mathbf{I}$ is the identity matrix, $\boldsymbol{\tau} = \mu \left(\nabla \mathbf{u} + (\nabla \mathbf{u})^T \right)$ is the viscous stress tensor and $\mathbf{n} = \nabla F / |\nabla F|$ is normal to the free surface. The kinematic boundary condition at the free surface is:

$$\frac{\partial f}{\partial t} + \mathbf{u} \cdot \nabla f = 0. \tag{10.3}$$

At the lateral walls, $x = \mp L/2$, slip boundary conditions are assumed in order to allow vertical motion of the contact points:

$$\mathbf{u} \cdot \mathbf{n}_w = 0, \tag{10.4}$$

where $\mathbf{n}_w$ is normal to the vertical endwalls. For simplicity, a static contact angle β is also imposed through

$$\mathbf{n} \cdot \mathbf{n}_w = \cos \beta, \tag{10.5}$$

although it may be interesting (in a future work) to use more realistic dynamic boundary conditions at the contact point [50], and even to include the effect of fluid inertia as in Ref. [269].

At the bottom wall, $y = 0$, a no-slip condition is applied:

$$\mathbf{u} = 0. \tag{10.6}$$

The system described by Eqs. (10.1)–(10.6) is augmented by the equation for the moving baffle and the associated boundary conditions. We consider moving baffles with either translational or angular motion for which the equations determining the baffle motion and boundary conditions are different. The case of a translating baffle is shown in Fig. 10.1 while the rotating case is considered in Sec. 10.4. With no vertical displacement or rotation of the baffle, the dynamical equations reduce to the following momentum balance in the x direction:

$$\ddot{x}_b + \frac{K}{M_b} x_b = \mathbf{a}_x + \frac{1}{M_b} \int_{\Sigma_b} (p \, \mathbf{n}_b + \boldsymbol{\tau} \cdot \mathbf{n}_b) \cdot \mathbf{i} \, d\Sigma_b. \tag{10.7}$$

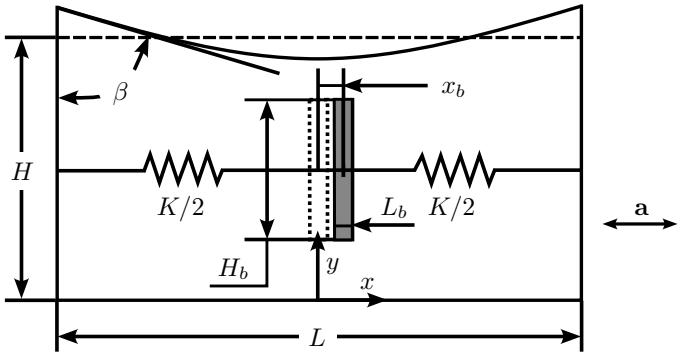


Figure 10.1: Sketch illustrating the 2D setup for the numerical model. The baffle is attached to the vertical endwalls via linear springs and the acceleration **a** is applied horizontally.

	ρ (kg/m^3)	ν (10^{-6} m^2/s)	σ (10^{-3} N/m)
5 cSt silicone oil	1000	5	20
Water	1000	1	80
Aluminium	2700	-	-

Table 10.1: Selected liquid properties and aluminium density at the reference temperature $T_0 = 20\,^\circ$C; the liquids are similar to 5 cSt silicone oil and water.

Here, x_b is the horizontal displacement of the baffle, K is the spring constant and $\mathbf{i}$ is a unit vector in the x direction. The external baffle surfaces Σ_b are defined in local coordinates, (X_b, Y_b), with $\mathbf{n}_b$ being a unit vector normal to the baffle surface. The baffle mass can be written as $M_b = \rho_b W_b L_b H_b$ in terms of its density ρ_b, width W_b (taken as unity in the 2D approximation), length L_b and height H_b. The right-hand side of the oscillator equation includes three terms accounting, respectively, for applied acceleration [as in Eqs. 10.1], pressure forces and viscous stresses exerted by the fluid on the baffle surfaces. The latter two terms couple the baffle motion with the fluid flow.

Since it moves as a rigid solid, the boundary conditions on the baffle surface Σ_b are assumed to be no-slip:

$$\mathbf{u} = \dot{x}_b\,\mathbf{i}. \tag{10.8}$$

10.2.1 Numerical model

Following the work of Gligor et al. [178, 201], results are obtained for a volume of liquid corresponding to $L \times H = 30\,\text{mm} \times 15\,\text{mm}$ ($\Gamma = L/H = 2$) and with an imposed contact angle of $\beta = 70°$. The liquid properties, which are those of 5 cSt silicone oil except for density, are taken from Ref. [178] and summarised in Table 10.1. This selection is motivated by recent microgravity experiments [9, 11, 77] and numerical results on sloshing mitigation techniques [178, 201]. The choice of parameters clearly affects both the sloshing modes and their control, but we note that the difference between the density value used here and the measured density

Mesh no.	Max mesh size	Mesh elements	Computational cost	Max $\mathbf{u}_x$ at mid section (m/s)	Deviation (%)
1	$L/25$	1015	149 s	0.833	3.476
2	$L/50$	1661	183 s	0.838	2.897
3	$\boldsymbol{L/100}$	**3646**	**347 s**	**0.851**	**1.390**
4	$L/200$	5981	434 s	0.863	—

Table 10.2: Results of mesh convergence tests for simulations comparable to the work of Faltinsen et al. [270]. The fluid is water and the periodic excitation has amplitude $A = 30\,\mathrm{mm}$ and period $T = 1.29\,\mathrm{s}$. The selected mesh (no. 3) is highlighted in bold, with deviations in maximum velocity measured with respect to mesh no. 4.

of $915\,\mathrm{kg/m^3}$ for 5 cSt silicone oil at 20 °C [168] is negligible compared to the density difference across the free surface and with respect to the baffle. The dimensionless ratios are nearly unchanged by the simplified choice of ρ in Table 10.1. The conditions at the contact line are much more critical for sloshing dynamics, as discussed in Ref. [178].

The baffle is assumed to consist of a $1\,\mathrm{mm} \times 8\,\mathrm{mm}$ aluminium rectangle with Young's modulus $E = 69\,\mathrm{GPa}$ and Poisson's ratio $\nu = 0.33$. We note that the pressure differences obtained here are not enough to cause any significant deformation so the baffle can be regarded as a rigid body. The selection of aluminium is motivated by its relatively light weight, which is a positive consideration in space applications.

The commercial software COMSOL Multiphysics is used to resolve the formulation of Eqs. (10.1)–(10.8) in dimensional variables with the finite element method. A *moving mesh* scheme with an arbitrary Lagrangian-Eulerian formulation is utilised to track the dynamics of the free surface, the fluid flow, and the moving baffle within it. In the time-dependent fluid domain, Eqs. (10.1)–(10.8) are written in mesh coordinates, which are then mapped to spatial coordinates. The mesh is smoothly deformed in accordance with the Winslow technique:

$$\frac{\partial^2 X}{\partial x^2} + \frac{\partial^2 X}{\partial y^2} = 0, \tag{10.9a}$$

$$\frac{\partial^2 Y}{\partial x^2} + \frac{\partial^2 Y}{\partial y^2} = 0, \tag{10.9b}$$

where (x, y) are the coordinates of the spatial frame and (X, Y) are the reference coordinates of the material frame, which coincides here with the mesh frame. The boundary conditions are $\mathbf{u}_{\mathrm{mesh}} = 0$ at the solid walls and $\mathbf{u}_{\mathrm{mesh}} = \mathbf{u}$ at the free surface. The mesh deformation must also be consistent with the baffle motion so that the displacement $\mathbf{d}_{\mathrm{mesh}} = x_b\mathbf{i}$ at the baffle walls.

The numerical problem is considerably simplified by the restriction to 2D dynamics. This is partly justified by the good agreement of previous 2D models of interfacial dynamics with the dynamics of both miscible [76] and immiscible [9, 11] liquids subjected to vibrational excitation under microgravity conditions. In experiments, (quasi) 2D dynamics can be achieved with an appropriate container design [9, 77].

For simplicity, the flow is initially taken to be at rest, $\mathbf{u} = 0$, with a flat free surface. The baffle starts from its equilibrium position $x_b = 0$ with velocity $\dot{x}_b = 0$. Since the nominal contact angle is not 90°, the system is allowed to gradually evolve toward $\beta_\mathrm{n} = 70°$ by imposing

$$\beta(t) = 90° + (\beta_\mathrm{n} - 90°)\,\mathcal{H}(t), \tag{10.10}$$

where $\mathcal{H}(t)$ is a smoothed Heaviside function:

$$\mathcal{H}(t) = \begin{cases} 0, & t < 0, \\ \frac{t}{\tau} - \frac{1}{2\pi}\sin\left(\frac{2\pi t}{\tau}\right), & 0 \le t \le \tau, \\ 1, & t > \tau; \end{cases} \tag{10.11}$$

which changes from 0 to 1 over the interval τ. Here we use $\tau = 2\,\mathrm{s}$, which is selected to reduce the transient oscillations of the free surface that can result from this choice of initialisation.

The time integration is performed with a generalised-α [81] scheme and with the streamline [82] and crosswind [83] stabilisation techniques. The maximum time step is 0.01 s with smaller steps automatically used by the solver when required by the Courant-Friedrichs-Levy (CFL) convergence condition for numerical stability.

10.2.2 Numerical convergence and validation

For the numerical convergence tests, we take the fluid parameters of water (see Table 10.1) rather than those representing silicone oil because of the availability of more definitive numerical and experimental data for comparison. In particular, we compare with two relevant references on sloshing phenomena, each confirmed by experimental results: the work of Faltinsen et al. [270] for unbaffled tanks with periodic excitation and that of Liu and Lin [53] for a 2D tank with baffles. The numerical code is validated by omitting the baffle evolution described by Eq. (10.7) and using the same dimensions and forcing as the containers in those references.

For comparison with the results of Faltinsen et al. [270], we simulate a 2D container of water with dimensions $L \times H = 1.73\,\mathrm{m} \times 0.6\,\mathrm{m}$ and a contact angle $\beta = 90°$ subjected to periodic horizontal vibrations with amplitude $A = 30\,\mathrm{mm}$ and period $T = 1.29\,\mathrm{s}$. The amplitude and period are both extracted from Fig. 7 of that reference. Mesh sizes are given in terms of the container length L.

Table 10.2 shows the results of the numerical convergence tests for each maximum mesh size selected in terms of the number of mesh elements, computational cost (in time) and solution accuracy. We take the maximum velocity of the fluid at $x = 0$ (the container midpoint) as a representative value for the convergence criterion and measure all deviations with respect to that of the finest mesh (no. 4). The results indicate that mesh no. 3 provides a good compromise between computational cost and numerical accuracy and is well suited for future extensions to 3D simulations. Hence, a maximum mesh size of $L/100$ is selected for the numerical results that follow.

To further compare with the model of Ref. [270], the evolution of the free surface at a particular position (FS3, located 0.05 m from the left wall) is shown in the upper panel of Fig. 10.2 for

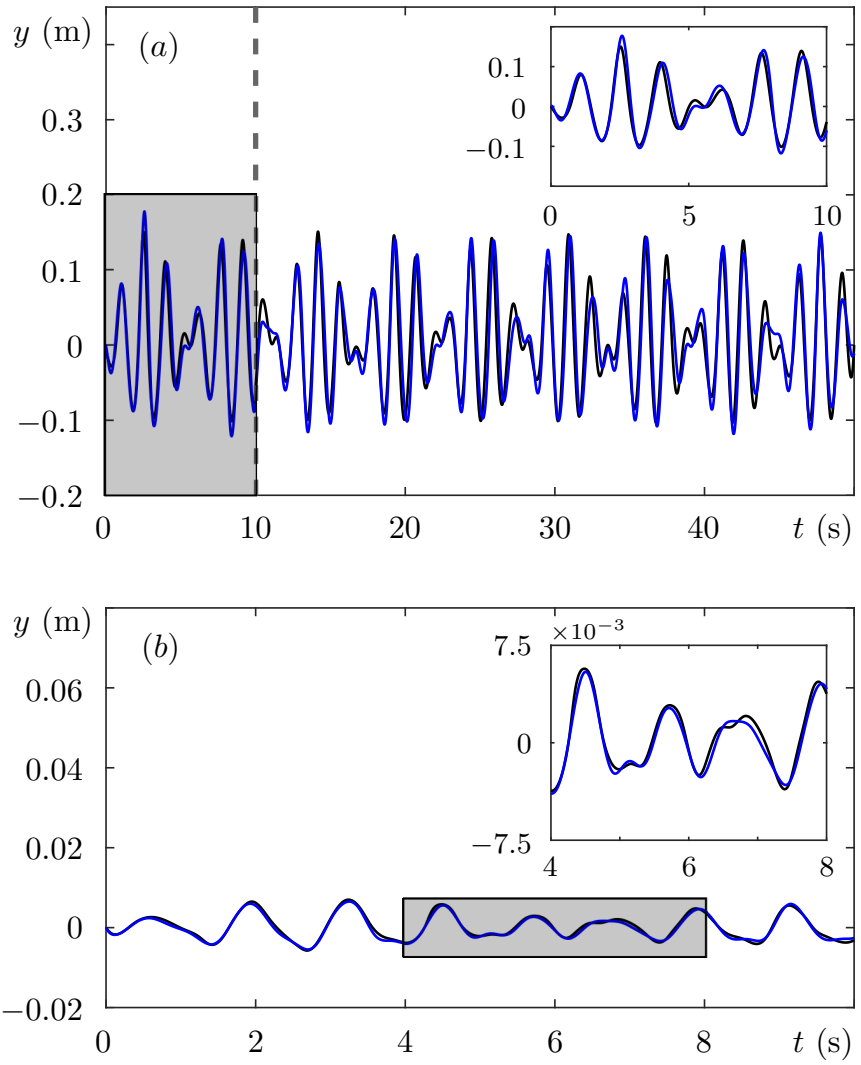


Figure 10.2: Comparison of the numerical model with published results. (*a*) Surface elevation at a selected point (FS3) for the current model (blue) and the reference work (black) of Faltinsen et al. [270], with no baffle. (*b*) Surface elevation at the right container boundary for the current model (blue) and the reference work (black) of Liu and Lin [53], with a fixed baffle. The grey shaded regions are shown in more detail in the insets.

quiescent initial conditions. The results of the current simulation match almost perfectly with the published results during the first 10 s and, even at larger times, the behaviour remains very similar.

Since the results of Faltinsen et al. [270] are obtained without a baffle affecting the flow, we also compare with the work of Liu and Lin [53] on sloshing in a container with a fixed, centred baffle attached to the bottom wall. Using the parameters of that reference (dimensions $L \times H = 1\,\text{m} \times 0.5\,\text{m}$, baffle height $H_b = 0.75\,H$ and periodic excitation with amplitude $A = 2\,\text{mm}$ and period $T = 1.187\,\text{s}$), we obtain the results shown in the lower panel of Fig. 10.2,

again for a maximum mesh size of $L/100$. The comparison is made for the free surface elevation at the right contact point. Again, the results match extremely well.

10.2.3 Pulse-like perturbation, asymmetry and decay time

The first sloshing mode is odd, with a wavelength of $\lambda = 2\,L$ (twice the container length). Since this sloshing mode is antisymmetric, it will naturally be excited by an asymmetric acceleration. Following recent work [178, 201, 224, 225], we define a specific pulse-like acceleration and apply it to the fluid system described in Sec. 10.2. The response of the liquid and baffle to this perturbation is then analysed.

The acceleration is applied along the x-axis and enters into Eq. (10.1b) via the volumetric force $\rho\,\mathbf{a}$ and into Eq. (10.7) as $\mathbf{a}_x$. This acceleration is switched on smoothly, using $\mathcal{H}(t)$ from Eq. (10.11), and then abruptly turned off:

$$\mathbf{a}\,(t) = 0.01\,\mathrm{m/s^2}\,\mathbf{i}\,\begin{cases} \mathcal{H}(t-t_0) & t-t_0 \leq \tau, \\ 0 & t-t_0 > \tau; \end{cases} \tag{10.12}$$

where $t_0 = \tau = 2\,\mathrm{s}$ are the selected time constants; with that value of t_0, the force begins just after the decay of transients induced by the transition to the nominal contact angle β_n from 90°.

As a result of this applied horizontal acceleration, the free surface acquires increasing asymmetry over time and, once the forcing is removed, starts sloshing back and forth. Since the sloshing mode is antisymmetric, we use the motion of the contact points to represent the magnitude of free surface deformation. The asymmetry $\mathcal{A}$ is defined as the difference between the y-coordinates of the contact points:

$$\mathcal{A}(t) = f(L/2,\,t) - f(-L/2,\,t). \tag{10.13}$$

To characterise the response, the decay time τ_d is measured according to the classical "5% settling time" definition. Specifically, sloshing motion is considered damped when $\mathcal{A}$ decreases below 5% of a reference value $\mathcal{A}^*$:

$$|\mathcal{A}(t)| \leq 0.05\,\mathcal{A}^*. \tag{10.14}$$

Although $\mathcal{A}^*$ is often taken as the peak value, we find it more convenient here to take $\mathcal{A}^* \simeq 1.4\,\mathrm{mm}$, which is the peak value obtained in the uncontrolled, no-baffle case, i.e., when no control strategies are applied and the system responds naturally to the applied perturbation.

10.3 Vertical baffle with horizontal motion

The results hereafter are obtained for the container defined in Sec. 10.2 and the fluid parameters of Table 10.1 that are similar to those of 5 cSt silicone oil.

We first note that in standard TMD applications, the control masses are physically attached to the primary structure through mechanical unions, such as pendula hanging from the roof

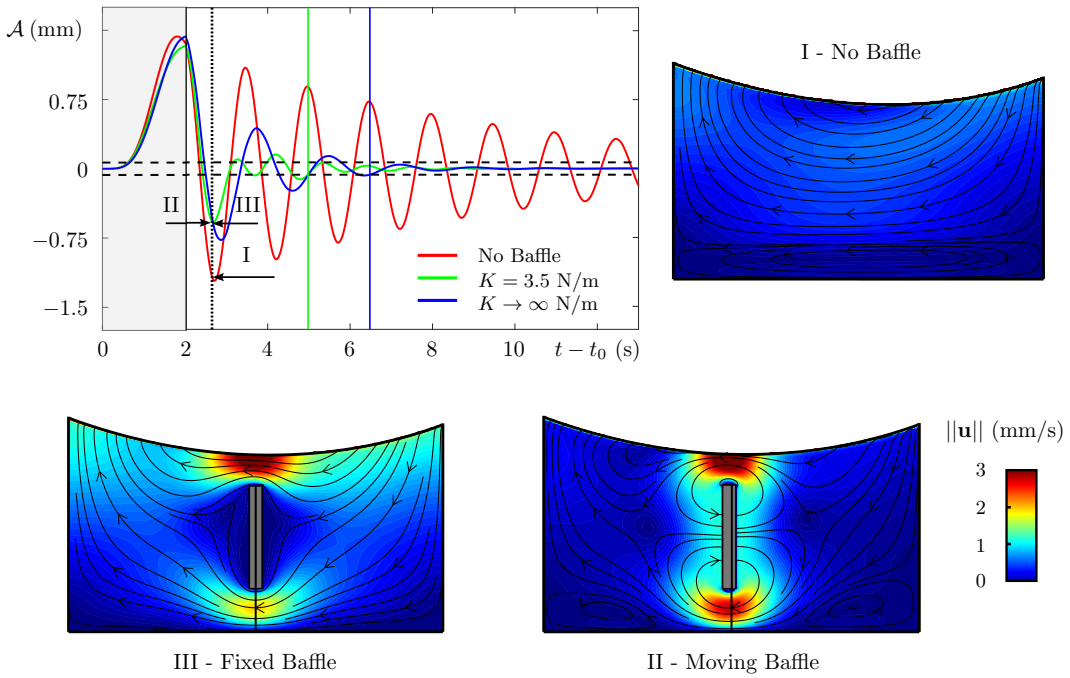


Figure 10.3: Comparison of three representative cases: The no-baffle case, a moving baffle with $K = 3.5\,\mathrm{N/m}$ and a fixed baffle. The upper left panel shows the response of $\mathcal{A}$ to the applied pulse-like perturbation (its 2 s duration is shaded grey). Snapshots of the fluid velocity, with colour indicating magnitude, are also shown for $t - t_0 = 2.65\,\mathrm{s}$ (marked with a dotted line). The green and blue solid lines indicate the settling time based on the 5% stability criteria (shown using two horizontal dashed lines).

of a building, so the coupling is relatively simple. Different criteria may be used to optimise or "tune" the restoring force and the damping — minimising the maximum displacement of the primary structure, the duration of transient vibrations or total kinetic energy, for example — but the basic resonance condition is easy to apply.

In the submerged moving baffle system, the coupling is significantly more complex because, aside from the linear spring force, the baffle interacts with the flow via pressure differences and viscous stresses, as described by Eq. (10.7). The baffle velocity then couples back into the flow equations via the boundary condition of Eq. (10.8). The complexity of this coupling makes it difficult to estimate a good value for the spring constant. An overly stiff spring will cause the system to resemble that of a fixed baffle at the central position [224].

A rough estimate for the optimal spring constant can be obtained from the observations that the baffle should centre its response at the sloshing frequency and that, at least in the case of a baffle that spans a significant part of the container height, it will be strongly coupled to the movement of the fluid. This means the effective inertial mass for spring-driven oscillations may be closer to the full mass (baffle mass M_b plus fluid mass M_f) than to that of the baffle alone.

The sloshing frequency can be estimated through the dispersion relation for capillary-gravity

waves [38]:

$$\varpi^2 = \left(gk + \frac{\sigma}{\rho} k^3 \right) \tanh\left(k\,H\right), \tag{10.15}$$

where $k = \pi/L$ is the wavenumber of the first (odd) sloshing mode. For a sufficiently deep layer in weightless conditions, this equation simplifies to $\varpi^2 = (\sigma/\rho)\,k^3$. By setting this natural sloshing frequency equal to that of a mass $M^* = M_f + M_b = \rho W(L\,H - L_b\,H_b) + \rho_b W_b\,L_b\,H_b \simeq 0.464\,\mathrm{kg}$ attached to a spring with stiffness K, one obtains

$$K = \frac{\sigma}{\rho} \left(\frac{\pi}{L} \right)^3 M^*. \tag{10.16}$$

For the system considered here, Eq. (10.16) gives $K \simeq 10.6\,\mathrm{N/m}$. We emphasise that this is only a rough estimate based on the assumption that fluid and baffle move in phase. Although this assumption clearly does not hold in reality, we shall see below that Eq. (10.16) does provide an acceptable (leading order) estimate for the optimal K — much better than if only the inertia of the baffle is considered.

10.3.1 Response to a pulse-like perturbation

With the initial guess for the spring constant from Eq. (10.16), a series of K values is selected between 0 and $50\,\mathrm{N/m}$. Recall that the expected behaviour should approach that of a fixed baffle as the spring constant becomes large.

The response of the system to the pulse-like perturbation defined in Sec. 10.2.3, which excites the first odd sloshing mode, is simulated over a time of 15 s, which is generally large enough to accurately measure the decay time and consistent with the previous work of Peromingo et al. [224, 225]. The main question is whether there are cases of moving baffles that perform better than the fixed-baffle case, which has a decay time of $\tau_d = 4.5\,\mathrm{s}$ for this particular applied perturbation.

Before analysing the results over the full range of K values, we consider three limiting and representative cases: the fixed-baffle limit of $K \to \infty$, an intermediate case with a spring constant of $K = 3.5\,\mathrm{N/m}$ and the no-baffle case. The decay of the asymmetry parameter $\mathcal{A}$ is shown for these three cases in Fig. 10.3, along with snapshots of the velocity field. Supplementary movie 1 accompanies this figure and shows the temporal evolution of the sloshing response in each case.

One can observe from the figure that sloshing dynamics with a finite spring constant $K = 3.5\,\mathrm{N/m}$ are qualitatively distinct from those in the no-baffle and fixed-baffle cases. The response no longer resembles an exponentially damped sinusoidal wave [224, 225] but, rather, a superposition of two damped sinusoidal waves, each with distinct amplitude, frequency and damping rate. This type of behaviour is typical of intermediate spring constants due to the resonant response of the moving baffle. The fitting function is thus taken to be of the form

$$\mathcal{A}_{\mathrm{fit}}(t) = A_0 + A_1 \sin\left(\omega_1 t + \phi_1\right) e^{-\sigma_1 t} + A_2 \sin\left(\omega_2 t + \phi_2\right) e^{-\sigma_2 t}, \tag{10.17}$$

where A_0 is a constant that usually tends to 0 and A_1 and A_2 are the amplitudes of the two dominant frequencies, ω_1 and ω_2. These two frequency components have phase shifts ϕ_1 and ϕ_2 and damping rates σ_1 and σ_2.

The least-squares fit is performed after using a fast Fourier transform to obtain initial values for the amplitudes and frequencies, which makes the procedure more robust and allows accurate extrapolation in (small K) cases where the decay time based on the 5% stability criterion is larger than the simulation time of 15 s. Over all simulations performed, the fitting error defined by $|\mathcal{A} - \mathcal{A}_{\text{fit}}|/|\mathcal{A}|$ and calculated using the (temporal) vector norms remains below 2%.

The calculated decay times are summarised in Table 10.3 for selected values of the spring stiffness. The table demonstrates that there is a range of values which improve upon the damping of the fixed-baffle system. With $K = 5\,\text{N/m}$, in particular, there is a decrease in the decay time of 40% compared to the fixed-baffle case, showing that the idea of TMDs can can indeed be extended to include moving baffles in fluid systems prone to sloshing.

The decay time relative to that in a fixed-baffle system is presented in the upper panel of Fig. 10.4 as a function of K. When this ratio is less than unity, there is an improvement due to the motion of the baffle. The inset shows more detail of the minimum, which occurs near $K \sim 5\,\text{N/m}$. The figure also shows that, as expected, increasing the stiffness of the spring causes the response to converge to that of the fixed-baffle system.

Although the decay time is a natural measure of how effective the baffle is at reducing sloshing, there can sometimes be surprising behaviour in $\mathcal{A}(t)$. In Fig. 10.3 for $K = 3.5\,\text{N/m}$, for example, one can see that the second maxima after the applied forcing turns off is larger that the first. This may happen due to the varying phase shift between the two sloshing modes of Eq. (10.17).

In order to confirm the conclusions drawn from measurements of the decay time, we evaluate the kinetic energy of the fluid at each time step with the integral $\int_\Omega \frac{1}{2}\rho||\mathbf{u}||^2 W d\Omega$ taken over the fluid domain Ω. The integral of this kinetic energy over the simulation time

$$\mathcal{I} = \int_4^{15} \left(\int_\Omega \frac{1}{2}\rho||\mathbf{u}||^2 W d\Omega \right) dt, \tag{10.18}$$

can then be used to compare the overall energy manifest as sloshing for each value of K.

The results of Eq. (10.18) are presented in Table 10.3 and in the lower panel of Fig. 10.4. The behaviour of the kinetic energy mirrors that of the decay time for the spring constants considered. Starting from the fixed-baffle ($K \to \infty$) case, decreasing spring stiffness improves the system performance until a minimum is reached near 5.5 N/m; note that this minimum is slightly shifted compared to that of the decay time. Further decrease in K makes sloshing worse as the dynamics approximate those of a tank with no baffle, shown here at $K = 0$.

Both $\mathcal{I}$ and τ_d indicate an optimal spring stiffness of $K \sim 5\,\text{N/m}$ for reducing sloshing. Moreover, the minima is quite broad, with good results observed over an approximate range of $3.5 - 8\,\text{N/m}$. Small deviations from the optimal spring constant will not significantly hinder performance.

K (N/m)	τ_d (s)	$\mathcal{I} \times 10^7$ (J s)
no baffle	21.77	12.13
1	19.71	9.21
2	9.04	4.19
2.5	6.16	3.15
3	4.16	2.65
3.5	2.98	2.39
4	2.85	2.27
5	**2.69**	**2.19**
6	2.90	**2.19**
10	3.61	2.34
50	3.77	2.73
∞	4.48	2.86

Table 10.3: Decay times τ_d and integrated kinetic energies $\mathcal{I}$ from Eq. (10.18) for the vertical baffle with linear springs along the x-axis. Decay times are measured with respect to the end of the forcing at $t - t_0 = 2\,\mathrm{s}$ (see Fig. 10.3). Green shading draws attention to K values that attenuate sloshing more than a fixed baffle. The first column corresponds to the no-baffle case.

10.3.2 Frequency response

The asymmetry $\mathcal{A}(t)$ in Sec. 10.3.1 shows the presence of two dominant sloshing modes whose amplitudes and frequencies, ω_1 and ω_2, vary with K. This motivates replacing the pulse-like forcing with an oscillatory function of equal amplitude that can more directly excite the corresponding frequency in the fluid and baffle:

$$\mathbf{a}(t) = 0.01 \sin(\omega\, t)\, \mathbf{i}\, \mathcal{H}(t - t_0)\ \mathrm{m/s^2}. \tag{10.19}$$

The frequency $f = \omega/(2\pi)$ is varied between 0.1 Hz and 2 Hz, with smaller frequency steps taken near the resonances, for five distinct cases: no baffle, a fixed baffle, and moving baffles with $K = 3.5$, 5 and 7.5 N/m. For each frequency value, the system is initialized from rest in the manner described in Sec. 10.2 and evolved until transient behaviour decays and constant-amplitude oscillations are observed in $\mathcal{A}(t)$ and baffle displacement. Note that this approach cannot reveal if there is hysteresis in the dynamics. However, it is known that many sloshing systems display significant nonlinearity and hysteresis [271, 272] and behave differently during up and down frequency sweeps; an analysis of this possibility is left for future work.

The results shown in Fig. 10.5 reveal the nature of the two modes. The first resonance is associated primarily with fluid motion (sloshing) and relatively small-amplitude baffle motion. In contrast, the second resonance is characterised by much larger baffle motion (provide K is not too large). These modes are illustrated directly for $K = 5\,\mathrm{N/m}$ to the right of the plots. We further note that $\mathcal{A}(t)$ has a phase shift with respect to $x_b(t)$ of 101° in the first mode and 42.7° in the second mode.

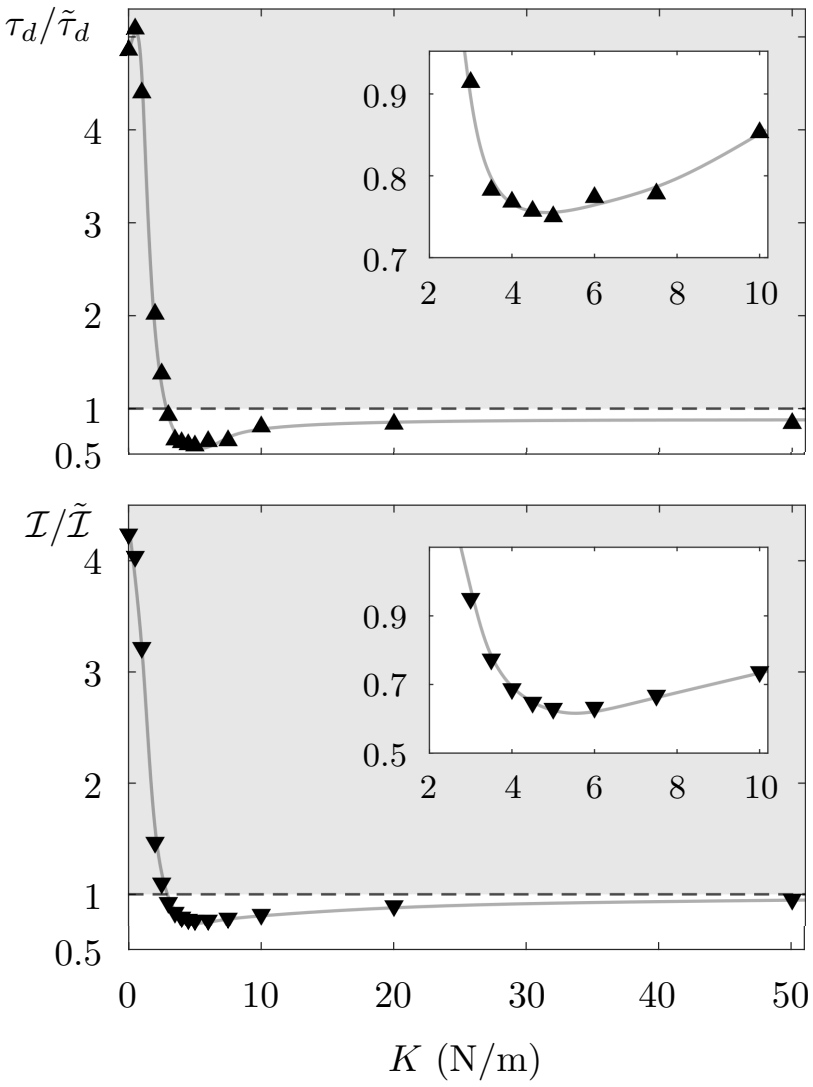


Figure 10.4: (Upper) Translating baffle decay time τ_d relative to that of a fixed baffle ($\tilde{\tau}_d$) versus K. The inset shows that the minimum decay time is obtained for $K \sim 5\,\mathrm{N/m}$. (Lower) Integrated kinetic energy $\mathcal{I}$ relative to that for a fixed baffle ($\tilde{\mathcal{I}}$) versus K. The inset indicates a minimum value at $K \sim 5.5$ N/m. Corresponding dimensional values for some of these data points can be found in Table 10.3. The no-baffle case is shown at $K = 0$ N/m.

The changing resonant behaviour as K varies can be understood from the plots of $\mathcal{A}/L$ and x_b/L in Fig. 10.5. The no-baffle case has a single large resonance at the natural sloshing frequency. The introduction of a moving baffle with small K shifts this peak to higher frequency while allowing large-amplitude baffle motion. As K increases further, another peak corresponding to less baffle displacement emerges near the fixed-baffle sloshing frequency (see the curves for $K = 3.5\,\mathrm{N/m}$). At a certain value of K near $4\,\mathrm{N/m}$ [see Fig. 10.5(c)], these two resonance modes exhibit sloshing of equal amplitude. Beyond that, sloshing is most pronounced in the lower-frequency mode and, in the fixed-baffle limit of $K \to \infty$, this is the only type of sloshing observed; the resonance mode associated with baffle oscillation moves to infinite frequency and zero amplitude.

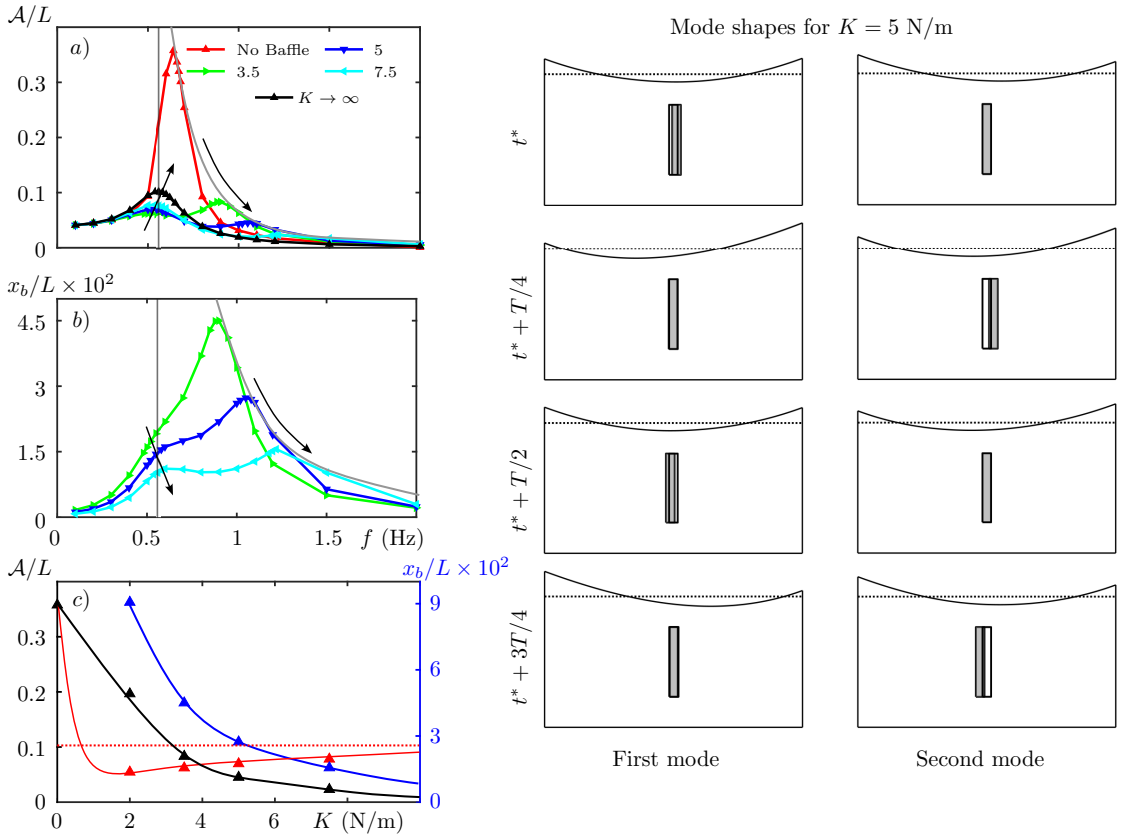


Figure 10.5: (a, b) Frequency response of the system with no baffle (red), a fixed baffle (black) and with $K = 3.5$, 5 and 7.5 N/m (green, blue, light blue) in terms of dimensionless asymmetry $\mathcal{A}/L$ and horizontal baffle displacement x_b/L. Arrows indicate the frequency shift of the resonant peaks with increasing K. The grey solid lines mark the fixed-baffle sloshing frequency of 0.579 Hz while the grey curve shows the decreasing trend of the right resonance peak amplitude. (c) Resonance peak amplitudes of $\mathcal{A}/L$ (left peak in red, right in black) and x_b/L (blue, with units on the right axis). The no-baffle case is plotted at $K = 0$. The panels on the right illustrate the modes of the two resonances peaks with $K = 5$ N/m over one period $T = 2\pi/\omega$. Note that t^* and T are different for each mode.

In summary, the lower-frequency peak in moving-baffle systems corresponds to a mode dominated by liquid sloshing, with relatively less baffle motion, while the higher-frequency peak corresponds to more baffle motion and, generally, stronger coupling between baffle and liquid motion. These resonance peaks merge for $K = 0$, a limit which resembles the no-baffle case since there is no spring force to oppose the motion of the fluid — the submerged baffle drifts along with the flow in a largely passive manner. In the fixed-baffle limit of $K \to \infty$, only the sloshing mode remains.

10.3.3 Viscous damping effect

As described in Sec. 10.2, the evolution of the baffle can be modelled using Eq. (10.7). However, the left-hand-side terms are those of a conservative oscillator while real systems are always

damped. To capture this effect, we add an additional viscous-damping term to Eq. (10.7):

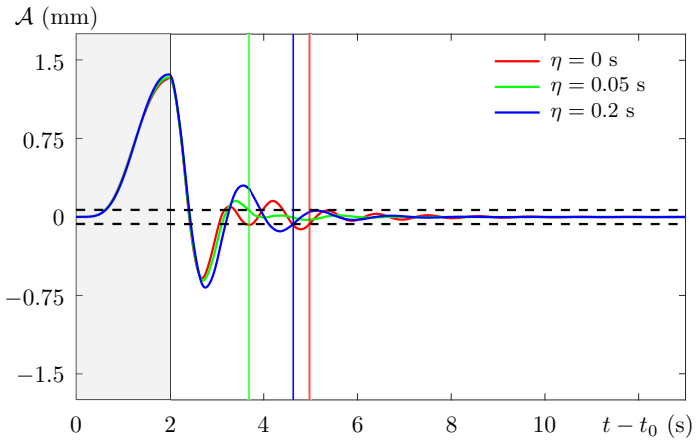


Figure 10.6: Comparison of sloshing response to the pulse-like excitation of Eq. (10.12) with $K = 3.5\,\mathrm{N/m}$ and viscous damping of $\eta = 0$, 0.05 and 0.2 s The interval when forcing is applied is shaded in grey while the red, green and blue solid lines mark the settling time based on the 5% stability criterion (delimited by two horizontal dashed lines).

$$\ddot{x_b} + \eta \frac{K}{M_b}\dot{x_b} + \frac{K}{M_b}x_b = \mathbf{a}_x + \frac{1}{M_b}\int_{\Sigma_b} (p\,\mathbf{n}_b + \boldsymbol{\tau}\cdot\mathbf{n}_b)\cdot\mathbf{i}\,d\Sigma_b, \tag{10.20}$$

where η is a dimensional parameter (units of seconds) whose value is typically smaller than one [273].

Taking into account that damping opposes baffle motion, we select a value of $K = 3.5\,\mathrm{N/m}$, which is somewhat lower than that of the minima, and vary η.

The results are presented in Fig. 10.6 and show an improvement of the system response for moderate levels of damping. Larger values can have a detrimental effect (see $\eta = 0.2\,\mathrm{s}$), comparable to increasing the spring stiffness. This is because an increase in either one reduces the amplitude of baffle motion, which is undesirable from a design perspective where one hopes to take advantage of the baffle-fluid interaction.

Using a representative small-damping value of $\eta = 0.01\,\mathrm{s}$ and a spring constant of $K = 3.5\,\mathrm{N/m}$, we repeat the sweep over frequency values of Sec. 10.3.2 and collect the results in Fig. 10.7. This figure demonstrates two effects. First, the higher-frequency (rightmost) peak is shifted leftward and reduced in amplitude, something which can be explained by the strong coupling between the sloshing and the (damped) baffle motion. The same explanation applies to the resonance peak in x_b/L (lower panel). The lower-frequency peak, on the other hand, has a larger amplitude with finite η since less baffle motion favours this sloshing-dominated mode (analogous to increasing K in Fig. 10.5).

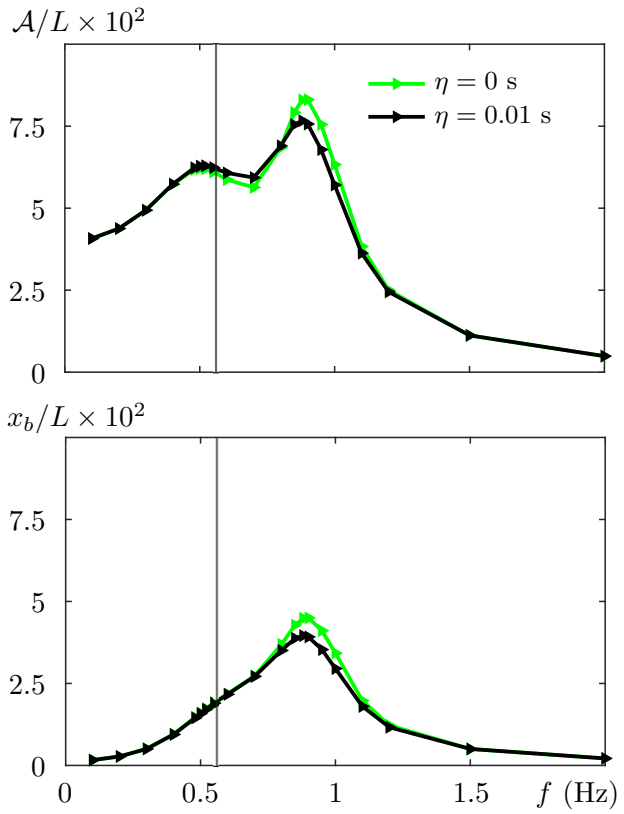


Figure 10.7: Frequency response of the system with a damped baffle. (Upper) Scaled asymmetry $\mathcal{A}/L$ versus frequency f. (Lower) Scaled baffle displacement x_b/L versus f. The grey solid line marks the fixed-baffle sloshing frequency of 0.5792 Hz.

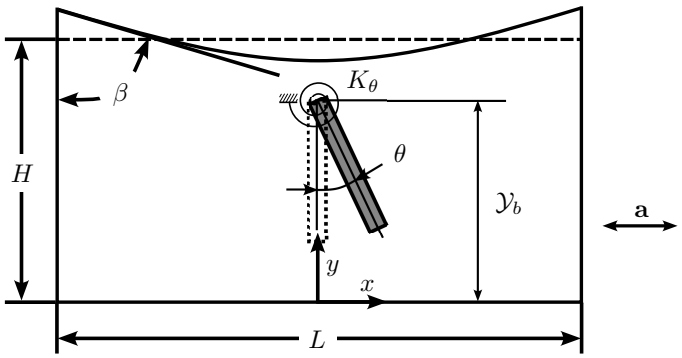


Figure 10.8: Sketch of the setup for a rotating baffle. The baffle is attached at the point $(x, y) = (0, \mathcal{Y}_b)$ with the acceleration **a** applied along the x-axis.

10.4 Rotating baffles

The previous section demonstrated the potential of sliding baffles, anchored by appropriately tuned springs, to improve upon the performance of fixed baffles [53, 54] for sloshing mitigation. Here, we extend this idea to the case of rotating baffles attached to torsion springs. From a mechanical perspective, such a design is arguably simpler to implement than the translational

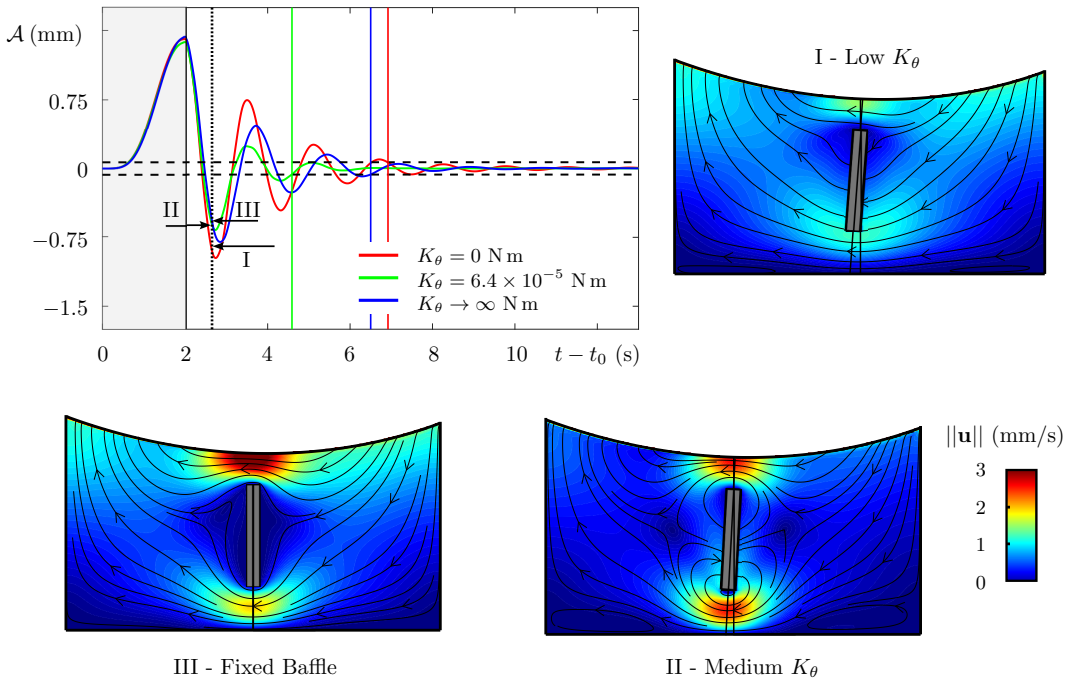


Figure 10.9: Comparison of three representative cases: small K_θ, intermediate K_θ, and a fixed baffle. The upper left panel shows the response of $\mathcal{A}$ to the applied pulse-like perturbation (its 2 s duration is shaded grey). Snapshots of the fluid velocity, with colour indicating magnitude, are also shown for $t - t_0 = 2.65$ s (marked with a dotted line). The red, green and blue solid lines indicate the settling time based on the 5% stability criteria (shown using two horizontal dashed lines).

motion considered above that, among other considerations, may require guides with bearings to constrain baffle motion to the preferred direction.

10.4.1 Single-arm rotating baffle

In this first study, a single-arm rotating baffle is assumed to be centred and oriented vertically at equilibrium with its pivot point at the upper end. This choice is supported by the snapshots of the flow in Fig. 10.3, which is largely horizontal in the centre of the domain and predominantly in the same direction. A baffle rotating about an intermediate point (the midpoint, for example) would experience counteracting torques and less rotation. A baffle rotating about its lower end may also be worth investigating, but could lead to undesirable splashing if the surface moves beneath the baffle height during sloshing.

A sketch of the considered rotating-baffle model is provided in Fig. 10.8; the baffle dimensions, L_b and H_b, are the same as in Fig. 10.1. The torque equation replacing Eq. (10.7) is:

$$\ddot{\theta} + \frac{K_\theta}{I_b}\theta = \frac{1}{I_b}\left(\int_{\Omega_b} \mathbf{r} \times \mathbf{a}_x \, \rho_b \, d\Omega_b + \int_{\Sigma_b} \mathbf{r} \times (p\,\mathbf{n}_b + \boldsymbol{\tau} \cdot \mathbf{n}_b) d\Sigma_b\right) \cdot \mathbf{k}, \tag{10.21}$$

where Ω_b indicates the baffle interior, $\mathbf{r}$ is the radius vector from the pivot point to an interior point and $\mathbf{k}$ is a unit vector in the z direction (out-of-plane). The moment of inertia is $I_b = M_b(L_b^2 + 4H_b^2)/12 \simeq M_b H_b^2/3$. Note that, for simplicity, torsion spring damping is not

included in this equation since its effects would be similar to those discussed in Sec. 10.3.3 and analogous to increasing the effective rigidity of the spring-baffle system.

The boundary condition (10.8) becomes:

$$\mathbf{u} = \mathbf{r} \times \dot{\theta}\mathbf{k}, \quad \text{on } \Sigma_b. \tag{10.22}$$

Again, baffle deformation in the current system is negligible because the pressure differences over the baffle are small compared to the elastic modulus of aluminium. It can be considered to rotate as a rigid body.

One may obtain a preliminary guess for the optimal torsion spring constant K_θ by analogy with Sec. 10.3, assuming that there is an effective mass $M^* > M_b$ that can be imagined to move as a solid body. Equating the frequency of the rotating case with that of linear translation gives $K/M^* = K_\theta/I^*$ where $I^* \simeq M^* H_b^2/3$. Using $K \sim 5\,\mathrm{N/m}$, which was the optimum value from Sec. 10.3 and corresponds to $M^* \sim (M_f + M_b)/2$, yields the estimate $K_\theta \sim H_b^2 K/3 \simeq 1.1 \times 10^{-4}\,\mathrm{N\ m}$.

As in Sec. 10.3.1, we vary the spring stiffness and characterise the system response in terms of the contact point asymmetry $\mathcal{A}$. The results are presented in Fig. 10.9 for three representative scenarios: a freely rotating baffle ($K_\theta = 0$), a rotating baffle with $K_\theta = 6.4 \times 10^{-5}$ N m and a fixed baffle. The main difference between these results and those of Fig. 10.3 is the performance of the freely rotating baffle ($K_\theta = 0$), which is quite different from the no-baffle case and the limit $K \to 0$ for translating baffles. This is due to the fact that the rotating baffle has an anchor point that constrains its motion and prevents drifting. Even without a restoring spring force, the baffle significantly affects the fluid flow and reduces the decay time for sloshing.

Intermediate spring constants, on the other hand, lead to similar behaviour for both types of moving baffles (see snapshots II of Fig. 10.3 and Fig. 10.9). Furthermore, since the baffle geometry is identical, the fixed-baffle limit is the same for both the translating and the rotating baffles.

The results of numerical simulations with a range of K_θ values are summarised in Table 10.4 and in Fig. 10.10, both in terms of τ_d and the integrated kinetic energy $\mathcal{I}$ of Eq. (10.18). As in the case of a translating baffle, beginning from the fixed-baffle limit and decreasing spring stiffness leads to reductions in both τ_d and $\mathcal{I}$. Eventually, a minimum is reached near $K_\theta \simeq 10^{-4}$ N m, although the optimum over τ_d and over $\mathcal{I}$ are shifted more than in the case of Fig. 10.4. Decreasing K_θ below the optimal range makes the response to sloshing worse than in the fixed-baffle case, although performance does not decline as rapidly or as much as in the case of a translating baffle.

A comparison of Figs. 10.4 and 10.10 and of Tables 10.3 and 10.4 suggests commensurate, if different, performance is available with the two moving baffle configurations investigated. Rotating baffles, for instance, are able to achieve slightly lower decay times. With $K_\theta = 0.64 \times 10^{-4}$ N m, we find $\tau_d = 2.31\,\mathrm{s}$, which is a reduction of 48.4% with respect to a fixed baffle and better than the 40% reduction for a translating baffle. However, translating baffles offer slightly more reduction in the integrated kinetic energy of the fluid. With $K = 5\,\mathrm{N/m}$, we find $\mathcal{I} = 2.19 \times 10^{-7}$ J s while, for the rotating baffle, the lowest value achieved is $\mathcal{I} = 2.24 \times 10^{-7}$

$K_\theta \times 10^4$ (N m)	τ_d (s)	$\mathcal{I} \times 10^7$ (J s)
0	5.79	4.62
0.16	4.92	4.08
0.32	4.72	3.69
0.48	3.79	2.78
0.64	**2.31**	2.47
0.72	2.59	2.37
0.8	2.60	2.29
1.28	2.67	**2.24**
3.2	2.85	2.28
12.8	3.73	2.58
∞	4.48	2.86

Table 10.4: Decay times τ_d and integrated kinetic energies $\mathcal{I}$ from Eq. (10.18) for a single rotating baffle. Decay times are measured with respect to the end of the forcing at $t - t_0 = 2\,\text{s}$ (see Fig. 10.9). Green shading draws attention to K_θ values that attenuate sloshing more than a fixed baffle.

J s with $K_\theta = 1.28 \times 10^{-4}$ N m.

These numerical results demonstrate that a single rectangular moving baffle can significantly improve upon the performance of an identical fixed baffle. Allowing either translational or rotational motion, with an appropriate choice of spring constant, will reduce the kinetic energy and decay time of sloshing. Note that there are many other baffle geometries that may be considered. Below, we follow the recent work of Peromingo et al. [225] and investigate a three-arm baffle, which is here allowed to rotate.

10.4.2 Three-arm rotating baffle

The three-arm baffle under consideration is sketched in Fig. 10.11, with the length of each arm taken to be $L_a = H_b/\sqrt{2} \simeq 5.66\,\text{mm}$. For simplicity, the pivot point is placed at the centre of mass although, as noted earlier, the average leftward or rightward flow will generate counteracting torques and, presumably, less rotation than if the pivot point were at the end of one arm, for example.

The torque equation determining the evolution of the angular variable θ for the three-arm baffle is of the same form as Eq. (10.21) and the no-slip boundary condition is as in Eq. (10.22). An estimate for the optimal value of K_θ can be obtained with the same argument based on effective inertia as applied in Sec. 10.4.1, this time with $I^* \simeq M^* L_a^2/3$ and, thus, $K_\theta \sim L_a^2 K/3$. Using the observed optimal value of $K \simeq 5\,\text{N/m}$ from Sec. 10.3, this gives $K_\theta \sim 5 \times 10^{-5}$ N m.

The results corresponding to different K_θ values are summarised in Table 10.5 and in Fig. 10.12. It is immediately clear that allowing this three-armed baffle to rotate does not improve performance nearly as much as the movement did with the simple translating or rotating rectangular baffles. This shows the crucial importance of geometric considerations including

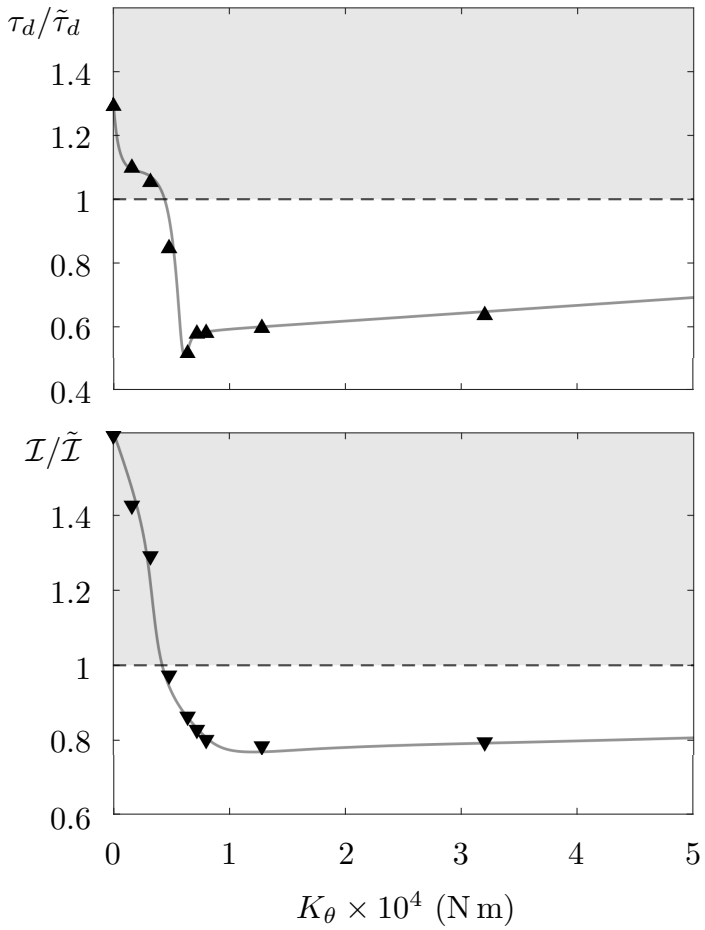


Figure 10.10: (Upper) Single rotating baffle decay time τ_d relative to that of a fixed baffle ($\tilde{\tau}_d$) versus K_θ. The minimum decay time is obtained for $K_\theta \sim 7 \times 10^{-5}$ N m. (Lower) Integrated kinetic energy $\mathcal{I}$ relative to that for a fixed baffle ($\tilde{\mathcal{I}}$) versus K_θ. The minimum value is obtained for $K_\theta \sim 10^{-4}$ N m. Corresponding dimensional values for some of these data points can be found in Table 10.4.

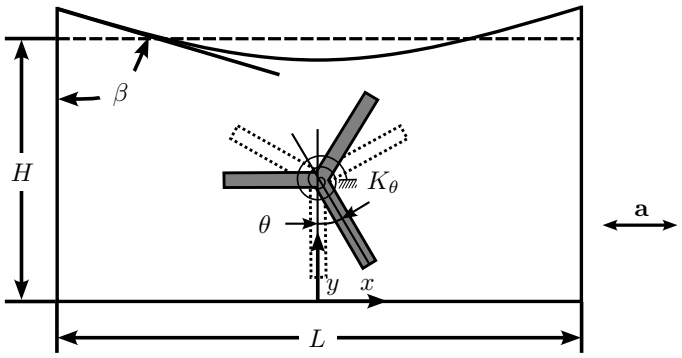


Figure 10.11: Sketch of the system with a three-arm rotating baffle. The pivot point is at $(0, H/2)$ and the acceleration $\mathbf{a}$ is applied horizontally.

baffle shape and pivot point placement. More complex baffles with customised shapes may

$K_\theta \times 10^5$ (N m)	τ_d (s)	$\mathcal{I} \times 10^7$ (J s)
0	3.85	2.45
0.8	3.9	2.43
1.6	3.02	2.42
1.76	3.01	2.42
1.92	**3.00**	2.42
2.56	3.07	2.42
2.88	3.17	2.42
3.2	3.23	2.42
6.4	3.26	2.44
9.6	3.26	2.45
∞	3.25	2.47

Table 10.5: Decay times τ_d and integrated kinetic energies $\mathcal{I}$ from Eq. (10.18) for a three-arm rotating baffle. Decay times are measured with respect to the end of the forcing (see Fig. 10.9). Green shading draws attention to K_θ values that attenuate sloshing more than a fixed baffle.

offer further opportunity for sloshing mitigation [225].

As with the results of Fig. 10.10, if one begins from the fixed-baffle case and reduces the torsion spring stiffness, a minimum is eventually achieved in both τ_d and $\mathcal{I}$, though not simultaneously. Further reductions lead to performance decline, although it remains considerably better than the no-baffle case. The performance enhancement is particularly mild for $\mathcal{I}$ (see the lower panel of Fig. 10.12) where the maximum difference with respect to the fixed-baffle case ($\tilde{\mathcal{I}}$) is only about 2%. Although $\mathcal{I}/\tilde{\mathcal{I}}$ always remains lower than unity (at least, for this particular pulse-like perturbation), the ratio $\tau_d/\tilde{\tau}_d$ does increase to approximately 1.2 for some K_θ values.

The behaviour of the rotating three-arm baffle can be partly understood from the relatively large area of the tank that it affects. The no-slip boundary conditions mean that a larger amount of surrounding fluid is entrained by the movement of the rotating baffle rather than participating in the sloshing flow. This picture is consistent with the lower values of $\mathcal{I}$ (compare the values in tables 10.3, 10.4 and 10.5), which are only weakly dependent on K_θ. The decay time τ_d varies slightly more with K_θ, but the best improvement is still less than 10% (see the left panel of Fig. 10.12).

10.5 Moving baffle simulations in an operational microgravity scenario

In light of the promising results of Sec. 10.3 for a pulse-like perturbation and the work of Gligor et al. [201] and Peromingo et al. [225] on sloshing control, the vertical spring-baffle system with horizontal motion is now subjected to a real microgravity perturbation recorded during a reboosting manoeuvre on board the International Space Station (ISS). The measured

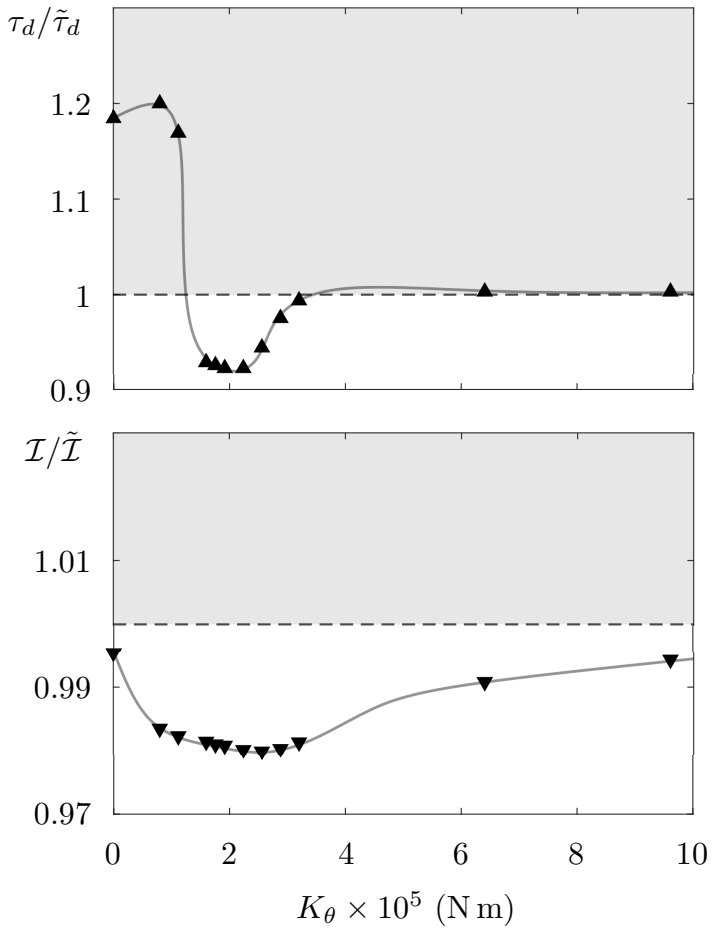


Figure 10.12: (Upper) Three-arm rotating baffle decay time τ_d relative to that of a fixed three-arm baffle ($\tilde{\tau}_d$) versus K_θ. The minimum decay time is obtained for $K_\theta \sim 2 \times 10^{-5}$ N m. (Lower) Integrated kinetic energy $\mathcal{I}$ relative to that for a fixed baffle ($\tilde{\mathcal{I}}$) versus K. The minimum value is obtained for $K_\theta \sim 3 \times 10^{-5}$ N m. Corresponding dimensional values for some of these data points can be found in Table 10.5.

acceleration signal enters as $\mathbf{a}(t)$ in Eqs. (10.1) and (10.7).

Figure 10.13 shows the evolution of the left contact point over time in terms of

$$\delta\mathcal{Y}_-(t) = f(-L/2, t) - f(-L/2, t_0 + \tau), \tag{10.23}$$

for the no-baffle, fixed-baffle, and moving baffle cases. Results are presented only for the first 75 s of the reboosting manoeuvre since this covers the transient response to the large pulse-like acceleration near $t = 20$ s, which provokes the most sloshing. Supplementary movie 2 is provided to accompany this figure and shows the temporal evolution of the sloshing response in the moving-baffle case.

The figure demonstrates a large improvement with a fixed baffle (blue curve) compared to no baffle (grey curve) and a further significant improvement for a moving baffle with $K = 5$ N/m (red curve). The specific decay times for the transient response to the pulse-like acceleration are 23.1 s (no baffle), 4 s (fixed baffle) and 1.3 s (moving baffle); these times are calculated in

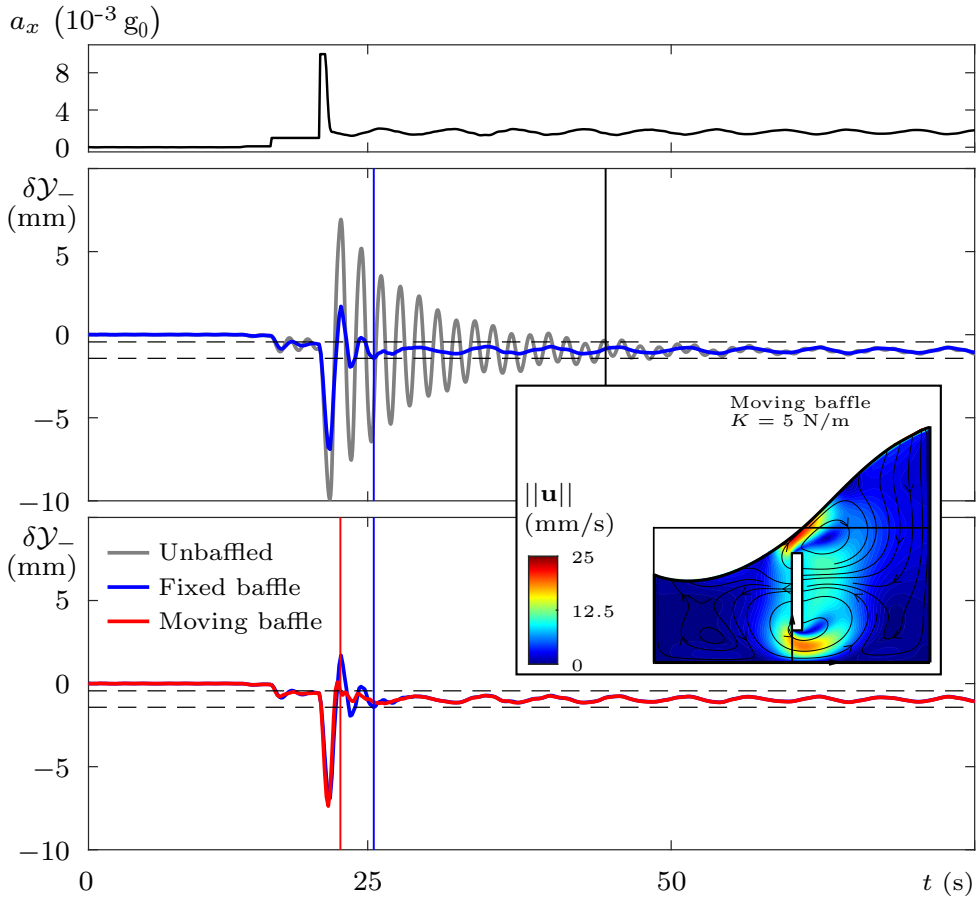


Figure 10.13: Effect of fixed and moving baffles on a fluid system subjected to perturbations taken from an ISS reboosting manoeuvre. (Upper) Acceleration measurements from the OSSRAW sensor on the ISS in units of ordinary gravity, g_0, over 75 s. (Middle) Evolution of the left contact point $\delta\mathcal{Y}_-$ for the no-baffle (grey curve) and the fixed-baffle cases (blue curve). Vertical black and blue lines denote the decay time based on the 5% stability criterion (marked with horizontal dashed lines). (Lower) Comparison between a fixed baffle (blue curve) and a moving baffle with $K = 5\,\mathrm{N/m}$ (red curve). The decay time (vertical red line) is significantly decreased for the moving baffle. The inset shows the flow and maximum deformation of the fluid surface for the moving baffle case.

the same manner as with the pulse-like acceleration of Sec. 10.2.3, with respect to the end of the pulse. The improvement factors can be represented in a simple way through a gain parameter $\mathcal{G}$ defined as the ratio of the no-baffle decay time to the baffle-mitigated decay time. For the fixed baffle, we have $\mathcal{G}_{\text{fixed}} = 5.8$ and, for the moving baffle, $\mathcal{G}_{\text{moving}} = 17.8$, which shows again that the improvement with a properly tuned baffle can be substantial. We emphasise once more that the moving-baffle system is passive and does not require an energy source.

Apart from the response to the large pulse-like part of the acceleration signal, Fig. 10.13 shows that after the associated sloshing motion decays ($t > 26\,\mathrm{s}$), the baffle, whether moving or fixed, is unable to reduce the low-frequency motion of the fluid that is driven by the periodic

component of the acceleration signal. This low-frequency behaviour is expected and consistent with the Bode diagrams in Fig. 10.5. Counteracting nonresonant forced oscillations like this may require an active control system [201]. For example, the recent work of Peromingo et al. [225] considered the same reboosting acceleration signal with active thermocapillary-based control and achieved a decay time of 7.5 s that reduced to 2.4 s when combined with a fixed vertical baffle. Although the passive moving baffle considered here performs better with resonant sloshing, the active control can easily adapt to nonresonant forcing.

10.6 Conclusions

The numerical investigations presented here examine a recent idea for sloshing control in microgravity: moving baffles constrained by springs. The idea draws directly from the success of TMDs, which are widely used in structural engineering. Allowing constrained translational or rotational motion, with a properly tuned restoring force, can significantly enhance the ability of a given baffle (defined by geometry and placement) to mitigate sloshing.

The numerical model used here was validated against the (no-baffle) results of Faltinsen et al. [270] and the baffled fluid system of Liu and Lin [53]. With a maximum mesh size selected from a mesh convergence study and set to 1% of the container length, the model developed here satisfactorily reproduces the correct sloshing behaviour. The validated model was then adapted to ideal microgravity conditions and the moving baffle designs of interest, beginning with a vertically-aligned baffle allowed to translate horizontally.

The response of the translating baffle system to a pulse-like perturbation shows that an optimum value for the spring stiffness K can be obtained that minimises the decay time or the integrated kinetic energy of the fluid, although not simultaneously. Enhancements of up to 40% for the decay time and 23.4% for the kinetic energy can be obtained compared to a fixed baffle. A Fourier analysis of the system response near the optimum K value reveals two dominant frequencies. The features of these two resonant modes depend strongly on K.

The pulse-like acceleration was replaced by a continuous periodic one so that the response to frequencies between 0.1 and 2 Hz could be determined. This frequency analysis shows that increasing the spring stiffness K reduces the amplitude of the original (no-baffle) resonance peak and shifts it to higher frequencies. At the same time, a second peak appears at a lower frequency, near that of sloshing in a fixed-baffle system. The first (higher-frequency) mode involves significant coupling between fluid and baffle motion. The second (lower-frequency) mode involves less baffle motion and may be described as sloshing-dominated. It remains in the limit $K \to \infty$ while the other resonant peak moves out to infinite frequency with vanishing amplitude.

The influence of spring damping was also investigated, with the results indicating that its effects are similar to increasing K and associated with reduced amplitude of the (higher-frequency) resonant mode with greater baffle motion.

The results of the frequency analysis can be used to compare with previous control strategies like that in Xie and Zhao [57], which relied on actively controlled baffles to achieve sloshing reduction by as much as 81.5%. The results obtained here demonstrate that nearly the same

sloshing reduction compared to the no-baffle case — up to 80.5% with $K = 5\,\mathrm{N/m}$ — can be achieved using a *passive* control strategy.

The same simple baffle was then considered with rotational rather than translational motion and similarly good performance was found, with reductions compared to the fixed-baffle case of 48.4% and 21.7% in the decay time and kinetic energy, respectively.

Motivated by the recent results of Peromingo et al. [225], a three-arm baffle was then considered and allowed to rotate about its centre of mass. Given that this particular baffle configuration is already quite effective without motion, including the rotational degree of freedom permits only small improvements — approximately 2% in kinetic energy and 10% in decay time.

More complicated baffle motion, including oblique translation or a combination of rotational and translational degrees of freedom was left for future studies. However, to the extent that the transient behaviour in this system is well-described by a linear combination of two resonant modes, a mixture of translations and rotations may be expected to resemble a superposition of the current results.

Finally, since the moving baffle strategy is intended to help control sloshing in microgravity applications, the horizontally translating baffle was reconsidered when driven by a real microgravity acceleration signal taken from an OSSRAW sensor on the ISS during a reboosting manoeuvre. The moving baffle is very successful at mitigating the resonant sloshing induced by an especially large peak in the acceleration. The transient sloshing lasts (according to a 5% criteria) for 23.1 s with no baffle, for 4 s with a fixed baffle, and only 1.3 s with a properly tuned moving baffle.

Overall, these results demonstrate the potential of passive, moving-baffle systems like those proposed here. However, since their effectiveness depends on properly tuned springs, it should be noted that many practical systems will have varying filling ratios and, thus, both the frequency and the effective damping of sloshing dynamics will change. If liquid is removed from the tank (as with propellant or water storage), the sloshing frequency is expected to decrease in accord with Eq. (10.15) while damping would increase due to finite-size effects. The lower hydrodynamic load on the baffle would render it too “stiff" and effectively decouple it from the sloshing motion. Such a detuned system would behave much like one with a fixed baffle. On the other hand, if liquid is added to the tank, not only would the spring be too weak for the increased fluid inertia, but the ratio H_b/H would also decrease and reduce the baffle's effect. To adapt the moving baffle strategy to systems with variable filling ratios, it may be necessary to investigate various extensions of the basic configurations treated here, like placing several baffles at different depths, each tuned for the corresponding level of liquid. Similarly, the use of multiple moving baffles may allow the system to be tuned for counteracting or controlling several distinct sloshing modes.

Although the moving-baffle control strategy analysed here was motivated by microgravity applications, it can also be utilised on ground, including liquid tanker trucks or cargo ships, where sloshing is a serious concern. The effect of gravity increases the sloshing frequency and necessitates larger spring constants to achieve the optimal response. Further investigation of numerical models and the testing of these with real experiments are called for. Additional insight may also come from a more in-depth analysis of the main dynamical modes using a

data-driven decomposition such as (multi-scale) proper orthogonal decomposition [274] or time-localised fitting that can estimate the damping for each mode.

Acknowledgments The work of D.G., C.P., P.S.S., J.P. and J.F was supported by the Ministerio de Ciencia e Innovación under Project No. PID2020-115086GB-C31, and by the Spanish User Support and Operations Centre (E-USOC), Center for Computational Simulation (CCS).

Chapter 11

Sloshing reduction with passive spring-mass baffles in partially filled containers

D. Gligor, P. Salgado Sánchez, J. Rodríguez and U. Martínez

Ocean Engineering **310**, 118675 (2024)

https://doi.org/10.1016/j.oceaneng.2024.118675

The potential for sloshing reduction of passive, moving baffles with translational motion constrained by springs is investigated numerically in partially filled containers. Simulations are based on the level-set formulation, considering water as the liquid under study and a baffle made of aluminum; this selection allows for direct validation of the model against experimental and analytical data. Depending on the filling ratio $\mathcal{V} \in (0, 1)$, which simply measures the volume of liquid relative to the total container size, one can find an optimal spring stiffness $K(\mathcal{V})$ that minimizes the kinetic energy and decay time of the sloshing response when subjected to a pulse-like acceleration. Results show that moving baffles significantly reduce sloshing compared to their fixed counterparts, with decreases up to 84.6% in decay time, τ_d. Frequency analyses for different $\mathcal{V}$ reveal one or two resonances in the range of 0.1–1.5 Hz whose amplitudes are directly influenced (lowered) by K, analogous to the behavior of Tuned Mass Dampers. For potential applications, the selection of K should look for an adequate sloshing response over the entire range of $\mathcal{V}$, and account for both quasi-static and harmonic excitation, conveniently weighted in accord with the expected operational loads.

11.1 Introduction

Liquid transportation and related phenomena have always been a subject of interest for society. Nowadays, the development of industrial and energetic networks requires fluid management in a wide variety of applications, ranging from liquefied natural gas (LNG) transport in ships or trucks, to propellant control in spacecraft, launchers, and rockets.

In this context, liquid sloshing is undoubtedly one of the top researched problems; any system involving a partially filled container presents this type of motion when subjected to quasi-steady or low-frequency excitation. In ocean engineering, for instance, LNG tank ships with filling ratios ranging from 10% to 70% may experience vigorous motion due to the back-and-forth motion of the liquid within [275]. It is well known that this sloshing can exert significant loads on the carrier structure. In particular, if such excitation is close to the structural resonances of the tank, it can lead to violent fluid oscillations that may compromise structural integrity [270, 276, 277].

Over the years, numerous theoretical, experimental and numerical research aiming to mitigate sloshing and related issues has been developed. The seminal monograph of [39] reviews both analytical and experimental results on liquid sloshing in containers with different shapes, albeit more focused on space vehicle technology applications. The reference works of Moiseyev and Rumyantsev [278], Ibrahim [40] and Faltinsen and Timokha [60] further delve on sloshing-related phenomena and offer valuable insights about sloshing mitigation strategies. Among the most widespread ones, we can highlight modifying the container geometry to triangular or prismatic shapes [37, 39, 40] or adding (passive) baffles with different shapes, positioning, or made up of low-stiffness, deforming materials.

Nowadays, the effect of baffles on sloshing motion is still a subject of interest for researchers, as their configurations (and combinations) can be easily modified to optimize their performance. Baffles generally increase the damping ratio of the fluid system when subjected to perturbations, albeit such improvement greatly depends on the their characteristics, e.g., position within the container [54, 58, 59], orientation, dimensions and shape, among others [224]. If placed in the vicinity of the free surface, either submerged or disrupting it, they strongly interact with the large velocities that usually develop there. By interfering with the underlying flow, baffles increase the dampening of sloshing modes and can significantly reduce liquid motion at the cost of introducing a certain force on the baffle via pressure gradients and the underlying fluid-structure coupling. This effect is complemented by increased viscous dissipation due to the additional boundary layers forming on the baffle surfaces. Besides that, the presence of baffles may also alter sloshing frequencies, influencing the interaction with low-frequency perturbations [51, 52, 60, 61]. The extensive literature on fixed baffles evidences a thorough study on the mentioned effects; see, e.g., [39, 52, 60] and references therein.

In recent years, more complicated approaches to sloshing reduction have been investigated. Some methods use elastic baffles [62, 63] that take advantage of the fluid-structure coupling and improve performance with respect to their (infinitely) rigid counterparts. For instance, during the rolling motion of a fluid container equipped with an elastic baffle, it deforms over time — with the corresponding energy absorption — and interacts with the liquid flow, reducing sloshing motion if the baffle stiffness (i.e., elastic modulus) is large enough. Other applications include air-trapping mechanisms [188, 189], which exploit the large impact pressure existing at the container walls to absorb part of the liquid kinetic energy, thus increasing the effective damping of the system.

As a natural extension of the aforementioned approaches, actively controlled baffles are arguably a promising solution. For instance, the recent numerical work of Xie and Zhao [57] introduces deep reinforced learning to provide active sloshing suppression. Here, two

horizontal baffles conveniently placed closer to the container end walls are actively moved to provide an optimal sloshing reduction of ∼81.48%, as determined by the learning algorithm. Note that this type of active systems entails a major drawback, requiring a power source to drive the motion of the baffle.

Albeit it may seem that elastic or active baffles would imply either a careful selection of baffle material and associated structural properties, or an external power source to drive baffle motion, one can find a simple alternative where stiff, moving baffles are attached to elastic elements such as cables or springs. As a representative example, the work of Koh et al. [56] presents the concept of constrained floating baffles (CFB), which demonstrated a notable reduction of the dynamic pressure on the container walls both numerically and experimentally. Another relevant approach exploiting the impact force of liquid sloshing can be found in the work of Kim et al. [64]. By attaching horizontal rigid baffles to elastic elements (springs), the large liquid impact force is absorbed by the springs and the sloshing response of the system is improved.

This same setup was numerically investigated by Iranmanesh and Nikbakhti [65] who also accounted for the additional liquid energy dissipation through recirculation zones. Despite this method being effective on the analyzed configuration, the selected spring constant may not be optimal for all possible filling ratios. In applications, one may argue that a fluid container may experience a reduction of its contained liquid over time. In this scenario, the system proposed by Iranmanesh and Nikbakhti [65] could be optimized for intermediate filling ratios while possibly failing for lower values: if the quantity of liquid decreases beyond a certain value, it may not reach the baffle(s) and, instead, the associated loads would be fully absorbed by the container end walls.

Despite the novelty of these approaches in the field of sloshing phenomena, the concept of moving devices for resonance control (sloshing resonances in this case) is not entirely new, as it is closely-related to the functioning of Tuned Mass Dampers (TMDs) [68] in structural engineering. TMDs are devices connected to a structure aiming to stabilize or mitigate the structural response near resonance. Typically, the (smaller) TMD mass is attached to one or more elastic springs, leading to the splitting of the main resonance peak into two smaller peaks at slightly different frequencies [69, 70]. From a design perspective, the use of TMDs constitutes one of the most extended approaches for earthquake motion reduction [71], damping wind disturbances of taller buildings [72] or stabilizing industrial machinery [73].

Recently, the works of Zheng et al. [66], Wang et al. [67] and Gligor et al. [84] have examined a similar spring-mass moving baffle system but applied to sloshing reduction. By placing a vertical baffle (or a slatted panel) and allowing it to move along the x direction of the fluid container (or perhaps rotate), a more pronounced sloshing mitigation is achieved with respect to their fixed counterparts over an optimum spring stiffness range. The enhancement is further amplified if we consider the unbaffled container response. These studies reasonably agree on these findings considering both the system response to a pulse-like acceleration and its dynamic response. A similar concept was presented by Kim et al. [64] with moving horizontal baffles, placed at the lateral walls of a rectangular container, that restrict the local (vertical) motion of the free surface.

In light of these results, the present work aims to extend the knowledge on moving baffle systems for ground applications. A wider range of filling ratios and different baffle configurations are considered, along with a discussion on the underlying flow mechanisms that need to be accounted for to optimize the sloshing performance in fluid containers. We highlight that the analysis here focuses on the sloshing mitigation from a fluid dynamics perspective, that is, considering mainly the motion that develops within the fluid domain as a result of the baffle interference. In this regard, we exclude from the analysis any further (complex) interaction with a potential structure containing the fluid deposit, namely a tank ship or a launch vehicle. We note that developing an engineering application for these systems would encompass an analysis of the complete system, thus addressing all the potential couplings between the different elements of the dynamical system. Such a scope could be subject of further analysis.

The manuscript is organized as follows. In Sec. 11.2, the mathematical and numerical model are summarized, and then validated in Sec. 11.3. Results for a baffle moving along the x-axis are presented in Sec. 11.4 by applying a pulse-like acceleration. Subsequently, Sec. 11.5 contains results for a two-moving baffle configuration subjected to the same perturbation. Based on these results, which are summarized in Sec. 11.6, a frequency analysis is performed to the former two-baffle configuration in Sec. 11.7. Finally, the main conclusions are drawn in Sec. 11.8.

11.2 Mathematical formulation

A rectangular container with inner dimensions $L \times H = L \times (H_1 + H_2)$ holding a liquid (H_1) and a gas (H_2) is considered. The system is subjected to perturbations oriented along the x-axis, parallel to the initially flat (unperturbed) free surface. A moving baffle with dimensions $L_b \times H_b$ is located in the middle of the container, at a height H_c with respect to the bottom wall. Baffle motion is restricted along the x direction by two linear springs, each with a constant $K/2$, that maintain the baffle around a centered ($x_b = 0$) position. This system is sketched in Fig. 11.1.

A level-set approach [85], which tracks the liquid-air interface by defining the level-set function ϕ, is adopted to simulate the sloshing dynamics of the interface. The time-evolution of ϕ is governed by:

$$\phi_t + \nabla \cdot (\mathbf{u}\phi) = \gamma \nabla \cdot \left[\varepsilon \nabla \phi - \phi(1-\phi) \frac{\nabla \phi}{|\nabla \phi|} \right], \tag{11.1}$$

where γ is a tuning parameter set to the maximum order of magnitude of the velocity field $\mathbf{u}$, and ε is a small diffusive term added for numerical stability, taken to be on the order of the maximum mesh element size. The term $\phi(1-\phi)\nabla\phi/|\nabla\phi|$ counteracts numerical diffusion and the tendency of the interface to increase in width.

The immiscible liquid-air system is considered as a continuum, and ϕ is used to define the transition across the free surface of the fluid densities and dynamic viscosities:

$$\begin{aligned} \rho &= \rho_1 + (\rho_2 - \rho_1)\mathcal{H}, \\ \mu &= \mu_1 + (\mu_2 - \mu_1)\mathcal{H}, \end{aligned} \tag{11.2}$$

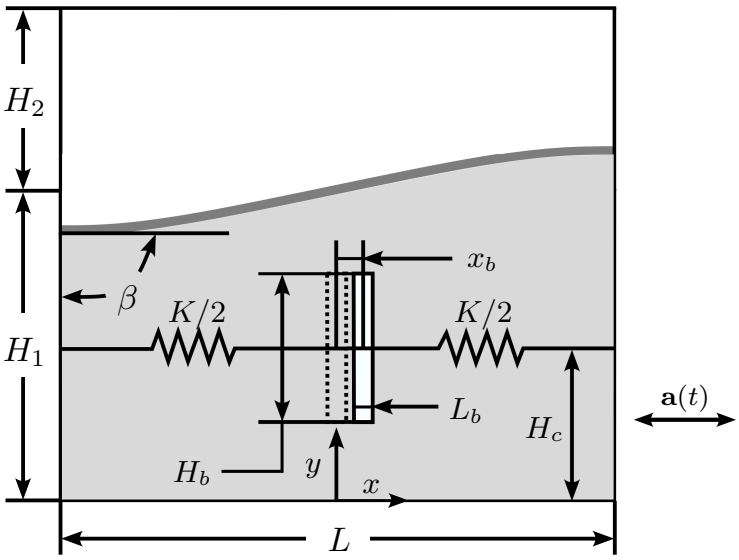


Figure 11.1: Sketch illustrating the 2D setup for the level-set formulation. A moving baffle is included, whose dimensions and positioning are depicted. The direction of the excitation acceleration $\mathbf{a}(t)$ is indicated.

where the smoothed Heaviside function $\mathcal{H}$ is defined as follows

$$\mathcal{H}(\tilde{\phi}) = \begin{cases} 0, & \tilde{\phi} < -\varepsilon, \\ \frac{1}{2} + \frac{\tilde{\phi}}{2\varepsilon} + \frac{1}{2\pi}\sin\left(\frac{\pi\tilde{\phi}}{\varepsilon}\right), & |\tilde{\phi}| \leq \varepsilon, \\ 1, & \tilde{\phi} > \varepsilon. \end{cases} \tag{11.3}$$

Here, $\tilde{\phi} = \phi - 0.5$, with the values $\phi = 0$, 1 corresponding respectively to the liquid and air denoted by subscripts 1 and 2 in Eq. (11.2). The free surface is defined by the contour $\phi = \mathcal{H} = 0.5$.

We consider laminar and incompressible flow so that the conservation of mass and momentum can be described by the Navier-Stokes equations [75]:

$$\nabla \cdot \mathbf{u} = 0, \tag{11.4a}$$

$$\rho\left(\frac{\partial \mathbf{u}}{\partial t} + (\mathbf{u}\cdot\nabla)\mathbf{u}\right) = -\nabla p + \mu\,\nabla^2\mathbf{u} + \rho\,\mathbf{G}(t) + \delta\mathbf{f}_\sigma, \tag{11.4b}$$

where p is the pressure field at each fluid and the term $\rho\,\mathbf{G}(t) = -g\mathbf{j} + \mathbf{a}(t)$ includes gravity and an external acceleration (perturbation). The additional force $\mathbf{f}_\sigma$ is included in Eq. (11.4b) to describe the effect of surface tension σ at the liquid-air interface by writing

$$\mathbf{f}_\sigma = (\sigma\kappa)\mathbf{n}, \quad \kappa = -\nabla\cdot\mathbf{n}, \quad \mathbf{n} = \frac{\nabla\phi}{|\nabla\phi|}. \tag{11.5}$$

Here, κ is the free surface curvature and $\mathbf{n}$ its normal vector. To localize the effect of σ in the vicinity of the free surface, $\mathbf{f}_\sigma$ is multiplied by δ

$$\delta = 6\,\phi(1-\phi)|\nabla\phi|. \tag{11.6}$$

The present formulation does not account for turbulent flow. If we consider a characteristic velocity $u_c = 0.1$ m/s — based on the numerical results presented in later sections —, a characteristic length $l_c = 0.01$ m — the baffle length L_b — and the density and dynamic viscosity of water, the Reynolds number $\mathrm{Re} = u_c\, l_c/\nu = 1000$. Typically, turbulence plays a critical role for $\mathrm{Re} > 3000$ [279, 280] and, despite the estimated Re is lower, it is $\mathcal{O}(10^3)$ so that it may be relevant in real applications. However, one can discuss in advance its effects as follows.

First, if the driving force is a pulse-like acceleration, fluid velocity would decrease over time and the above estimate represents an upper bound for Re. Therefore, turbulent flow, if present, would tend to relaminarize with time. If the driving force is harmonic, on the other hand, Re could locally oscillate. To ensure that Re is low enough at resonance, we shall consider forcing amplitudes and frequencies that do not drive fluid velocities exceeding the abovementioned value. By doing so, we can assure that the Reynolds number would oscillate between the range $\mathrm{Re} \in [0,\, 1000]$.

Furthermore, by considering laminar flow, the additional effect of turbulent dissipation on the sloshing response, characterized by its decay time and amplitude, is not accounted for. In this sense, the present numerical results are somewhat conservative, since they would be further improved by turbulence.

A two-dimensional (2D) approximation is further assumed, with the problem depending only on the horizontal (x) and vertical (y) coordinates. In the time-dependent fluid domain, Eqs. (11.4) — along with additional boundary conditions described later — are written in mesh coordinates, which are then mapped to spatial coordinates. The mesh is smoothly deformed in accordance with the Winslow technique [79]:

$$\frac{\partial^2 X}{\partial x^2} + \frac{\partial^2 X}{\partial y^2} = 0, \tag{11.7a}$$

$$\frac{\partial^2 Y}{\partial x^2} + \frac{\partial^2 Y}{\partial y^2} = 0, \tag{11.7b}$$

where $(x,\, y)$ are the spatial coordinates of the spatial frame and $(X,\, Y)$ are the reference coordinates of the material frame, which coincide here with the mesh frame. The boundary conditions for (11.7) are $\mathbf{u}_{\mathrm{mesh}} = 0$ at the container and baffle walls.

11.2.1 Initial and boundary conditions

Initially, fluids are quiescent with a flat free surface. Navier-slip conditions are assumed on all solid walls to preserve the contact angle and allow contact line motion. At the solid walls, a null normal velocity is imposed

$$\mathbf{u} \cdot \mathbf{n}_w = 0, \tag{11.8}$$

together with an artificial frictional force that opposes fluid motion

$$\mathbf{f}_v = (\rho\nu)/\delta_v \mathbf{u}, \tag{11.9}$$

where δ_v is the slip length. This frictional force includes an additional term to enforce a prescribed contact angle

$$\mathbf{f}_\beta = [\sigma\delta(\mathbf{n}_w - \mathbf{n}\cos\beta)], \tag{11.10}$$

	ρ (kg/m^3)	ν (10^{-6} m^2/s)	σ (10^{-3} N/m)
Water	1000	1	80
Air	1.2	14.7	
Aluminum	2700	—	—

Table 11.1: Selected fluid properties and aluminum density at the reference temperature $T_0 = 20\,^{\circ}\mathrm{C}$.

where $\mathbf{n}_w$ is a unit vector normal to the wall. Note the use of δ to localize this force in the vicinity of the free surface.

11.2.2 Moving baffle

The system described by Eqs. (11.1)–(11.10) is augmented by the equation for the moving baffle and the associated boundary conditions. Here, we consider a baffle made of aluminum with only translational motion; see Fig. 11.1. Note that no significant baffle deformation due to pressure differences is anticipated and, therefore, the baffle is considered perfectly rigid.

With no vertical displacement or rotation of the baffle, its dynamics can be described by the following momentum balance along the x direction:

$$\ddot{x}_b + \frac{K}{M_b} x_b = \mathbf{a} \cdot \mathbf{i} + \frac{1}{M_b} \int_{\Sigma_b} (p\,\mathbf{n}_b + \boldsymbol{\tau} \cdot \mathbf{n}_b) \cdot \mathbf{i}\, d\Sigma_b. \tag{11.11}$$

Here, x_b is the horizontal displacement of the baffle, K is the spring constant, $\mathbf{i}$ is a unit vector in the x direction and $\boldsymbol{\tau}$ is the fluid viscous stress tensor. The external baffle surfaces Σ_b are defined in local coordinates, (X_b, Y_b), with $\mathbf{n}_b$ being a unit vector normal to the baffle surface. The baffle mass can be written as $M_b = \rho_b W_b L_b H_b$ in terms of its density ρ_b, width W_b (taken as unity in the 2D approximation), length L_b and height H_b. The right-hand side of the oscillator equation includes three terms accounting for the applied acceleration $\mathbf{a}$ [as in (11.4b)], pressure forces and viscous stresses exerted by the fluid on the baffle surfaces, respectively. The latter two terms couple baffle motion with the flow.

We note that, if the liquid-gas interface (H_1) is such that it is directly in contact with the baffle, an additional term concerning σ should be included. This contribution is negligible compared to the pressure differences across the baffle.

The boundary conditions on the baffle walls Σ_b are also assumed to be Navier-slip (as with the container). Here, however, the relative velocity to the baffle

$$\mathbf{u}_{\mathrm{rel}} = \mathbf{u} - \dot{x}_b \mathbf{i} \tag{11.12}$$

is introduced in Eqs. (11.8) and (11.9). Similarly, the contact angle with the baffle is considered equal to that of the container walls and, therefore, Eq. (11.10) is extended to Σ_b.

11.3 Numerical integration, convergence and validation

The problem considered here is considerably simplified by the restriction to 2D dynamics. This approach can be considered valid under normal gravity conditions if the container out-of-plane dimension is such that the considered excitation does not induce out-of-plane motion. In the present work, the applied perturbation is directed exclusively along the x direction.

The commercial software COMSOL Multiphysics is used to resolve Eqs. (11.4)–(11.11) in dimensional variables with the finite element method. The time integration is performed with a generalized-α [81] scheme stabilized with streamline [82] and crosswind [83] techniques. The maximum time step is 0.05 s with smaller steps automatically used by the solver when required by the Courant-Friedrichs-Levy convergence condition for numerical stability.

For the numerical results presented throughout this report, we take the physical properties of water and air (see Table 11.1) because of the availability of extensive numerical and experimental data for comparison. In particular, we compare our results against two relevant references on sloshing phenomena: the work of Faltinsen et al. [270] for unbaffled tanks with periodic excitation, and that of Liu and Lin [53] for a 2D tank with fixed baffles. Once the relevant numerical parameters are selected, our numerical predictions are further compared against the works of [56], where a constrained floating baffle is analyzed, and Kim et al. [64], where horizontal moving baffles are introduced.

The relevant numerical parameters considered here are the mesh size $\mathcal{S}$ and slip length δ_ν arising from the Navier-slip boundary condition, and the interface thickness ε, which is arguably the most relevant one. A large ε may significantly alter the free surface dynamics by adding excessive numerical damping, given the large region over which the liquid-gas transition occurs. On the other hand, a small ε compared $\mathcal{S}$ may lead to numerical convergence issues.

By default, COMSOL Multiphysics uses in its standard level-set formulation $\varepsilon = \mathcal{S}$. Regarding δ_ν, a widely used value in vibrated fluids is the vibrational viscous boundary layer [9, 11], defined as $\delta_v = \sqrt{\nu/\omega}$, where ω is the frequency of the vibrational excitation. In the present section, we shall use the resulting value (for the given properties) as a reference. Lastly, the mesh size is also a critical parameter to analyze both the underlying fluid flow and the free surface dynamics. Here, we consider an unstructured triangular mesh, with an initial mesh size $\mathcal{S} = L/100$.

Hereafter, we perform a sensitivity analysis on these numerical parameters. For this purpose, we consider factors of 2, 1, 1/2 with respect to the reference values: $\mathcal{S}^* = \varepsilon^* = L/100$ and δ_v.

11.3.1 Comparison with Faltinsen et al. [270]

First, for comparison with the results of Faltinsen et al. [270], we simulate a partially filled container of dimensions $L \times H = 1.73\,\text{m} \times 0.6\,\text{m}$ subjected to periodic horizontal vibrations with amplitude $A = 30\,\text{mm}$ and period $T = 1.29\,\text{s}$, and a contact angle $\beta = 90°$. The amplitude and period are both extracted from Fig. 7 of that reference. The vertical displacement of a point next to the left end wall (labelled FS3 in the previous reference) is compared with the experimental measurements carried out by the authors.

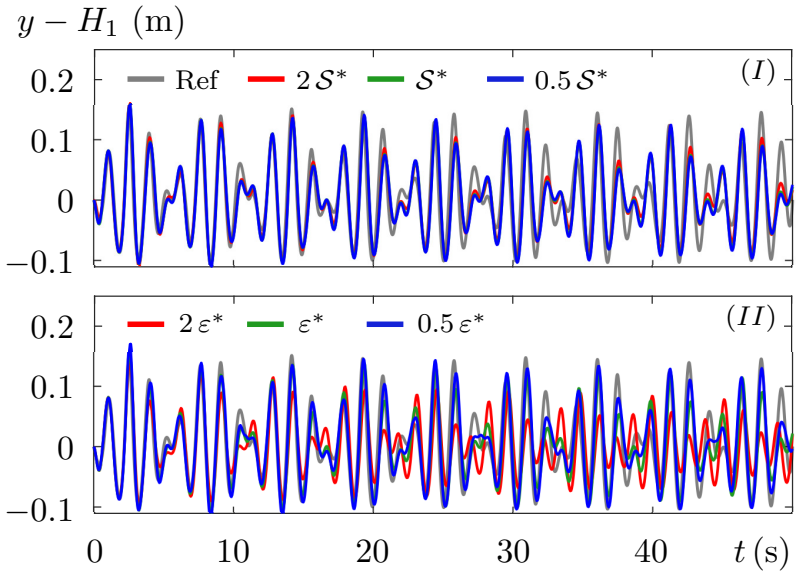


Figure 11.2: Comparison of the numerical model for an unbaffled container: surface elevation at a selected point (FS3) for the current model (blue, green and red) and the reference work (gray) of Faltinsen et al. [270]. We note that labels $\mathcal{S}^*$ and ε^* are both equal to $L/100$, introduced for simplicity. Panel (I) shows the effect of the mesh size: red, green and blue lines for $\mathcal{S} = L/50,\ L/100$ and $L/200$. Panel (II) shows the effect of the interface thickness effect: red, green and blue lines for $\varepsilon = L/50,\ L/100$ and $L/200$.

The results are depicted in Fig. 11.2, where a good agreement is found between the red, green and blue curves and the gray curve, extracted from Faltinsen et al. [270]. At a first glance, we observe that $\mathcal{S}$ [panel (I)] does not significantly affect the free surface dynamics. The interface thickness [panel (II)], however, presents a non-negligible influence. If we compare the depicted curves, we observe that, for a fixed mesh size, increasing the interface thickness negatively influences the free surface dynamics.

To provide a quantitative comparison, and given that there are small frequency shifts between the reference curve and the numerical work presented here, we introduce the following integral

$$\mathcal{I} = \int_0^{50} (y - H_1)\, dt, \tag{11.13}$$

which accounts for the integrated vertical displacement with respect to the initial fluid layer height. Then, we can quantify the error and address the model sensitivity to the studied parameters. The results of this analysis are presented in Table 11.2.

As anticipated, the most influencing parameter is ε. For a fixed value of $\mathcal{S} = L/100$, doubling the interface thickness presents an error of 23.71%. Focusing now on the mesh size, if we start from a maximum mesh size of $\mathcal{S} = L/100$, a decrease toward $\mathcal{S} = L/200$ reduces the error by just 1% at roughly 4 times the computational cost. Similarly, modifying δ_ν does not seem to significantly affect the result.

We highlight that the integral parameter $\mathcal{I}$ in (11.13) is based on the vertical displacement of the contact point, a point located on the gas-liquid interface. The level-set formulation

$\mathcal{S}$ ($\times L/100$)	ε ($\times L/100$)	δ^* ($\times \delta_v$)	$\mathcal{I}$ (m s)	Error (%)
2	1	1	2.3037	−8.82
1	**1**	**1**	**2.3483**	**−7.05**
1/2	1	1	2.3732	−6.06
1	1/2	1	2.5315	0.19
1	2	1	1.9273	−23.71
1	1	1/2	2.2752	−9.95
1	1	2	2.3875	−5.50

Table 11.2: Results of the convergence tests performed for the test case #1 [270]. The numerical parameters considered are the maximum mesh size ($\mathcal{S}$), interface thickness (ε) and slip length (δ_v). The error is calculated as $(\mathcal{I} - \mathcal{I}_{\text{ref}})/\mathcal{I}_{\text{ref}}$, where $\mathcal{I}_{\text{ref}} = 2.5265$ m s.

includes a finite interface thickness, 2ε, which hinders the accurate measuring of certain properties, namely y-displacement, at the free surface. The overall effect is the appearance of a certain dampening effect, more pronounced for larger timescales as evidenced by Fig. 11.2, (II).

11.3.2 Comparison with Liu and Lin [53]

Despite the reasonable agreement of the previous results, we note that the reference work of Faltinsen et al. [270] lacks the influence of passive baffles within the fluid bulk. To extend our numerical results, we also compare our model with the work of Liu and Lin [53] on sloshing in a container with a fixed, centered baffle attached to the bottom wall. For this purpose, we use the parameters therein — container dimensions $L \times H = 1\,\text{m} \times 0.5\,\text{m}$, baffle height $H_b = 0.75\,H$ and periodic excitation with amplitude $A = 2\,\text{mm}$ and period $T = 1.187\,\text{s}$ — and obtain the results presented in Fig. 11.3, again performing a sensitivity analysis on the relevant numerical parameters. Here, we compare the free surface elevation at the right contact point.

Similarly to the former results, the level-set exhibits good agreement. Following the same procedure as before, we define the integral $\mathcal{I}$ from 0 to 10 s. Table 11.3 presents the parameter sensitivity analysis. Regarding the numerical parameters, we observe that keeping the interface thickness while reducing the maximum mesh size reduces the error, though to a lesser extent on each iteration. Increasing the interface thickness has a negative effect, as stated earlier; decreasing it, however, does not seem to improve the solution for the small contact point displacement observed here. Last, the slip length seems to have a negligible role.

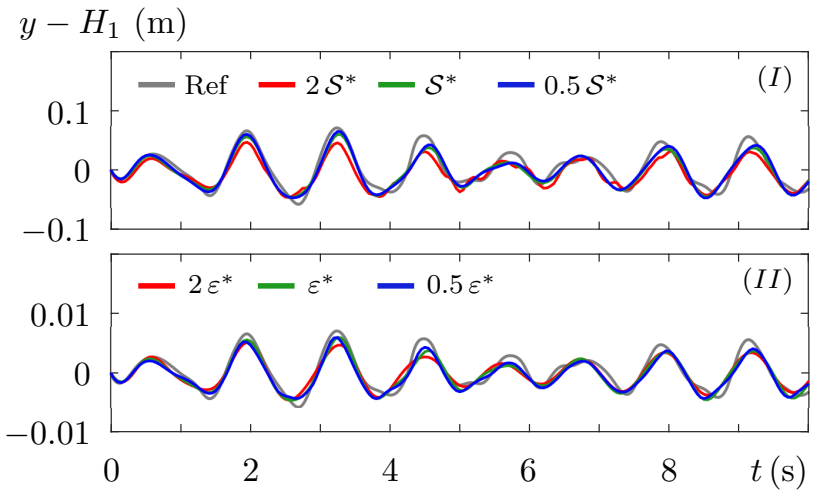


Figure 11.3: Comparison of the numerical model for baffled container: surface elevation at the right boundary for the current model (blue, green and red) and the reference work (gray) of Liu and Lin [53]. We note that labels $\mathcal{S}^*$ and ε^* are both equal to $L/100$, introduced for simplicity. Panel (I) shows the effect of the mesh size: red, green and blue lines for $\mathcal{S} = L/50,\ L/100$ and $L/200$. Panel (II) shows the effect of the interface thickness effect: red, green and blue lines for $\varepsilon = L/50,\ L/100$ and $L/200$.

11.3.3 Parameters selection

Based on these results, we can extract the following conclusions on the effect of the numerical parameters.

As stated earlier, measuring variables on the free surface, namely vertical y coordinate, may be considered imprecise due to the formulation of the level-set involving an interface thickness of the order of the mesh size. However, the numerical results obtained in the present study suggest a reasonable agreement when compared to both reference works. The most relevant parameter is undoubtedly the interface thickness ε, which has an inherent dampening effect: the larger it is, the worse the level-set captures the dynamics of the free surface. The mesh size also plays a key role on the numerical results, although selecting $\mathcal{S} = L/100$ seems to suffice. Finally, the estimate of δ_ν based on the vibrational viscous boundary layer is a good approach.

This selection of mesh parameters yields an unstructured mesh with the following properties: 26016 triangular elements, with an average quality of 0.9446 in terms of skewness.

11.3.4 Validation with floating and horizontal moving baffles

Finally, to test the selected numerical parameters and compare the results with experiments, we use the reference works of Koh et al. [56] and Kim et al. [64] for a constrained floating baffle and horizontal moving baffles, respectively.

The floating baffle, with a density of 520 kg/m^3, is constrained via four cables connected to the center of the bottom container wall. The container geometry and fluid layer depth, along

$\mathcal{S}$ ($\times L/100$)	ε ($\times L/100$)	δ^* ($\times \delta_v$)	$\mathcal{I}$ (m s)	Error (%)
2	1	1	0.0205	−19.80
1	**1**	**1**	**0.0223**	**−12.71**
1/2	1	1	0.0234	−8.64
1	1/2	1	0.0221	−13.61
1	2	1	0.0204	−20.05
1	1	1/2	0.0221	−13.56
1	1	2	0.0226	−11.69

Table 11.3: Results of the convergence tests performed for the test case #2 [53]. The numerical parameters considered are the maximum mesh size ($\mathcal{S}$), interface thickness (ε) and slip length (δ_v). The error is calculated as $(\mathcal{I} - \mathcal{I}_{\text{ref}})/\mathcal{I}_{\text{ref}}$, where $\mathcal{I}_{\text{ref}} = 0.0256$ m s.

with the angular momentum equation for the rigid-body motion (rotation) of the floating baffle can be found therein. Figure 18 in the work of Koh et al. [56], showing the pressure evolution at the P4 position, can be directly compared with our numerical results for this configuration, shown in Fig. 11.4. Despite the transient peak at $t = 1$ s, we observe that both the pressure oscillations and moving baffle positions at an arbitrary time do present a good agreement.

The results of Kim et al. [64] for moving baffles constitute another benchmark to further validate our numerical model. More specifically, figures 4 and 5 of that reference show the time evolution of the free surface during the initial stages of the liquid sloshing for two configurations: the unbaffled and two-baffled container. We reproduce these experiments using the model developed in the present work (and the previously selected parameters), with the experimental parameters (baffle system mass, excitation period and amplitude, etc.) detailed therein. The results of the comparison are depicted in Fig. 11.5.

We note slight differences in the results. These can be explained considering that we are selecting a maximum mesh size of $L/100$. Therefore, during drop ejection, the smallest drops (and their dynamic) cannot be correctly captured [9]. Moreover, although these experiments are carried out in a container with a small transverse direction (0.07 m compared to a length of 0.874 m and a height of 0.535 m), and thus a two-dimensional approach is justified, some features such as bubble trapping are more likely in our model compared to the experimental results (compare e.g., moving baffles snapshots at 2.032 s). Despite these subtle differences, this additional validation provides further confirmation on the suitability of the developed model.

11.4 Single vertical baffle with horizontal motion

As stated in Sec. 11.2, the system subject to study is a fluid container with inner dimensions $L \times H = 1$ m $\times$ 1 m, where a certain part of it is filled with water ($H_1 = \mathcal{V} \times H$), and the

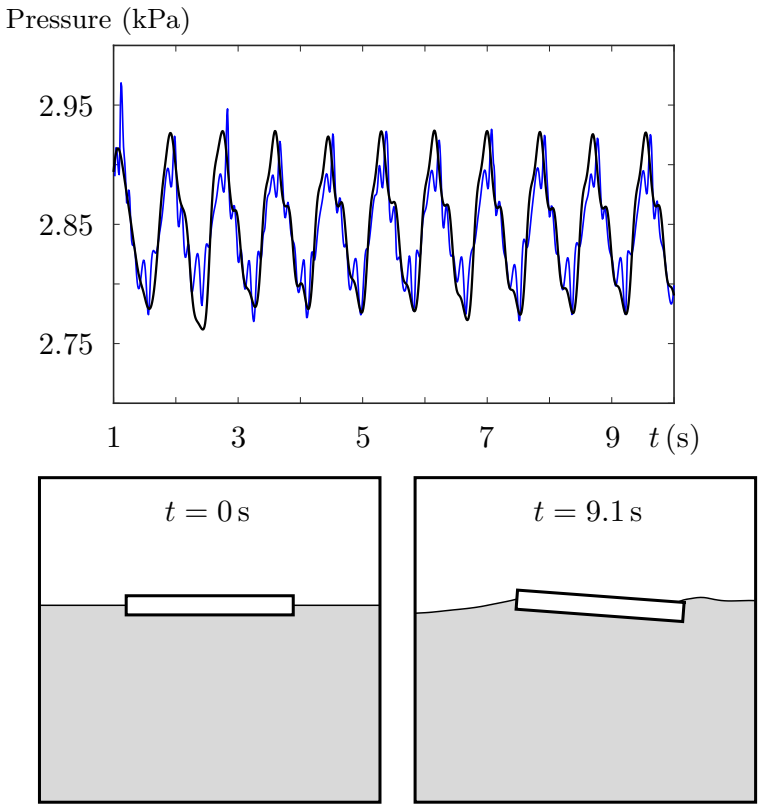


Figure 11.4: Comparison of the level-set model (and selected parameters) with the work of Koh et al. [56] for a constrained floating baffle. (Upper panel) Time evolution of pressure (in kPa) over 9 s at the P4 point (left end wall, 20 mm above the container bottom). The blue curve is extracted from the experimental results of that reference. (Lower panels) Insets showing the initial liquid-air-baffle configuration and the baffle position as well as free surface deformation at 9.1 s.

remaining is filled with air (H_2). We refer hereafter to the amount of liquid with respect to the container volume, as the filling ratio

$$\mathcal{V} = H_1/H. \tag{11.14}$$

The contact angle is set to $\beta = 90°$ and $\mathcal{V}$ is varied within the interval $\mathcal{V} \in [0.15, 0.95]$ in 0.05 steps. An aluminum baffle of dimensions $L_b \times H_b = 0.02\,\text{m} \times 0.5\,\text{m}$ is located at a distance $H_c = 0.5$ m from the bottom wall and allowed to move in the horizontal direction constrained by two identical linear springs of stiffness $K/2$. The aim is to reduce the sloshing motion that the fluid contained within would experience when subjected to an arbitrary perturbation applied in the horizontal direction, and asses the effect of the equivalent spring stiffness K for different baffle configurations.

The recent works of Wang et al. [67] and Gligor et al. [84] under normal gravity and microgravity, respectively, investigated the influence of a moving baffle subjected to pulse-like and/or harmonic excitation, finding that there is an optimum K that minimizes the decay time, the system kinetic energy, and the peak pressure and associated structural loads. Although [67] analyzed various filling ratios, there is a lack of numerical data regarding the vertical

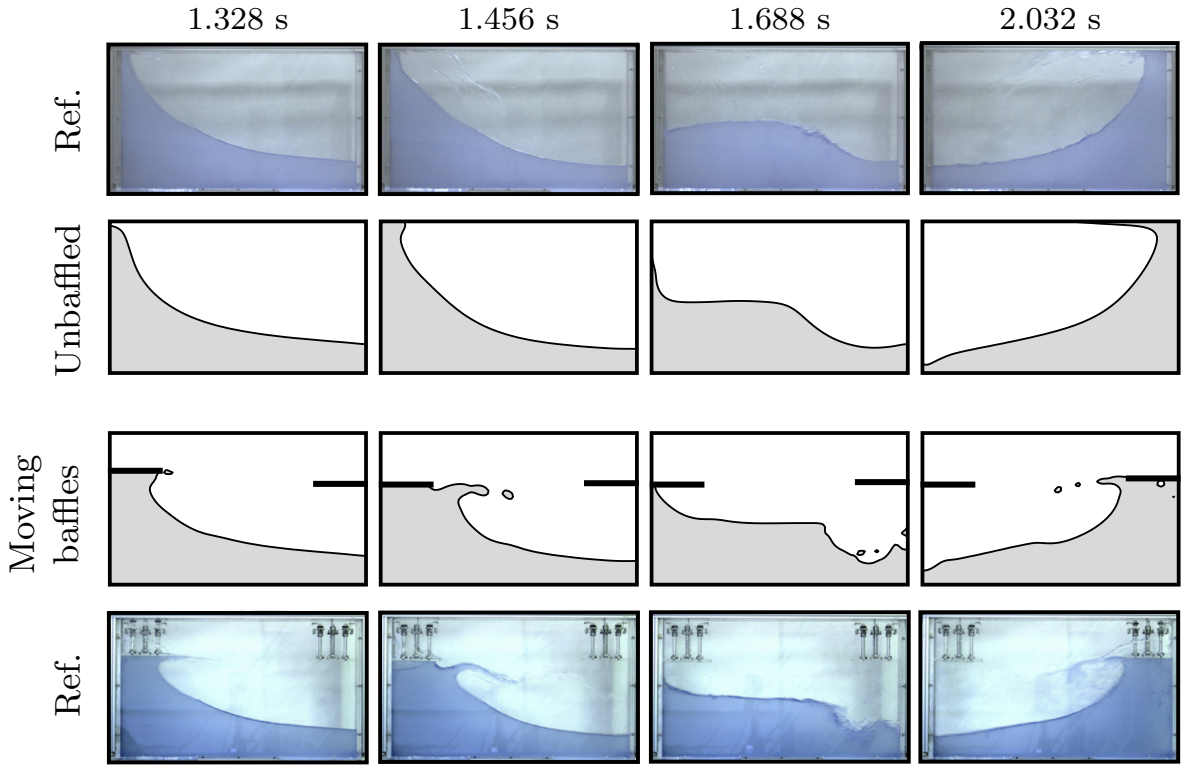


Figure 11.5: Comparison of the level-set model (and selected parameters) with the work of Kim et al. [64]. (Ref. panels) Snapshots depicting the time evolution during the initial stages of the liquid sloshing motion for the unbaffled (top) and moving baffle configuration (bottom). Reproduced with permission from Kim et al. [64]. (Middle panels) Snapshots depicting the time evolution at the same time instants for the level-set model (and selected parameters) developed here.

baffle positioning with respect to the bottom wall as well as other moving baffle configurations exploiting, for example, viscous dissipation via slots or using multiple baffles. Moreover, both studies evidenced that the baffle is more effective when located closer to the free surface: see, e.g., the results of [67] for a 25% filling ratio. The streamline plots given in [84] also allow for a better understanding of the coupling between baffle motion and the bulk flow.

To evaluate the performance of the proposed spring-mass baffle system, we first define an acceleration (perturbation) that drives the first (odd) sloshing mode, whose wavelength is $\lambda = 2\,L$, i.e., twice the container length. Since this mode is asymmetric, it is naturally excited by an asymmetry-inducing perturbation. A pulse-like acceleration driving the fluid to an initial asymmetric distribution is thus an ideal scenario for a preliminary evaluation.

Following the recent work of Gligor et al. [84], we define a smoothed acceleration, followed by a sudden drop. Such a specific type of forcing can be attributed, for example, to the sudden brake of a tanker truck. Note that any other external sources driving this initial asymmetry, such as a rotation of the container (e.g., a tanker ship rotation due to the effect of waves) would yield a similar effect to the acceleration introduced here. The acceleration is applied along the x-axis and enters into Eqs. (11.4b) and (11.11) via the volumetric force $\rho\,\mathbf{G}(t)$ and

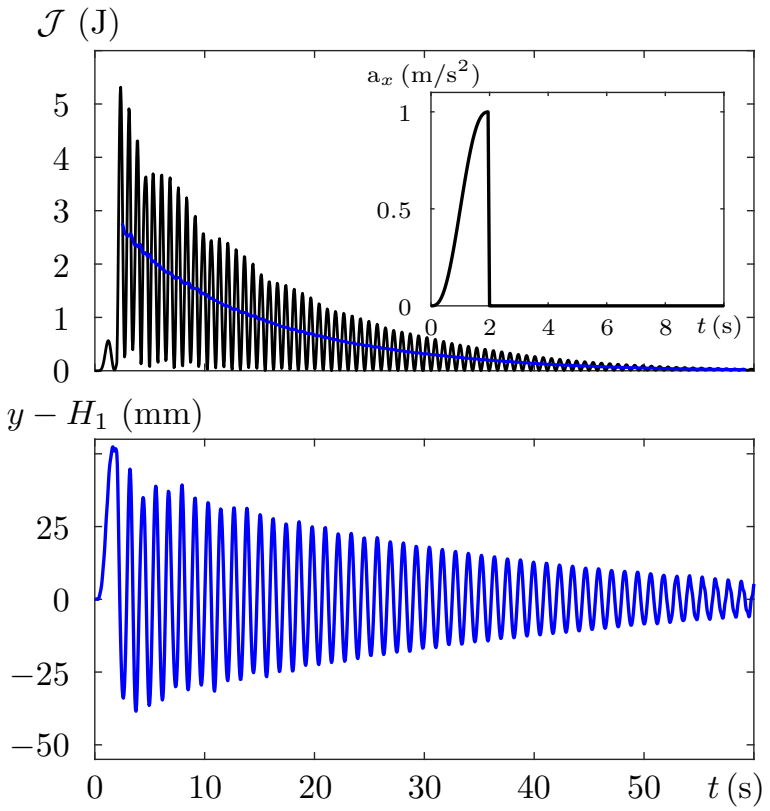


Figure 11.6: Sloshing response for an unbaffled container with $\mathcal{V} = 0.5$ after applying the acceleration perturbation depicted in the inset. (Upper panel) Evolution of the instantaneous $\mathcal{J}$ (black) and time-averaged value $\bar{\mathcal{J}}$ (blue curve) (blue) of the kinetic energy. (Lower panel) Evolution of the right contact point displacement.

a, respectively. As stated earlier, the acceleration is initialized smoothly, using $\mathcal{F}(t)$

$$\mathcal{F}(t) = \begin{cases} 0, & t < 0, \\ \frac{t}{\tau} - \frac{1}{2\pi}\sin\left(\frac{2\pi t}{\tau}\right), & 0 \leq t \leq \tau, \\ 1, & t > \tau; \end{cases} \tag{11.15}$$

and then is abruptly switched off by writting

$$\mathbf{a}\,(t) = 1\,\mathrm{m/s^2}\,\mathbf{i} \begin{cases} \mathcal{F}(t) & t \leq \tau, \\ 0 & t > \tau; \end{cases} \tag{11.16}$$

where $\tau = 2\,\mathrm{s}$ is the selected time constant. The inset in Fig. 11.6 shows the applied forcing over a 10 s span. This acceleration drives the fluid to an asymmetric configuration, with an interface tilted towards the right end wall. By the time it is removed at $t = 2$ s, the liquid starts sloshing back-and-forth.

To characterize the response, we use the system kinetic energy, as calculated in the work of Gligor et al. [84]:

$$\mathcal{J} = \frac{1}{2}\int_{\Omega} \rho \mathbf{u}^2 W d\Omega, \tag{11.17}$$

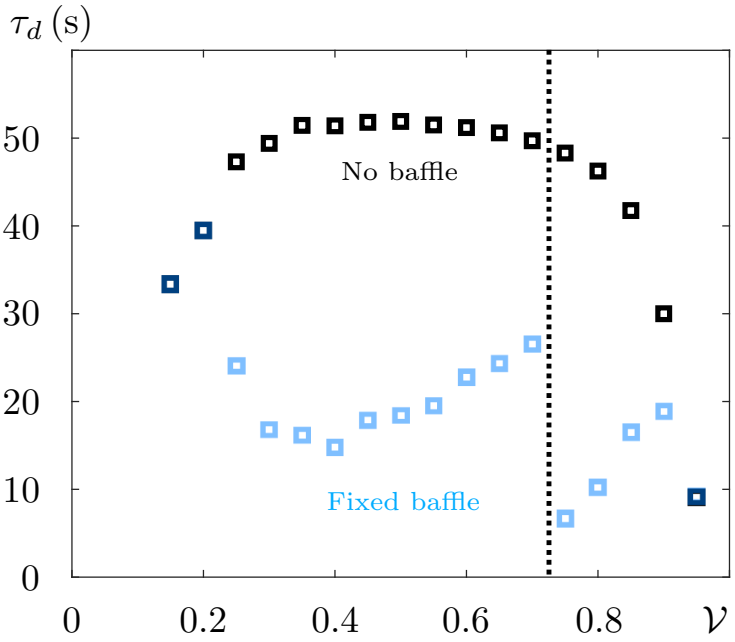


Figure 11.7: Decay times τ_d for the unbaffled (black) and the fixed vertical baffle (light blue) cases for $\mathcal{V} \in [0.15, 0.95]$ (in steps of 0.05). The vertical dotted line denotes the appearance of the U-shaped container sloshing mode as $\mathcal{V}$ is reduced.

where Ω denotes the fluid domain (including both liquid and air) and $W = 1$ m denotes an out-of-plane container dimension of size unity. Recall that the contact point displacements may not be accurate enough for the level-set method.

A representation of the typical sloshing response for an unbaffled container with $\mathcal{V} = 0.5$ is presented in Fig. 11.6. The system is subjected to **a**, illustrated in the inset, and its response is shown in terms of $\mathcal{J}$ (upper panel) and the right contact point displacement (lower panel). The instantaneous $\mathcal{J}$ (black) and its time-average (over one oscillation period) value $\bar{\mathcal{J}}$ (blue curve) are illustrated.

The criterion used hereafter to obtain the decay time τ_d is based on $\bar{\mathcal{J}}$ and follows the classical "5% settling time". Specifically, sloshing motion is considered damped when $\bar{\mathcal{J}}$ decreases below 5% of the maximum reached value. We note that the maximum value of $\bar{\mathcal{J}}$ may differ for different $\mathcal{V}$. Therefore, it is deemed that using the maximum value for each $\mathcal{V}$ is more "realistic" than considering a common reference value for all the explored filling ratios.

11.4.1 Results for a fixed baffle

Prior to analyzing moving baffles, we first compare the results of a fixed baffle, $K \to \infty$, with those corresponding to the unbaffled case; see Fig. 11.7.

Regarding the unbaffled tank (black markers), we observe a plateau in τ_d between $\mathcal{V} = 0.25$ and 0.8 at around 50 s. We note that these results are consistent with shallow liquid layers being increasingly influenced by the proximity of the bottom container wall (finite depth effects), whereas fluid containers at (almost) full capacity experience a similar effect due to

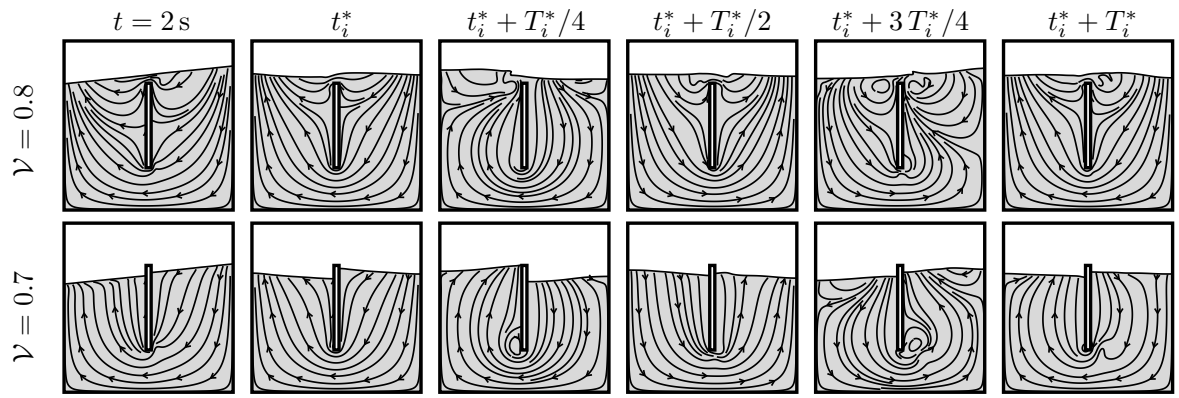


Figure 11.8: Snapshots depicting different instants (labelled) of the system evolution for the fixed baffle case with $\mathcal{V} = 0.8$, 0.7. (First column) Before the sudden release of the applied acceleration. (Second to sixth columns) Insets showing an oscillation period T_i^*. Note that t_i^* and T_i^* are different for each $\mathcal{V}$. For $\mathcal{V} = 0.8$, the presence of the baffle influences the common liquid sloshing motion by interfering the streamlines; see the inset at t_i^*. For $\mathcal{V} = 0.7$, the U-shaped container mode is shown.

the small air gap above.

For the fixed baffle case (light blue markers), we observe a significant improvement in τ_d except for the lowest and the largest filling ratios. For $\mathcal{V} \leq 0.2$, the baffle does not interact with the liquid, since H_1 is lower than the baffle bottom boundary. For $\mathcal{V} \geq 0.9$, the baffle has a negligible effect, since the larger flow velocities are located in the vicinity of the upper container boundary. At $\mathcal{V} \approx 0.75$, a sudden increase appears when the free surface is initially aligned with the baffle upper boundary.

For a better understanding of the underlying dynamics, Fig. 11.8 includes snapshots at $t = 2$ s, corresponding to the end of the acceleration application, and four lapses over the oscillation period — note that the period T_1^* presented in these panels is not the one corresponding to the kinetic energy $\mathcal{J}$, but the one corresponding to the contact points motion. The insets strongly suggest that decreasing $\mathcal{V}$ below 0.75 triggers the appearance of an additional mode that resembles the sloshing motion typical of U-shaped containers; see, e.g., [281]. Besides the common sloshing motion related to the back-and-forth movement of the free surface, the bulk flow must adapt to this new configuration and thus, the mass transfer must occur via the lower gap between the baffle and the container bottom wall; see lower panels in Fig. 11.8. The baffle divides the fluid domain in two vertical "channels" and, as a consequence, there is an up-and-down motion of the free surface that alternate between both sides of the baffle. This causes the kinetic energy to decrease at a slower rate. This mode, although dominant at around $\mathcal{V} = 0.7 - 0.75$, has a decreasing influence as $\mathcal{V}$ is reduced; see the minimum at $\mathcal{V} = 0.4$ in Fig. 11.7.

In the remainder of this manuscript, we refer to this mode either as "U-shaped mode" or "U-shaped container mode".

11.4.2 Results for a moving baffle

Although the fixed vertical baffle already provides a reasonable reduction in τ_d, the recent works of [67] and [84] have shown that moving baffles may provide additional improvements with respect to their fixed counterparts.

An initial estimate of the spring stiffness can be obtained as follows [84]. First, the sloshing frequency ϖ can be estimated via the dispersion relation of capillary-gravity waves [38] for a layer of liquid of density ρ_1 and height H_1:

$$\varpi^2 = \left(gk + \frac{\sigma}{\rho_1}k^3\right)\tanh\left(k\,H_1\right), \tag{11.18}$$

which, after neglecting surface tension over a length scale $\lambda = 2\,L \sim \mathcal{O}(1)$ m greater than the capillary length $\lambda_c = \sqrt{\sigma/(\rho_1 g)} \sim \mathcal{O}(10^{-3})$ m, and substituting $k = \pi/L$, $H_1 = \mathcal{V} \times H$, simplifies to

$$\varpi^2 = \pi\left(\frac{g}{L}\right)\tanh\left(\pi\,\frac{\mathcal{V}}{\Gamma}\right), \tag{11.19}$$

where $\Gamma = L/H = 1$ for the present simulations.

Then, we consider a single degree-of-freedom system consisting of a mass M^* attached to a spring with stiffness K. Under the assumption that ϖ coincides with its natural frequency $\sqrt{K/M^*}$, one obtains the following estimate for K:

$$K = \pi\left(\frac{g}{L}\right)\tanh\left(\pi\,\frac{\mathcal{V}}{\Gamma}\right)M^*, \tag{11.20}$$

where M^* is the total mass of the fluid-baffle system, $M^* \simeq M_f + M_b = \rho_1 W(L\,H_1 - L_b\,H_b) + \rho_b W\,L_b\,H_b$. As an example, a spring stiffness $K = 16720$ N/m can be estimated for $\mathcal{V} = 0.8$.

In this manuscript, $\mathcal{V}$ varies and thus, the spring stiffness would be subject to changes as well. As a result, a sweep in K is considered for each $\mathcal{V}$ within the interval $K \in [100,\,200000]$ N/m. These values are arbitrarily selected as a reference: every sweep is tuned for each value of $\mathcal{V}$ to obtain the minimum decay time (if it exists), while the maximum K could be lowered if the baffle motion is shown to be small enough that it can be considered (almost) fixed.

The procedure followed for each $\mathcal{V}$ is summarized in Fig. 11.9. For a given value of $\mathcal{V}$, a K sweep is performed and, as a result, we obtain the gray curves. These curves tend to the unbaffled and fixed baffle cases when the K is sufficiently low and sufficiently large, respectively. In between, a large variety of results regarding the optimum K may arise. At $\mathcal{V} = 0.4$, as in Fig. 11.9, a clear minimum at $K \approx 4000$ N/m can be distinguished. Upon reaching the minimum, τ_d grows and asymptotically reaches the decay time of the fixed baffle scenario.

Other filling ratios, namely $\mathcal{V} = 0.7$, exhibit a minimum at larger spring constants ($K = 8000$ N/m) very similar to the fixed baffle case ($\tau_d = 25.9$ for the minimum and $\tau_d = 26.6$ for the fixed case). Here, τ_d exhibits a local maximum. This behavior can be explained considering the coexistence of the first sloshing mode and that of U-shaped containers. The second row in Fig. 11.8 showed this type of motion.

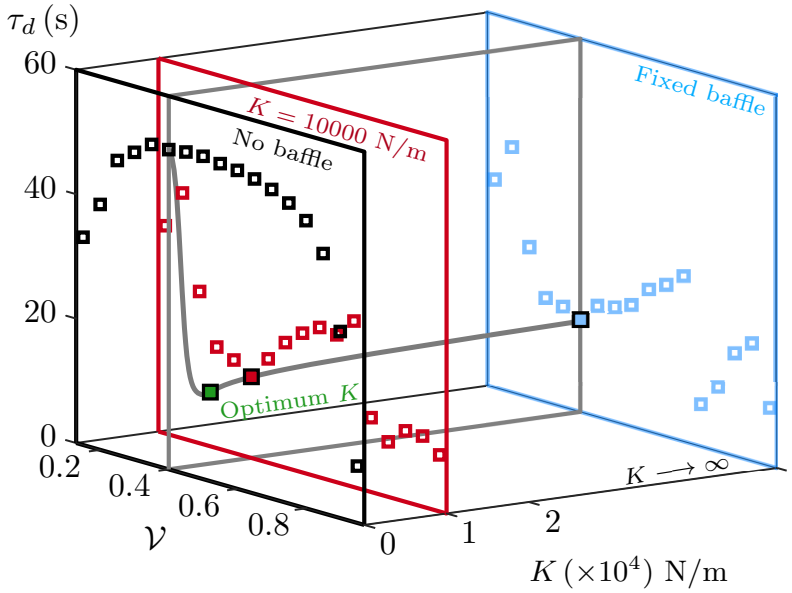


Figure 11.9: Decay times τ_d as a function of $\mathcal{V}$ for the unbaffled (black), moving baffle with $K = 10000$ N/m (red) and fixed baffle (blue markers) cases. The gray plane and solid curve depict the K sweep for $\mathcal{V} = 0.4$, which shows the transition from the unbaffled case, similar to $K \to 0$ to the fixed baffle case, $K \to \infty$, with an optimum K value (green marker) lower than 10000 N/m. Following the same procedure (if possible and the minimum does exist) and projecting the resulting on the front plane, we obtain the results in Fig. 11.10.

By performing this same procedure for all discrete values of $\mathcal{V}$ considered in this work, and projecting all of them in a single plane, we obtain the results of Fig. 11.10 (green markers). Although not presented here, we note that the optimum K value notably differs between small and large $\mathcal{V}$. Therefore, a single value of K cannot be used to minimize τ_d for all $\mathcal{V}$. As a compromise solution, we have selected a spring constant $K = 10000$ N/m (red markers), which yields lower τ_d when the baffle is fully submerged. Even if the baffle motion is allowed, the sharp transition between $\mathcal{V} = 0.7$ and 0.75 corresponding to the mixed first and U-shaped sloshing modes does not improve.

A comparison of the results between the fixed (blue) and moving baffle evidences an improvement at large $\mathcal{V}$. In (almost) any other case, the results are very similar. In light of this, one could analyze the effect of the baffle vertical size and positioning to improve its performance.

11.4.3 Effect of baffle size and vertical position

To analyze the influence of the baffle vertical size and position, H_b and H_c, we perform K sweeps for all combinations of three filling ratios, $\mathcal{V} = 0.75$, 0.5 and 0.4, baffle heights $H_c = 0.4$, 0.5 and 0.6 m, and baffle sizes $H_b = 0.25$, 0.5 and 0.75 m. A summary of the main results is included in Table 11.4 for the fixed and the moving baffle with $K = 10000$ N/m cases.

The results evidence that any increase in H_b favors the appearance of the U-shaped mode and increases notably the associated values of τ_d. Reducing the baffle size, without an adequate

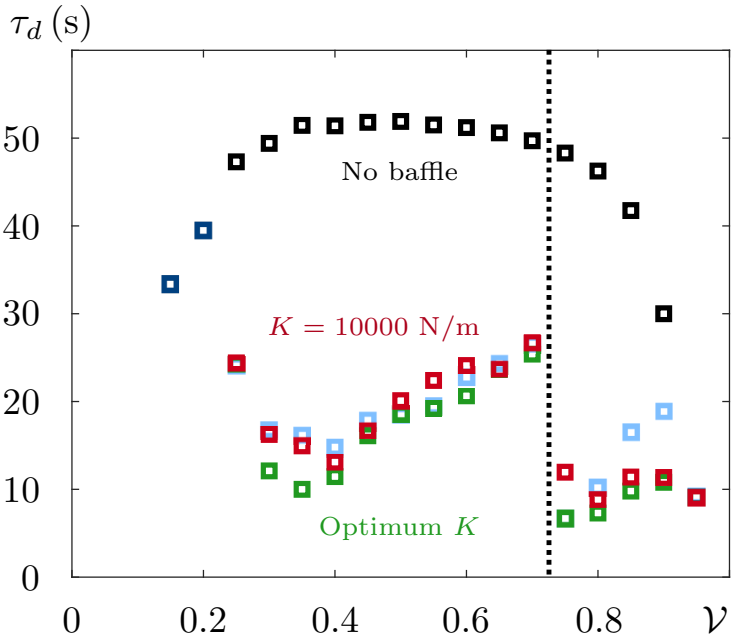


Figure 11.10: Decay times τ_d as a function of $\mathcal{V}$ for the unbaffled (black), fixed baffle (blue), moving baffle with $K = 10000$ N/m (red) and moving baffle with optimum K for each $\mathcal{V}$ (green) cases. The dotted vertical line represents the appearance of the U-shape mode, as in Fig. 11.7.

placing within the container (H_c) may reduce the baffle interference with the sloshing motion, thus obtaining larger τ_d. Placing the standard baffle ($H_b = 0.5$ m) at a lower height seems to have a negative effect: for large $\mathcal{V}$, decreasing H_c means a lower interference with the larger flow velocities closer to the free surface; for intermediate to lower ones, decreasing H_c narrows the gap through which the mass transfer occurs in the U-shaped mode and compromises baffle performance. Baffles placed at larger H_c may trigger the U-shaped mode at larger $\mathcal{V}$ (as evidenced by the values of τ_d for $\mathcal{V} = 0.75$) or have reduced interference with the liquid flow for lower $\mathcal{V}$.

In short, further enhancement on the performance of moving baffles would require both preventing the development of the unwanted U-shaped mode and assuring that the baffle remains fully submerged over a wider range of $\mathcal{V}$. Both criteria could be met, for instance, by splitting the original baffle into two (or more) parts.

Compared to previous studies [66, 67], the analysis carried out in this section shows different dynamics at larger and smaller $\mathcal{V}$, closely related to the baffle vertical size. Therefore, a solution comprising a single baffle always submerged, or a baffle spanning over the entire container height, is far from being optimal despite improving the sloshing performance.

On the other hand, one could establish a parallelism between the current results and the well-known pendulum equivalence for sloshing motion [40], where there is a rigid mass moving in unison with the tank besides the masses of the different sloshing modes. The rigid mass increases with the liquid layer height and, by extension, a single submerged baffle would inevitably lose effectiveness as it separates from the free surface. A baffle spanning over most of the container height would imply adding an excessive amount of weight and reaching a

$\mathcal{V}$	H_c (m)	H_b (m)	τ_d fixed	τ_d moving $K = 10000$ N/m
0.75	0.5	0.5	6.70	11.95
0.75	0.5	0.75	60	35.10
0.75	0.5	0.25	27.10	21.20
0.75	0.4	0.5	15.55	8.55
0.75	0.6	0.5	26.60	29.05
0.5	0.5	0.5	18.4	20.10
0.5	0.5	0.75	60	33.30
0.5	0.5	0.25	17.65	14.80
0.5	0.4	0.5	52.25	42.85
0.5	0.6	0.5	16.35	14.00
0.4	0.5	0.5	14.80	13.10
0.4	0.5	0.75	51.70	38.65
0.4	0.5	0.25	23.60	23.20
0.4	0.4	0.5	27.15	32.50
0.4	0.6	0.5	21.25	20.15

Table 11.4: Effect of the vertical baffle size and position, H_b and H_c, on τ_d in both fixed and moving baffle with $K = 10000$ N/m configurations and for three different filling ratios.

suboptimal performance over a wider range of filling ratios.

Based on these results and conclusions, and aiming at further improving the sloshing reduction capabilities of moving baffles, we propose to use of a pair of baffles with different characteristics in subsequent sections. By considering two (or more) moving baffles, fine tuning the associated values of K becomes more complex, albeit the resulting multiple-baffle design would potentially achieve a significantly better performance over a wider range of $\mathcal{V}$; this is analyzed in detail hereafter.

11.5 Two vertical baffles with horizontal motion

We now split the original baffle into two parts with dimensions $L_b \times H_b = 0.02\,\text{m} \times 0.25\,\text{m}$, placed at $H_{c1} = 0.7$ m and $H_{c2} = 0.25$ m and associated to the spring constants K_1 and K_2, where the subscripts 1 and 2 refer to the upper and lower baffles, respectively.

First, note that performing a full optimization of the new two-baffle arrangement for each $\mathcal{V}$ would entail a large computational cost, considering all combinations of K_1 and K_2. Instead, we use some of the lessons learned from Sec. 11.4 to anticipate appropriate values:

– The results for the single vertical baffle suggested optimum K values around 1000 N/m and 10000 N/m for small and large $\mathcal{V}$, respectively.

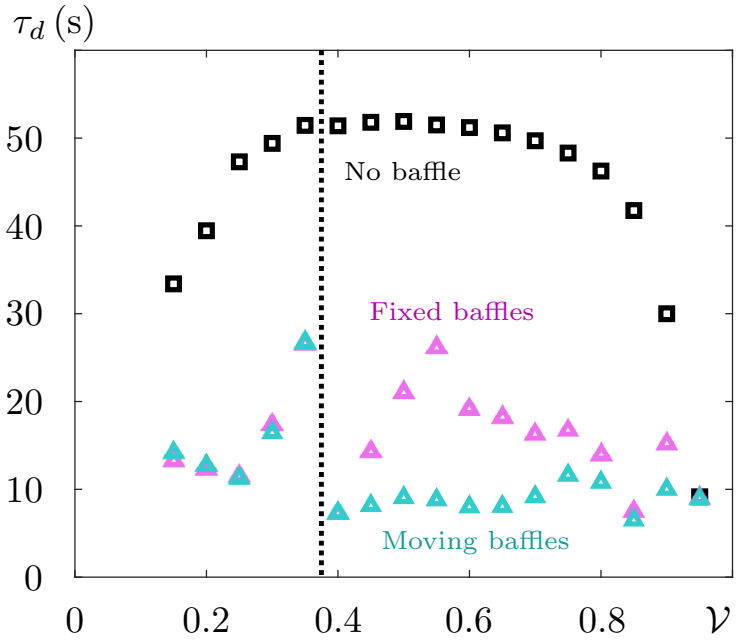


Figure 11.11: Decay times τ_d as a function of the $\mathcal{V}$ for the unbaffled case (black squares), two moving baffles with $K_1 = 15000$ N/m and $K_2 = 2500$ N/m (turquoise), and two fixed baffles (magenta triangles). The dotted vertical line represents the transition to the U-shaped mode.

- Reducing the baffle size implies (i) lower inertia and (ii) reduced pressure load on the baffle. Note that, if the inertia is lower, the pressure forces induced by the fluid flow would be able to achieve larger displacements, and vice versa. Both effects act in opposite sense.
- Below a certain $\mathcal{V}$, the upper baffle would no longer be effective and, as a consequence, only the lower (submerged) baffle would be suppressing sloshing motion. Additional stiffness may be therefore required on K_2 as a compromise solution between good performance for low and intermediate $\mathcal{V}$.

From these considerations, we select $K_1 = 15000$ N/m and $K_2 = 2500$ N/m. The results of the subsequent analysis are summarized in Fig. 11.11, where a substantial improvement is obtained in the intermediate-large $\mathcal{V}$ range, while the U-shaped container mode occurs now at $\mathcal{V} \approx 0.35 - 0.4$.

For larger $\mathcal{V}$, we observe a substantial improvement comparing fixed and moving baffles. The difference reaches its maximum value at $\mathcal{V} \approx 0.575$ when the upper baffle is no longer submerged. This transition, continuous for the moving baffle case, reflects a sudden increase on τ_d for decreasing $\mathcal{V}$ in the fixed baffle case.

A series of snapshots showing the system response to the pulse-like acceleration for both moving and fixed baffle configurations is presented in Fig. 11.12 to ease the understanding of the sloshing dynamics. These results delve further on the outperforming of the moving baffle approach with a tuned spring constant compared to the fixed baffle. Such (damping) enhancement can be understood as follows: first, there is a strong fluid-structure interaction

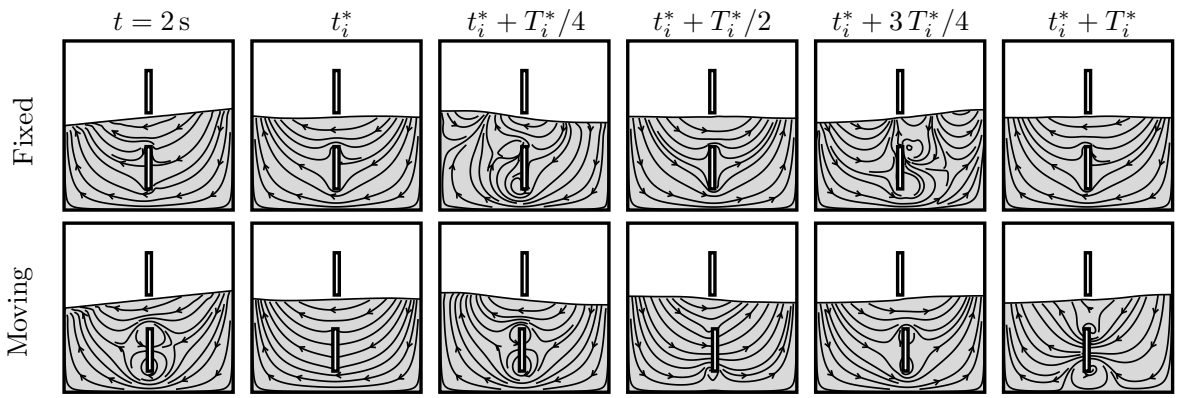


Figure 11.12: Snapshots depicting different instants (labelled) of the system evolution for the fixed and moving, two-baffle cases with $\mathcal{V} = 0.55$. (First column) Before the sudden release of the applied acceleration. (Second to sixth columns) Insets showing an oscillation period T_i^*.

between the bulk flow and the baffle — see, for instance, the perpendicular streamlines in Fig. 11.12 — along with increased viscous dissipation due to the baffle obstructing the flow. Besides, there is also a phase difference between the baffle motion and the excitation force, and by extension, a phase lag between sloshing and baffle motion. Although initially in phase as a consequence of the applied perturbation forcing, (see lower row, t_i^*, shortly after the forcing release), the springs restoring force soon opposes the sloshing motion (lower row, $t_i^* + T_i^*/4$). Furthermore, as observed on the lower panels, a large amount of fluid surrounding the baffle is drawn by it, acting as a "rigid solid" and effectively opposing the sloshing motion. As a side effect, additional recirculation zones appear and the viscous dissipation could be further increased within the bulk flow. The fixed baffle, on the contrary, would not benefit from this.

The results presented in Fig. 11.11 exhibit a mean value around 10 s, a significant improvement with respect to the unbaffled case (by $\sim 80\%$). The worst performance is again related to the U-shaped mode, which is still present and causes a peak on τ_d near $\mathcal{V} \approx 0.375$.

11.5.1 Results for slotted-baffles

To deal with this, we modify the lower baffle design and introduce a small slot (1 cm vertical gap) in the middle to allow for additional mass transfer across the baffle, while keeping other parameters as in the previous configuration. The expected outcome is a mitigation (if not complete suppression) of the U-shaped mode. We note that increasing the size of the slots or increasing their number, for a fixed baffle geometry, despite hindering even more the U-shaped mode, may be counter-productive as the pressure differences across the baffle would decrease, leading to a reduced fluid-baffle coupling. Besides, as suggested by Eq.(11.11), the balancing of the terms may be affected, and a change of the spring stiffness would likely be required.

In the absence of a sudden change in τ_d associated to the appearance of the U-shaped mode, Fig. 11.13 evidences this anticipated design improvement. While the values of τ_d remain very similar for intermediate and large $\mathcal{V}$, a small peak at $\mathcal{V} = 0.35$ is still present although it is notably reduced in both fixed and moving baffles configurations.

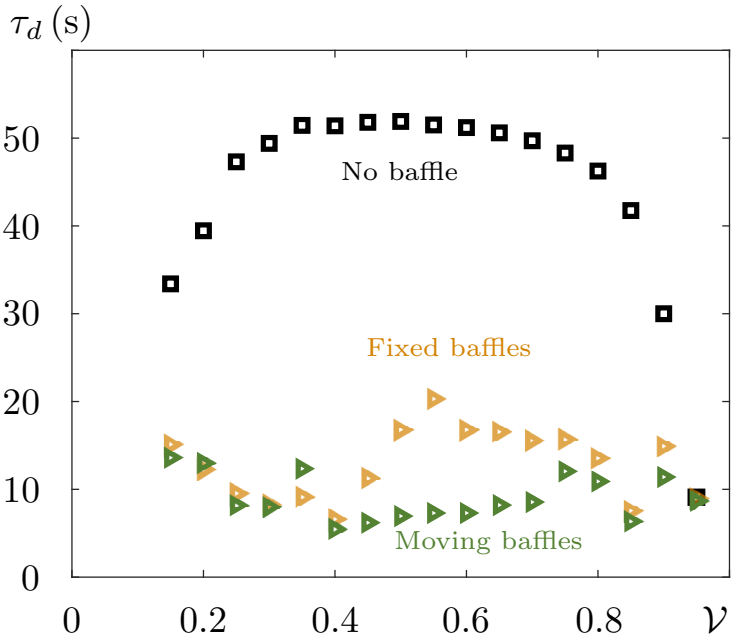


Figure 11.13: Decay times τ_d as a function of $\mathcal{V}$ for the unbaffled case (balck squares), two moving baffles with $K_1 = 15000$ N/m and $K_2 = 2500$ N/m (drak green), and two fixed baffles (light orange triangles). The lower baffle has a 1 cm wide slot in the central region to allow fluid transfer through the baffle body.

The effect of the slot can be further understood with the insets presented in Fig. 11.14 (upper row). For a filling ratio $\mathcal{V} = 0.55$, as in Fig. 11.12, adding a slot enables the intended fluid transfer from one side of the baffle to the other. Although the baffle horizontal displacement may be slightly affected, the system presents an increased dissipation: in the vicinity of the baffle slot, due to the reduced cross-section, larger velocities develop. The large velocity gradient increases viscous dissipation and, furthermore, induces liquid recirculation that interferes with sloshing motion.

After reducing the dominant role of the U-shaped container mode, further improvements could still be obtained for lower $\mathcal{V}$ below 0.4. With the current extension of the lower baffle, the lowest filling ratios are barely influenced by the baffle presence, regardless of whether it is fixed or not. If we extend the lower baffle so that it almost reaches the container bottom, this interaction, albeit weak and more similar to a fixed baffle, would help to reduce τ_d. Based on this, we extend the lower baffle to $H_{b,2} = 0.365$ m and include two slots of 1 cm width instead of one. The baffle is such that there is another 1 cm gap between the baffle lower boundary and the container bottom. As mentioned earlier, enlarging the baffle height would increase the hydrodynamic forcing due to a larger interference with the bulk flow. Albeit with a larger inertia, we would expect the pressure differences across the baffle sides to be substantially greater and thus increase $K_2 = 4000$ N/m in anticipation.

We note that, up to the last design, we have kept the baffle mass almost constant (except for the 1 cm slot introduction). It is worth noting that, in the context of commercial applications, adding too much weight to these sloshing mitigation methods is not desirable. However, in

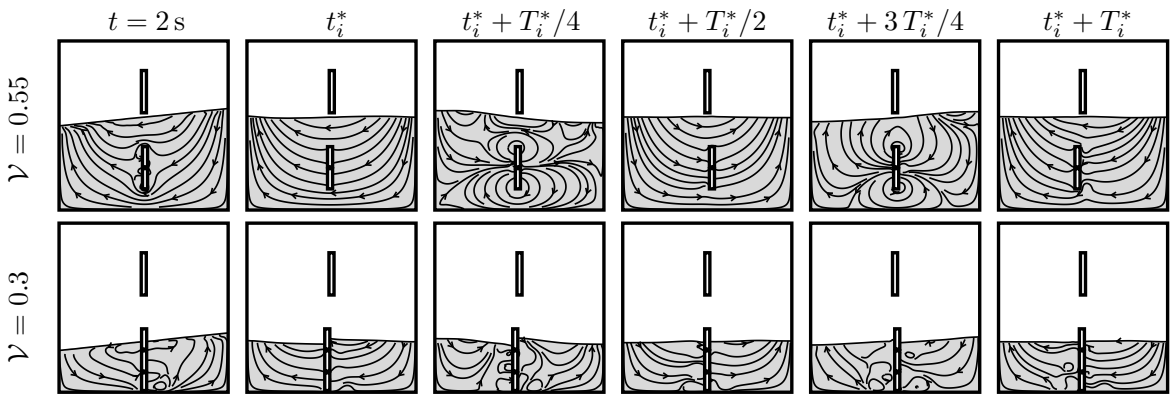


Figure 11.14: Snapshots depicting different instants (labelled) of the system evolution for the two moving baffles case: the upper row shows the $H_b = 0.25$ m baffle with an intermediate slot and $\mathcal{V} = 0.55$; the lower row presents the extended baffle $H_b = 0.365$ m with two slots and $\mathcal{V} = 0.3$. (First column) Before the sudden release of the applied acceleration. (Second to sixth columns) Insets showing an oscillation period T_i^*. The selected $\mathcal{V}$ are, for each baffle configuration, those that most improve τ_d compared to their fixed counterparts.

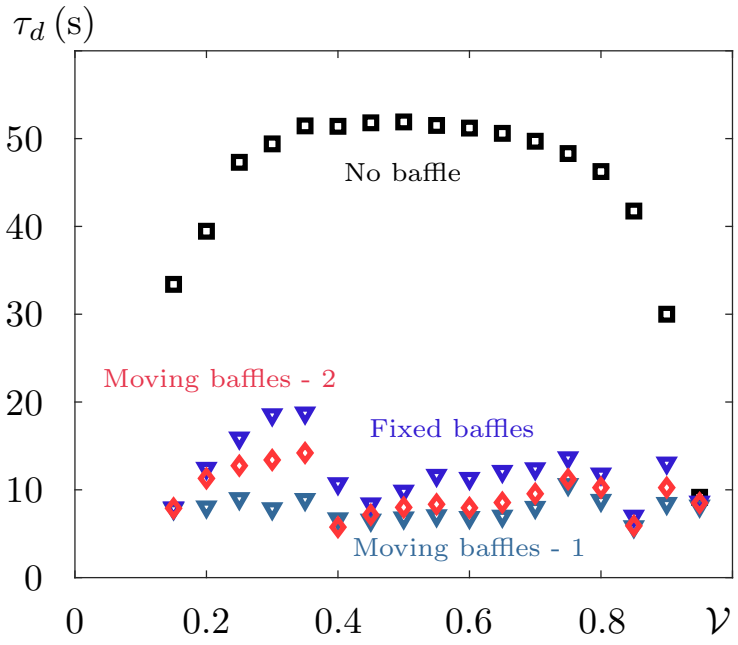


Figure 11.15: Decay times τ_d as a function of $\mathcal{V}$ for the unbaffled case (black squares), two moving baffles with two stiffness sets, (1) with $(K_1, K_2) = (15000, 4000)$ (indigo) and (2) (10000, 8000) N/m (red diamonds); and two fixed baffles (red and dark blue triangles). The lower baffle has two slots of 1 cm width each to allow fluid transfer through the baffle body.

the present formulation, the ratio baffle-to-liquid mass at full capacity of the container, i.e., $\mathcal{V} = 1$, is 0.0273, with the baffle representing only the 2.73% of the total system mass. For a relatively small weight penalty, the sloshing performance of the system for all $\mathcal{V}$ ratios is improved by an 80% factor: from $\tau_d \sim 50$ s to $\tau_d \sim 10$ s.

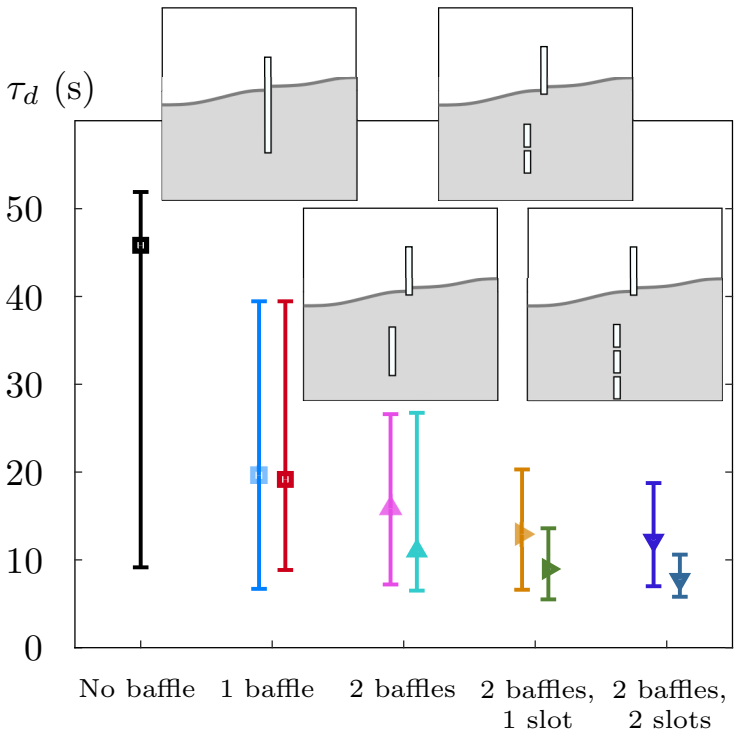


Figure 11.16: Mean τ_d for the different tested configurations: unbaffled container (black), single fixed (light blue) and moving baffle (red), two fixed (light magenta) and moving (turquoise) baffles, two baffles with the lower one including a 1 cm wide slot, fixed (light orange) and moving (dark green) and two baffles with an enlarged lower one with two slots in fixed (dark blue) and moving (indigo) configuration. The color coding is the same as in Figs. 11.10, 11.11, 11.13 and 11.15. Above, snapshots of the different configurations are displayed for visual guidance. The error bars represent the maximum and minimum τ_d over $\mathcal{V} \in (0, 1)$.

The results concerning the last baffle configuration are presented in Fig. 11.15. Again, the fixed baffle configuration already provides a reasonable reduction in τ_d for all $\mathcal{V}$, though slightly detrimental for the decay time at low $\mathcal{V}$; now due to the very limited fluid transfer between the baffle sides, only through the 1 cm slots. The system response under these design modifications is analogous to separating the container into two halves, with sloshing motion at their natural frequency and almost isolated from one another. By allowing constrained baffle motion, the back-and-forth liquid motion is coupled via the baffle displacement and, as evidenced by these results, we obtain a uniform τ_d over $\mathcal{V}$.

11.6 Summary of results

A summary of all the results discussed throughout Secs. 11.4 and 11.5 is presented in Fig. 11.16. It displays the mean τ_d (markers) along with error bars representing the absolute maximum and minimum values for each baffle configuration (fixed and moving).

As discussed above, a single baffle configuration is not very effective for all $\mathcal{V}$. For two baffles,

one can easily observe a decrease in the mean τ_d for both moving and fixed configurations, albeit larger in the moving baffle case. The dispersion of the maximum and minimum absolute values evidences the presence of the U-shaped container mode.

Adding slots to the lower baffle decreases both the mean τ_d and its dispersion, and allows for a better mass transfer between the container halves, therefore hindering the undesired effect of the U-shaped container mode. The last configuration, enlarging the lower baffle with additional slots, barely improves the system response for the fixed configuration. The moving configuration, on the other hand, exhibits a large enhancement, with an almost uniform τ_d across the entire range of $\mathcal{V}$ explored.

Overall, we have obtained a baffle configuration that, in a passive manner, greatly reduce the sloshing motion driven by a pulse-like acceleration, characterized by a decrease in τ_d from ~ 46 s to ~ 8 s for the most optimum baffle design/arrangement.

11.7 Frequency analysis

The results discussed above suggest themselves for further investigation. In this sense, now we analyze the system response to harmonic excitation to ensure that, despite improving the response of the first sloshing mode, the fluid-baffle coupling does not introduce other low-frequency modes of relevance. So far, only the (dominant) first sloshing mode was shown to be reduced.

For this purpose, the driving acceleration $\mathbf{a}$ is now replaced by

$$\mathbf{a}(t) = D\omega^2 \sin(\omega\, t)\, \mathcal{F}(t)\ \mathbf{i}, \tag{11.21}$$

and initialized smoothly via Eq. (11.15). A frequency sweep at a fixed amplitude of $D = 10$ mm is performed within the interval $\omega/(2\pi) \in [0.1,\ 1.5]$ Hz. This range is deemed as representative, covering the first sloshing frequencies, as predicted via Eq. (11.18), i.e., $\varpi/(2\pi) = 0.876$, 0.846 and 0.716 Hz for $\mathcal{V} = 0.75$, 0.50 and 0.25, respectively. To ease the comparison with available studies [67, 84], we carry out the analysis using the vertical displacement of the right contact point instead of $\mathcal{J}$.

Figure 11.17 includes the results of this analysis for the last baffle configuration (2 baffles, the lower one with two slots), both fixed and moving, and $\mathcal{V} = 0.75$, 0.50 and 0.25; results for the unbaffled container are also included for reference.

First, we note that the frequency response is consistent with that shown in the work of Wang et al. [67], where the main sloshing frequency is notably reduced for all $\mathcal{V}$ due to the baffle action, regardless of its configuration (fixed or moving). In the unbaffled case, the diagram displays a second peak that corresponds to the second odd sloshing mode, characterized by a wavelength $\lambda = 2L/3$. Using again Eq. (11.18), the associated frequency is expected at approximately 1.5 Hz for each filling ratio. For baffled containers, however, this mode can be delayed to larger ω or its amplitude reduced so that it is imperceptible, in favor of other modes related to the presence of the spring-mass baffle system.

The fluid system with moving baffles shows different behavior depending on the spring constants. The optimum pair $K_1 = 15000$ N/m and $K_2 = 4000$ N/m obtained in Sec. 11.5

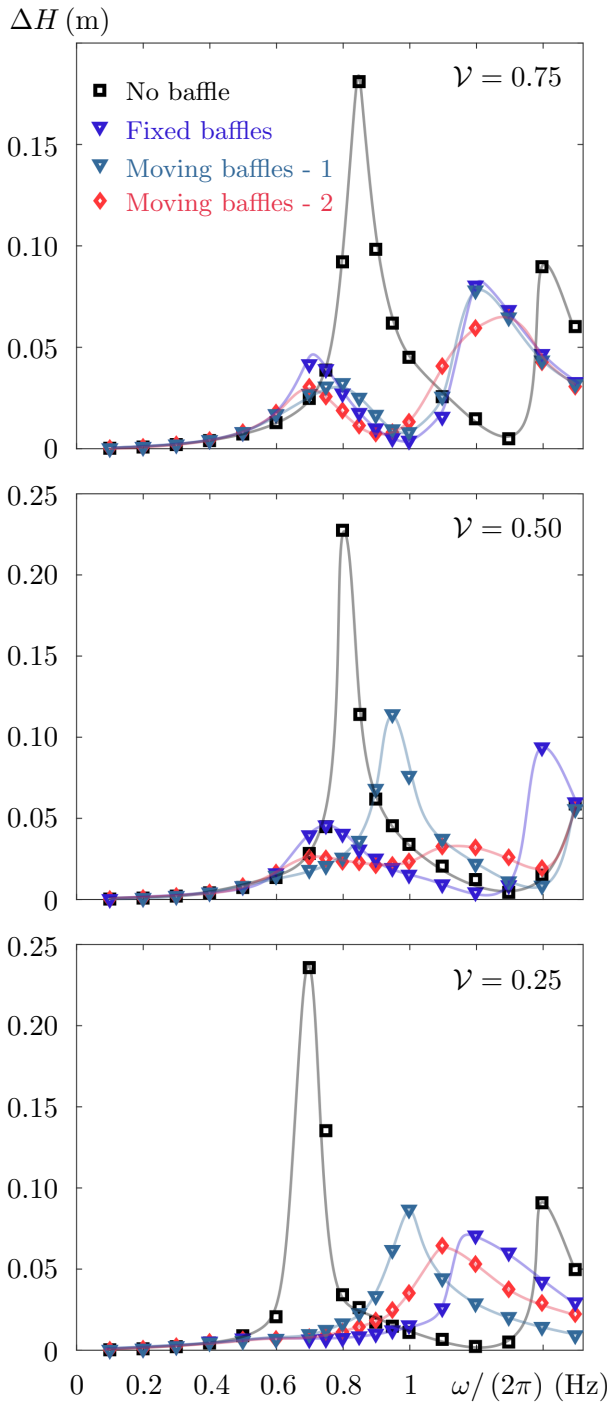


Figure 11.17: Frequency analysis showing the right contact point oscillation amplitude ΔH as a function of $\omega/(2\pi)$ for $\mathcal{V} = 0.75$, 0.50 and 0.25. Results are included for the unbaffled container (black) and in the two-baffle two-slots configuration shown in Fig. 11.14, both fixed (blue) and moving with spring stiffnesses: $(K_1, K_2) = (15000, 4000)$ N/m for moving baffles - 1 (indigo), and (10000, 8000) N/m for moving baffles - 2 (red).

shows a significant reduction of the contact point maximum elevation for the first sloshing frequency, albeit the resulting peak value is larger compared to the fixed baffle case. By

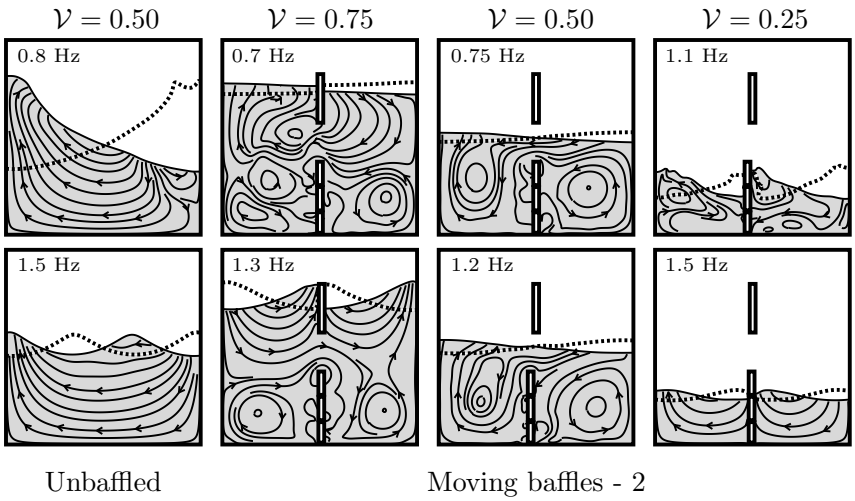


Figure 11.18: Snapshots depicting the maximum free surface displacement at the resonances of Fig. 11.17. (First column) First and second sloshing modes ($\lambda = 2L$, $2L/3$, respectively) for the unbaffled container with $\mathcal{V} = 0.50$. (Second column, upper panel) Coexistence of the first sloshing and the U-shaped container modes. (Second column, lower panel) Sloshing mode of each container half with $\lambda = L$. (Third column, upper panel) Low amplitude first odd sloshing mode. (Third column, lower panel) Low amplitude first odd sloshing mode coupled with the baffle motion. (Fourth column, upper panel) Sloshing of each container half. (Fourth column, lower panel) Oscillatory wave mode with $\lambda = L/2$.

analyzing together the time evolution of the bulk flow and that of the baffle displacements, we observe that the upper baffle is barely affected by the fluid motion, whereas the lower baffle is easily drawn from the equilibrium position. That is: the upper baffle acts as a fixed baffle — see the superposition of the dark blue and indigo curves in Fig. 11.17 for $\mathcal{V} = 0.75$ — and the lower baffle is not opposing the bulk flow efficiently; it is almost in phase with the sloshing motion.

As a result, we opt to slightly modify the spring constants to $K_1 = 10000$ N/m and $K_2 = 8000$ N/m, from now on referred to as "moving baffles - 2" as in Fig. 11.17. This new selection yields an improved frequency response for all $\mathcal{V}$, with the most noticeable effect appearing at intermediate values. The results corresponding to the pulse-like acceleration would inevitably be altered. In this regard, the diamond red markers in Fig. 11.15 present a slightly worsening for low $\mathcal{V}$, while intermediate and large $\mathcal{V}$ remain relatively unaltered.

For $\mathcal{V} = 0.75$, two smaller resonance peaks arise for all baffled containers. The first one, at lower ω, corresponds to a mode resembling the usual sloshing in U-shaped containers, see the second column, upper panel, in Fig. 11.18. Despite this mode being no longer dominant when the system is subjected to a pulse-like acceleration, here we observe that its influence is non-negligible under harmonic excitation. The second peak, at larger ω, corresponds to an oscillatory mode with $\lambda = L$, as presented in the lower panel for $\mathcal{V} = 0.75$ in Fig. 11.18. Here, the baffle presence favors the sloshing mode of each container half.

Intermediate filling ratios, represented by $\mathcal{V} = 0.50$, also exhibit a first peak corresponding in

all cases to the first sloshing mode, as evidenced by the upper panel of Fig. 11.18, now with a much lower amplitude. The larger peak observed at $f \sim 1.5$ Hz corresponds to the second sloshing mode. The red markers, however, indicate the presence of an additional mode at $f = 1.2$ Hz. This mode could arguably be an interaction between the first odd sloshing mode $\lambda = 2L$ and the baffle motion, as suggested by the relatively flat interface right above the baffle.

At lower filling ratios, represented by $\mathcal{V} = 0.25$, the first odd sloshing mode vanishes as it does for $\mathcal{V} = 0.75$, while the U-shaped container mode is not present. Another peak at ranging frequencies from 1 - 1.2 Hz appears, corresponding to the sloshing of each individual container half ($\lambda = L$). For larger ω, a wave oscillatory mode with a wavelength of $\lambda = L/2$ starts to develop, as evidenced by the lower panel in Fig. 11.18, $\mathcal{V} = 0.25$.

In light of these results, proper optimization and selection of the spring constants should be performed. This optimization would need to account for the expected fluid container dominant loading: either quasi-static or harmonic. The optimum solution for each type of acceleration may differ and thus the associated selection of optimal spring constants.

11.8 Conclusions

The present numerical work examined a recent idea for sloshing control: moving baffles constrained by springs. Tuning the spring constant K notably enhances the sloshing reduction capabilities of a given baffle, similarly to the concept of TMD in structural mechanics. An extensive validation of the numerical model, based on the level-set formulation, was performed against the results of Liu and Lin [53] and Faltinsen et al. [270] for baffled and unbaffled containers, respectively, and the works of Koh et al. [56] for a constrained floating baffle and Kim et al. [64] for horizontal moving baffles.

The model was then adapted to a $L \times H = 1\,\text{m} \times 1\,\text{m}$ container equipped with a centered vertical baffle in either fixed or moving configurations and varying filling ratios, $\mathcal{V}$. We analyzed the sloshing response of the system by using its decay time τ_d and time-averaged kinetic energy when subjected to an arbitrary pulse-like acceleration and compared to that of the unbaffled configuration. A significant improvement was achieved, both with fixed and moving baffles, with an average reduction in τ_d from ~ 46 s to ~ 20 s. For moving baffles, the optimal spring constant K depends on $\mathcal{V}$. Moreover, a sharp transition at $\mathcal{V} = 0.70 - 0.75$ was identified, likely related to the appearance of a sloshing mode similar to that of U-shaped containers.

Altering the baffle vertical dimension (H_b) and placement (H_c) was shown to be detrimental due to the appearance of the U-shaped container sloshing mode or due to lower interaction between the bulk flow. To deal with both issues, we introduce a new baffle configuration based on the splitting into two halves located at $H_{c,1} = 0.7$ m and $H_{c,2} = 0.25$ m, each of them having a height $H_b = 0.25$ m, while the spring constants were also modified to $K_1 = 15000$ N/m and $K_2 = 2500$ N/m for the upper and lower portions. As a direct result, an average τ_d of ~ 12 s for the moving baffle configuration was achieved. A further step towards suppressing the U-shaped mode involved the introduction of a 1 cm wide slot on the central region of

the lower baffle to enhance the mass transfer between the two container halves. Despite the small decrease to an average $\tau_d \sim 9$ s, we found an almost uniform τ_d for all $\mathcal{V}$ except for the lowest $\mathcal{V}$. Enlarging the lower baffle towards the bottom wall without reaching it, along with an additional 1 cm slot, leads to a complete uniformity of $\tau_d \sim 8$ s for all $\mathcal{V}$.

With the former baffle configuration, a frequency analysis ranging from 0.1 to 1.5 Hz showed the enhancement on the sloshing response for $\mathcal{V} = 0.75$, 0.50 and 0.25. The first odd sloshing mode was mainly replaced by a (lower amplitude) mode similar to the U-shaped mode ($\mathcal{V} = 0.75$), its maximum amplitude largely decreased ($\mathcal{V} = 0.50$), or vanished ($\mathcal{V} = 0.25$). The baffled container exhibited a peak at $f \approx 1.2$ Hz corresponding to a sloshing mode with $\lambda = L$, whereas a third peak was observed for frequencies closer to 1.5 Hz, corresponding to the second odd sloshing mode $\lambda = 2L/3$. These results show a worse response for the moving baffle compared to the fixed one for the first set of spring constants. Adjusting the spring constants to K_1 and K_2 to 10000 N/m and 8000 N/m — based on the observed dynamics — improves the dynamic response, although hindering the response to the pulse-like perturbation. We thus conclude that the optimization of the spring constants should consider both quasi-static and pulse-like accelerations.

Overall, the results presented in this manuscript delve further into the potential of moving spring-mass baffle systems for passive sloshing suppression. The extensive numerical research has demonstrated that, despite not being able to find a unique criterion for optimization, general guidelines can be followed for a proper tuning of the system.

Acknowledgments This work was supported by the Ministerio de Ciencia e Innovación under Project No. PID2020-115086GB-C31, and by the Spanish User Support and Operations Centre (E-USOC), Center for Computational Simulation (CCS).

Chapter 12

Experiments on sloshing mitigation using tuned oscillating baffles

Dan Gligor, Pedro A. Marques, Pablo Salgado Sánchez, Jeff Porter, Miguel A. Méndez and J. M. Ezquerro

Physics of Fluids **36**, 092122 (2024)

https://doi.org/10.1063/5.0225917

We experimentally confirm the efficacy of submerged oscillating baffles for sloshing mitigation in a partially-filled open container of water. As with the more typical applications of tuned mass dampers, when the natural frequency of the baffle is close that of the first sloshing mode, the main resonance peak is split into two peaks of lower amplitude. The reduction in resonant sloshing amplitude is superior to that of a fixed baffle.

Tuned mass dampers (TMDs) rely on the simple idea of coupling a spring-mass or pendulum-type damped oscillator to a larger structure in order to reduce its unwanted vibrations [68]. They are widely used in buildings and bridges to mitigate the effects of earthquakes and strong winds. Tuned liquid dampers [74] are a variation of this strategy where the damper is a container of liquid that is free to slosh back and forth. The frequency of this sloshing can be adjusted by selecting the container and the liquid depth in order to optimally dampen resonant vibrations of the primary structure.

In many important applications, however, such as propellant management or the transport of liquids in trucks and tanker ships [275], it is the sloshing itself that is the problem. Much effort has gone toward understanding the dynamics and consequences of sloshing [39–41] and developing mitigation strategies. Passive strategies for reducing sloshing motion include modifications of the container geometry [37, 39, 40] and, as the most common solution, the introduction of baffles [39, 52, 60]. Active strategies include those based on controllable baffles [57], the use of thermocapillary flows [201], thruster firings for ballistic rockets [282], and applied magnetic fields for ferrofluid-based propellants [43].

Recently, flexible elastic baffles have been investigated [62, 63] as well as solid baffles attached by springs [64, 67, 84]. These innovations can be seen as another application of the TMD

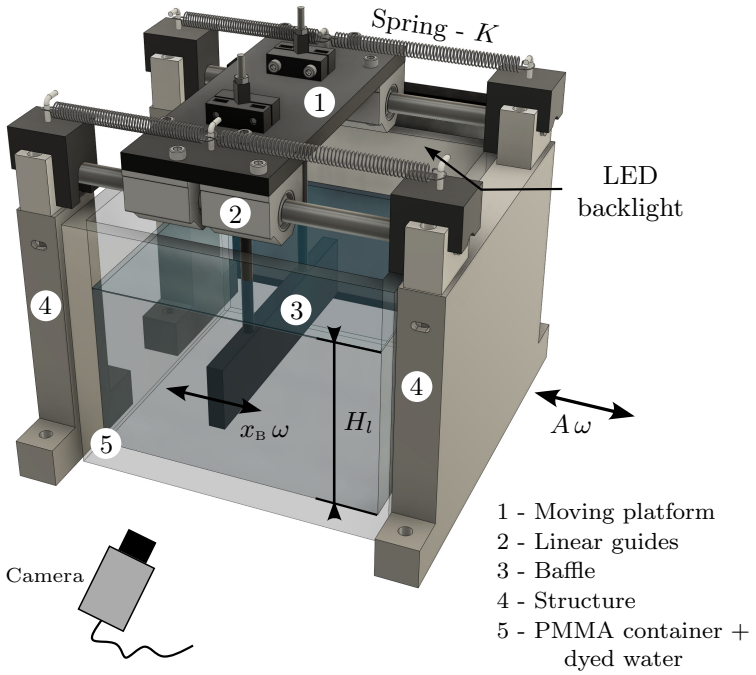


Figure 12.1: Sketch of the experimental setup: a moving platform (1) is bolted to four linear guides (2) that slide over two steel shafts that are clamped to the main structure (4); the baffle (3) is submerged using two rigid beams to ensure its correct position. The transparent PMMA container (5) holds dyed water. Both the interface and baffle positions are recorded by a camera using LED backlight illumination.

strategy or as an inversion of the tuned liquid damper — the primary system is the liquid itself whereas the secondary system is the oscillating baffle. The experiments of Kim et al. [64] considered horizontal spring-attached baffles placed above the resting level of the liquid in order to absorb impact forces; contact only occurred above a certain sloshing amplitude, in a nonlinear regime. The experiments of Idelsohn et al. [62] considered flexible baffles either fixed by one end at the bottom or hung above the liquid. No resonance criteria was used in selecting the Young's modulus.

This Letter provides more direct experimental evidence for the effectiveness of the TMD approach by measuring the effect of an oscillating, centrally-placed submerged baffle subjected to a linear (Hooke's law) restoring force. The strategy investigated experimentally here works well for both small and large sloshing amplitudes since it relies on the interaction of the baffle with the bulk flow; there is no threshold amplitude required. We find significant improvement with respect to a standard fixed baffle for sloshing mitigation.

The experimental setup, shown in Fig. 12.1, is built around a transparent polymethyl methacrylate (PMMA) container with a square cross section of 175 mm $\times$ 175 mm and a height of 150 mm. This container is partially filled with blue-dyed demineralized water up to a height H_l. We select demineralized water for its low viscosity — and, thus, low viscous dissipation in the bulk flow. The surface tension of water is well known but, due to the high

Bond number of Bo = 4292, the influence of surface tension is negligible. The container is placed within a robust metal structure that includes a mobile platform which slides over two parallel rails via linear guides. This sliding motion is constrained by four elastic springs. A small baffle, 10 mm thick, 170 mm wide and 40 mm high, is rigidly attached to the platform using bolts and submerged in the fluid. These baffle dimensions are selected in order to achieve a significant interaction with the bulk flow with largely two-dimensional dynamics. Images of the sloshing liquids were acquired with an SP-12000M-CXP camera operating with backlighting illumination from an LED panel positioned on the opposite side of the container. The central baffle, oriented vertically, is positioned 30 mm from the container bottom and maintains a gap of 2.5 mm from the lateral walls. The container is clamped to a metal structure, which is attached to the SHAKESPEARE [107] facility table at the von Karman Institute for Fluid Dynamics. We note that the experimental setup used here is relatively simple and that the baffle reacts passively to the excited sloshing motion. Modifications of the basic rectangular geometry or the addition of PID controllers for the baffle motion may be considered in future experiments.

The whole setup is subjected to harmonic lateral oscillations, along the same direction (x) as the baffle motion, with amplitudes A of 0.5 or 1 mm and excitation frequency $f = \omega/2\pi$ varying between 1 and 5 Hz. The relatively small amplitude triggers planar sloshing for all investigated conditions, so that the dynamic response of the system is fully characterized by the free surface elevation $h(x,t)$ and the horizontal displacement $x_b(t)$ of the baffle, each measured from their equilibrium positions. Both quantities were measured from the images, acquired at 30 frames per second, while the frequency of the applied forcing was measured using an Endevco 7293 accelerometer mounted on the sloshing table.

To identify the leading order harmonic sloshing mode and its spatial profile, the interface dynamics $h(x,t)$ is projected onto the acceleration frequency to obtain the Fourier coefficients:

$$\sigma_1\phi_1(x) = 2\left\langle h(x,t), \cos(\omega t)\right\rangle_T, \tag{12.1a}$$
$$\sigma_2\phi_2(x) = 2\left\langle h(x,t), \sin(\omega t)\right\rangle_T, \tag{12.1b}$$

where the brackets denote the time average over the forcing period $T = 2\pi/\omega$. The spatial profiles $\phi_1(x)$ and $\phi_2(x)$ are normalized so that $\max(|\phi(x)|) = 1$. The sloshing amplitude at frequency ω is defined as $\sigma = \sqrt{\sigma_1^2 + \sigma_2^2}$ and the (leading order) interface can be reconstructed from $\sigma_1\phi_1(x)\cos(\omega t) + \sigma_2\phi_2(x)\sin(\omega t)$. The amplitude σ is a measure of $\max(h(x,t))$ for steady oscillations but does not depend on the selection of a particular point in x and, thus, avoids the problems caused by shifting nodes as the frequency variation triggers mode transitions.

Figure 12.2 compares the results of four sets of experiments: no baffle, a fixed baffle, and moving baffles with spring constants $K = 200\,\mathrm{N/m}$ and $300\,\mathrm{N/m}$. As with other TMD applications, appropriately tuned spring constants result in a splitting of the main resonance peak into two smaller peaks, notably reducing the amplitude of resonant sloshing with respect to the unbaffled and fixed baffle cases. Specifically, for $K = 200\,\mathrm{N/m}$, the amplitude of the primary resonance peak is lower by a factor of 0.609 compared to a fixed baffle and, for $K = 300\,\mathrm{N/m}$, by a factor of 0.767.

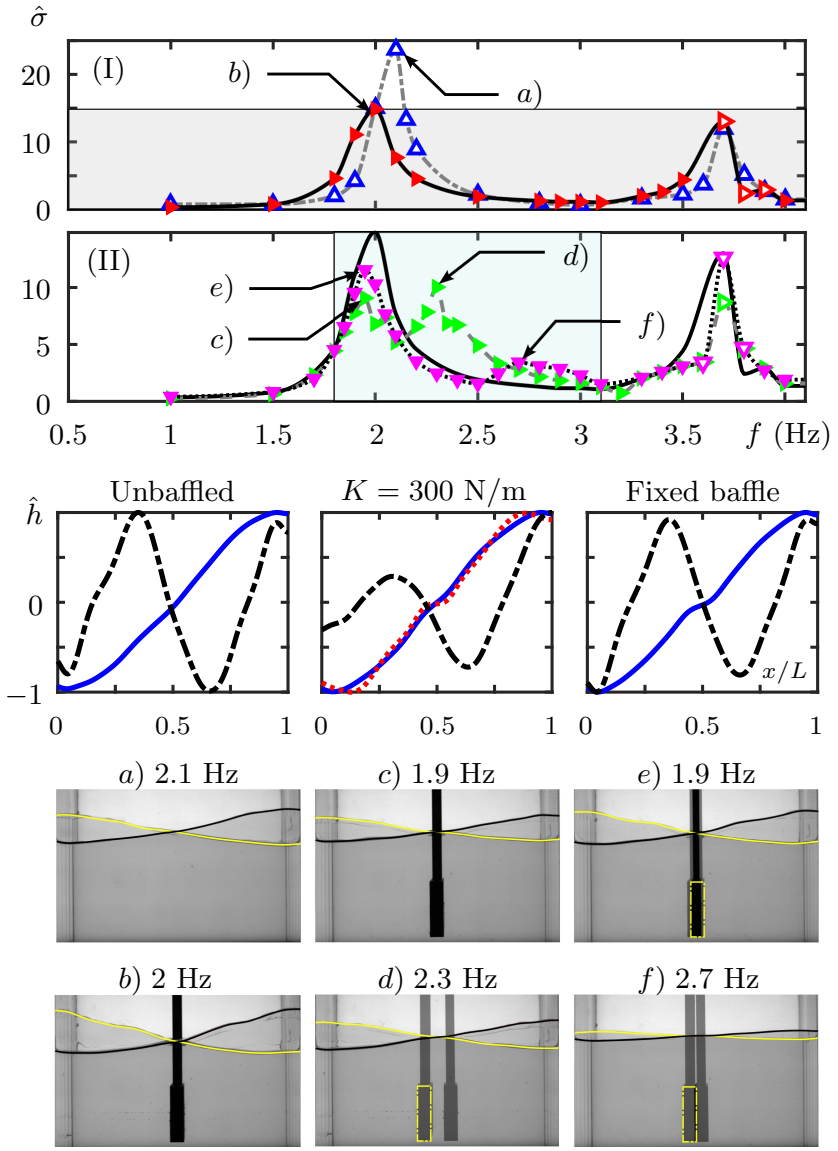


Figure 12.2: Sloshing amplitude while varying forcing frequency. (I) Nondimensional amplitude $\hat{\sigma} = \sigma/A$ for unbaffled (blue markers) and fixed baffle configurations (red). (II) $\hat{\sigma}$ for moving baffle configurations with $K = 300\,\mathrm{N/m}$ (magenta) and $K = 200\,\mathrm{N/m}$ (green); the solid black curve shows the fixed baffle case for reference. The filled markers correspond to the nominal forcing amplitude $A = 1\,\mathrm{mm}$ while the open markers are for $A = 0.5\,\mathrm{mm}$. Except with no baffle, $A = 1\,\mathrm{mm}$ yielded the most reliable measurements (in particular, the behaviour of the linear guides was smoother) at most frequencies. $A = 0.5\,\mathrm{mm}$ was sometimes used at higher frequencies to reduce splashing. The middle panels show normalized modal shapes $\hat{h} = h/\max(|h|)$ (a selected snapshot) at the resonance peaks: the first sloshing mode in the vicinity of 2 Hz (blue solid curves), the second sloshing mode in the vicinity of 3.7 Hz (black dashed curves) and the mode near 2.7 Hz for $K = 300\,\mathrm{N/m}$ (middle panel, red dotted curve). The lower snapshots corresponding to the labeled points $a) - f)$ in (I) and (II) and depict interface and baffle positions at two times separated by half the forcing period.

The primary resonance peak near 2 Hz corresponds to the first odd sloshing mode with wavelength $\lambda \simeq 2L$, although the wave is slightly distorted in the central region due to the baffle (see the continuous blue curves in the middle panels of Fig. 12.2). The baffle also reduces the resonance frequency since it hinders fluid (mass) transfer from one side to the other, slowing the dynamics (see Peromingo et al. [224] for a more detailed discussion). The maximum amplitude of this first resonance peak increases with the spring stiffness, ultimately converging to the fixed-baffle response. The secondary resonance peak, which is associated with a similar surface wave shape as the first odd sloshing mode (see the dotted red curve in the middle panel of Fig. 12.2), is characterized by greater baffle displacement (see snapshots *d*) and *f*)). Its amplitude is strongly affected by the spring constant K, reflecting the importance of the ratio between the natural frequency of the moving baffle, ω_b, and that of the liquid sloshing, ω_l: this ratio must be close to unity if the baffle is to substantially reduce sloshing. The experiment considers the two ratios $\omega_b/\omega_l = 1.198$ and 1.467, where $\omega_l/(2\pi) = 2.067$ Hz. Finally, the third resonance peak corresponds to the second odd sloshing mode with $\lambda \simeq 2L/3$, whose amplitude is largely insensitive to the baffle since the center of the container is an approximate node of the fluid motion.

Figure 12.2 demonstrates how the moving baffle reduces sloshing amplitude by splitting the main peak associated with the first odd sloshing mode and broadening its total frequency band (shaded region in panel II). The amplitude diagrams in panel II suggest that, for this baffle configuration, the optimal spring constant for reducing the amplitude of the resonant sloshing near 2 Hz is close to $K = 200$ N/m. The performance at this value is clearly better than for $K = 300$ N/m or for $K = 100$ N/m; the results of the latter experiments, which were slightly worse than for a fixed baffle, are not shown in the figure. We note that changes in the baffle system (due to alterations in the platform mass, for example) or the container size and shape will affect the resonance frequency ratio ω_b/ω_l and, thus, the optimum spring stiffness. The reader is referred to the numerical work of Gligor et al. [84, 283] for a more systematic approach to optimization (tuning) of the spring constant in microgravity and ground applications, respectively.

The relationship between the motion of the fluid and that of the baffle is shown in Fig. 12.3 for the case of $K = 300$ N/m, where the resonance peaks are more easily distinguished than with $K = 200$ N/m. The horizontal displacement of the center of mass of the liquid, $\hat{x}_{\text{G}}$, is obtained from the measured surface height while the dimensionless baffle displacement, $\hat{x}_{\text{B}}$, is observed directly. Both quantities are nodimensionalized with A. Panels (I) and (II) show the clear difference between the primary sloshing resonance near 2 Hz (marked with a red line), which involves more displacement of the fluid than of the baffle, and the secondary peak near 2.7 Hz (marked with a green line), which involves much more baffle motion. This second peak is near the natural baffle frequency (measured without fluid) of 3.03 Hz, but is lower due to the additional inertia and dissipation from its interaction with the fluid.

The isolated moving baffle system (i.e., without fluid) is well-approximated by a damped oscillator. Its natural frequency $\omega_b/(2\pi)$ and damping coefficient ξ were experimentally determined from a step response analysis and found to be $\omega_b/(2\pi) = 2.47$ Hz and $\xi = 0.0221$ for $K = 200$ N/m, and $\omega_b/(2\pi) = 3.03$ Hz and $\xi = 0.018$ for $K = 300$ N/m. The standard

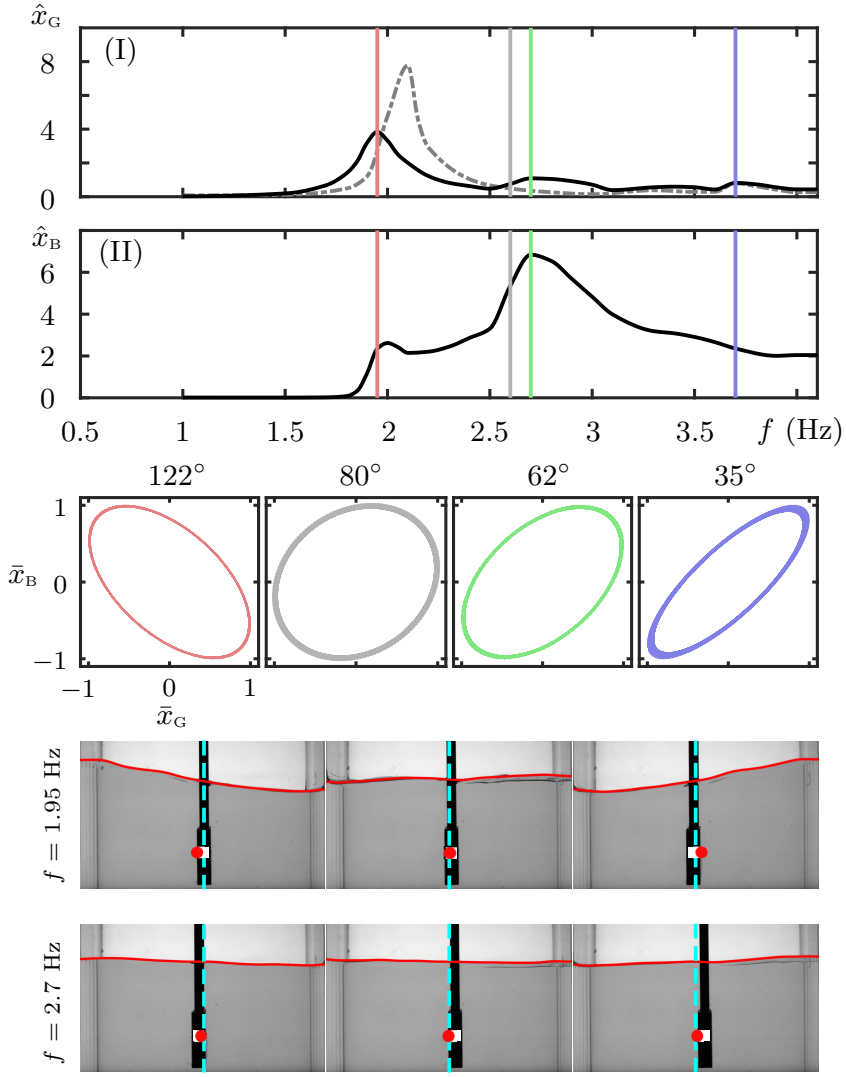


Figure 12.3: Center-of-mass and baffle displacement (nondimensionalized with A) while varying forcing frequency. (I) Maximum horizontal displacement $\hat{x}_{\text{G}}$ of the liquid center of gravity for no baffle (grey dashed curve) and for a moving baffle with $K = 300\,\text{N/m}$ (black curve). (II) Maximum displacement $\hat{x}_{\text{B}}$ of the baffle. (Middle panels) Phase plots of rescaled displacements: $\bar{x}_{\text{B}}(t) = \hat{x}_{\text{B}}(t)/\max(\hat{x}_{\text{B}})$ and $\bar{x}_{\text{G}}(t) = \hat{x}_{\text{G}}(t)/\max(\hat{x}_{\text{G}})$ illustrating the phase shift (labelled). The corresponding frequencies are marked with vertical lines in panels (I)-(II). (Lower panels) Snapshots of sloshing near the two maxima showing the center of gravity (red circular markers) and the baffle displacement (white square markers).

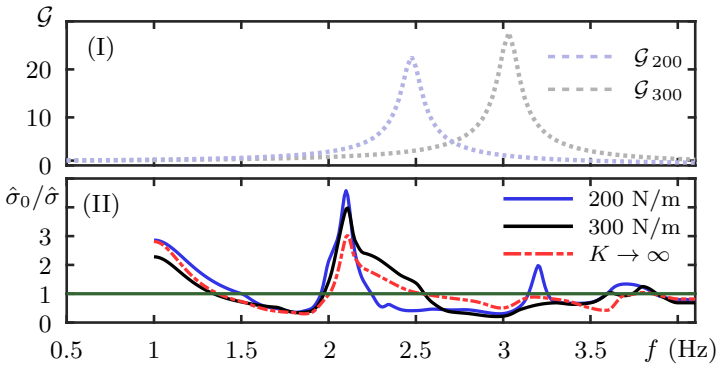


Figure 12.4: Gain functions and reduction factors for the moving baffle configurations. (I) Gain functions of the uncoupled baffle system, modelled as a damped oscillator, for $K = 200\,\mathrm{N/m}$ and $K = 300\,\mathrm{N/m}$. (II) Reduction factors, $\hat{\sigma}_0/\hat{\sigma}$, of the full system (see also Fig. 12.2) as compared to the unbaffled case. The dashed red curve shows the fixed-baffle reduction factor for reference.

gain (transfer) function

$$\mathcal{G}^{-1} = \sqrt{\left(1 - \left(\frac{\omega}{\omega_b}\right)^2\right)^2 + 4\xi^2 \left(\frac{\omega}{\omega_b}\right)^2} \tag{12.2}$$

for the baffle is shown in panel (I) of Fig. 12.4 and can be compared to the reduction factor of the complete fixed and moving baffle configurations calculated from the ratio between the measured amplitude, $\hat{\sigma}$, and that of the unbaffled case, $\hat{\sigma}_0$. Panel (II) of Fig. 12.4 shows that this ratio depends crucially on K. As noted above, the baffle hinders mass transfer between the two halves of the container and, thus, lowers the sloshing resonance frequency; this effect explains the increase in $\hat{\sigma}$ ($\hat{\sigma}_0/\hat{\sigma} < 1$) for $f \in [1.5, 2]$. Near the resonance frequency of the first sloshing mode, both moving baffles systems provide a significant reduction in amplitude, and perform better than a fixed baffle (red dashed curve). This improvement diminishes with further increase in frequency, however, and the performance is worst near the natural frequencies of the uncoupled baffle systems — the minima of the reduction factors in panel (II) are (approximately) aligned with the maxima of the (fluid free) baffle gains in panel (I).

A determination of the physical mechanisms behind the observed increase in the damping of sloshing motion with (properly tuned) moving baffles, as seen in Fig. 12.4, will depend on future experiments that incorporate velocimetry techniques such as PIV or PTV. However, the recent work of Gligor et al. [283] provides numerical evidence for several suspected mechanisms based on the flow characteristics seen in 2D models. The strong fluid-structure interaction between the bulk flow and the vertically oriented baffle, which is approximately perpendicular to the streamlines of the unhindered (baffle-free) sloshing motion, alters the path of the liquid and leads to recirculation zones and increased viscous dissipation. There can be an enlarged central region where the liquid surrounding the baffle moves similarly to a "rigid" solid. These mechanisms are dependent on the natural frequency ω_b of the baffle, which determines the resonance location where maximum displacement occurs, and on the phase lag of the baffle displacement with respect to the forcing.

In summary, this Letter experimentally demonstrates how the idea of TMDs can be extended

to fluid systems in which undesired sloshing modes are a problem. The performance of a properly tuned moving baffle is superior to that of an equivalent fixed baffle, with a sloshing reduction of approximately 40% achieved in the experimental setup considered here. The coupling between fluid and baffle motion splits the first odd sloshing resonance peak into two of lower amplitude. The first is associated with more displacement of the fluid's center of mass and less baffle movement while the second involves more baffle displacement and less fluid movement. The shape of the surface wave is similar in both cases. The next higher-frequency odd sloshing mode is minimally affected by a centrally placed baffle since this position is an approximate node of the fluid motion. We expect that variations of TMDs will prove useful for many applications where fluid management is a key concern, including oceanographic and aerospace engineering.

The work of P.S.S., J.P. and J.M.E. was supported by the Ministerio de Ciencia e Innovación under Project No. PID2020-115086GB-C31, and by the Spanish User Support and Operations Centre (E-USOC), Center for Computational Simulation (CCS). We thank the same project for supporting the stay of D.G. under the Short Training Program at the von Karman Institute. P.A.M. acknowledges the financial support from FNRS under FRIA grant No. FC47297.

Chapter 13

Discussion

This Thesis provided an overview of various mechanisms oriented towards the control of fluid phenomena, especially sloshing, both for ground and microgravity applications.

The first step in the analysis was to consider a rectangular container of fluid with a free surface under microgravity conditions. The size of the system was selected on the basis of previous microgravity experiments [8, 9] and the upcoming MarPCM ISS experiment [111]. In the absence of any external forcing, this system has a unique minimum energy configuration. This configuration is mainly determined by (minimizing) the free surface energy and by the contact properties of the fluid (liquid) with its substrate. The existence of such a configuration means that the system is stable in the presence of (sufficiently small) external perturbations and possesses an effective restoring force in microgravity.

The investigations presented here looked at the potential of Marangoni flows to induce interface deformation and, in particular, low-frequency sloshing-type motion.

13.1 Thermomechanical coupling

As shown in previous work [30, 35], Marangoni flows induce deformation of the free surface. The work of Sen and Davis [35] is particularly relevant for rectangular systems since this manuscript provides a reference for the expected asymmetric motion of liquids when a horizontal thermal gradient is imposed. In fact, a linear dependence of the asymmetry of the contact points on the Prandtl (Pr) and Marangoni (Ma) numbers is obtained; see Eq. (3.23). From a qualitative perspective, one can understand the effect of each non-dimensional number as follows.

By taking the tangential projection of the stress balance at the free surface, Eq. (3.24), one can obtain an estimate of the tangential velocity, $\mathbf{u}_t \sim \gamma \Delta T/\mu \propto \Delta T$, which is proportional to the applied thermal gradient and, by extension, the Marangoni number.

Regarding the Prandtl number, it is observed numerically that the vortices arising from this induced tangential velocity that are close to the contact points are the ones largely responsible for "resistance" to motion of the fluid surface. With lower viscosity, these vortices develop

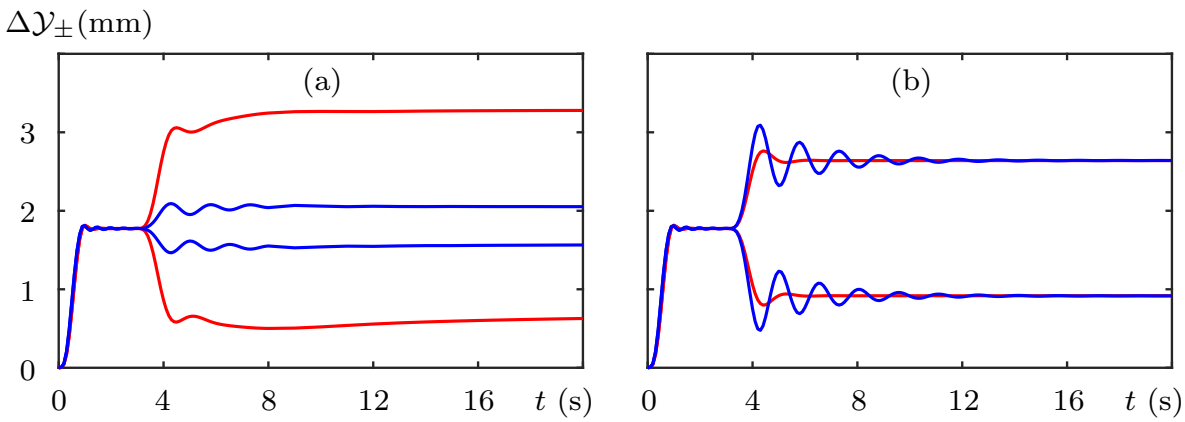


Figure 13.1: (a) Temporal evolution of the contact points $\Delta\mathcal{Y}_\pm = f(\pm L/2, t) - H$ at Ma = 32000 for $\nu = 20$ cSt (blue curve) and 100 cSt (red curve). The initialization of β (to 70°) and of ΔT, occur at $t = 0$ s and 3 s, respectively. (b) Temporal evolution of the contact points $\Delta\mathcal{Y}_\pm$ when subjected to a smoothed step acceleration — similar to that of the temperature in Eq. (3.18) — whose final value is $1.5 \cdot 10^{-3}\,\mathrm{g}_0$. Adapted from [178], Chapter 3.

more quickly, which leads to less asymmetry for the same Marangoni number, as illustrated in the snapshots of Fig. 3.6. These predictions align with the numerical results for the asymmetry with different viscosity values and for increasing thermal gradients, as seen in Fig. 3.4.

Numerical results such as the ones in Fig. 13.1 (a) indicate that a key feature of the transient dynamics that characterizes the system prior to settling into an asymmetric state caused by the thermocapillary effect is the out-of-phase oscillatory motion of the contact points. This motion is very similar to the first sloshing mode with a wavelength twice that of the container length.

The observed transient evolution points to a thermomechanical coupling between the free surface motion and the applied thermal gradient. A parallel can be established between the imposition of a thermal gradient and the introduction of a step acceleration to the system. The step function can be decomposed into an infinite number of harmonics, with the lower ones having the largest amplitudes. These are expected to excite the first sloshing mode before its eventual decay due to damping. Since inertial acceleration acts on the fluid just as gravity would, the free surface acquires a certain inclination, similar to the asymmetry that appears due to a thermal gradient. Both effects (transient and steady) are depicted in Fig. 13.1 (b), with the system subjected to a smoothed step acceleration. The oscillations for the lower viscosity fluid (20 cSt, blue curve) exhibit the same period as in the case of thermal forcing, corresponding to the first odd sloshing mode. Unlike the case of thermal excitation, the steady asymmetry resulting from the application of an inertial force is independent of the fluid viscosity. This is expected since the final state is an equilibrium solution that balances the interfacial energy and the potential energy associated with the inertial forcing. The final inclination of the interface is proportional to the Bond number $\mathrm{Bo} = \rho \mathrm{g}^* L^2/\sigma$, with g^* being the inertial acceleration. Viscosity only influences the transient dynamics.

The analogy between inertial forcing and thermal excitation suggests the feasibility of inducing free surface displacement with thermal gradients via the thermocapillary effect. Moreover, thermal gradients can be used to mitigate unwanted free surface motion, such as sloshing.

The previous statement, supported by numerical results, can be further assessed using a frequency sweep analysis of the applied thermal gradient and the free surface response, which results in Bode-type diagrams as in Fig. 3.9. These Bode-type diagrams exhibit two main features:

(i) The main resonance peak corresponds to the first sloshing mode, while subsequent peaks are associated with higher-order antisymmetric modes. We note that this triggering of exclusively antisymmetric modes is due to the excitation type: there is a phase lag of 180° between the temperatures at the vertical endwalls. If this phase lag is removed and synchronous heating and cooling is applied to both endwalls, then symmetric sloshing modes are triggered.

(ii) The phase lag between the motion of the contact points and the applied thermal gradient is 90°, a result that is especially relevant for control applications.

A detailed discussion of the effect of several important properties such as fluid viscosity, container length and height, and contact properties can be found in Chapter 3. Among these, the effect of contact properties is particularly interesting. In practice, it can be difficult to obtain an accurate measurement of the contact angle. Instead, an apparent contact angle is often predicted or measured experimentally, and this varies considerably depending on evaporation (if present), contaminants, and the presence of gravity (see, for instance, the works of Tsoumpas et al. [284] and Baldygin et al. [285] and references therein). Note that the resonances in the Bode-type diagrams in Fig. 3.9 indicate a major change in behaviour between the hydrophilic and hydrophobic cases, which is most pronounced for the phase lag (when sufficiently far from the 90° contact angle case).

The analysis carried out here is a prelude to designing an effective controller to combat liquid sloshing in microgravity via the thermocapillary effect, which expands the available fluid control strategies, including those based on vibrations [77, 120] or magnetic fields [43, 206, 286].

13.2 Sloshing control with thermocapillary effect

In light of the former results, a controller is designed and tuned for specific applications such as control of liquid sloshing. The selection of a particular mode to be controlled is not arbitrary: as depicted in Fig. 4.3, the largest response to an oscillating temperature gradient will be the first sloshing mode; a higher-order mode could also be controlled, but with a larger thermal gradient, which may not be achievable.

One of the most simple, effective, and robust controllers is a PID controller. To implement it here, the control signal is the applied thermal gradient, which is imposed in an asymmetric manner to effectively control the first (or any odd subsequent) sloshing mode. The response of the system is "measured" — this could be achieved with optical diagnosis tools such as

a camera and backlight illumination — via the contact points and their asymmetry. The asymmetry is then used to construct the feedback signal assuming that the desired state for the system is a symmetrical one. In other words, we imagine that an inertial forcing (perturbation) causes the free surface to move, introducing an asymmetry, that the thermocapillary controller aims to counteract. The resulting error signal is then processed by the PID controller, which gives the commanded thermal gradient to be applied. A graphical description of the proposed system is provided in Fig. 4.5.

In order to evaluate the performance of the controller, a reference inertial force (acceleration) is defined. The selection of this force, which is not specifically addressed in Chapter 4, is based on the following rationale.

In space applications, fluid systems are typically subjected to the following types of inertial forcing: quasi-steady loads during a certain interval of time, which are induced by orbital maneuvers such as reboosting or attitude corrections, pulse-like loads, which are generated during the initiation of orbital maneuvers such as the thruster firing during a reboosting of the impact experienced during a docking maneuver or the separation of upper stages in launch vehicles, and oscillatory loads, which are associated with mechanical systems (rotating mechanisms, cyclical behavior of mechanical components, etc.) or structural resonant modes triggered by other external forces or human activity within a microgravity environment (e.g., on the ISS).

Among these forces, we can dismiss the quasi-steady ones for the system studied here. The reason for this is the controller's ability to overcome inertial forces with extremely low frequencies ($f \to 0$). As suggested by the Bode diagrams in Fig. 3.9, for the lowest analyzed frequencies there is a difference of almost two orders of magnitude in the system response with respect to the applied thermal forcing compared to the peak of the first sloshing mode resonance. Therefore, although control is possible, the required thermal gradients would not be easily achievable. In this scenario, the fluid system considered here could not be returned to the initial symmetric equilibrium and would instead exhibit a permanent (quasi-steady) inclination due to the inertial forcing.

Regarding oscillatory forces, we note that the relevant oscillatory acceleration cannot be defined unless a real system is thoroughly analyzed. The structural modes of a large vehicle or satellite, as well as the perturbations induced by crew activity, will vary depending on the particular case.

In contrast, pulse-like loads are some of the most representative mechanical loads expected in a space environment. Moreover, pulse-like accelerations are associated with perturbations that vanish over time, so the system naturally returns to the initial equilibrium provided that the perturbation does not trigger certain irreversible phenomena such as drop ejection [8] or breakup of the fluid domain [145].

The next step involves defining two objective functions based on the ability of the controller to dampen sloshing motion (damping enhancement) and a surrogate of the controller power "consumption" (cost).

For this purpose, the acceleration measured by an OSSRAW sensor aboard the ISS during a

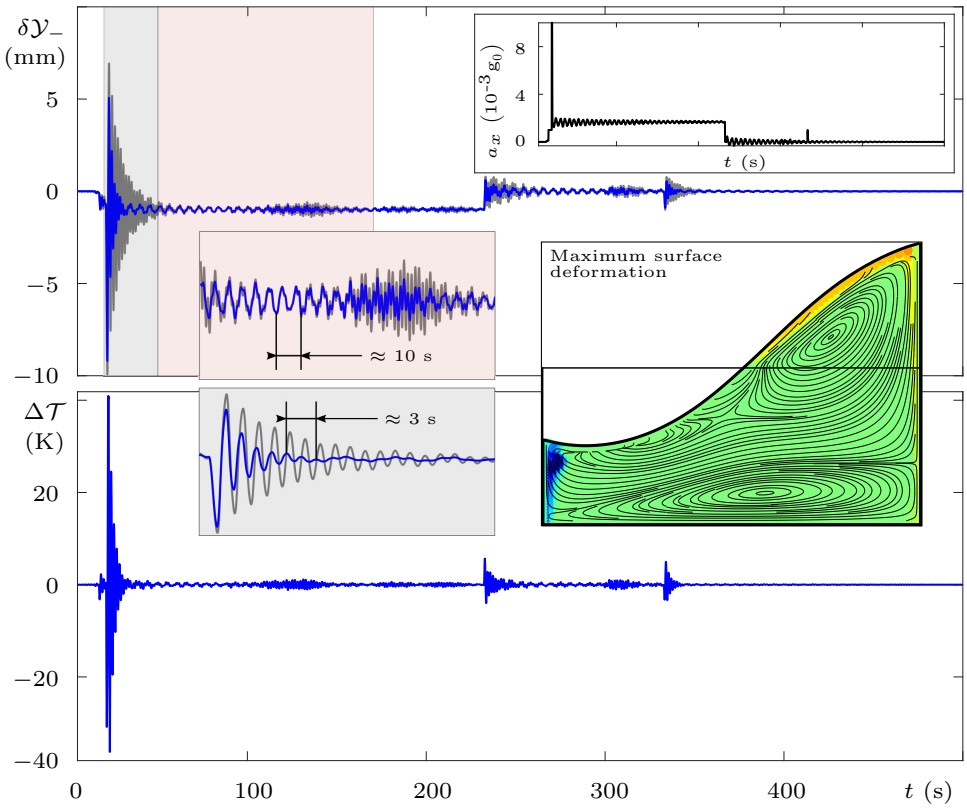


Figure 13.2: Effect of derivative control on a fluid system subjected to perturbations taken from an ISS reboosting maneuver. The upper inset shows the acceleration measurements from the OSSRAW sensor in units of g_0 over 500 s. The uncontrolled response (grey curve) is shown for comparison. The addition of a controller with derivative gain $K_D = 852$ (K s)/m has a stabilizing effect (blue curve) on the resonant sloshing oscillations. The left shaded insets focus on controller performance during sloshing (lower, grey) and for the driven lower-frequency mode (upper, pink). The inset to the right of those shows the maximum deformation of the fluid surface. The lower panel shows the thermal modulation signal output by the controller.

reboosting maneuver was introduced to the current system and the controller performance was evaluated. Figure 13.2 shows a comparison between the controlled and uncontrolled response of the fluid system when subjected to the reboosting signal. This signal is composed of all three types of inertial forcing mentioned previously, and the system response serves as confirmation of the previous assumptions.

The quasi-steady (average) forcing level between $t \approx 10$ s and $t \approx 220$ s induces a steady tilt of the fluid interface that cannot be overcome, similarly to the lower frequency perturbations ($f \approx 0.1$ Hz) probably arising from structural modes of the ISS itself. As pointed out in the Introduction (Chapter 1, Section 1.2), achieving thermal gradients large enough to reverse a steady tilt would imply using a large proportional gain. This would increase the cost of the controller without improving the damping enhancement of sloshing motion (see Fig. 4.7). Given the trade-off arising from these conditions, mitigation of sloshing is

prioritized over reversing a quasi-steady inclination: the resulting fluid configuration would be an arrangement derived from the balance of interfacial and potential energy (this one arising from the introduced quasi-steady force).

With regard to the pulse-like acceleration characterizing the early stages of the maneuver, we observe that the thermocapillary controller with only derivative gain offers outstanding performance. Although the performance improvement is noticeable, it should be noted that rapid transients (large derivatives) often lead to temperature modulations that could not be easily achievable by conventional systems.

As anticipated in the Introduction, the system analyzed here possesses a unique minimum energy fluid configuration determined by surface tension and contact properties. Although this is an advantage in terms of recovering the initial fluid configuration naturally in the absence of an external force or a controller, any perturbation that drives the system away from the minimum energy configuration must overcome a restoring force.

With given fluid properties, including contact angle and surface tension, one way to alter the minimum energy configuration is by changing the amount of fluid or the container geometry. For example, by considering smaller fluid volumes within a rectangular container, the equilibrium can be shifted towards disconnected solutions (e.g., droplets adhered to the container corners or puddles). On the other hand, changing the container geometry can lead to new potential arrangements of the liquid (see, e.g., the work of [16]).

If a system has a family of free surface configurations with the same surface energy, the system could ideally be driven from configuration "A" to configuration "B" with zero effort. Since this is not realistic for most fluids, mainly due to viscosity and dissipation, an external perturbation that can drive the system from "A" to "B" must overcome a certain energy barrier. Fluid configurations with the same energy can be achieved with symmetric geometries (with rotational symmetry, for example).

If we restrict the analysis to two-dimensional dynamics, the container shape with the greatest number of equilibrium positions of equal energy is a perfect circle. The transition from a hypothetical state "A" to a state "B", under the laminar flow hypothesis, would involve overcoming the bulk viscosity of the fluid along with the boundary condition imposed by the substrate.

An intermediate case would be a system that possesses at least two equilibrium positions, which are close to each other, so that the system could be driven from one to the other if desired. This is the case if an elliptical geometry is considered instead of a circular one.

13.3 Influence of the geometry - Circular and elliptical geometries

The previous considerations lead to the idea of using alternate geometries, namely circular and elliptical, to evaluate the potential of Marangoni flows to control interface motion and, in particular, sloshing. As noted before, the specific rationale behind the use of such geometries is the smaller free surface energy differences between different fluid orientations.

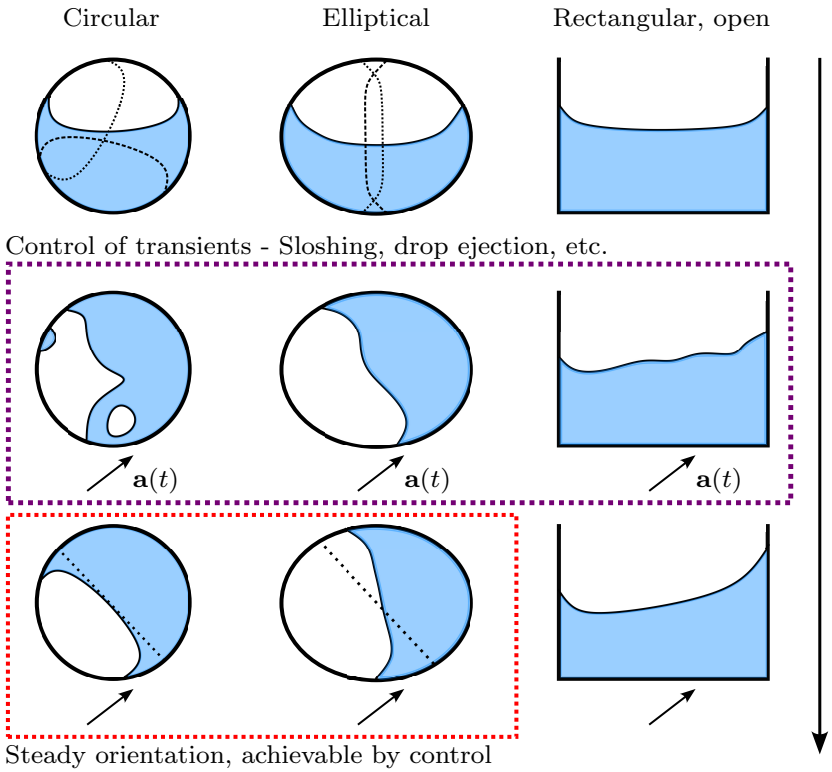


Figure 13.3: Possible time evolution of a two-phase fluid system in variable container geometries when subjected to an arbitrary quasi-steady acceleration in the absence of any internal element to counter the fluid displacement. The figures in the upper row depict an initial (equilibrium) state (solid line) along with other equilibrium configurations (dotted and dashed lines). In the elliptical case, the initial equilibrium is unstable. The middle row depicts potential transient states where sloshing, drop ejection or bubble formation may occur. The lower row depicts the expected steady-state configuration, with the fluid interface more perpendicular to the inertial forcing except for the rectangular container, where surface energy is more difficult to overcome. Based on the results in Chapters 3 and 4, we propose the use of the thermocapillary effect to control transient evolution and to induce reorientation of the free surface — this statement is mainly valid for circular and slightly elliptical geometries, since required thermal gradients would be too large in the rectangular case.

For this purpose, Fig. 13.3 illustrates the time evolution of liquid-gas systems in circular, elliptical and open rectangular containers when subjected to an arbitrarily oriented inertial acceleration. The first row shows an arbitrary equilibrium orientation. In the case of the circular container, this initial configuration is only one of an infinite number of equivalent symmetry-related configurations (see the dashed and dotted lines). The liquid in the elliptical container is initially in an unstable equilibrium position, with the minimum energy configurations corresponding to the dashed and dotted lines. The open rectangular container case, on the other hand, has a unique minimum energy configuration, which is the one shown. After the introduction of an inertial acceleration, the system evolves. This perturbation also introduces kinetic energy to the system and, during the transient dynamics, sloshing modes may be excited (among other phenomena such as drop ejection, bubble formation, etc.). The

fluid motion transmits forces to the container, which are then translated to the supporting structure. For example, if these kinds of containers are placed within a satellite as liquid propellant deposits, the sloshing forces would induce loads that need to be compensated by the Attitude and Orbit Control System (AOCS). With observation missions such as space telescopes (e.g., James Webb Space Telescope), this could be a critical issue.

During such transient stages, sloshing could be controlled using the thermocapillary effect, as suggested by the results of Chapters 3–8. After this transient state, the fluid system would eventually reach a new stable configuration. This configuration tends to reorient the fluid interface so as to be more perpendicular to the inertial forcing since this minimizes the total energy: kinetic, potential, if any, and surface energy. Upon comparing the expected equilibrium shapes of the circular and elliptical geometries, we note that the interface in the circular case would be (on average) fully perpendicular to the inertial forcing whereas in the elliptical case the acceleration amplitude is a relevant parameter that determines how much the (average) interface is rotated from the purely vertical minimum energy configuration. A similar argument applies to the rectangular case.

Based on these expected types of dynamics, one could imagine driving the system from its initial equilibrium to a certain orientation with the aim of minimizing the effects of inertial forcing on the system. For instance, if the direction of a force is known beforehand (e.g., prior to orbital maneuvers), the interface could be repositioned before the forcing begins and, thus, the system would be minimally perturbed by this force. In this scenario, movement could be induced by Marangoni flows. For fluid systems with a unique minimum energy configuration, rotating the interface could be challenging. On the other hand, systems with multiple minimum energy states, such as circular and elliptical containers, could leverage this effect to achieve a low-cost reorientation of the fluid interface.

The numerical research on the interface reorientation dynamics in other geometries was carried out first in Chapter 5, with a circular container holding equal volumes of liquid and air in microgravity (see the sketch of the configuration in Fig. 5.3). The ability of Marangoni flows to reorient the fluid interface is confirmed, as shown in Fig. 5.5. Moreover, adding horizontal vibrations enhances this reorientation when considering a repositioning maneuver from $\Theta = 0 \longrightarrow 90°$. As discussed previously, this improvement is due to the *vibroequilibria effect* [8, 77, 120, 145], which tends to orient the fluid interface to be more perpendicular to the excitation force, minimizing the overall system energy.

As illustrated in Fig. 13.3, the system does not (initially) have a preferred orientation (minimum energy configuration). However, once a thermal gradient is imposed, this is no longer true. By introducing a temperature difference between the left and right cell walls, the thermocapillary effect locally alters the surface tension and drives fluid motion — kinetic energy is thereby also introduced — in the vicinity of the contact points. This leads to the fluid rotating counter-clockwise, almost as a rigid body. When the free surface orientation exceeds $\Theta_\infty = 90°$, the thermal gradient across the free surface is inverted, which then inverts the associated velocities, leading to behavior similar to that of an underdamped system until the final equilibrium near $\Theta_\infty = 90°$ is reached. In this final configuration, the interfacial energy is approximately the same as in the initial state; the equilibrium position is now determined mainly by the minimization of kinetic energy.

Again, as in rectangular geometries, it should be noted that the responsiveness of the fluid system greatly depends on contact properties as well as the applied thermal gradient, as demonstrated in Fig. 6.4. As the contact angle gets closer to 90°, the system response shows larger damping with the same thermal gradient. This effect can be understood by looking at the projection of the velocity tangential to the circular boundary. Contact angles $\beta < 90°$ are associated with larger tangential velocities that contribute to the rotation of the whole fluid domain as a rigid solid and produce faster rotating motion. A contact angle of $\beta = 90°$ provides no tangential velocity projection and, thus, the system response is slower. The significant effect of the contact angle indicates the need to properly model the contact line dynamics for these kinds of systems.

The contact angle is usually considered constant and the results for many phenomena, both numerical and experimental, are not significantly affected by this assumption [8, 11, 120]. In other cases, the dynamics is strongly dependent on the contact properties (e.g., capillary flows [287] or liquid drops moving over substrates [288]). Contact angles depend on the underlying flow (among other effects), and the effective value exhibits hysteretic behavior for advancing and receding motion of a liquid in contact with a substrate [289]. Dynamic contact angles have been extensively described under different considerations and their hysteretic behavior, via friction, provides additional damping for fluids in low gravity conditions, as indicated by the work of Utsumi [50].

For the system analyzed here, this hysteretic behavior could be understood as an additional force that would potentially slow down the dynamics in circular containers. As seen in Fig. 6.5, the contact angle hysteresis causes a large increase in damping, which can even stop fluid motion for sufficiently low thermal gradients.

The results confirm that a change in geometry from rectangular to circular improves the system's responsiveness to the thermocapillary effect. If we focus more on the sloshing modes instead of the interface reorientation, it is clear that the two systems are not equivalent. Exciting low-frequency sloshing modes with Marangoni flows is not as easy for circular systems: When excited with a frequency close to the first sloshing mode, the motion of the interface becomes increasingly large and nonlinear. At a certain point, the fluid interface no longer oscillates about the initial orientation $\Theta = 0°$, and the inclination of the interface increases over time, stopping only when it is oriented perpendicular to the applied thermal gradient. Therefore, no Bode-type diagrams could be obtained for circular geometry and a proper characterization was not possible with the current model. Instead, a strategy for repositioning the interface to ensure that the influence of perturbations over the fluid container is minimal would be preferable.

The case of elliptical containers was analyzed in Chapter 7. The numerical results presented indicate slightly different dynamics depending on the eccentricity. To understand these results, one must account for a couple of effects. For small eccentricities, containers with elliptical geometry behaves similarly to circular ones, and Marangoni flows will tend to reorient the free surface perpendicular to the applied temperature difference. If the major axis of the ellipse is oriented in the same direction as the thermal gradient, the initial condition (as depicted in Fig. 7.2) is unstable since it does not have the minimum free surface energy. In this case, both the surface tension and the thermocapillary effect induce an anticlockwise interface

reorientation (i.e., they are complementary). Evidence of this action is presented in Fig. 7.3 for $\delta > 0$, where the temporal evolution with the elliptical geometry (gray) exhibits a larger frequency than in the circular case (black).

On the other hand, if the major axis of the ellipse is oriented perpendicular to the thermal gradient, then the effects of surface tension and Marangoni flow are in opposition: the isothermal (unforced) equilibrium position of the interface is a horizontal one and any deviation increases the interfacial energy. If the Marangoni flow is large enough to overcome this energy difference, then the new equilibrium position will be a vertical one; if not, the balance between these two driving forces can yield different results.

The latter case is of particular interest because numerical research shows that the eccentricity (or in this case, the dimensionless parameter δ) leads to a pitchfork bifurcation of the interface orientation, given by: $\Theta_\infty = 90^\circ + A\sqrt{\delta_{\mathrm{cr}} - \delta}$,. The location of the pitchfork bifurcation, δ_{cr}, along with an additional transition from one branch to the other at δ_{sym}, are well characterized and their dependence on the temperature is found to be approximately linear regardless of the contact angle, as suggested by a leading-order balance of surface tension and thermocapillary forces.

These results point to the significant potential benefits of combining an optimal tank container geometry with the use of the thermocapillary effect for fluid management purposes. It is worth noting that the application of thermal gradients provides two key advantages with respect to other technologies for fluid management. No elements need to be placed within the fluid domain, so there is no penalty on the amount of fluid to be transported, and no moving parts are required, since the control is performed via localized heating/cooling over the external boundaries of the container. However, control strategies based on Marangoni flows cannot be regarded as passive methods since power is required to produce the desired thermal gradients.

In general, the thermocapillary effect can be leveraged in a variety of small-scale systems to mitigate unwanted sloshing dynamics. However, as stated in previous sections, quasi-steady forcing cannot be effectively dealt with using this approach. Pulse-like accelerations, if large enough or sustained for a sufficient amount of time, also present a major problem. Thus, depending on the scenario, the sloshing mitigation might not be sufficient. Moreover, if we focus on ground systems, the applicability of Marangoni flows will be most useful for systems with characteristic sizes on the order of the capillary length. The limitations of the methods presented are clear and the concepts developed here are most applicable for capillary-scale problems or in microgravity. Therefore, additional mechanisms need to be explored which, on their own or combined, could provide enhanced performance.

To illustrate the limitations — and potential solutions — of the control systems proposed here, Fig. 13.4 could be used as a "guideline". Typically, both for ground and microgravity applications, we can consider three main energies affecting the behaviour and controllability of the fluid system. The potential energy may come from gravity, centrifugal forces, sustained (quasi-steady) accelerations or other relevant potential fields. The kinetic energy of the fluid becomes of critical importance during transient phases or while subjected to a time-varying forcing, for instance. The interfacial energy, as discussed in previous sections, has a notable

influence both in equilibrium configurations and, furthermore, in almost any microgravity application.

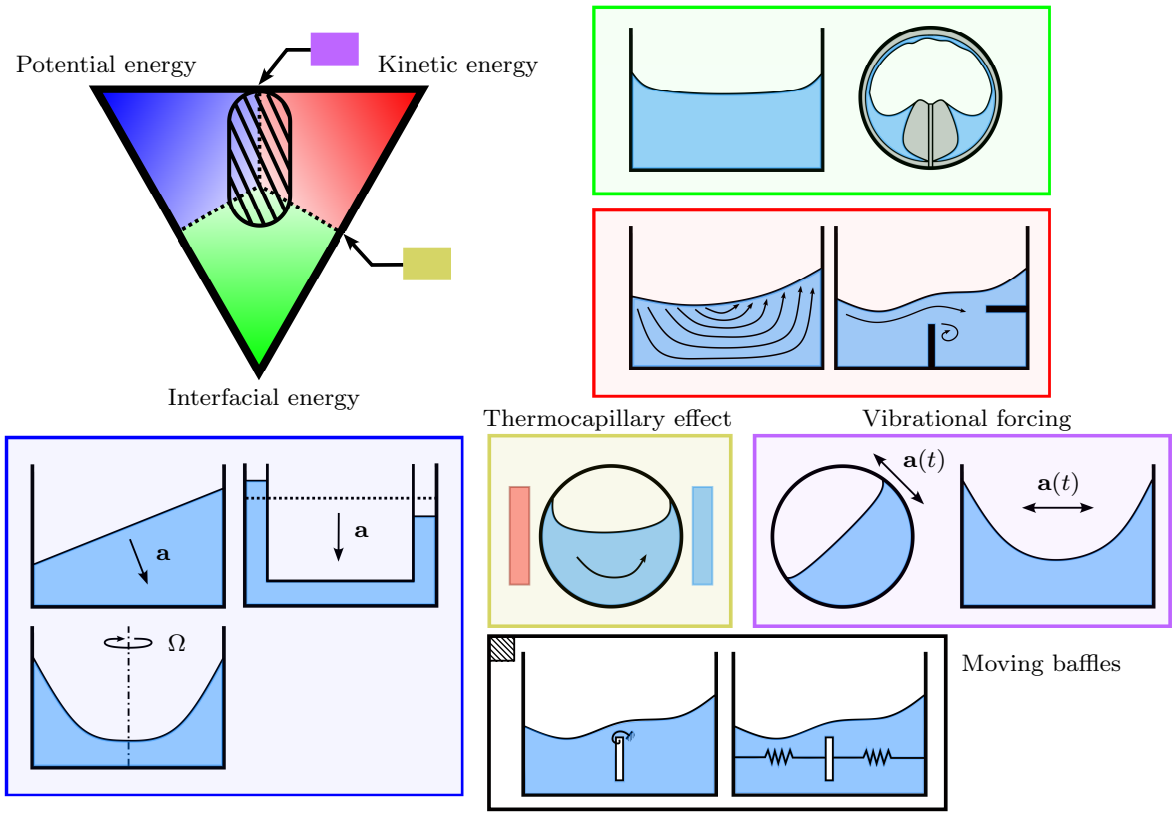


Figure 13.4: Main energies involved in sloshing motion and control along with examples of control applications. (blue) Potential energy arising from inertial, centrifugal or gravitational forces. Gravity influences the control of ship motion using U-tube anti-roll tanks [290]. (Green) Interfacial energy, arising from the interfacial tension and contact properties of fluids and their substrates, as with vanes in Propellant Management Devices (PMDs) [46]. (Red) Kinetic energy of the fluid and fixed baffles to mitigate sloshing motion [39]. Other combined strategies include: vibrational forcing [144, 145, 231] or the thermocapillary effect [178, 220]. Furthermore, the use of moving baffles [84, 106, 283] leverages the fluid kinetic energy, partially "storing" it as potential energy. If placed near the free surface, in systems where surface energy is not negligible (capillary scale, microgravity, etc.), it could also interact with the interfacial energy.

In microgravity, the thermocapillary effect increases the system kinetic energy as a result of surface tension differences arising from thermal gradients across fluid interfaces. Therefore, a balance between these two will drive the system towards new equilibrium configurations, as evidenced in rectangular [178], circular [220] and elliptical [291] geometries.

If a sufficiently large inertial force or a large potential energy (e.g., the one induced by gravity) is present, this interfacial-kinetic equilibrium would be displaced, moving it towards the potential-kinetic side. Unless the interfacial tension is large enough or the system size close to the capillary scale, the interfacial energy typically has a negligible effect on the control (and partly, behaviour) of large fluid masses. Thus, mechanisms focusing on those energies

should be considered.

Regarding potential energy, introducing (or modifying preexistent) potential fields such as electric, magnetic or inertial ones may involve the use of external mechanisms: spinning the container for centrifugal forces, inducing magnetic fields with coils, etc. Another alternative could be "storing" potential energy by leveraging the (mainly kinetic) energy of the fluid system via elastic elements.

The kinetic energy can be reduced in a straightforward manner through the dissipative effect of viscosity (both in the fluid bulk and at the boundaries). Any obstacle placed within a the fluid will will reduce kinetic energy and hinder fluid motion. Moreover, the interaction of these obstacles with the bulk flow will result in a permanent modification of the flow structure, leading to the appearance of recirculation zones, stagnation points, etc.

For sloshing control purposes, the most widespread solution involves the use of passive baffles.

13.4 Sloshing mitigation with baffles

Baffles have been widely used for sloshing suppression purposes, both on ground [53] and in space applications [39]. In the latter, their use is especially critical due to the absence of a strong restoring force. The literature on baffles is extensive and includes various configurations for them: vertical, horizontal, spanning a certain container height or length, ringed baffles in cylindrical containers, baffles with different shapes, etc. Although the effectiveness of different configurations changes according to the container geometry (prismoidal, cylindrical, spherical, etc.), the expected load, and the feasibility of introducing certain types of baffles, the basic working principles of these structures in the fluid container remain very similar [224].

To model sloshing in a simple way, equivalent mechanical models (EMMs) have been derived following the analogy between fluid motion and (damped) pendulum dynamics [39, 40]. This allows us to extract valuable data and compare theoretical and experimental results. These sloshing equivalent models help examine the assumption that the fluid motion can be separated into several contributions corresponding to the oscillatory modes and a quiescent mass. The results support the idea that the fluid domain can be divided into different regions where the sloshing motion is more or less pronounced and, thus, the placement of the baffles, which are obstacles to fluid flow, cannot be neglected.

The numerical investigation in Chapter 9 assessed the effect of the baffle on sloshing. The parameters that were varied include the length and height of the baffle, the vertical and horizontal positioning, the baffle orientation, and the number of baffles. The results confirmed that baffles are more effective when placed closer to the free surface because of the increased interference with the larger velocities in that region.

Although baffles placed near the surface clearly appear to be the most optimal ones for sloshing control (see Fig. 9.15), they face the major disadvantage that the filling ratio of the liquid container should be known. Typically, whether the fluid is propellant, water, or any other working fluid, containers are filled and emptied during their operation. Placing baffles

very close to the free surface restricts this optimum configuration to a determined range of filling ratios. If the filling ratio is too large and the liquid is well above the baffles, their beneficial effect is reduced. However, if the liquid height is lower than that of the baffles, then they are not in regular contact and their performance is poor. Moreover, in microgravity scenarios, designs that incorporate free surface baffles could easily cause part of the fluid to get stuck, thereby decreasing the amount of usable fluid. This effect is in addition to the amount of fluid that is already displaced by introducing the baffles.

The use of baffles for sloshing mitigation has the advantage that it can be combined with other compatible passive or active strategies. In light of the sloshing control available with the thermocapillary effect described earlier in this Thesis, the synergy of both mechanisms was analyzed. The results were first introduced in Chapter 8 and later extended with the baffle configurations analyzed in Chapter 9.

Using both strategies together provides an alternative solution to some of the major problems identified for the thermocapillary controllers: large thermal gradients and heating/cooling rates. Baffles, as analyzed in [224], reduce the sloshing amplitude at faster rates but also cause the sloshing frequency to decrease in the baffle configurations considered. Since the asymmetry is directly driven by the sloshing amplitude and the heating/cooling rate is affected by the sloshing frequency, these combined effects would reduce the requirements on the controller. Thus, the synergy between these two sloshing mitigation strategies could be exploited to achieve better performance for fluid systems in microgravity.

There is a clear difference in the scalability of the different approaches considered here. Whereas baffles can be scaled with the container size and are applicable to large-scale structures such as tank ships or launch vehicles, the thermal control does not scale easily to large systems. Even for if the necessary thermal modulations are relatively small, applying a temperature gradient over larger areas implies a proportional increase in the heating/cooling power required. For small-scale systems, with low thermal inertia and thin container walls, the heating/cooling power is feasible. For large-scale systems, which are subjected to greater hydrodynamic loads when sloshing is triggered, the walls must be thicker, and the size of the system implies larger thermal inertia. Consequently, the performance of the thermal controller would be worse, even if the required power is achievable.

We further note that large systems with fixed baffles must withstand cyclical hydrodynamic loads on the baffles that may, over time, lead to their failure. Moreover, as noted in the case of free surface baffles, placing them in a fixed position means that they will function well for a certain range of filling ratios where they can be optimized (shape, placement, orientation, etc.) but their performance will be suboptimal at other filling ratios.

Given these considerations, alternatives can be found in the literature including constrained floating baffles [56] and rigid baffles attached to elastic elements [64, 67] for ground applications. The idea of constrained floating baffles could solve the problem of optimum placement by using the buoyancy force and a passive or active system to adjust the attachment cable; however, in space applications, this is not an option. Despite not fully resolving the problem of optimal baffle placement with variable filling levels, moving baffles are an interesting approach for sloshing suppression due to their analogy with Tuned Mass Dampers (TMDs), which are

widely used in structural engineering applications. By tuning the TMD mass, which is linked with elastic and dissipative elements to the structure of interest, the main resonance can be split and its peak value reduced. Fluids can also be considered in this paradigm instead of rigid masses to construct tuned liquid dampers (TLD). These are particularly relevant since the fluid is used as the damping device. Here, our aim is to reduce the sloshing motion of the liquid using a moving internal element. The baffle motion is constrained in the manner of References [64, 67], by using elastic elements (springs) to attach them to the container.

13.5 Moving baffles in microgravity

As noted earlier, in microgravity there is typically no strong potential force like gravity acting on fluids, although one can be intentionally introduced via spinning, sustained accelerations or magnetic fields, among others. Elastic elements can also be included that, through interaction with the fluid flow, allow sustained exchange of potential and kinetic energy (see Fig. 13.4, striped region). This energy exchange is part of a TMD-like approach for sloshing mitigation: by tuning the elastic constant, a moving baffle is able to mitigate sloshing more efficiently than a fixed one.

For simplicity, we assume the baffle motion in microgravity is associated with a single degree of freedom (DOF), constrained by an elastic element (spring). As a result, the numerical model must include an additional differential equation describing the baffle motion: a momentum balance along a single direction (for a translational DOF) or a torque equation (for a rotational DOF).

The first approach, which was described in Chapter 10, analyses the response of a rectangular container — selected, for the sake of comparison, to be the same as the one in Chapter 3 — subjected to either a pulse-like acceleration or harmonic excitation.

The performance of the system was quantified via two relevant parameters: the asymmetry of the contact points and the kinetic energy. When subjected to a pulse-like load, both magnitudes exhibit a minimum as the spring constant is varied. This minimum corresponds to a substantial improvement compared to analogous fixed baffles, demonstrating the effectiveness of the TMD-like approach. Moreover, this minimum is relatively broad, meaning that uncertainties and tolerances of spring elements are not critical and would not be likely to hinder the performance of the moving baffle in a real application.

In the absence of experimental results, the mechanisms behind the increased damping of sloshing motion in microgravity can be speculated on. These potential mechanisms were described in Chapter 9.

Figure 10.3 shows some of the most relevant features of the liquid flow. A comparison of flow structure between the cases of moving and fixed baffles shows that a large amount of fluid moves along with the baffle almost like a solid body; this also illustrates how the fluid stagnates near the baffle as well as its interference with the sloshing flow and the creation of large areas of viscous dissipation due to velocity gradients. Moreover, the phase lag between the liquid sloshing (or the contact point asymmetry) and the baffle motion can be tuned via the spring constant to achieve optimal results.

A closer look at the results displayed in Fig. 10.3, comparing the unbaffled container and fixed/moving baffle configurations, seems at first to contradict the intuitive effect of a baffle on sloshing frequency. As described in Chapter 9, it was observed that the baffle is essentially an obstacle that causes most streamlines to lengthen and become more complex; the frequency decreases as a result. However, the green curve in Fig. 10.3 indicates the presence of a faster (and lower amplitude) oscillation. In fact, this is exactly the desired effect of using a moving baffle and the working principle of TMDs: a larger peak is split into two smaller peaks whose resonant frequencies are in the vicinity of the former resonance (one is smaller, while the other one is larger). The results displayed in Fig. 10.5 confirm the splitting of the main sloshing peak, which explains the higher frequency observed in the pulse-like response.

The sustained excitation of harmonic loading allows one to more clearly observe the phase lag between the baffle and fluid motion. Eqs. (10.7) or (10.21) could be used as a starting point. Based on Eq. (10.7), we can anticipate that the pressure term is expected to drive the baffle motion when the frequency of the excitation matches that of the first odd sloshing mode. In this equation, for a small baffle mass the spring term on the left hand side would compensate for the pressure term. The pressure differences across the baffle are directly proportional to the fluid momentum along the x axis, that is, $\Delta p \sim \rho u^2$. For sloshing motion, (horizontal) velocity reaches its maximum value when the asymmetry is minimum ($\mathcal{A} \to 0$). Therefore, one would expect the maximum baffle motion (x_b) to occur when the asymmetry changes sign. Consequently, a phase lag of approximately 90° between the asymmetry and the baffle motion can be expected, and this is confirmed by the results of Fig. 10.5. Note that this analysis is mainly valid for small baffle displacements. If the baffle displacement and its derivatives are larger, the balance must account for the additional terms and the phase lag could shift.

More complex geometries also exhibit behavior that reveals an optimum spring stiffness, and this optimum can change significantly depending on the geometry and the specific fluid-structure interactions; it depends on the size of the projected area over in the central region of the container and the viscous effects due to the span of the baffle, etc.

In summary, the microgravity results presented in Chapter 10 assess the effectiveness of the proposed method and confirm that the behavior is analogous to TMDs for this system. The observed trends are very similar to those presented in the work of Wang et al. [67], where an optimum spring stiffness is also found for the fluid configurations considered, although without quantifying the effect of the baffle on the resonance peaks (frequency splitting, for example).

Although this work is motivated by both microgravity [84] and ground [67] results, the greater convenience of ground experiments led us to focus attention on them to further investigate sloshing control with moving baffles. In large fluid systems on ground, the energy diagram shown in Fig. 13.4 would be shifted toward the potential-kinetic energy side, since interfacial energy in large systems such as those described in subsequent sections is almost negligible.

13.6 Moving baffles in ground applications — Numerical and experimental results

	$\frac{L\sqrt{gL}}{\nu}$	$\frac{a_0}{g}$	$\frac{W}{L}$	$\frac{D}{2\sqrt{M_b K}}$	$\frac{\omega_b}{\sqrt{g/L}}$	$\frac{\rho L^3}{M_b}$	$\frac{H_b}{L}$	$\frac{W_b}{L}$
Numerical	$3.13{\cdot}10^6$	0.1	1	0	~ 3.89	74.07	0.25 - 0.5	1
Experiment	$2.29{\cdot}10^5$	0.1	1	0.022	~ 2.08	6.49	0.23	0.97

Table 13.1: The values presented here are calculated using: $K_n = 2000$ N/m, $K_e = 200$ N/m, $M_{b,n} = 13.5$ kg, $M_{b,e} = 0.826$ kg, where the subscript n, e stand for numerical and experimental, respectively. The filling ratio $\mathcal{V}$ and baffle vertical position (H_c) are excluded since these both vary in the experiment and the numerical model. The Bo number, which is $\text{Bo}_n = 140143$ and $\text{Bo}_e = 4292$ is excluded from the table because both values lie in the Bo $\gg 1$ limit so surface tension is negligible.

In order to analyze the performance of moving baffles on ground, we compare the numerical results for a larger (confined) fluid system with a container length of 1 m (Chapter 11) and the experimental results partly addressed in Chapter 12.

Before comparing these two systems, we perform a dimensional analysis of the system presented in Chapter 10. Details of this analysis can be found in Annex A, first for a pulse-like load (Subsection 13.6.1) and then for a harmonic excitation (Subsection 13.6.3).

13.6.1 System response to pulse load

For a pulse-like load, the dimensionless parameters calculated in Tab. 13.1 are comparable except for two parameters: $\frac{L\sqrt{gL}}{\nu}$, which is related to the viscosity term in the Navier-Stokes equation (and whose inverse appears in the momentum equation) and $\frac{\rho L^3}{M_b}$, a term which compares the fluid and baffle masses. The first term satisfies $\frac{L\sqrt{gL}}{\nu} \gg 1$ and is not especially relevant for our analysis (recall that the aim of the moving baffle system is to reduce sloshing more than viscosity alone does). The second term arises from the baffle momentum equation 10.20. This term is one order of magnitude lower for the experimental setup due to the increased mass that is a side effect of using the sliding platform; the baffle itself does not have significant mass but the linear guides do. This quantity multiplies the integral term (see Eqs. A.8).

Although a single order of magnitude may not have a significant impact, this term could affect the dynamics to some degree. When this term is large enough (large containers or small baffle mass; presumably the latter), the pressure term would be balanced by the elastic spring restoring force, with the inertial term being smaller. In both cases (numerical and experimental), the pressure (forcing) term is, at least, one order of magnitude larger than the inertial one.

Overall, based on the dimensionless parameters presented in Table 13.1, a comparison between numerical and experimental results seems feasible, provided that the remaining parameters, $\mathcal{V}$ and H_c/L are similar.

Regarding the experimental results, a pulse-like acceleration is introduced to the system depicted in Figure 7.1b and the system response is assessed. Using the same detection algorithm as with the harmonic loading, the free surface position is determined over the course

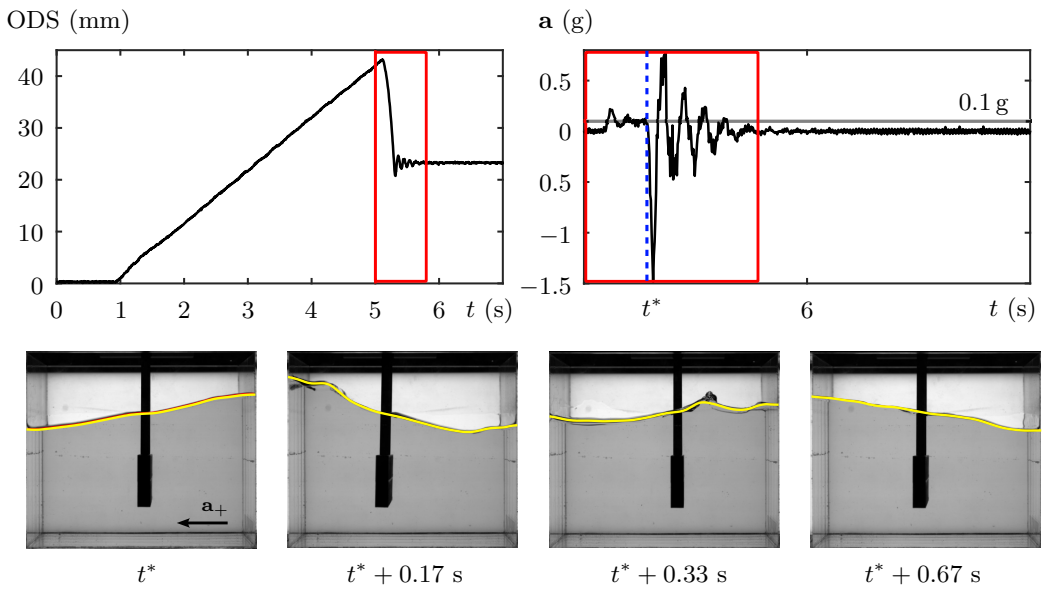


Figure 13.5: (Upper left panel) Optical Displacement Sensor (ODS) signal measuring the SHAKESPEARE [107] displacement during a typical "kick" run. (Upper right panel) Acceleration signal experimentally measured by the accelerometer for the "kick" runs, with the relevant part of the acceleration signal highlighted in red color. The vertical dashed blue line depicts the starting time t^* of the snapshot series. The initial part, prior to the hard stop of the kick signal, corresponds to motion with (ideally) constant acceleration: 0.1 g (see the solid gray line). (Lower panels) Time series showing different instants of the "kick" runs for a moving baffle with $K = 200$ N/m. The $\mathbf{a}_+$ arrow indicates the positive direction of the measured (inertial) acceleration.

of a "kick run". Figure 13.5 shows part of the typical "kick run". First, the SHAKESPEARE table [107] is homed and driven to a position close to the maximum allowed displacement with a (small) constant velocity to prevent any significant motion of the baffle or free surface. Upon reaching this position (see the red rectangle), a constant acceleration is imposed. Two types of sensors are used: an Optical Displacement Sensor (ODS) and an accelerometer. The latter shows an acceleration of approximately 0.1 g (the desired constant acceleration for the pulse-like load to prevent excessive spillage and free surface motion) while the ODS records a parabolic profile of the displacement. Once reaching its final position, the shaking table abruptly stops. This apparently excites some of the natural frequencies of the shaking table and an oscillation of the acceleration signal can be observed that decays to zero.

The inertial forcing initially causes the free surface to tilt as well as inducing baffle motion (when the baffle is allowed to move). Once the table stops, the fluid moves as shown in the lower panels in Fig. 13.5. These panels illustrate the back-and-forth motion of the liquid, as expected for the first odd sloshing mode.

The detected free surface motion is later processed using the Proper Orthogonal Decomposition (POD) method, and the time evolution of the leading mode (the first sloshing mode) is fit to an exponentially decaying function, with a characteristic decay time τ. By doing so, a large amount of "noise" is filtered out such as wave breaking, drop ejection, etc.

The results of these runs considering the effect of the baffle vertical positioning or the container filling ratio on the system response is addressed. The selection of these specific parameters is not arbitrary, but follow the precedent established in the reference studies of Peromingo et al. [224] and Gligor et al. [283].

13.6.2 Baffle height and filling ratio

The vertical positioning of the baffle is relevant, especially its in terms relative position with respect to the free surface. Starting from this premise, four scenarios may arise:

(i) The baffle is submerged and far below the free surface. Given that larger velocities occur near the free surface, this is the reason why the lower baffle (in the 2 baffle configuration) is relatively ineffective for large filling ratios [283].

(ii) The baffle is submerged, but close to the free surface. This scenario is the best one for a targeted optimization of the spring stiffness.

(iii) The baffle is partly submerged, protruding from the free surface. This scenario still produces reasonable fluid-structure interaction, although the the effectiveness of the sloshing mitigation is reduced.

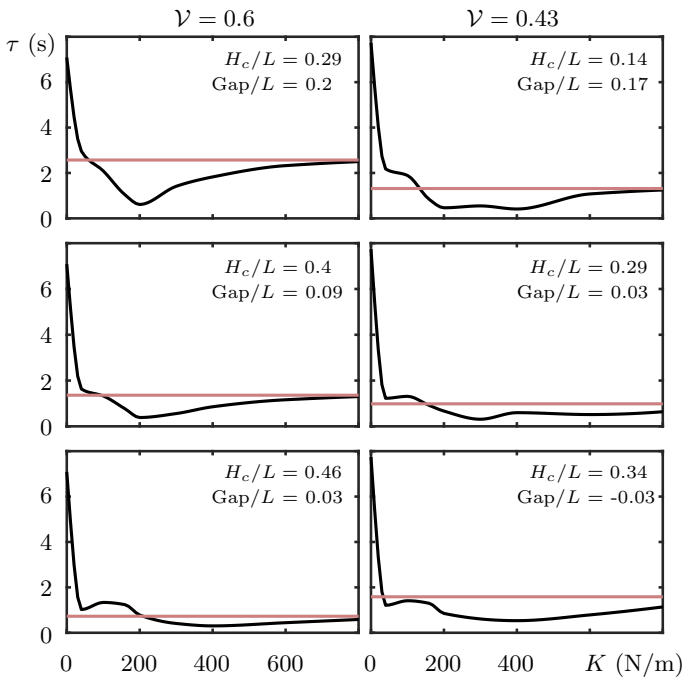
(iv) The baffle is above the free surface and has no effect on the flow.

The transition from scenarios (i) and (iii) is depicted in Fig. 13.6 (a). A decreasing gap between the baffle and free surface increases the fluid loading on the moving (or fixed structure) and, thus, a larger spring constant is needed to maintain the performance enhancement compared to the fixed baffle counterpart. The results for the lower filling ratio $\mathcal{V} = 0.43$, on the other hand, suggest that this improved behavior is only sustained as long as the baffle is fully submerged. The last panel ($H_c/L = 0.34$, Gap/L = -0.03) reveals a decline in performance for both fixed and moving baffles due to the lower interaction. Analogously, if the vertical position of the baffle is fixed, reducing the filling ratio reduces the gap and leads to similar behavior.

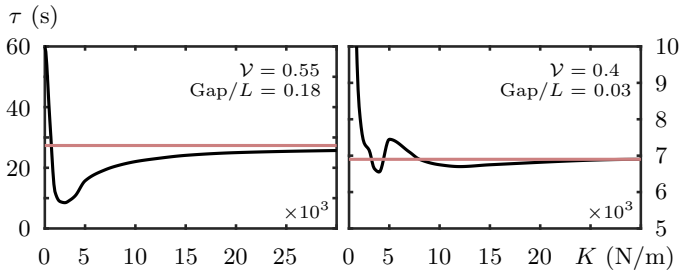
The numerical results in Fig. 13.6, (b) (extracted from Chapter 11, Section 11.5) show analogous trends despite small differences in the non-dimensional parameters, which further supports the previous statements related to dimensional analysis.

Thus, both numerical and experimental results for moving baffles on ground confirm the existence of an optimum stiffness value that yields the minimum decay time. Moreover, these results are in agreement as to the trend of this optimum: for a fixed baffle position and increasing filling ratios $\mathcal{V}$, the baffle interaction grows along with the height of the liquid layer. Hence, the baffle is subject to larger hydrodynamic forces and the spring constant must be larger to more effectively oppose the sloshing motion; otherwise, the baffle moves together (in phase) with the sloshing flow. This trend highlights the fact that, with a single moving baffle, a there is no universal constant for optimum performance and any potential application will have an associated range of operational scenarios where the baffle movement is beneficial.

The limitation on the feasibility of such a system cannot be overcome unless a different approach is considered. The idea explored numerically consisted of the use of two baffles, one



(a) $H_b/L = 0.23$



(b) $H_b/L = 0.25$, $H_c/L = 0.25$

Figure 13.6: (a) Experimental: Decay time τ as a function of spring stiffness with the setup depicted in 12.1 for two filling ratios, $\mathcal{V} = 0.6$ and $\mathcal{V} = 0.43$ with $H_b/L = 0.23$, and different baffle heights. Each panel displays the decay time for a specific filling ratio and baffle height combination (solid black line) and the decay time for a fixed baffle (solid red line) corresponding to $K \to \infty$. Here, the "Gap" is calculated as $H_l - (H_c + H_b/2)$. (b) Numerical [283]: Decay time τ with the two-baffle setup described in Chapter 11, Section 11.5. Results are consistent with the references [84, 283].

optimized for larger filling ratios and another for lower filling ratios.

The results presented in Chapter 11 shed light on this approach and show considerable improvement in the overall performance, as demonstrated by Fig. 11.11. Moreover, the introduction of slots to enable some fluid transfer between the container halves proves to be beneficial in suppressing U-shaped container sloshing modes (up-and-down motion instead of back-and-forth). Alternatively, one could think about using porous baffles instead of additional perforations. This, however, is not addressed in reference [283] and could be a potential option for future research.

The moving baffles achieve a performance enhancement for all operational scenarios regardless of the filling ratio when subjected to loads similar to a pulse-like load introduced in the first part of the work. This may correspond to accelerating or braking of tank trucks or the impact of waves on tanker ships. However, fluids can also be subjected to harmonic loads that simultaneously excite different harmonics. Although one could obtain a characteristic power spectrum for random vibration (e.g., for ground transportation), we instead perform a frequency sweep for the optimum baffle configuration and obtain the amplitude response of the fluid motion.

13.6.3 System response to harmonic loading

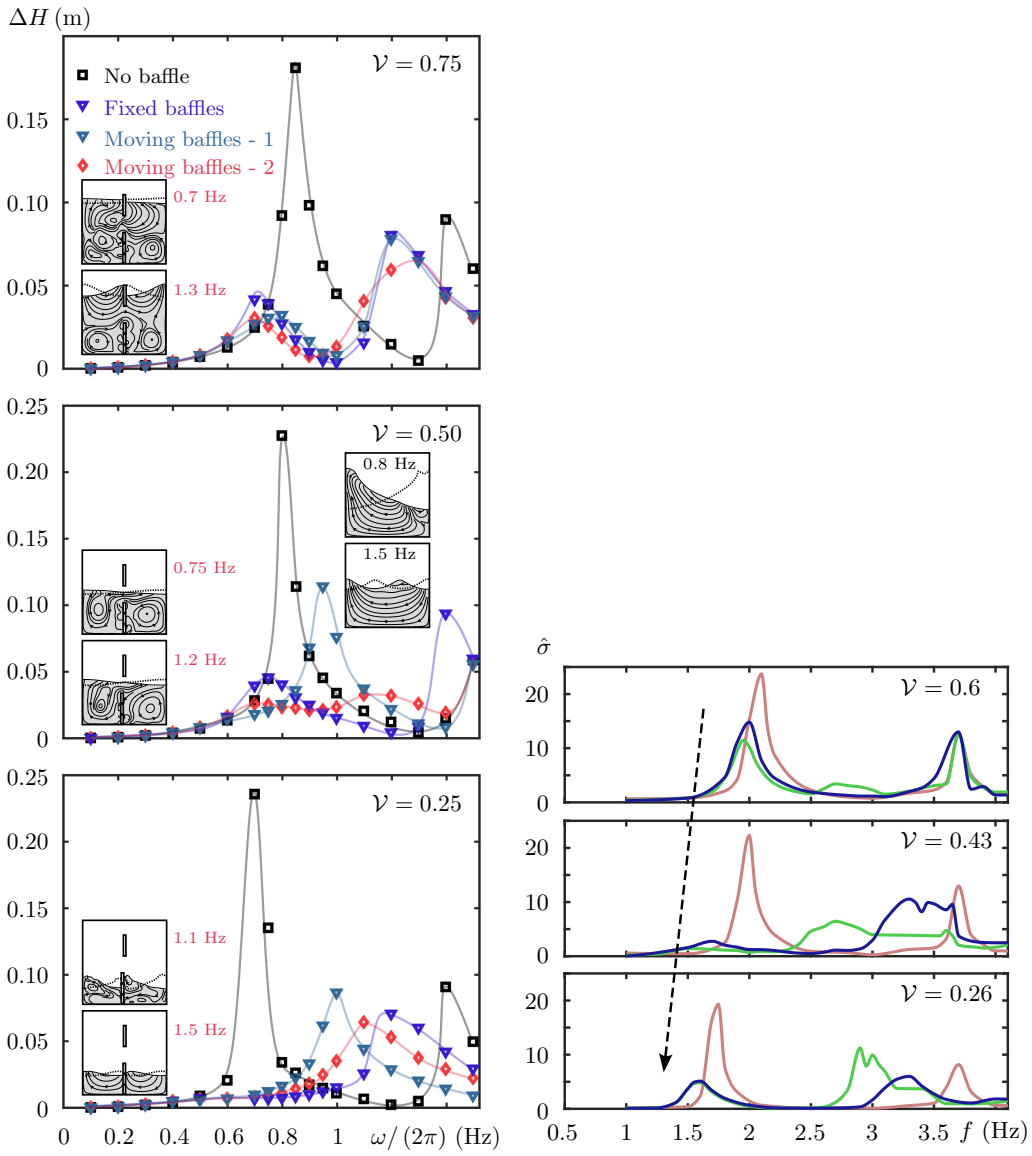
Following the dimensional analysis detailed in Annex A and substituting the relevant parameters, we can again be confident that the numerical and experimental results can be compared.

Figure 13.7 (a) shows the frequency response in terms of the amplitude of the right contact point oscillations for the unbaffled container and the final baffle configuration as detailed in Chapter 11. The baffle motion is fixed or constrained by springs with two sets of spring constants: the optimum one for the pulse-like acceleration and a modification of this one. Figure 13.7 (b), on the other hand, presents the experimental results obtained for the setup described in Chapter 12, also with the unbaffled container and a single fixed or moving baffle. In the latter case, the spring constant is $K = 300$ N/m.

The numerical and experimental results in the analyzed frequency range show TMD-like behaviour, similar to the case of microgravity [84]. Of particular relevance is the comparison between the numerical results for $\mathcal{V} = 0.5,\ 0.25$ and all the filling ratios of the experimental ones, where the same trends are observed. As the stiffness is increased (the limit $K \longrightarrow 0$ is assumed to represent the unbaffled case) towards the fixed baffle case, the primary peak splits. The first peak always has a lower amplitude (even for the fixed baffle case), while the second moves to larger frequencies.

The bottom panel of the experimental results, with $\mathcal{V} = 0.26$, are particularly interesting from an engineering point of view since the spring stiffness is not optimum for decreasing filling ratios (it was selected to achieve optimum behavior for $\mathcal{V} = 0.6$; see Chapter 12). Despite its suboptimal behavior, the system still performs better than the unbaffled case. A practical application involving decreasing liquid levels over time should account for this effect to ensure that no harmful resonances are introduced for a filling ratio different from the one used for the tuning process.

Regarding this secondary peak, Fig. 12.4 (I) shows the frequency of the moving baffle alone (i.e., without being submerged in liquid). This frequency was obtained by fitting experimental data to a second order system with viscous damping, although it can also be well approximated as $\omega_b = \sqrt{K/M_b}$. A closer look at this figure reveals that the peaks in Fig. 12.2 (II) do not perfectly match even though these peaks are resonances of the moving baffle motion — see panel (II) in Fig. 12.3. The numerical results in Fig. 13.7 (a) also suggest a similar trend: the natural frequency of the lower baffle is $f_{m,1} = \sqrt{4000/18.63}/(2\pi) = 2.33$ Hz and



(a) Lower baffle: $H_c/L = 0.19$, $H_b/L = 0.365$ **(b)** $H_c/L = 0.29$, $H_b/L = 0.23$

Figure 13.7: (a - Numerical) Frequency analysis showing the right contact point oscillation amplitude ΔH as a function of $\omega/(2\pi)$ for $\mathcal{V} = 0.75$, 0.50 and 0.25. Results are included for the unbaffled container (black) and in the two-baffle two-slots configuration, both fixed (blue) and moving with spring stiffnesses: $(K_1, K_2) = (15000, 4000)$ N/m for moving baffles - 1 (indigo), and (10000, 8000) N/m for moving baffles - 2 (red). Adapted from [283], Chapter 11. (b - Experimental) Nondimensional amplitude $\hat{\sigma} = \sigma/A$ for varying forcing frequency (see Chapter 12 for details on the notation). The different line colorings correspond to three configurations: unbaffled (red), moving baffle with $K = 300$ N/m (green) and fixed baffle (blue). The (dashed) trend line shows the frequency shift of the first sloshing mode with decreasing filling ratios [see Eq. (11.18)] for clean tanks. The first sloshing mode frequencies are 2.1, 2 and 1.75 Hz for $\mathcal{V} = 0.6$, 0.43 and 0.26, respectively. These values are in good agreement with the frequencies predicted by the dispersion relation: 2.06, 1.97 and 1.73 Hz.

$f_{m,2} = \sqrt{8000/18.63}/(2\pi) = 3.29$ Hz, with 1 and 2 denoting the moving baffles - 1 and 2 as in the figure notation. Both frequencies are larger than the frequencies corresponding to the secondary peaks.

An explanation for this effect was already suggested in Chapter 10, with a rough estimate of the optimum spring stiffness made by considering not just the baffle mass, but also the extra fluid mass; see Eq. (11.20). Of course, it is not so simple because the baffle does not move the whole fluid mass. However, a region in the vicinity of the baffle with unknown span may be effectively considered to be "rigidly" attached to the baffle and this causes the natural frequency to decrease. Confirmation is provided by the experimental velocimetry results.

The second odd sloshing mode, whose excitation frequency is approximately 3.6 Hz in the experimental setup, remains largely unaffected by the baffle unless the filling ratio is decreased (that is, the gap between baffle and free surface reduces). One may speculate on whether the moving baffle would alter the amplitude diagram for large filling ratios if properly tuned, but this would mean increasing the spring stiffness and worsening the system performance for the first sloshing mode and was not considered here.

The experimental results provided by the velocimetry confirm the suspected phenomena driving the increased damping of sloshing modes, as detailed in Chapter 9. Furthermore, the information provided by these results can be helpful to understand the formation of recirculation zones and the beneficial effect of slotted baffles.

13.6.4 Moving baffles - velocity fields

Prior to introducing the velocimetry results, we note that the images below do not show the interface at exactly the correct height — 105 mm for a filling ratio $\mathcal{V} = 0.6$, with $H_l = 105$ mm. The reason for this is the partial removal from the FOV of a small region (~ 3 mm) close to the lower container boundary to eliminate unwanted reflections.

In the unbaffled case, we can observe the main features of the first and second sloshing modes: a wavelength of $\lambda_1 = 2L$, $\lambda_2 = 2L/3$, with L being the container length (here, $L = 175$ mm). The snapshot times labeled (I,II) in Fig. 2.6 have been selected so that the velocity is as close as possible to its maximum value. The experimentally determined velocity fields are consistent with the analytical solutions of the inviscid sloshing problem for rectangular containers [40]. Note the relatively mild decay of the velocity magnitude with container depth for the first mode, while the decay is significantly faster for the second mode. These results strengthen the idea that subsequent sloshing modes would benefit from baffles located closer to the free surface.

The velocity fields with a moving baffle configuration as in Chapter 12 were presented in Fig. 2.7 for $K = 200$ N/m and the two frequencies corresponding to the split resonance peaks, as depicted in Fig. 12.2 (green markers). The panels labeled with (I) show some of the features already mentioned in Chapters 9—11: the baffle intersects the (previous) streamlines, which causes them to deviate along the external surface of the baffle. This results in a region where the fluid largely moves along with the baffle (i.e., analogous to a rigid body). In Chapter 10 it was speculated that the fluid contained within a circular region centered on the baffle with

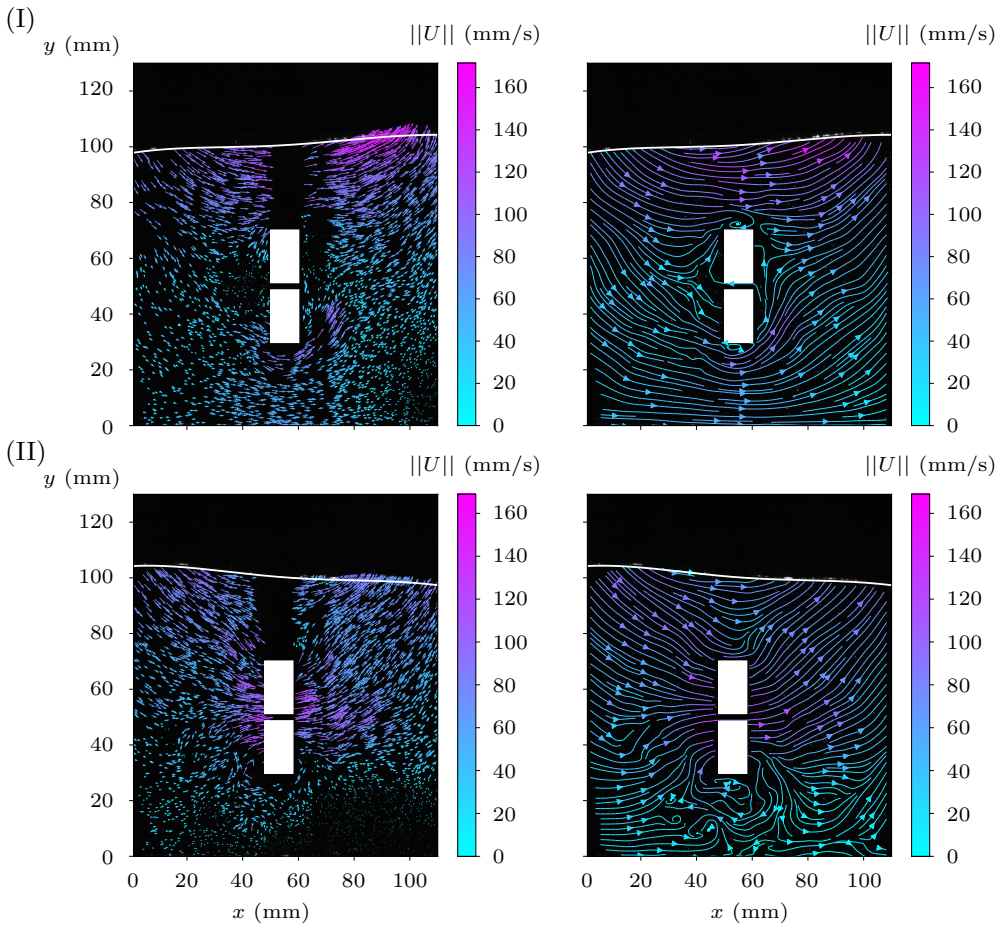


Figure 13.8: (Left) Results of PTV detection using TracTrac [110] for the translational moving baffle, with a centered slot of 2.5 mm; the baffle height is 40 mm including the slot. (Right) Post-processed data showing the streamline. Results correspond to the container with a (translational) moving baffle with $K = 200$ N/m and (I) $A = 1$ mm, $f = 1.95$ Hz, (II) $A = 1$ mm, $f = 2.3$ Hz.

radius $R = H_b/2$ would provide a good approximation to this rigid mass and could be used to estimate the optimum stiffness of the fluid-baffle system. This simple approach, which ignores the more complex interactions that are present, seems to work reasonably well. Considering the parameters of the experimental setup (container and baffle dimensions, moving baffle mass, fluid density, etc.) and including the fluid mass for the calculations, we obtain the natural frequencies of $f = 2.2$ Hz and $f = 2.69$ Hz for $K = 200$ N/m and $K = 300$ N/m , respectively. These values match the locations of the secondary peaks quite well.

The accuracy of this approach, however, is likely to depend on the sloshing mode. For the first sloshing mode, for example, the "amount" of fluid drawn along with the baffle can be reasonably approximated by a circle (or a cylinder in 3D). However, one might expect that subsequent modes would need to account for a smaller "fluid mass" since the velocity field is more concentrated in the vicinity of the free surface.

The panels (II) corresponding to the secondary frequency peak (after splitting) reveal different

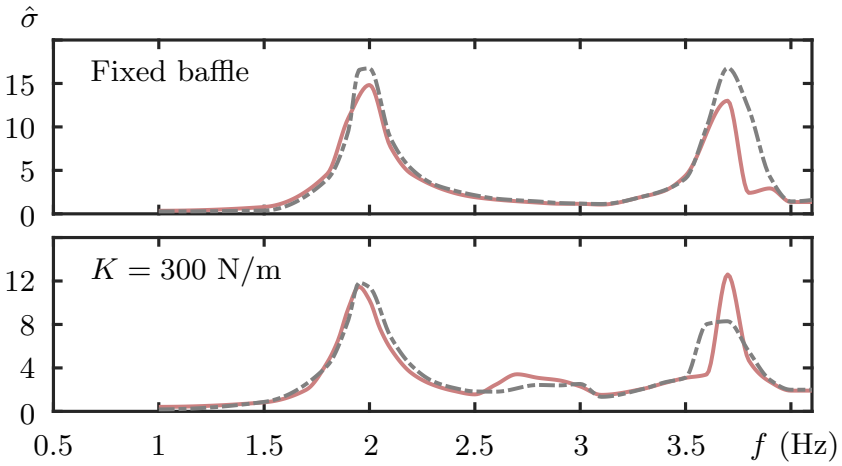


Figure 13.9: Nondimensional amplitude $\hat{\sigma} = \sigma/A$ for varying forcing frequency. The different colors correspond to a filling ratio $\mathcal{V} = 0.6$ with a solid baffle (solid red line) and a slotted baffle (dashed gray line). (Upper panel) Effect of a slot on sloshing amplitude for the container with a fixed baffle. (Lower panel) Effect of a slot on sloshing amplitude for the container with a moving baffle, $K = 300$ N/m.

characteristics. The velocities in the vicinity of the baffle are larger than those closer to the free surface, which suggests that the baffle is acting as a wavemaker. Increasing the spring stiffness K moves the secondary peak to higher frequencies. At the same time, as the stiffness increases the displacement is smaller and the effectiveness of the baffle as a wavemaker is reduced (see Fig. 12.2).

The geometric effect of a 2.5 mm centered slot on the same baffle configuration with two filling ratios is analyzed. Although reducing the pressure differences across the baffle may have a slight deleterious effect (see Figures 13.9 and 13.10 for $\mathcal{V} = 0.6,\ 0.43$, moving baffle), this can be mitigated by the formation of recirculation zones. A comparison of figures 2.7 and 13.8 reveals almost identical velocity fields. An extended time series of the velocity field (not included in Fig. 13.8) would allow one to see small-scale "jets" due to the pressure differences between the baffle surfaces. These jets have a limited reach, although they may contribute to the dissipation mechanisms. We note that the jets are not completely two-dimensional and due to the particles leaving the illuminated laser sheet, they are sometimes "missed" by the tracking algorithm [110].

The effect of this slot is assessed for two filling ratios and compared to the solid baffle, both in a fixed and moving configuration ($K = 300$ N/m). As shown by figures 13.9 and 13.10, the slot hampers sloshing mitigation in the vicinity of the first resonance for both fixed and moving baffles, regardless of the filling ratio. Such behavior is consistent with reduced fluid-baffle coupling. Furthermore, it is precisely this decreasing liquid-baffle interaction that leads to lower amplitude of the secondary peaks emerging from the splitting (i.e., the peaks associated with the resonance of the moving spring-baffle system, where the baffle acts as a wavemaker driving the sloshing motion). The second sloshing mode does not exhibit a clear behavioral trend.

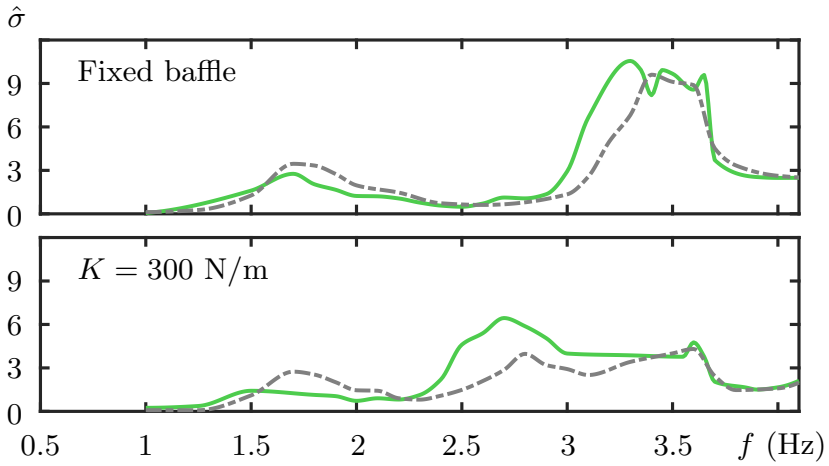


Figure 13.10: Nondimensional amplitude $\hat{\sigma} = \sigma/A$ for varying forcing frequency. The different colors correspond to a filling ratio $\mathcal{V} = 0.43$ with a solid baffle (solid red line) and a slotted baffle (dashed gray line). (Upper panel) Effect of a slot on the sloshing amplitude for the container with a fixed baffle. (Lower panel) Effect of a slot on the sloshing amplitude for the container with a moving baffle, $K = 300$ N/m.

The results on the kick load and frequency response of moving baffle systems demonstrate the enhanced performance of these configurations when compared to their fixed counterparts. Overall, Chapters 11 and 12 show the inherent complexity of finding an optimum value (and baffle configuration) to enhance sloshing reduction. However, based on the behaviour of TMDs, we observe that the moving baffle system, if properly tuned, cannot effectively handle the mitigation of two sloshing modes (at least, with the present experimental setup). This problem is similar to the effect of decreasing filling ratios: a single baffle tuned for a given filling ratio cannot mitigate sloshing for all potential operating scenarios. Instead, an additional baffle can be introduced and tuned. Following the same logic, a solution to this potential problem could be found by thinking of multiple baffles as multiple degrees of freedom. One could consider introducing a supplemental DOF to the translational baffle setup [106] and tuning it to achieve enhanced performance over several sloshing modes.

13.7 Moving baffles in ground applications: two degrees of freedom

The mechanical complexity of the setup can be greatly increased if an additional baffle is introduced: the mechanical limitations of the experimental setup (limited available space, mainly) make it difficult to add more moving elements. Therefore, the simplest alternative would be to modify the current setup to introduce, for example, a rotational degree of freedom along with the translational one. To compare the combined performance, we introduce a system that can rotate; if desired, it also allows the translational DOF.

The modified experimental setup is depicted in Fig. 13.11, which includes the moving platform capable of introducing translational motion when desired. Otherwise, the platform can be

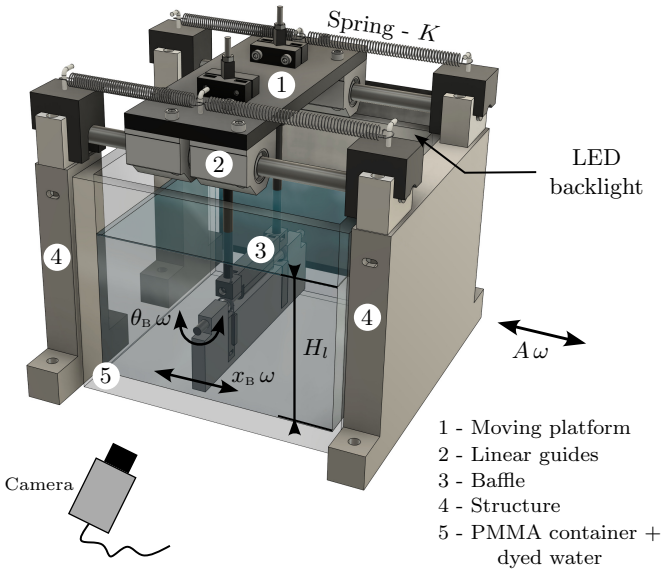


Figure 13.11: Sketch of the 2-DOF experimental setup: a moving platform (1) is bolted to four linear guides (2) that slide over two steel shafts that are clamped to the main structure (4); the baffle (3) is submerged using two rigid beams to ensure its correct position. The transparent PMMA container (5) holds dyed water. The rotational DOF is allowed by the rotation of the baffle around a shaft, constrained by two rotational springs placed next to the supporting beams.

constrained to restrict this DOF. We note some differences compared to the original setup: the moving baffle rotates around a shaft, which is attached to an adapter that slightly increases the effective length. We note that the only rotating part is the baffle, whose height has been preserved ($H_b/L = 0.23$). The baffle is vertically placed so that the center position $H_c/L = 0.29$, similar to the purely translational case. By doing so, we aim to obtain a system whose response can be compared to the translational DOF baffle despite the shaft and adapter piece. The flexibility of this experimental setup is a major advantage considering the adaptability of these moving baffles that would be required to widen their appeal in engineering applications.

As in the translational case, varying the spring constant produces a splitting of the main sloshing resonance, as evidenced in Fig. 13.12. The second sloshing mode, on the other hand, remains relatively unaffected by presence of the baffle. Despite the central region (adapter), which acts as a small fixed baffle, and the proximity to the free surface, there is no mitigation effect; experimental results show only a small frequency shift and, more importantly, a detrimental widening of the peak.

A PTV analysis of the torsional baffle is presented in Fig. 13.13. The velocity field shows an interaction of the first sloshing mode with the baffle rotational motion, displaying a V-shaped velocity profile. This profile is not unexpected, since the combination of sloshing flow and baffle motion (rotation around its shaft) could yield such a pattern of streamlines. With regard to this figure, we note that the shadowing from the baffle rotation causes a considerable loss of PTV capabilities over a larger area than for the translating baffle. We therefore

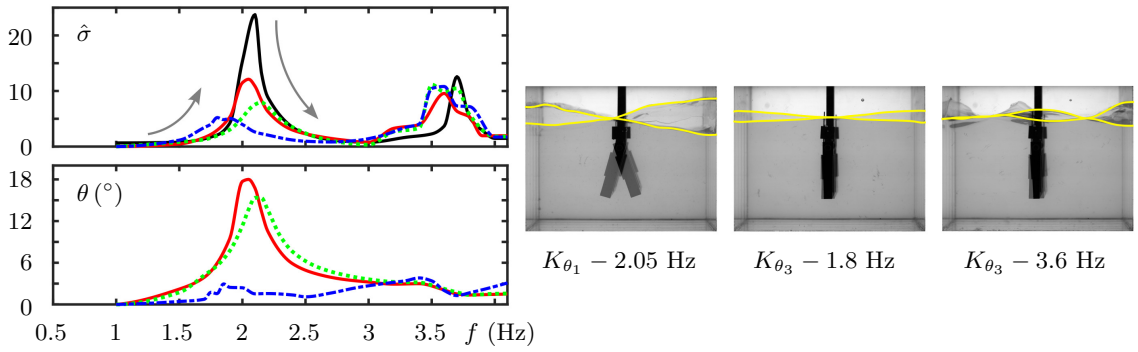


Figure 13.12: (Left, upper panel) Nondimensional amplitude $\hat{\sigma} = \sigma/A$ for unbaffled (solid black line, reference) and three rotating baffle configurations with $K_{\theta_{1-3}} = 23.464$ (solid red), 44.95 (dotted green) and 71.94 (dashed blue) N mm fixed baffle configurations (red). The gray arrows depict a transition of the main resonance peak analogous to those experimentally observed in Fig. 12.2 for linear springs (constraining translational displacement) and numerically, both in microgravity Fig. 10.5 and ground applications Fig. 11.17. (Left, lower panel) Baffle rotation amplitude (in degrees) as a function of the forcing frequency for different spring stiffness values. The right panels show the detected free surface position in two superposed snapshots, delayed in time by half the forcing excitation period, for the lowest and largest spring stiffness values.

rely on interpolation of the velocity field in these regions, which increases the experimental uncertainty.

The next step was introducing 2 degrees of freedom as a means to control both sloshing modes and improve the overall system performance over the full frequency range. To this end, several combinations of torsional and linear springs were tested, motivated by the separate results for each DOF. The results are depicted in Fig. 13.14, where the nondimensional amplitude of the free surface motion, the baffle rotation amplitude and the nondimensional linear displacement are presented for three combinations of torsional and linear springs. Compared to figures 12.2 and 13.12, the most noticeable feature is the strong mitigation of the second sloshing mode for all cases.

Although these results are promising, the mitigation cannot be exclusively attributed to the 2-DOF moving baffle. As noted earlier, the moving part of the baffle retains the original dimensions of the setup (i.e., $H_b = 40$ mm). However, in order to mechanically adapt the design to the various torsional springs, a supporting structure was designed that consisted of a PLA part spanning 96 mm (out of 175 mm) of the container width and 12 mm of the container height. This setup leaves a gap of approximately 8 mm to the free surface (Gap/L = 0.05). An analogy can be drawn between this case and the translational baffle at a fixed height for lower filling ratios; see the results in Fig. 13.10 for the moving baffle. Given that $\mathcal{V} = 0.43$ and $H_c/L = 0.29$, the gap left between the baffle and the free surface is 5 mm (Gap/L = 0.03). In this case, even though the stiffness is not tuned for the second sloshing mode, we observe a large reduction in its amplitude, which is consistent with the proximity of the moving baffle to the free surface. Similarly, for the 2-DOF baffle, proximity to the free surface is expected to be partly responsible for reducing the second mode, albeit to a lesser

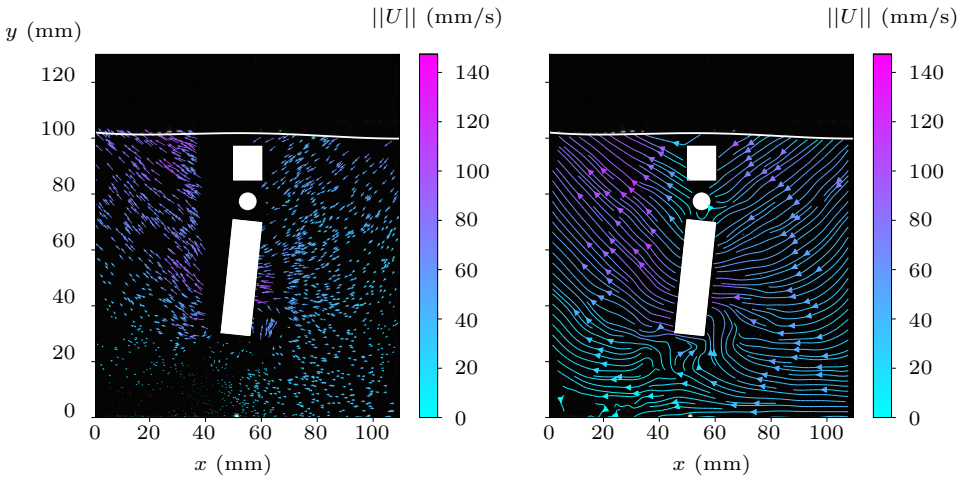


Figure 13.13: (Left) PTV detection results using TracTrac [110] for the rotational moving baffle. (Right) Post-processed data showing the streamlines. The results correspond to the container with a (rotational) moving baffle with $K_\theta = 44.95$ N mm, excited with $A = 1$ mm and $f = 2.1$ Hz.

extent because of the reduced span.

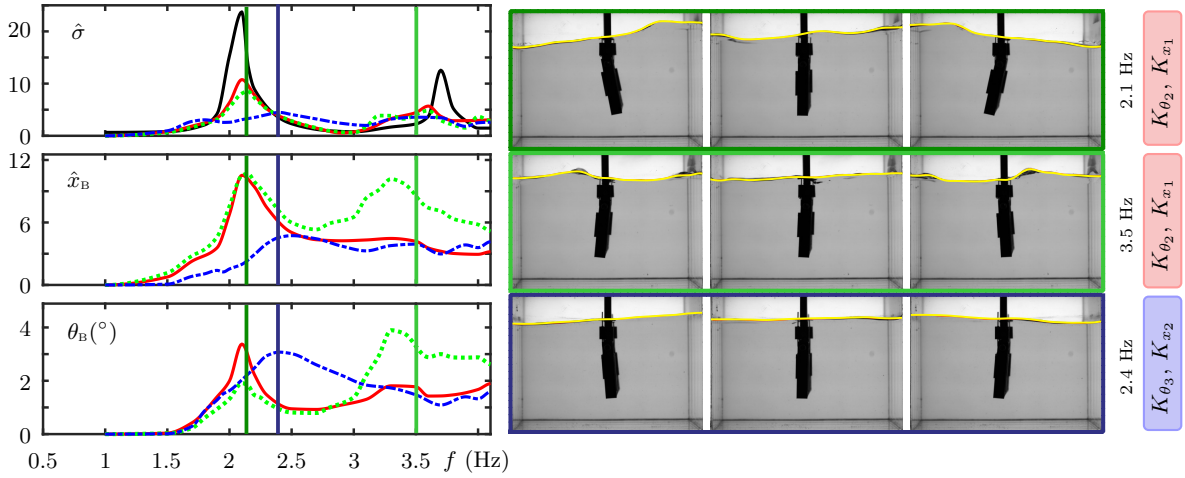


Figure 13.14: (Left three panels) Nondimensional amplitude $\hat{\sigma} = \sigma/A$, baffle rotation amplitude (in degrees) and nondimensional linear displacement for: unbaffled (solid black line, reference) and three translational-rotational baffle configurations with $[K_{\theta_2}, K_{x_1}] = [44.95\,\text{N mm}, 200\,\text{N/m}]$ (solid red), $[K_{\theta_2}, K_{x_2}] = [44.95\,\text{N mm}, 300\,\text{N/m}]$ (dotted green) and $[K_{\theta_3}, K_{x_2}] = [71.94\,\text{N mm}, 300\,\text{N/m}]$ (dashed blue) N mm. Vertical lines mark the frequencies depicted in the snapshots. (Right three panels) Snapshots showing interface and baffle position (rotation + translation) for the labeled configurations.

Consistent with the single DOF approach, Fig. 13.14 shows the expected resonance splitting. We note that the selected spring constant combinations are based on the optimal results for the standalone systems, and avoid excessive stiffness of any spring. Conversely, if one spring

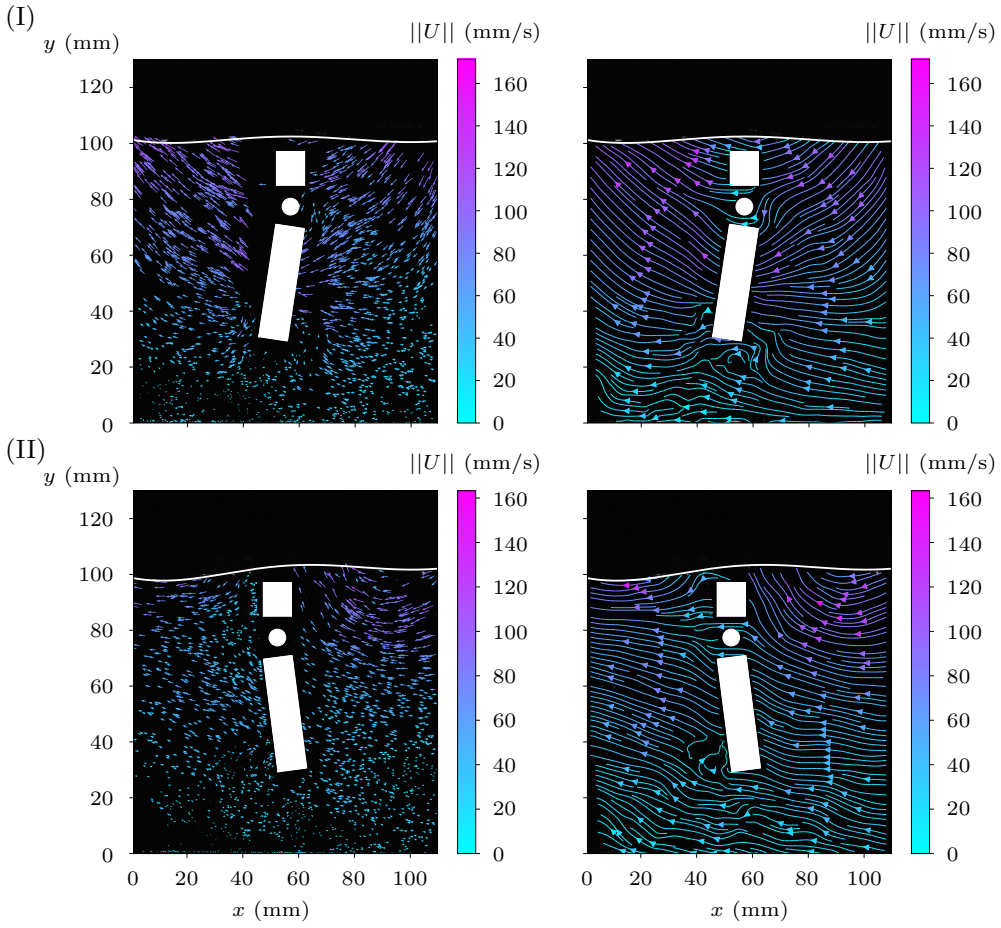


Figure 13.15: (Left) PTV detection results using TracTrac [110] for the translational-rotational moving baffle. (Right) Postprocessed data showing the streamlines. Results correspond to a (translational) moving baffle with $K_\theta = 44.95$ N mm and $K_x = 300$ N/m with (I) $A = 1$ mm, $f = 2.1$ Hz and (II) $A = 1$ mm, $f = 3.6$ Hz.

constant is too low, then that DOF absorbs a large part of the forces exerted by the fluid flow, which leads to worse performance for the other DOF. Both spring constants should be carefully tuned to achieve the optimal sloshing reduction.

The results for the first $[K_\theta, K_x]$ pair (solid red line) show that the moving baffle already provides a reasonable sloshing reduction. If we increase the linear spring constant (dotted green line), a larger secondary peak emerges at $f \approx 3.3$ Hz in both the baffle rotation θ_B and displacement $\hat{x}_B$ curves. The prominence of these peaks points to a resonance of the moving baffle. The phase lag between the baffle rotation and translation is 151°: one can understand this mode as driven by the translational motion with the baffle rotating "effortlessly" in response to the advancing and receding motions.

An increase of the torsional spring (dashed blue line) ($K_{\theta_2} \to K_{\theta_3}$) notably reduces the baffle rotation while also shifting the main resonance to $f \approx 2.4$ Hz. The phase lag here is 32°, which is closer to being in phase. In this scenario, the linear and rotational motions can be

thought of as largely “constructive”, which yields larger fluid velocities near the baffle.

To provide more insight into the bulk flow, PTV is performed for a particular case of the 2-DOF baffle. The results presented in Fig. 13.15 also exhibit a “V-shaped” velocity profile in the vicinity of the first resonance and a highly directional velocity field within the fluid bulk, likely due to the motion induced by the baffle.

Chapter 14

Conclusions and future work

This Thesis presented a comprehensive numerical and experimental investigation of sloshing motion and control mechanisms. Sloshing motion is associated with the development of hydrodynamic forces that may grow very large and alter the dynamics and control of a transport vehicle or lead to structural integrity failure, among other effects. Liquid sloshing is a known phenomenon affecting fluid management in ground applications. In the absence of gravity, this problem is of keen interest since it directly affects the attitude of space vehicles, becoming a critical concern in space exploration.

We first investigated Marangoni flows and their interactions with the motion of a free surface in Chapter 3. Marangoni flows were shown — as theoretically demonstrate by the seminal work of Sen and Davis [35] — to induce motion of the free surface when subjected to both steady and oscillatory thermal gradients. Asymmetric thermal gradients in rectangular geometries (i.e., heating one side while cooling the other) are able to excite odd sloshing modes. The largest resonance is the one corresponding to the first odd sloshing mode [178] with a wavelength that is twice the container length $\lambda = 2L$. These results point to the potential of the thermocapillary effect to be used in sloshing control applications, particularly for small-scale systems in microgravity. A sloshing control system is proposed based on implementing a PID controller that converts an externally measured asymmetry (e.g., using optical diagnosis) into a thermal modulation applied to the fluid container.

Chapter 4 [201] further investigated this topic. The performance of a thermocapillary-based PID controller is assessed and optimized, accounting for a cost function and the system decay time, obtained when the fluid system is perturbed with a kick-type load. An optimum set of proportional and derivative constants (K_P, K_D) can be obtained from this optimization procedure and tested with real microgravity perturbations by introducing the accelerations measured aboard the ISS during a reboosting maneuver to the numerical model. For small-scale systems, the thermocapillary controller is found to greatly enhance sloshing mitigation compared to an uncontrolled response. The preliminary results are encouraging for the development of microgravity applications oriented towards enhancing the efficiency of fluid management in capillary systems or in line with current research to develop PMDs for CubeSats, for example (see the recent work of Hart et al. [47] and references therein). With this setup, repositioning a fluid interface with Marangoni flows would involve using a power

supply to provide the system with a driving force that overcomes surface tension and contact forces.

The study conducted in rectangular geometries revealed the strong influence of (and limitation due to) minimum surface energy constraints: for given contact properties, there is typically a unique free surface position corresponding to minimum energy. The equilibrium is clearly defined, and any perturbation must overcome a restoring force to induce free surface motion or a rearrangement of the fluid configuration. With two-dimensional geometries, this limitation can be overcome by using circular geometry, since rotational symmetry with respect to the central axis implies an infinite number of equivalent minimum-energy configurations.

The work presented in Chapter 5 [220] introduces the numerical analysis carried out in circular geometries. Here, the ability of a fixed thermal gradient to reorient a fluid interface is confirmed by numerical analysis. For a constant temperature difference applied in the horizontal direction, the free surface reorients itself perpendicular to the applied gradient, which is similar to the effect of vibrations on fluid interfaces [9, 120, 144, 145]. Larger thermal gradients lead to a notable decrease in the amount of time required for the free surface to achieve this perpendicular orientation, indicating an inverse relationship. Furthermore, the introduction of supplemental vibrations enhances the performance of this repositioning, further reducing transition times and exerting a stabilizing effect.

Based on these numerical results, a potential microgravity experiment concept, *ThermoSlosh*, was described: a cylindrical aluminum cell half filled with silicone oil (or another working fluid) whose temperature can be controlled through Peltier elements located on four external sides of the aluminum cell and, also, with the ability to excite vibrations in a single direction. The execution of such an experiment would encompass an experimental study of the effect of steady and low-frequency thermal forcing, including the combined effect of thermal excitation and vibrations, and evaluating the ability of the thermocapillary effect to control and reposition fluids in microgravity.

An extension of this analysis was developed in Chapter 6 [233], where the effect of different working fluids was considered, as well as the contact angle (static and dynamic). The latter property is particularly relevant: Hydrophilic contact conditions lead to quantitatively enhanced behavior and system responsiveness. Another very relevant result of this work is related to the interface positioning capability of Marangoni flows when including feedback control (e.g., PID). A proper optimization of the controller constants, similar to that done in rectangular geometries, allows one to design a system capable of achieving any desired orientation by inducing small thermal modulations.

For more practical applications, it may be appropriate to have predefined stable configurations in case the driving force is no longer available, so that the fluid naturally returns to a desired equilibrium position. As introduced in Chapter 7 [291], this can be achieved with an elliptical container, which has two minimum surface energy positions. With a fixed thermal gradient, a pitchfork bifurcation is observed in the orientation of the free surface as a function of δ (a measure of eccentricity), along with a secondary transition to the symmetric branch. This pitchfork bifurcation is highly dependent on the applied thermal gradient and contact properties, as shown in previous publications [178, 201].

Overall, numerical analysis of the proposed sloshing control confirms the potential of Marangoni flows for fluid management purposes. However, this strategy cannot deal with large inertial or sustained forcing. Considering the results with both rectangular and circular geometries in the presence of a microgravity perturbation, we observe that Marangoni flows are not able to fully handle such situations on their own. This is understandable since the fluid motion induced by inertial forcing occurs throughout the fluid, whereas Marangoni flow is concentrated near the free surface (or fluid interface) and requires a certain amount of time to spread over the full length of the container. The velocity penetrates into the fluid bulk via viscosity, but Marangoni flows are in some sense weaker.

These results show the need for additional mechanisms other than thermocapillary-based controllers to achieve good performance in many applications. Such a mechanism must interact with the fluid flow when stronger inertial forcing is present. This problem is solved in subsequent numerical studies through the use of passive baffles.

Passive baffles are widely used in fluid management, both on ground and in microgravity applications. Sloshing mitigation is one of their key functions. The extensive analysis carried out in Chapter 9 [224] highlights the importance of baffle geometry and placement for the sloshing response of the system. The findings within this study shed light on the underlying mechanisms for the sloshing mitigation effect of baffles, which can be grouped into four key effects: intersection with the (unobstructed) sloshing flow, increased viscous dissipation, the stagnation of fluid around the baffle, and modification of the container geometry. Together, these effects explain the superior performance of certain baffles. For example, vertical baffles placed in the middle of the container or horizontal-type baffles protruding through the endwalls close to the free surface interact with large flow velocities. This interaction leads to the development of flow bottlenecks in some regions that, in turn, increase spatial velocity gradients and viscous dissipation. Depending on the baffle geometry, the container may be effectively split (vertically or horizontally) and the baffle creates stagnant fluid in the middle of the container or closer to the free surface, thus reducing its mobility. All of these effects also cause a decrease in the sloshing frequency compared to the unbaffled case. The study is completed with the use of a PID thermocapillary control, as also considered in Chapter 8 [225]. The synergy between the thermocapillary control and the effect of the baffles can lead to enhanced performance.

Among the sloshing mitigation mechanisms reported in Chapter 9 [224], we highlight the baffle interaction with the fluid streamlines and stagnation zones. These mechanisms, combined with baffle motion with a single DOF, constitute a TMD-like approach for sloshing control: introduce a moving "mass" that, by interacting with the sloshing flow, can split and reduce the amplitude of the main sloshing resonance.

Following this premise, Chapter 10 [84], explored this TMD approach. With a pulse-like load, enhancements of up to 40% in decay time could be obtained for a translating vertical baffle compared to a fixed one with the same geometry. Insight was provided by a frequency analysis that showed frequency splitting with the appearance of two resonances, both of lower amplitude than the original, as the linear spring stiffness was varied. Thus, the TMD approach is effective in reducing sloshing motion. Other configurations were also tested including a rotational DOF, and showed good results when subjected to pulse-like loads.

Motivated by the numerical results in microgravity, a model was developed to confirm the effectiveness of a TMD approach on ground. For this purpose, the system size is considerably larger than in the microgravity case, similar to potential ground applications. The results of the analysis are collected in Chapter 11 [283]. The system investigated is that of a vertical centered baffle allowed to move in the horizontal direction and constrained by elastic elements (not modeled). Results with one baffle indicate that a single baffle cannot provide optimum sloshing mitigation for all filling ratios. As the filling ratio changes, so does the interaction between the underlying flow and the baffle, which directly impacts the optimum spring constants for larger and smaller filling ratios. This problem suggests that using two baffles optimized for distinct filling ratios would allow for an greater range of sloshing mitigation. In addition, the use of slots was observed to generate additional viscous dissipation by enhancing the formation of recirculation zones. The frequency analysis carried out for the two-baffle configuration again clarifies the role of frequency splitting. Compared to the results in Chapter 10 [84], this analysis considers varying filling ratios for a specific moving baffle configuration (set of spring constants). This provides a relatively complete assessment of the potential operational scenarios for the liquid container. The results show that optimization of the spring constants should account for several filling ratios because the dynamics can vary substantially.

Overall, the numerical work with moving baffles on ground, along with the microgravity results, supports their potential for sloshing mitigation. A proof of concept is presented along with the experimental setup described and tested in Chapter 12 [106]. Experimental results show that performance with moving baffles is enhanced compared to fixed ones. The results in this chapter (and the related publication) are for a translational baffle and a fixed filling ratio ($\mathcal{V} = 0.6$), and are in excellent agreement with the proposed TMD-like approach.

The associated results (in preparation for publication) described in Chapter 13 delve further into the sloshing enhancement of moving baffles. Similar to the results of the frequency sweep described in Chapter 11 [283] for various filling ratios, the moving baffle is still able to reduce sloshing despite not being optimized for all filling ratios. We highlight the immense benefits for practical applications of these results: the tuning of the spring constant can be carried out solely for the most "dangerous" filling ratio (that is, the requirement for extensive experimental campaigns can be relaxed). The moving baffle system is expected to still be effective far from this condition. If we take, for example, the results in Fig. 13.7, we observe that the worst performance corresponds to the lowest filling ratio $\mathcal{V} = 0.3$, where a different resonance acquires importance. However, given that it is a higher-order mode, hydrodynamic loads are expected to notably decrease compared to the first odd sloshing mode.

Rotating baffles were also tested as an example of an alternate design exploiting the same TMD approach. Experiments demonstrated the feasibility of such designs for sloshing mitigation. However, it was found that higher-order modes were relatively unaffected by these single-DOF approaches. Such modes could be suppressed with a proper tuning of the spring constant or by using at least two Degrees of Freedom; these are the focus of the latest experimental results.

As shown in Fig. 13.14, allowing a vertical baffle to move in the horizontal direction while also rotating leads to excellent sloshing suppression when the spring constants are properly

tuned. Despite a lack of more experimental data for different filling ratios, the current results, including the velocity fields obtained using PTV, suggest that the influence of these two DOFs is associated with a significant alteration of the velocity field; the combination of translation and rotation strongly affects the flow.

In summary, the results on moving baffles shed light on their substantial potential for sloshing suppression. The application of such devices benefits from being adaptable to practically any system and geometry, although it may be complicated to design appropriate attachments to the fluid container.

14.1 Future work

The various topics addressed in this Thesis have in common the development of sloshing mitigation methods. However, due to the slightly different themes, the future work could be structured as follows:

Thermocapillary effect in circular and elliptical geometries

Given the numerical results presented in this Thesis and the conceptual design of the "ThermoSlosh" experiment, subsequent steps could involve developing a ground experiment to better characterize contact forces and the need to properly model contact line dynamics. As stated in Chapter 13, the experimental concept can be adapted with several modifications.

To prevent gravity from dominating the fluid dynamics, the cell should have a transverse direction (longitudinal axis of a cylinder) that is smaller than the capillary length $l_c = \sqrt{\sigma/(\rho_1 - \rho_2)\, g}$. We note that both the cell design (cell height) and fluid properties (via densities and surface tension) should be taken into account. As an example, the selection of immiscible fluids could involve water and low-viscosity silicone oils.

The transverse cell dimension would need to be aligned with the gravity direction to prevent fluid instabilities related to gravitationally unstable configurations [1, 2]. Therefore, the setup could be very similar to that of Fig. 5.1.

If the design is completely modular and the required eccentricity is achievable within manufacturing tolerances, appropriate elliptical cells could be designed and tested.

Moving baffles on ground

Given the amount of numerical and experimental data, more ground experiments could be undertaken for different container geometries. In particular, cylindrical geometries (horizontal or upright) or spherical ones would be of great interest due to their relevance in key engineering applications: tank truck deposits, LNG containers, liquid propellant boosters for rockets, space vehicle propellant deposits or liquid containers for life support systems in microgravity, among many others.

Furthermore, and contrary to the experiments in Chapters 12 and 13, the liquid container should be **closed** and a redesign of the baffle attachments should be considered to demonstrate the feasibility and reliability of such designs.

Moving baffles in microgravity

Moving baffles were primarily tested for small-scale systems, mainly to allow a comparison of their performance with thermocapillary-based control. A subsequent step should involve developing larger-scale numerical models and/or three-dimensional geometries.

Although the present results (numerical and experimental) could be reused, more experimental evidence is necessary to further develop reliable numerical models. For example, a microgravity experiment would be of great help in determining the parameters that affect contact line dynamics (see [9, 287]); some effects of minor importance on ground become very consequential in microgravity systems.

Another potential way forward could include adding cryogenic fluids to the numerical models currently used. In this regard, there is little understanding of the effect that a moving part within a cryogenic fluid bulk may have on the system dynamics and, more specifically, on the thermodynamic properties of the liquid-gas mixture. This effect could become relevant when the filling ratio allows direct contact between the liquid-gas interface and the baffle, which would then resemble a wavemaker.

Other potential research lines on baffles

The current work considered rigid baffles due to their simplicity, both in terms of manufacturing and numerical modeling. However, it might be interesting to analyze baffles made of porous or foam-like materials, which can be expected to have a similar effect to the introduction of slots.

Appendix A

Dimensional analysis

In the following Annex, we provide details of the dimensional analysis carried out for the fluid system described in Chapter 10. More specifically, Eqs. 10.1–10.6 (but including gravity in the forcing terms) and Eq. (10.20) are considered, along with the boundary condition on the baffle, Eq. (10.8). For simplicity, we consider a viscous dissipation constant D instead of a dissipation term proportional to the spring stiffness ($\eta\, K$). Furthermore, we use the capillary-gravity dispersion relation for waves, Eq. (1.2), to properly define the scalings.

Note that the dimensional analysis would be different considering the free sloshing or the forced response of the system. In the former, the characteristic time is on the order of $1/\omega_0 \sim \sqrt{L/g}$, as shown by the dispersion relation, whereas in the latter, the characteristic time is the inverse of the excitation frequency ($1/\omega$). We use the container length L and ρL^3 as characteristic length and mass, respectively.

A.1 System response to kick load

If we consider the system response to a pulse acceleration, with the acceleration as $\mathbf{a}(t) = a_0 \cdot \delta(t - t_0)\mathbf{e}_x$, we can assume a response that is characterized by relaxation oscillations at the sloshing frequency. Under this hypothesis, we consider laminar and incompressible flow so that the conservation of mass and momentum can be described by the Navier-Stokes equations [75]:

$$\nabla \cdot \mathbf{u} = 0, \tag{A.1a}$$

$$\rho\left(\frac{\partial \mathbf{u}}{\partial t} + (\mathbf{u}\cdot\nabla)\mathbf{u}\right) = -\nabla p + \mu\,\nabla^2\mathbf{u} + \rho\,\mathbf{a}(t), \tag{A.1b}$$

where $\mathbf{u}$ and p are the velocity and pressure fields, and ρ and μ refer to the density and dynamic viscosity. The term $\rho\,\mathbf{a}(t)$ in equation (A.1b) captures the effect of the applied acceleration (perturbation). A two-dimensional (2D) approximation is assumed, with the problem depending only on the horizontal (x) and vertical (y) coordinates. At the free surface, $F = y - f(x,t) = 0$, the balance between pressure, viscous stresses and surface tension σ is

expressed by

$$-\mathbf{n}\cdot(-p\,\mathbf{I}+\boldsymbol{\tau})=\sigma(\nabla\cdot\mathbf{n})\,\mathbf{n}, \tag{A.2}$$

where $\mathbf{I}$ is the identity matrix, $\boldsymbol{\tau}=\mu\left(\nabla\mathbf{u}+(\nabla\mathbf{u})^T\right)$ is the viscous stress tensor and $\mathbf{n}=\nabla F/|\nabla F|$ is normal to the free surface. The kinematic boundary condition at the free surface is:

$$\frac{\partial f}{\partial t}+\mathbf{u}\cdot\nabla f=0. \tag{A.3}$$

At the lateral walls, $x=\mp L/2$, slip boundary conditions are assumed in order to allow vertical motion of the contact points:

$$\mathbf{u}\cdot\mathbf{n}_w=0, \tag{A.4}$$

where $\mathbf{n}_w$ is normal to the vertical endwalls. For simplicity, a static contact angle of 90° is also imposed through

$$\mathbf{n}\cdot\mathbf{n}_w=0, \tag{A.5}$$

At the bottom wall, $y=0$, a no-slip condition is applied:

$$\mathbf{u}=0. \tag{A.6}$$

$$\ddot{x_b}+\frac{D}{M_b}\dot{x_b}+\frac{K}{M_b}x_b=\mathbf{a}_x+\frac{1}{M_b}\int_{\Sigma_b}(p\,\mathbf{n}_b+\boldsymbol{\tau}\cdot\mathbf{n}_b)\cdot\mathbf{i}\,d\Sigma_b, \tag{A.7}$$

where D is the (dimensional) viscous dissipation coefficient.

Introducing the scalings for the kick load, we obtain the following dimensionless equations for the fluid and baffle motion:

$$\nabla\cdot\hat{\mathbf{u}}=0, \tag{A.8a}$$

$$\left(\frac{\partial\hat{\mathbf{u}}}{\partial\hat{t}}+(\hat{\mathbf{u}}\cdot\nabla)\hat{\mathbf{u}}\right)=-\nabla\hat{p}+\frac{\nu}{L\sqrt{gL}}\nabla^2\hat{\mathbf{u}}-\mathbf{e}_z+\frac{a_0}{g}\delta(\hat{t})\mathbf{e}_x, \tag{A.8b}$$

$$\ddot{\hat{x}}_b+2\frac{D}{2\sqrt{M_bK}}\frac{\omega_b}{\sqrt{g/L}}\dot{\hat{x}}_b+\frac{\omega_b^2}{g/L}\hat{x}_b=\frac{a_0}{g}\delta(\hat{t})+$$

$$\frac{\rho L^3}{M_b}\frac{W_b}{L}\int_{(H_c-H_b/2)/L}^{(H_c+H_b/2)/L}(\hat{p}\,\mathbf{n}_b+\hat{\boldsymbol{\tau}}\cdot\mathbf{n}_b)\cdot\mathbf{i}\,d(y/L), \tag{A.8c}$$

$$\tag{A.8d}$$

along with the boundary conditions, of which we will only include here the ones at the free surface

$$\frac{\partial\hat{F}}{\partial\hat{t}}+\hat{\mathbf{u}}\nabla\hat{F}=0, \tag{A.9a}$$

$$-\mathbf{n}\cdot(-\hat{p}\,\mathbf{I}+\hat{\boldsymbol{\tau}})=\frac{\sigma}{\rho gL^2}(\nabla\cdot\mathbf{n})\,\mathbf{n}, \tag{A.9b}$$

Thus, accounting for the container and baffle geometries and dimensions, the dimensionless parameters are as follows:

$$\left(\frac{L\sqrt{gL}}{\nu},\ \frac{a_0}{g},\ \mathcal{V},\ \frac{W}{L},\ \frac{D}{2\sqrt{M_bK}},\ \frac{\omega_b}{\sqrt{g/L}},\ \frac{\rho L^3}{M_b},\ \frac{H_b}{L},\ \frac{W_b}{L},\ \frac{H_c}{L},\ \mathrm{Bo}\right) \tag{A.10}$$

where $\omega_b^2 = K/M_b$. Note that the definition of $\mathcal{V}$ and H_c was not introduced in Chapter 10 due to the fixed fill ratio and baffle position; the definitions of these parameters can be extracted from Chapter 11.

These dimensionless parameters are calculated for comparable baffle configurations: two-baffle configurations as in Chapter 11, Section 11.5 with a filling ratio such that only the lower one is in contact with the liquid. This ensures a configuration as close as possible to that presented in Chapter 12.

A.2 System response to harmonic loading

Analogous to the case of a kick load, we perform a dimensional analysis of the relevant equations. Considering the system response to a harmonic acceleration, with acceleration as $\mathbf{a}(t) = A\omega^2 \sin(\omega t)\mathbf{e}_x$, we may assume a response characterized by the forced oscillations, with the characteristic timescale of $1/\omega$. Under the same hypotheses made for the kick load analysis, we obtain the following dimensionless equations for the fluid and baffle motion.

The dimensionless equations are now

$$\nabla \cdot \hat{\mathbf{u}} = 0, \tag{A.11a}$$

$$\left(\frac{\partial \hat{\mathbf{u}}}{\partial \hat{t}} + (\hat{\mathbf{u}} \cdot \nabla)\hat{\mathbf{u}}\right) = -\nabla \hat{p} + \frac{\nu}{L^2\omega}\nabla^2\hat{\mathbf{u}} - \frac{g}{A\omega^2}\frac{A}{L}\mathbf{e}_z + \frac{A}{L}\sin(\hat{t})\mathbf{e}_x, \tag{A.11b}$$

$$\ddot{\hat{x}}_b + 2\frac{D}{2\sqrt{M_bK}}\frac{\omega_b}{\omega}\dot{\hat{x}}_b + \frac{\omega_b^2}{\omega^2}\hat{x}_b = \frac{A}{L}\sin(\hat{t}) + \frac{\rho L^3}{M_b}\frac{W_b}{L}\int_{(H_c-H_b/2)/L}^{(H_c+H_b/2)/L} (\hat{p}\,\mathbf{n}_b + \hat{\boldsymbol{\tau}}\cdot\mathbf{n}_b)\cdot\mathbf{i}\,d(y/L). \tag{A.11c}$$

For the free surface motion, the dimensionless equations are:

$$\frac{\partial \hat{F}}{\partial \hat{t}} + \hat{\mathbf{u}}\nabla\hat{F} = 0, \tag{A.12a}$$

$$-\mathbf{n}\cdot(-\hat{p}\,\mathbf{I} + \hat{\boldsymbol{\tau}}) = \frac{\sigma}{\rho L^3\omega^2}(\nabla\cdot\mathbf{n})\,\mathbf{n}, \tag{A.12b}$$

where the inverse of the Weber number $\mathrm{We} = \rho L^3\omega_f^2/\sigma$ appears.

And the system is characterized by the nondimensional parameters

$$\left(\frac{\omega L^2}{\nu},\ \frac{g}{A\omega^2},\ \frac{A}{L},\ \mathcal{V},\ \frac{W}{L},\ \frac{D}{2\sqrt{M_bK}},\ \frac{\omega_b}{\omega},\ \frac{\rho L^3}{M_b},\ \frac{W_b}{L},\ \frac{H_b}{L},\ \frac{H_c}{L},\ \mathrm{We}\right). \tag{A.13}$$

Appendix B

Image processing algorithm

This Annex provides a brief description of the algorithm used for processing the image data acquired during the experimental campaigns at VKI with the SHAKESPEARE shaking table. It is worth noting that the methodology notably differs depending on the use of a backlight or laser sheet illumination. Thus, the specific details of each one are addressed separately.

B.1 Backlight illumination

We note that the dimensions of the LED backlight illumination panel ensure that the entire length of the container is illuminated, but the total height is not. Therefore, the image must first be cropped through the definition of a Region of Interest (ROI). The image is preprocessed with a Gaussian blur to reduce the image noise.

Afterwards, the detection of the interface is carried out by applying a gradient operator via a custom kernel (Sobel-like kernel). The specific operator being used for the current analysis is M^*, defined as follows:

$$M_1 = \begin{bmatrix} -1 & -2 & -1 \\ -1 & -2 & -1 \\ -1 & -2 & -1 \\ -1 & -2 & -1 \end{bmatrix}, \; M_2 = \begin{bmatrix} 0 & -1 & 0 \\ 0 & 0 & 0 \\ 0 & 1 & 0 \end{bmatrix}, \; M^* = \begin{bmatrix} M_1 \\ M_2 \\ -M_1 \end{bmatrix} \tag{B.1}$$

With backlight illumination, the fluid interface can be observed as a slim dark line. To improve the contrast between water and air, blue coloring is added. Thus, the interface thickness is slightly increased or, if the contact line is pinned, the contrast between fluid domains helps the detection algorithm to identify the interface.

Ideally, a single kernel should be enough to detect the interface. However, the present setup produces slightly three-dimensional behavior: the interface may tilt towards or away from the backlight (i.e., along the camera-backlight axis). This tilting, although small, causes bright and dark regions on the fluid interface that may render interface detection difficult. To avoid this difficulty and improve the contrast, we use two operators: M^* and $-M^*$. The effect of

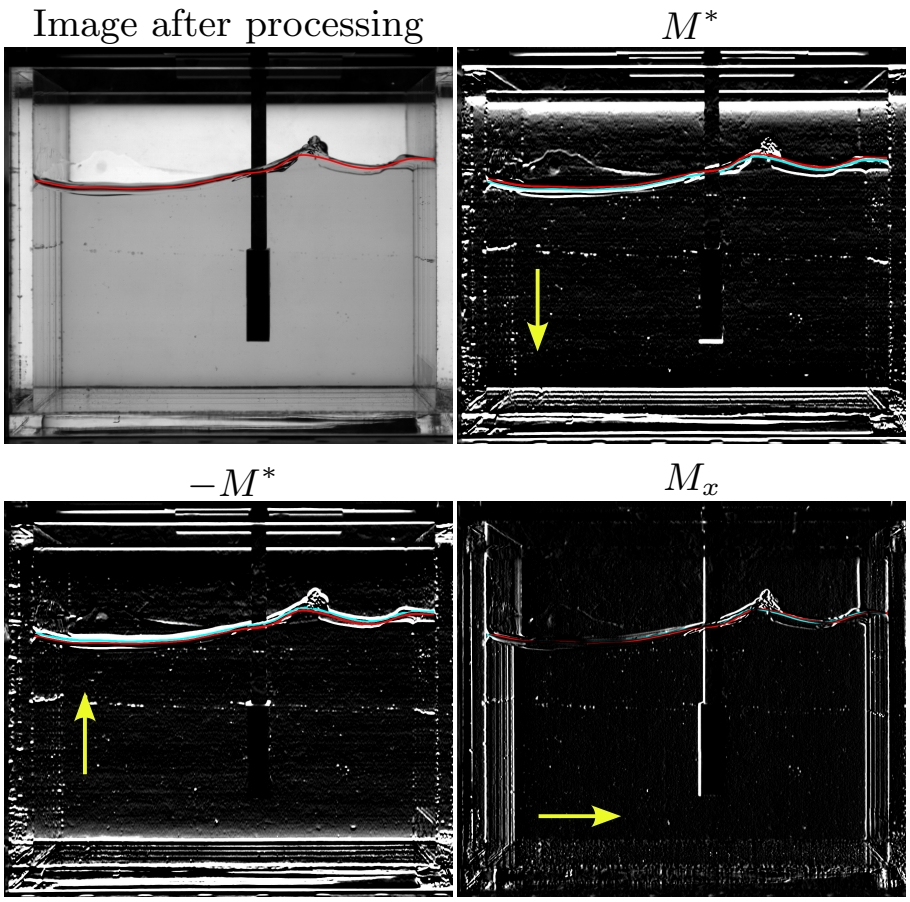


Figure B.1: From top to bottom, left to right: image after processing with detection algorithm and post-processed images after applying M^*, $-M^*$ and M_x operators with ImageJ.

both gradients on the post-processed image is depicted in Fig. B.1. Note that, for display purposes, the image is rescaled between 0 and 255 (unsigned 8 bit format).

The sequence for detecting the interface is as follows:

First, once the images are processed with the aforementioned gradients, we correct the vertical shift introduced by the kernels. A correlation of both images is obtained when the images are vertically shifted by a certain number of pixels. The pixel value for which the correlation between images is maximum indicates a correct superposition of the regions where the interface should be located, thus eliminating (or largely reducing) the shift introduced by the gradient operators. As a direct consequence, the interface thickness grows slightly and the maximum value after using the gradient operator increases (thus, the peak detection is easier).

Prior to detection of the interface, the gradient image is filtered to remove "noisy" regions that may interfere with the detection algorithm. For instance, droplets, vapour or receding contact lines may produce regions visible with the gradient operators that are not part of the actual interface.

For this purpose, a mask is used that counts the number of connected pixels in an image with an intensity greater than a certain value. Essentially, this process labels several regions, with the interface presumably being the largest one. Once these regions are labeled, each region is processed to determine its span along the container length, similar to a projected length. Thus, smaller regions such as droplets or other imperfections in the image are removed because of their small size along the length of the container.

Ideally, the interface should span the entire length of the container. However, because of reflections and the baffle, this is not the case. The criteria to remove unwanted reflections and determine the actual interface should be assessed on a case-by-case basis to make the filtering more effective.

In the present analysis, for example, if the maximum projected length of an element is the actual image length, all remaining elements are automatically removed. If the maximum projected length is between $L/2$ and $3L/4$, all elements with lengths lower than $2/5L$ are discarded.

The code includes an additional verification step for regions closer to the container endwalls. The algorithm checks if these regions contain a trace of the fluid interface that may have been filtered out, attempting to retain the position of the contact line in that region.

Once the image is pre-processed, the detection algorithm performs a standard peak detection on each pixel column of the image. For this, the pixel values along columns are first smoothed out using a Butterworth filter and then the peak detection algorithm searches for the largest one.

However, interface detection with these methods does not yield perfect results. Reflections and imperfections may produce points that are not related to the actual interface (see Fig. B.1). These points coming from the detection algorithm can only be removed by post-processing tools that identify them as outliers.

For this purpose, a regression based on Radial Basis Functions, using Gaussian functions, is implemented within an iterative loop that removes outliers until the error function decreases below a certain threshold. The remaining points are then interpolated to retrieve the whole interface shape and smoothed again with a Butterworth filter. This particular action may be detrimental to the detection algorithm in the vicinity of the container endwalls. However, the following must be taken into account: in these regions, the interface reaches almost vertical orientations because of the liquid wetting the corners and perhaps also inertia (due to sloshing, for instance). By using vertical gradient operators, these regions are neglected. Moreover, the peak detection algorithm is performed along the image columns, and thus is not correctly detected. Given that the main dynamics of the ground experimental setup are not significantly affected by the contact line dynamics, neglecting the detection of this region is not a major concern.

We note that the detection algorithm for the baffle motion differs from the one used for the interface. A much simpler approach is considered, albeit one that is completely different depending on whether the baffle motion is translational or rotational.

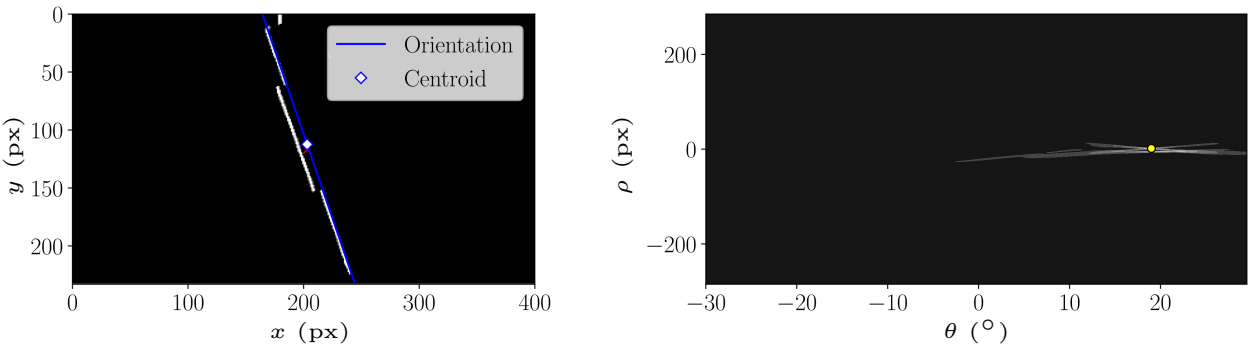


Figure B.2: Results of the image processing algorithm for the purely rotational baffle case. (Left) Original image and detected baffle orientation at an arbitrary time. The blue line denotes the detected baffle orientation. The diamond marker denotes the detected centroid, a magnitude which is not relevant for the processing algorithm. (Right) Output of the Radon transform in the (ρ, θ) plane: the yellow dot depicts the location of maximum intensity in terms of the projection position (with respect to the image centroid) and the projection angle in degrees. Note that the orientation is defined with respect to the vertical position of the baffle.

B.1.1 Baffle position processing - translation

The detection of the baffle displacement is performed via another custom kernel:

$$M_x = \begin{bmatrix} 1 & 0 & 0 & 0 & -1 \\ 2 & 0 & 0 & 0 & -2 \\ 3 & 1 & 0 & -1 & -3 \\ 2 & 0 & 0 & 0 & -2 \\ 1 & 0 & 0 & 0 & -1 \end{bmatrix} \tag{B.2}$$

As a means to reduce the computational cost of the detection algorithm, the image is reduced to a small number of rows centered on the baffle, always ensuring that the baffle motion remains bounded within it. By applying the M_x operator, a pre-processed image such as the one in Fig. B.1 (lower, right panel) can be obtained. Again, a peak detection operation is performed, and the position of the left baffle boundary over time can be obtained and stored.

B.1.2 Baffle position processing - rotation

If the baffle is allowed to rotate, a detection using the M_x gradient operator may be used and, based on the position of two points, the baffle rotation can be obtained. However, this method sometimes performs poorly, resulting in an overestimation of the baffle rotation angle.

Therefore, an alternative method to accurately detect the baffle rotation is introduced. First, the image is cropped, including the whole baffle and the applied M_x operator, similar to the case of a translational baffle. This step ensures that, for small baffle rotations (which is the case for the experimental results obtained), the left baffle boundary is significantly enhanced.

Due to the high image resolution, we perform a Lanczos resampling of the image to reduce its size and increase the processing velocity prior to processing it.

The next step of the image processing algorithm is based on the Radon transform [292–294] — for more details of this implementation for image processing purposes, the reader is referred to the work of Sanchis and Jensen [293].

This transform yields accurate results when detecting the orientation of high-contrasted elements such as fluid interfaces in PIV or PTV or, as in the present analysis, detecting the orientation of certain objects after increasing their contrast with surrounding media via gradient operators. An example of the algorithm output for the baffle position is shown in Fig. B.3.

B.2 Laser sheet illumination - PTV

As detailed in Chapter 2, particle tracking velocimetry is also performed with the current setup as a means to obtain data for the flow field, particularly when moving baffles are present.

The detection algorithm must now account for a very different type of illumination, via a laser sheet within the liquid bulk. Given the length of the fluid container, which has an inner dimension of 175 mm, we anticipate that not all cases will permit the interface to be detected with such good resolution as with backlight illumination.

The reason for this lies with the experimental setup itself since the laser sheet illuminates a region in the vicinity of the container midplane (in the camera - container direction). In this scenario, motion of the fluid interface towards the camera or away from it may cause unwanted reflections or a blurring of the interface width. Moreover, the trace particles can get stuck on the surface of the moving baffle. The amount of particles within the fluid bulk is not particularly critical. The fluid interface, on the other hand, presents a major problem due to the baffle being suspended from the moving platform via two 3D printed PLA beams. These beams may act as stirrers, causing the interface particles to detach and become trapped within the fluid bulk. In addition, 3D printing produces a rough surface finish, which may also help trap these particles. Therefore, one expects the determination of the interface shape to become less accurate between subsequent experiment runs.

In any case, the main purpose for the PTV experiments was to determine the flow structures developing within the fluid bulk and the interaction of the sloshing flow with the baffles. Interface detection is desirable, if possible, but a secondary concern.

The detection algorithm used for interface detection relies on the same principle as the detection of the baffle rotation, the Radon transformation. As noted earlier, some particles attach to the free surface and are illuminated by the laser sheet. Taking into account that there are no illumination sources except for the laser sheet, the contrast between the particles on the free surface and the air (dark) or the liquid bulk (mostly dark except for the illuminated particles) can be used to determine the interface location. Prior to obtaining the interface, a pre-processing step is taken, which consists of enhancing the image contrast and brightness and applying filtering.

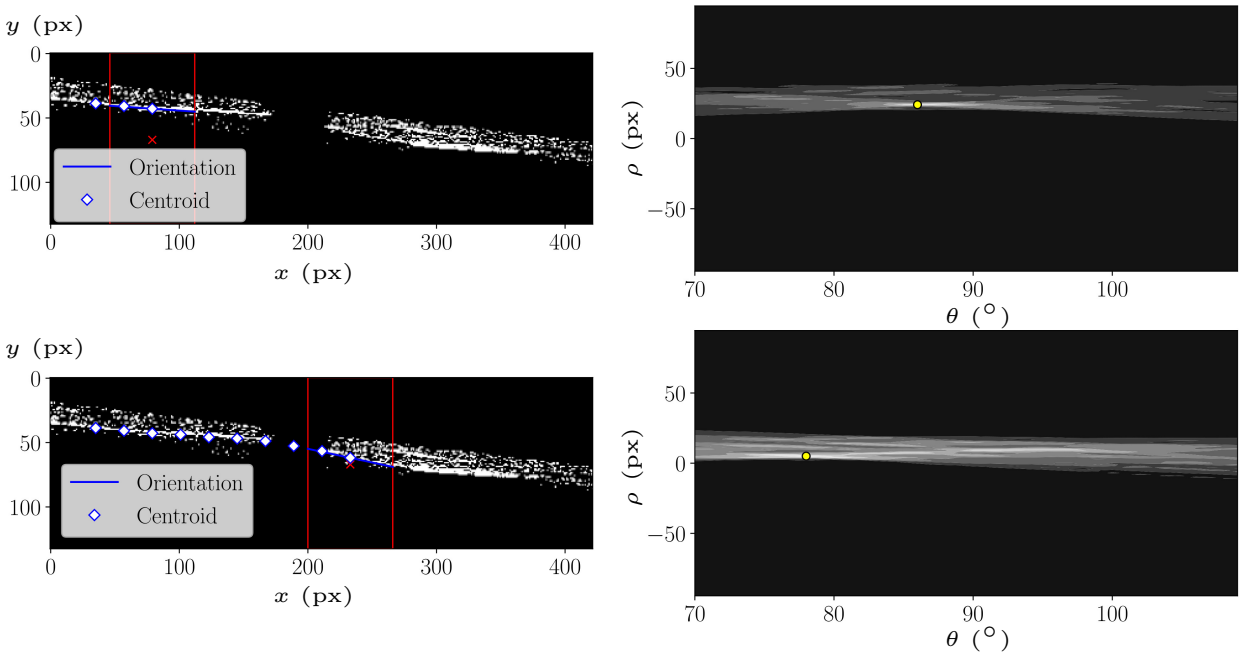


Figure B.3: Results of the image processing algorithm for PTV images. (Left) Recontrasted image and detected interface orientation and centroid. (Right) Output of the Radon transform in the (ρ, θ) plane: the yellow dot marks the location of maximum intensity in terms of the projection position (with respect to the image centroid) and the projection angle in degrees.

It is worth noting that the interface displays discontinuous behavior. Even if all of the interface is illuminated, the projected shadow of the baffle divides the interface into at least two illuminated regions. Furthermore, the interface may have a complex shape that cannot be captured by a single Radon transform. To deal with this, the interfacial region is divided into several overlapping regions. In each region or "window", the Radon transform captures the orientation and position of the interface, as shown in Fig. B.3. By fitting and filtering potential outliers, coupled with a subsequent regression via Radial Basis Functions (RBF), the interface shape is finally obtained.

After extracting the interface motion, particle tracking velocimetry is performed. In this regard, we note that the tracking algorithm is an implementation of an open-source code for PTV analysis: TracTrac. For more details of the numerical implementation, the reader is referred to the reference work of Heyman [110]. The PTV code provides reasonable results with proper tuning of the numerical parameters, as detailed in Chapter 2.

An additional step must be performed, however. The PTV algorithm detects particle motion in the camera FOV. That is, the velocities are measured in "pixels per frame", which is not very meaningful. A calibration with the same setup and a known pattern (e.g., a dotted pattern) must be performed to establish an equivalence between pixels and a dimensional length scale such as meters. The frame rate of the camera, on the other hand, is a known value stored as metadata in the video files.

References

[1] Rayleigh. "Investigation of the character of the equilibrium of an incompressible heavy fluid of variable density". In: *Proceedings of the London Mathematical Society* s1-14.1 (Nov. 1882), pp. 170–177.

[2] Geoffrey Ingram Taylor. "The instability of liquid surfaces when accelerated in a direction perpendicular to their planes. I". In: *Proceedings of the Royal Society A* 201.1065 (1950), pp. 192–196.

[3] C. Colin, X. Rion, and J. Fabre. "Bubble coalescence in gas-liquid flow at microgravity conditions". In: *Micogravity Science and Technology* 20 (2008), pp. 243–246.

[4] D. Gligor et al. "Influence of gravity on the frozen wave instability in immiscible liquids". In: *Physical Review Fluids* 5 (2020), p. 084001.

[5] Y. Gaponenko, A. Mialdun, and V. Shevtsova. "Pattern selection in miscible liquids under periodic excitation in microgravity: Effect of interface width". In: *Physics of Fluids* 30 (2018), p. 062103.

[6] V. Shevtsova et al. "Two-scale wave patterns on a periodically excited miscible liquid-liquid interface". In: *Journal of Fluid Mechanics* 795 (2016), pp. 409–422.

[7] T. Lyubimova et al. "Band instability in near-critical fluids subjected to vibration under weightlessness". In: *Physical Review E* 95 (2017), p. 013105.

[8] P. Salgado Sánchez et al. "Finite-size effects on pattern selection in immiscible fluids subjected to horizontal vibrations in weightlessness". In: *Physical Review E* 99 (2019), p. 042803.

[9] P. Salgado Sánchez et al. "Interfacial phenomena in immiscible liquids subjected to vibrations in microgravity". In: *Journal of Fluid Mechanics* 865 (2019), pp. 850–883.

[10] T. P. Lyubimova et al. "Faraday waves on band pattern under zero gravity conditions". In: *Physical Review Fluids* 4 (2019), p. 064001.

[11] P. Salgado Sánchez et al. "Effect of initial interface orientation on patterns produced by vibrational forcing in microgravity". In: *Journal of Fluid Mechanics* 884 (2020), A38.

[12] T. G. Hammond et al. "Gene expression in space". In: *Nature Medicine* 5 (1999), pp. 359–359.

[13] A. McPherson and J. M. DeLucas. "Microgravity protein crystallization". In: *npj Microgravity* 1 (2015), p. 15010.

[14] A.I. Grigoriev, A.R. Kotovskaya, and G.A. Fomina. "The human cardiovascular system during space flight". In: *Acta Astronautica* 68.9 (2011). 17th IAA Humans in Space Symposium, pp. 1495–1500.

[15] E. L. Kordyum. “Plant cell gravisensitivity and adaptation to microgravity”. In: *Plant Biology* 16 (2014), pp. 79–90.

[16] Paul Concus, Robert Finn, and Mark Weislogel. “Capillary surfaces in an exotic container: results from Space experiments”. In: *Journal of Fluid Mechanics* 394 (1999), pp. 119–135.

[17] F. J. Higuera. “Liquid-fuel thermocapillary flow induced by a spreading flame”. In: *Journal of Fluid Mechanics* 473 (2002), pp. 349–377.

[18] A. J. Russo, R. L. Akau, and J. L. Jellison. “Thermocapillary flow in pulsed laser beam weld pools”. In: *Welding J. (Welding Research Suppl.)* 69 (1990), pp. 23–9.

[19] K. C. Mills et al. “Marangoni Effects in Welding”. In: *Philosophical Transactions: Mathematical, Physical and Engineering Sciences* 356.1739 (1998), pp. 911–925.

[20] D. Schwabe and A. Scharmann. “Some evidence for the existence and magnitude of a critical Marangoni number for the onset of oscillatory flow in crystal growth melts”. In: *Journal of Crystal Growth* 46 (1979), pp. 125–131.

[21] J. C. Brice. *Crystal growth*. Blackie and Son, 1986.

[22] Rodrigo Leite Pinto et al. “Enhanced interfacial deformation in a Marangoni flow: A measure of the dynamical surface tension”. In: *Phys. Rev. Fluids* 3 (2 Feb. 2018), p. 024003.

[23] Tatiana Gambaryan-Roisman. “Marangoni convection, evaporation and interface deformation in liquid films on heated substrates with non-uniform thermal conductivity”. In: *International Journal of Heat and Mass Transfer* 53.1 (2010), pp. 390–402.

[24] Stergios G. Yiantsios et al. “Surface deformation and film corrugation during drying of polymer solutions induced by Marangoni phenomena”. In: *International Journal of Heat and Mass Transfer* 89 (2015), pp. 1083–1094.

[25] A. A. GOLOVIN, A. A. NEPOMNYASHCHY, and L. M. PISMEN. “Nonlinear evolution and secondary instabilities of Marangoni convection in a liquid–gas system with deformable interface”. In: *Journal of Fluid Mechanics* 341 (1997), pp. 317–341.

[26] Xue Ma et al. “Experiments on Marangoni spreading – evidence of a new type of interfacial instability”. In: *Journal of Fluid Mechanics* 958 (2023), A33.

[27] Jian-Fu Zhao et al. “Topological structure evolvement of flow and temperature fields in deformable drop Marangoni migration in microgravity”. In: *International Journal of Heat and Mass Transfer* 54.21 (2011), pp. 4655–4663.

[28] T. P. Lyubimova et al. “Influence of high frequency vibrations on fluid flow and heat transfer in a floating zone”. In: *Crystal Research and Technology* 38 (2003), pp. 635–653.

[29] T. P. Lyubimova, D. V. Lyubimov, and A. O. Ivantsov. “The influence of vibrations on melt flows during detached Bridgman crystal growth”. In: *Journal of Crystal Growth* 385 (2014), pp. 77–81.

[30] V. Shevtsova et al. “Subcritical and oscillatory dynamic surface deformations in non-cylindrical liquid bridges”. In: *Fluid Dynamics and Material Processing* 4 (2008), pp. 43–54.

[31] K.A. Cliffe and S.J. Tavener. “Marangoni–Bénard Convection with a Deformable Free Surface”. In: *Journal of Computational Physics* 145.1 (1998), pp. 193–227.

[32] Chen Jyh-Chen and Hwu Farn-Shiun. “Oscillatory thermocapillary flow in a rectangular cavity”. In: *International Journal of Heat and Mass Transfer* 36.15 (1993), pp. 3743–3749.

[33] M. Hamed and J. M. Floryan. “Marangoni convection. Part 1. A cavity with differentially heated sidewalls”. In: *Journal of Fluid Mechanics* 405 (2000), pp. 79–110.

[34] A. Nepomnyashchy, I. Simanovskii, and J. C. Legros. *Interfacial Convection in Multilayer Systems*. Springer New York, NY, 2006.

[35] A. K. Sen and S. H. Davis. “Steady thermocapillary flows in two-dimensional slots”. In: *Journal of Fluid Mechanics* 121 (1982), pp. 163–186.

[36] P. Salgado Sánchez et al. “Pattern selection for thermocapillary flow in rectangular containers in microgravity”. In: *Phys. Rev. Fluids* 7 (5 May 2022), p. 053502.

[37] H. Lamb. *Hydrodynamics*. Cambridge University Press, 1945.

[38] T. B. Benjamin and F. J. Ursell. “The stability of the plane free surface of a liquid in vertical periodic motion”. In: *Proceedings of the Royal Society of London A: Mathematical, Physical and Engineering Sciences* 225 (1954), pp. 505–515.

[39] H. N. Abramson. *The Dynamic Behavior of Liquids in Moving Containers, with Applications to Space Vehicle Technology*. NASA, 1966.

[40] R. A. Ibrahim. *Liquid Sloshing Dynamics - Theory and Applications*. Cambridge university press, 2005.

[41] R. A. Ibrahim, V. N. Pilipchuk, and T. Ikeda. “Recent advances in liquid sloshing dynamics”. In: *Applied Mechanical Reviews* 54 (2001), pp. 133–199.

[42] A. Dalmon et al. “Comparison Between the FLUIDICS Experiment and Direct Numerical Simulations of Fluid Sloshing in Spherical Tanks Under Microgravity Conditions”. In: *Microgravity Science and Technology* 31 (2019), pp. 123–138.

[43] A. Romero-Calvo et al. “StELIUM: A student experiment to investigate the sloshing of magnetic liquids in microgravity”. In: *Acta Astronautica* 173 (2020), pp. 344–355.

[44] A. Romero-Calvo, F. Maggi, and H. Schaub. “Magnetic Positive Positioning: Toward the application in space propulsion”. In: *Acta Astronautica* 187 (2021), pp. 348–361.

[45] D. E. Jaekle Jr. “Propellant management device conceptual design and analysis - Galleries”. In: *33rd Joint Propulsion Conference and Exhibit*. AIAA, 1997.

[46] Jason W. Hartwig. “A Detailed Historical Review of Propellant Management Devices for Low Gravity Propellant Acquisition”. In: *52nd AIAA/SAE/ASEE Joint Propulsion Conference*. AIAA, 2016.

[47] Samuel T. Hart, E. Glenn Lightsey, and Álvaro Romero-Calvo. “Characterization of a Phase Change Propellant Management Device”. In: *Acta Astronautica* 228 (2025), pp. 842–852.

[48] R. A. Ibrahim. “Liquid sloshing dynamics with aerospace applications”. In: *Proceedings of the 9th ASAT conference* (2001), p. 155.

[49] H. A. Snyder. “Sloshing in microgravity”. In: *Cryogenics* 39 (1999), pp. 1047–1055.

[50] M. Utsumi. “Slosh Damping Caused by Friction Work Due to Contact Angle Hysteresis”. In: *AIAA Journal* 55 (2017).

[51] J.R. Cho, H.W. Lee, and S.Y. Ha. “Finite element analysis of resonant sloshing response in 2-D baffled tank”. In: *Journal of Sound and Vibration* 288.4 (2005), pp. 829–845.

[52] K. C. Biswal, S. K. Bhattacharyya, and P. K. Sinha. “Non-linear sloshing in partially liquid filled containers with baffles”. In: *International Journal for Numerical Methods in Engineering* 68.3 (2006), pp. 317–337.

[53] Dongming Liu and Pengzhi Lin. “Three-dimensional liquid sloshing in a tank with baffles”. In: *Ocean Engineering* 36.2 (2009), pp. 202–212.

[54] M.A. Goudarzi and S.R. Sabbagh-Yazdi. “Analytical and experimental evaluation on the effectiveness of upper mounted baffles with respect to commonly used baffles”. In: *Ocean Engineering* 42 (2012), pp. 205–217.

[55] W. Chih-Hua, O.M. Faltinsen, and B.-F. Chen. “Numerical study of sloshing liquid in tanks with baffles by time-independent finite difference and fictitious cell method”. In: *Computers & Fluids* 63 (2012), pp. 9–26.

[56] C.G. Koh et al. “Modelling of liquid sloshing with constrained floating baffle”. In: *Computers & Structures* 122 (2013). Computational Fluid and Solid Mechanics 2013, pp. 270–279.

[57] Y. Xie and X. Zhao. “Sloshing suppression with active controlled baffles through deep reinforcement learning–expert demonstrations–behavior cloning process”. In: *Physics of Fluids* 33 (2021), p. 017115.

[58] M.A. Goudarzi, S.R. Sabbagh-Yazdi, and W. Marx. “Investigation of sloshing damping in baffled rectangular tanks subjected to the dynamic excitation”. In: *Bulletin of Earthquake Engineering* 8 (4 2010), pp. 1055–1072.

[59] Peng Huang. “A comprehensive investigation on liquid sloshing of rectangular water tank with vertical baffles”. In: *Ocean Engineering* 288 (2023), p. 116126.

[60] O. M. Faltinsen and A. N. Timokha. *Sloshing*. Cambridge University Press, 2009.

[61] V.S. Sanapala et al. “Numerical simulation of parametric liquid sloshing in a horizontally baffled rectangular container”. In: *Journal of Fluids and Structures* 76 (2018), pp. 229–250.

[62] S.R. Idelsohn et al. “Interaction between an elastic structure and free-surface flows: experimental versus numerical comparisons using the PFEM”. In: *Computational Mechanics* 43 (2008), pp. 125–132.

[63] Sung-Chul Hwang et al. “Numerical simulations of sloshing flows with elastic baffles by using a particle-based fluid–structure interaction analysis method”. In: *Ocean Engineering* 118 (2016), pp. 227–241.

[64] Sung-Pill Kim et al. “Experimental study on sloshing reduction effects of baffles linked to a spring system”. In: *Ocean Engineering* 170 (2018), pp. 136–147.

[65] A. Iranmanesh and R. Nikbakhti. “Numerical study on suppressing liquid sloshing of a rectangular tank using moving baffles linked to a spring system”. In: *Ocean Engineering* 229 (2021), p. 109002.

[66] Jinhai Zheng, Peng Dou, and Mi-An Xue. “Dynamics coupling analysis between elastic supporting structure and TLD with and without slat screen”. In: *Structures* 46 (2022), pp. 969–987.

[67] Chenyi Wang et al. “Numerical investigation on suppression effect of movable part with spring system”. In: *Ocean Engineering* 280 (2023), p. 114541.

[68] S. Elias and V. Matsagar. “Research developments in vibration control of structures using passive tuned mass dampers”. In: *Annual Reviews in Control* 44 (2017), pp. 129–156.

[69] M. Gutierrez Soto and H. Adeli. “Tuned Mass Dampers”. In: *Archives of Computational Methods in Engineering* 20 (4 2013), pp. 419–431.

[70] D. J. Wagg. “A review of the mechanical inerter: historical context, physical realisations and nonlinear applications”. In: *Nonlinear Dynamics* 104 (1 2021), pp. 13–34.

[71] A. J. Clark. “Multiple passive tuned mass dampers for reducing earthquake induced building motion”. In: *Proceedings of the 9th world conference on earthquake engineering*. Vol. 5. 1988, pp. 779–784.
[72] Robert J. McNamara. “Tuned Mass Dampers for Buildings”. In: *Journal of the Structural Division* 103 (1977), pp. 1785–1798.
[73] Min-Li Chang et al. “Experimental study on adjustable tuned mass damper to reduce floor vibration due to machinery”. In: *Structural Control and Health Monitoring* 17.5 (2010), pp. 532–548.
[74] Tanmoy Konar and Aparna (Dey) Ghosh. “A review on various configurations of the passive tuned liquid damper”. In: *Journal of Vibration and Control* 29.9-10 (2023), pp. 1945–1980.
[75] L. D. Landau and E. M. Lifshitz. *Fluid Mechanics*. Pergamon books Ltd., 1987.
[76] Y. A. Gaponenko et al. “Interfacial pattern selection in miscible liquids under vibration”. In: *Soft Matter* 11 (2015), pp. 8221–8224.
[77] P. Salgado Sánchez et al. “Vibroequilibria in microgravity: comparison of experiments and theory”. In: *Physical Review E* 100 (2019), p. 063103.
[78] Alan M Winslow. “Numerical solution of the quasilinear poisson equation in a nonuniform triangle mesh”. In: *Journal of Computational Physics* 1.2 (1966), pp. 149–172.
[79] P. M. Knupp. “Winslow Smoothing on Two-Dimensional Unstructured Meshes”. In: *Engineering with Computers* 15.3 (1999), pp. 263–268.
[80] COMSOL Multiphysics. *COMSOL Multiphysics Reference Manual*. 2017.
[81] S. Erlicher, L. Bonaventura, and O. S. Bursi. “The analysis of the Generalized-α method for non-linear dynamic problems”. In: *Computational Mechanics* 28 (2002), pp. 83–104.
[82] I. Harari and T. J. R. Hughes. “What are C and h?: Inequalities for the analysis and design of finite element methods”. In: *Computer Methods in Applied Mechanics and Engineering* 97 (1992), pp. 157–192.
[83] R. Codina. “A discontinuity-capturing crosswind-dissipation for the finite element solution of the convection-diffusion equation”. In: *Computer Methods in Applied Mechanics and Engineering* 110 (1993), pp. 325–342.
[84] D. Gligor et al. “Sloshing mitigation in microgravity with moving baffles”. In: *Acta Astronautica* 219 (2024), pp. 639–652.
[85] E. Olsson and G. Kreiss. “A conservative level set method for two phase flow”. In: *Journal of Computational Physics* 210 (2005), pp. 225–246.
[86] Marcello Lappa. “Coalescence and Non-coalescence Phenomena in Multi-material Problems and Dispersed Multiphase Flows: Part 2, A Critical Review of CFD Approaches”. In: *Fluid Dynamics & Materials Processing* 1.3 (2005), pp. 213–234.
[87] Inc Ansys. *Ansys Fluent Theory Guide (2021 R2)*. 2021.
[88] The OpenFOAM Foundation. *OpenFOAM User Guide (version 12)*. 2024.
[89] O. C. Zienkiewicz, R. L. Taylor, and P. Nithiarasu. *The Finite Element Method for Fluid Dynamics, 6th Edition*. Butterworth-Heinemann, 2005, p. 451.
[90] A. Quarteroni. *Numerical Models for Differential Problems, 2nd edition*. Springer Milano, 2014, p. 658.
[91] Thomas J.R. Hughes et al. “The Continuous Galerkin Method Is Locally Conservative”. In: *Journal of Computational Physics* 163.2 (2000), pp. 467–488.

[92] Olaf Schenk et al. “PARDISO: a high-performance serial and parallel sparse linear solver in semiconductor device simulation”. In: *Future Generation Computer Systems* 18.1 (2001). I. High Performance Numerical Methods and Applications. II. Performance Data Mining: Automated Diagnosis, Adaption, and Optimization, pp. 69–78.

[93] J. Chung and G. M. Hulbert. “A Time Integration Algorithm for Structural Dynamics With Improved Numerical Dissipation: The Generalized-α Method”. In: *Journal of Applied Mechanics* 60.2 (1993), pp. 371–375.

[94] Kenneth E. Jansen, Christian H. Whiting, and Gregory M. Hulbert. “A generalized-α method for integrating the filtered Navier–Stokes equations with a stabilized finite element method”. In: *Computer Methods in Applied Mechanics and Engineering* 190.3 (2000), pp. 305–319.

[95] Endre Süli and David F. Mayers. *An Introduction to Numerical Analysis*. Cambridge University Press, 2003.

[96] R. Courant, K. Friedrichs, and H. Lewy. “On the Partial Difference Equations of Mathematical Physics”. In: *IBM Journal of Research and Development* 11.2 (1967), pp. 215–234.

[97] I. Babuška and R. Narasimhan. “The Babuška-Brezzi condition and the patch test: an example”. In: *Computer Methods in Applied Mechanics and Engineering* 140.1 (1997), pp. 183–199.

[98] Thomas J.R. Hughes, Leopoldo P. Franca, and Marc Balestra. “A new finite element formulation for computational fluid dynamics: V. Circumventing the Babuška-Brezzi condition: a stable Petrov-Galerkin formulation of the stokes problem accommodating equal-order interpolations”. In: *Computer Methods in Applied Mechanics and Engineering* 59.1 (1986), pp. 85–99.

[99] Alexander N. Brooks and Thomas J.R. Hughes. “Streamline upwind/Petrov-Galerkin formulations for convection dominated flows with particular emphasis on the incompressible Navier-Stokes equations”. In: *Computer Methods in Applied Mechanics and Engineering* 32.1 (1982), pp. 199–259.

[100] Thomas J.R. Hughes, Leopoldo P. Franca, and Michel Mallet. “A new finite element formulation for computational fluid dynamics: VI. Convergence analysis of the generalized SUPG formulation for linear time-dependent multidimensional advective-diffusive systems”. In: *Computer Methods in Applied Mechanics and Engineering* 63.1 (1987), pp. 97–112.

[101] T.E. Tezduyar. “Stabilized Finite Element Formulations for Incompressible Flow Computations”. In: ed. by John W. Hutchinson and Theodore Y. Wu. Vol. 28. Advances in Applied Mechanics. Elsevier, 1991, pp. 1–44.

[102] Thomas J.R. Hughes, Leopoldo P. Franca, and Gregory M. Hulbert. “A new finite element formulation for computational fluid dynamics: VIII. The galerkin/least-squares method for advective-diffusive equations”. In: *Computer Methods in Applied Mechanics and Engineering* 73.2 (1989), pp. 173–189.

[103] G. Hauke and T.J.R. Hughes. “A unified approach to compressible and incompressible flows”. In: *Computer Methods in Applied Mechanics and Engineering* 113.3 (1994), pp. 389–395.

[104] Thomas J.R. Hughes, Michel Mallet, and Mizukami Akira. "A new finite element formulation for computational fluid dynamics: II. Beyond SUPG". In: *Computer Methods in Applied Mechanics and Engineering* 54.3 (1986), pp. 341–355.

[105] Thomas J.R. Hughes and Michel Mallet. "A new finite element formulation for computational fluid dynamics: III. The generalized streamline operator for multidimensional advective-diffusive systems". In: *Computer Methods in Applied Mechanics and Engineering* 58.3 (1986), pp. 305–328.

[106] D. Gligor et al. "Experiments on sloshing mitigation using tuned oscillating baffles". In: *Physics of Fluids* 36.9 (Sept. 2024), p. 092122.

[107] Pedro A. Marques et al. "Experimental analysis of heat and mass transfer in non-isothermal sloshing using a model-based inverse method". In: *Applied Thermal Engineering* 231 (2023), p. 120871.

[108] Mendez, M.A., Németh, L., and Buchlin, J-M. "Measurement of Liquid Film Thickness via Light Absorption and Laser Tomography". In: *EPJ Web of Conferences* 114 (2016), p. 02072.

[109] Pedro A. Marques et al. "Characterization of cryogenic sloshing via image velocimetry, free surface tracking and data assimilation". In: *21th International Symposium on Application of Laser and Imaging Techniques to Fluid Mechanics* (2024).

[110] Joris Heyman. "TracTrac: A fast multi-object tracking algorithm for motion estimation". In: *Computers & Geosciences* 128 (2019), pp. 11–18.

[111] J. Porter et al. "The "Effect of Marangoni Convection on Heat Transfer in Phase Change Materials" experiment". In: *Acta Astronautica* 210 (2023), pp. 212–223.

[112] U. Martínez et al. "Ray-tracing images for melting PCM bridges in microgravity". In: *Advances in Space Research* 72.5 (2023), pp. 1915–1928.

[113] P. Salgado Sánchez et al. "Optical Processing of Melting PCM Bridges in Microgravity Using SVD and ANNs". In: *Microgravity Science and Technology* 37 (2025), p. 12.

[114] V. Shevtsova et al. "The IVIDIL experiment onboard the ISS: Thermodiffusion in the presence of controlled vibrations". In: *Comptes Rendus Mecanique* 339 (2011), pp. 310–317.

[115] A. Mialdun et al. "Preliminary analysis of Diffusion Coefficient Measurements in ternary mIXtures 4 (DCMIX4) experiment on board the International Space Station". In: *The European Physical Journal E* 42 (2019), p. 87.

[116] C. S. Cockell et al. "Space station biomining experiment demonstrates rare earth element extraction in microgravity and Mars gravity". In: *Nature Communications* 11 (2020), p. 5523.

[117] A. N. Kraiko. "The formulation of problems of lubrication theory for journal bearings". In: *Journal of Applied Mathematics and Mechanics* 66 (2002), pp. 757–765.

[118] I. Martinez. *Nozzles*. Technical Report. Universidad Politecnica de Madrid, 2022.

[119] H. S. Greenside and W. M. Coughran. "Nonlinear pattern formation near the onset of Rayleigh-Bénard convection". In: *Physical Review A* 30 (2021), pp. 398–428.

[120] J. Fernández et al. "The CFVib experiment: Control of Fluids in microgravity with Vibrations". In: *Microgravity Science and Technology* 29 (2017), pp. 351–364.

[121] P. Salgado Sanchez et al. "The effect of thermocapillary convection on PCM melting in microgravity: results and expectations". In: *Proceeding of the 72th International Astronautical Conference (IAC)* (2020).

[122] J. M. Ezquerro et al. “The Thermocapillary Effects in Phase Change Materials in Microgravity experiment: design, preparation and execution of a parabolic flight experiment”. In: *Acta Astronautica* 162 (2019), pp. 185–196.

[123] J. M. Ezquerro et al. “Experimental evidence of thermocapillarity in phase change materials in microgravity: measuring the effect of Marangoni convection in solid/liquid phase transitions”. In: *International Communications in Heat and Mass Transfer* 113 (2020), p. 104529.

[124] P. Salgado Sanchez et al. “Thermocapillary effects during the melting of phase change materials in microgravity: heat transport enhancement”. In: *International Journal of Heat and Mass Transfer* 163 (2020), p. 120478.

[125] A. Borshchak Kachalov et al. “The combined effect of natural and thermocapillary convection on the melting of phase change materials in rectangular containers”. In: *International Journal of Heat and Mass Transfer* 168 (2021), p. 120864.

[126] R. Varas et al. “Thermocapillary effects during the melting in microgravity of phase change materials with a liquid bridge geometry”. In: *International Journal of Heat and Mass Transfer* 178 (2021), p. 121586.

[127] A. Borshchak Kachalov et al. “Optimization of thermocapillary-driven melting in trapezoidal and triangular geometry in microgravity”. In: *International Journal of Heat and Mass Transfer* 185 (2022), p. 122427.

[128] M. Frank, M. Lappa, and P. Capobianchi. “Investigation of thermocapillary migration of nanodroplets using molecular dynamics”. In: *Physics of Fluids* 33 (2021), p. 042110.

[129] D. Schwabe. “Thermocapillary Liquid Bridges and Marangoni Convection under Microgravity—Results and Lessons Learned”. In: *Microgravity Science and Technology* 26 (2014), pp. 1–10.

[130] F. Romano et al. “Limit cycles for the motion of finite-size particles in axisymmetric thermocapillary flows in liquid bridges”. In: *Physics of Fluids* 29 (2017), p. 093303.

[131] M. K. Smith and S. H. Davis. “Instabilities of dynamic thermocapillary liquid layers. Part 1. Convective instabilities”. In: *Journal of Fluid Mechanics* 132 (1983), pp. 119–144.

[132] F. Preisser, D. Schwabe, and A. Scharmann. “Steady and oscillatory thermocapillary convection in liquid columns with free cylindrical surface”. In: *Journal of Fluid Mechanics* 126 (1983), pp. 545–567.

[133] Y. Gaponenko et al. “Effect of the supporting disks shape on nonlinear flow dynamics in a liquid bridge”. In: *Physics of Fluids* 33 (2021), p. 042111.

[134] M. K. Smith. “Instability mechanisms in dynamic thermocapillary liquid layers”. In: *Physics of Fluids* 29 (1986), p. 3182.

[135] H. C. Kuhlmann and S. Albensoeder. “Three-dimensional flow instabilities in a thermocapillary-driven cavity”. In: *Physical Review E* 77 (2008), p. 036303.

[136] M. Lappa. “On the formation and propagation of hydrothermal waves in liquid layers with phase change”. In: *Computers and Fluids* 172 (2018), pp. 741–760.

[137] L. J. Peltier and S. Biringen. “Time-dependent thermocapillary convection in a rectangular cavity: numerical results for a moderate Prandtl number fluid”. In: *Journal of Fluid Mechanics* 257 (1993), pp. 339–357.

[138] P. Salgado Sanchez et al. “Thermocapillary effects during the melting of Phase Change Materials in microgravity: steady and oscillatory flow regimes”. In: *Journal of Fluid Mechanics* 908 (2021), A20.

[139] N. Martínez et al. “Effect of surface heat exchange on phase change materials melting with thermocapillary flow in microgravity”. In: *Physics of Fluids* 33 (2021), p. 083611.

[140] E. Bucchignani and D. Mansutti. “Horizontal thermocapillary convection of succinonitrile: Steady state, instabilities, and transition to chaos”. In: *Physical Review E* 69 (2004), p. 056319.

[141] P. Zhu, L. Duan, and Q. Kang. “Transition to chaos in thermocapillary convection”. In: *International Journal of Heat and Mass Transfer* 57 (2013), pp. 457–464.

[142] A. Boaro and M. Lappa. “Multicellular states of viscoelastic thermovibrational convection in a square cavity”. In: *Physics of Fluids* 33 (2021), p. 033105.

[143] V. Shevtsova et al. “Experimental and theoretical study of vibration-induced thermal convection in low gravity”. In: *Journal of Fluid Mechanics* 648 (2010), pp. 53–82.

[144] J. Porter et al. “A review of fluid instabilities and control strategies with applications in microgravity”. In: *Mathematical Modelling of Natural Phenomena* 16 (2021), p. 24.

[145] J. Fernández et al. “Instabilities of vibroequilibria in rectangular containers”. In: *Physics of Fluids* 29 (2017), p. 024108.

[146] M. Lappa. “Patterning behavior of gravitationally modulated supercritical Marangoni flow in liquid layers”. In: *Physical Review E* 93 (2016), p. 053107.

[147] S. Madruga and C. Mendoza. “Enhancement of heat transfer rate on phase change materials with thermocapillary flows”. In: *The European Physical Journal Special Topics* 226 (2017), pp. 1169–1176.

[148] A. Mialdun et al. “Experimental evidence of thermal vibrational convection in a nonuniformly heated fluid in a reduced gravity environment”. In: *Physical Review Letters* 101 (2008), p. 084501.

[149] B-F. Wang, Q. Zhou, and C. Sun. “Vibration-induced boundary-layer destabilization achieves massive heat-transport enhancement”. In: *Science Advances* 6 (2020).

[150] J-C. Li et al. “Dynamic behavior in a storage tank in reduced gravity using dynamic contact angle method”. In: *Microgravity Science and Technology* 32 (2020), pp. 1039–1048.

[151] M. Strani, R. Piva, and G. Graziani. “Thermocapillary convection in a rectangular cavity: asymptotic theory and numerical simulation”. In: *Journal of Fluid Mechanics* 130 (1983), pp. 347–376.

[152] P. Salgado Sánchez et al. “Effect of thermocapillary convection on the melting of phase change materials in microgravity: experiments and simulations”. In: *International Journal of Heat and Mass Transfer* 154 (2020), p. 119717.

[153] B-C. Sim and A. Zebib. “Effect of free surface heat loss and rotation on transition to oscillatory thermocapillary convection”. In: *Physics of Fluids* 14 (2002), p. 225.

[154] Y. Kousaka and H. Kawammura. “Numerical Study on the Effect of Heat Loss upon the Critical Marangoni Number in a Half-Zone Liquid Bridge”. In: *Microgravity Science and Technology* 18 (2006), pp. 141–145.

[155] D. E. Melnikov and V. M. Shevtsova. “The effect of ambient temperature on the stability of thermocapillary flow in liquid column”. In: *International Journal of Heat and Mass Transfer* 74 (2014), pp. 185–195.

[156] P. Salgado Sánchez et al. “Dynamics of weakly coupled parametrically forced oscillators”. In: *Physical Review E* 94 (2016), p. 022216.

[157] L. Yang and G. M. Homsy. “Steady three-dimensional thermocapillary flows and dryout inside a V-shaped wedge”. In: *Physics of Fluids* 18 (2006), p. 042107.

[158] D. V. Lyubimov et al. “Interface orienting by vibration”. In: *Comptes Rendus de l’Académie des Sciences - Series IIB - Mechanics-Physics-Chemistry-Astronomy* 325 (1997), pp. 391–396.

[159] K. Beyer et al. “Compressible Potential Flows with Free Boundaries. Part I: Vibrocapillary Equilibria”. In: *Journal of Applied Mathematics and Mechanics* 81 (2001), pp. 261–271.

[160] K. Beyer, M. Günther, and A. Timokha. “Variational and finite element analysis of vibroequilibria”. In: *Computational Methods in Applied Mathematics* 4 (2004), pp. 290–323.

[161] I. Gavrilyuk, I. Lukovsky, and A. Timokha. “Two-dimensional variational vibroequilibria and Faraday’s drops”. In: *Journal of Applied Mathematics and Physics* 55 (2004), pp. 1015–1033.

[162] V. Shevtsova and J. C. Legros. “Oscillatory convective motion in deformed liquid bridges”. In: *Physics of Fluids* 10 (1998), p. 1621.

[163] A.C. Or and R.E. Kelly. “The effects of thermal modulation upon the onset of Marangoni-Benard convection”. In: *Journal of Fluid Mechanics* 456 (2002), pp. 161–182.

[164] B.L. Smorodin, A.B. Mikishev, and A.A. Nepomnyashchy. “Thermocapillary instability of a liquid layer under heat flux modulation”. In: *Physics of Fluids* 21 (2009), p. 062102.

[165] A.B. Mikishev and A. A. Nepomnyashchy. “Marangoni instability of a liquid layer with insoluble surfactant under heat flux modulation”. In: *European Physical Journal Special Topics* 219 (2013), pp. 81–88.

[166] A. Samoilova and A. Nepomnyashchy. “Longitudinal Modulation of Marangoni Wave Patterns in Thin Film Heated From Below: Instabilities and Control”. In: *Frontiers in Applied Mathematics and Statistics* 7 (2021), p. 679332.

[167] R. Savino and M. Lappa. “Assessment of thermovibrational theory: application to g-jitter on the Space Station”. In: *Journal of Spacecrafts and Rockets* 40 (2003), pp. 201–210.

[168] S. Someya and T. Munakata. “Measurement of the interface tension of immiscible liquids interface”. In: *Journal of Crystal Growth* 275 (2005), e343–e348.

[169] V Bychkov et al. “The Rayleigh-Taylor instability in inertial fusion, astrophysical plasma and flames”. In: *Plasma Physics and Controlled Fusion* 49.12B (Nov. 2007), B513–B520.

[170] John Lindl. “Development of the indirect-drive approach to inertial confinement fusion and the target physics basis for ignition and gain”. In: *Physics of Plasmas* 2.11 (1995), pp. 3933–4024.

[171] J. A. F. Plateau. *Statique experimentale et theorique des liquides soumis aux seules forces moleculaires*. vol. 2. Paris: Gauthier-Villars, 1873.

[172] Lord Rayleigh Sec. R.S. “XIX. On the instability of cylindrical fluid surfaces”. In: *London, Edinburgh & Dublin Philosophical Magazine and Journal of Science* 34.207 (1892), pp. 177–180.

[173] John William Strutt. “VI. On the capillary phenomena of jets”. In: *Proceedings of the Royal Society of London* 29.196-199 (1879), pp. 71–97.

[174] Kyoung Ok Lee and Mario A. Medina. “Using phase change materials for residential air conditioning peak demand reduction and energy conservation in coastal and transitional climates in the State of California”. In: *Energy and Buildings* 116 (2016), pp. 69–77.

[175] Ravi Kandasamy, Xiang-Qi Wang, and Arun S. Mujumdar. “Application of phase change materials in thermal management of electronics”. In: *Applied Thermal Engineering* 27.17 (2007), pp. 2822–2832.

[176] Pascal Henry Biwole, Pierre Eclache, and Frédéric Kuznik. “Phase-change materials to improve solar panel’s performance”. In: *Energy and Buildings* 62 (2013), pp. 59–67.

[177] N. S. Dhaidan and J. M. Khodadadi. “Melting and convection of phase change materials in different shape containers: A review”. In: *Renewable and Sustainable Energy Reviews* 43 (2015), pp. 449–477.

[178] D. Gligor et al. “Thermocapillary-driven dynamics of a free surface in microgravity: Response to steady and oscillatory thermal excitation”. In: *Physics of Fluids* 34 (2022), p. 042116.

[179] K. Kumar and L. S. Tuckerman. “Parametric instability of the interface between two fluids”. In: *Journal of Fluid Mechanics* 279 (1994), pp. 49–68.

[180] E. Talib, S. V. Jalikop, and A. Juel. “The influence of viscosity on the frozen wave stability: theory and experiment”. In: *Journal of Fluid Mechanics* 584 (2007), pp. 45–68.

[181] D. V. Lyubimov and A. A. Cherepanov. “Development of a steady relief at the interface of fluids in a vibrational field”. In: *Fluid Dynamics* 21 (1986), pp. 849–854.

[182] G. Gandikota et al. “Dynamic equilibrium under vibrations of H2 liquid-vapor interface at various gravity levels”. In: *Physical Review E* 89 (2014), p. 063003.

[183] A. Bourdelle et al. “Modeling and Control of Propellant Slosh Dynamics in Observation Spacecraft with Actuator Saturations”. In: *8th European Conference for Aeronautics and Aerospace Science (EUCASS)* (2019).

[184] H. Mai R. Belakroum M. Kadja and C. Maalouf. “An efficient passive technique for reducing sloshing in rectangular tanks partially filled with liquid”. In: *Mechanics Research Communications* 37 (2010), pp. 341–346.

[185] E. Demirel and M. M. Aral. “Liquid Sloshing Damping in an Accelerated Tank Using a Novel Slot-Baffle Design”. In: *Water* 10 (2018), p. 1565.

[186] U. Gopalakrishnan et al. “Investigation on the effect of baffle position on sloshing in tanks”. In: *AIP Conference Proceedings* 2134 (2019), p. 040005.

[187] J. Wang, C. Wang, and J. Liu. “Sloshing reduction in a pitching circular cylindrical container by multiple rigid annular baffles”. In: *Ocean engineering* 171 (2019), pp. 241–249.

[188] H. Kim et al. “Reduction of sloshing effects in a rectangular tank through an air-trapping mechanism – a numerical study”. In: *Journal of Mechanical Science and Technology* 32 (2018), pp. 1049–1056.

[189] H. Kim et al. “Numerical estimation on applying air-trapping mechanism to suppress sloshing loads in a prismatic tank”. In: *Journal of Mechanical Science and Technology* 34 (2020), pp. 2895–2902.

[190] A. Samoilova and A. Nepomnyashchy. “Longitudinal Modulation of Marangoni Wave Patterns in Thin Film Heated From Below: Instabilities and Control”. In: *Frontiers in Applied Mathematics and Statistics* 7 (2021), p. 679332.
[191] A. Samoilova and A. Nepomnyashchy. “Controlling of longwave oscillatory Marangoni patterns on a rhombic lattice”. In: *Mathematical Modelling of Natural Phenomena* 16 (2021), p. 1.
[192] J. Olle et al. “Onsite vibrational characterization of DCMIX2/3 experiments”. In: *Acta Astronautica* 32 (2017), pp. 409–419.
[193] D. Dubert et al. “Characterization of the accelerometric environment of DCMIX2/3 experiments”. In: *Microgravity Science and Technology* 30 (2018), pp. 683–697.
[194] D. Dubert et al. “On the Monitoring of the Vibratory Environment of DCMIX4 Campaign. Preliminary Results”. In: *Microgravity Science and Technology* 32 (2020), pp. 615–628.
[195] R. Wunenburger et al. “Frozen wave induced by high frequency horizontal vibrations on a liquid-gas interface near the critical point”. In: *Physical Review E* 59 (1999), pp. 5440–5445.
[196] M. Troitiño et al. “Symmetry breaking in large columnar frozen wave patterns in weightlessness”. In: *Microgravity Science and Technology* (2020).
[197] G. Gandikota et al. “Faraday instability in a near-critical fluid under weightlessness”. In: *Physical Review E* 89 (2014), p. 013022.
[198] E. Labrador et al. “Secondary Faraday waves in microgravity”. In: *Journal of Physics: Conference Series* 2090 (2021), p. 012088.
[199] I. Torres, P. Salgado Sánchez, and J. Porter. “Faraday waves in alternating multi-layer systems in microgravity”. In: *AIP Conference Proceedings* 2872.1 (Sept. 2023), p. 040007.
[200] M. M. Weislogel and H. D. Ross. *Surface settling in partially filled containers upon step reduction in gravity*. Tech. rep. NASA Technical Memorandum, 1990, pp. 1–19.
[201] D. Gligor et al. “Thermocapillary-driven dynamics of a free surface in microgravity: Control of sloshing”. In: *Physics of Fluids* 34 (2022), p. 072109.
[202] *http://isssp.bit.edu.cn/en/*. Last visited: December 2022.
[203] H. Ueda, F. Yamazaki, and W. Liu. “Sloshing Assessment of Oil Tanks in Keiyo Petrochemical Industrial Complex under Long-Period Seismic Ground Motion”. In: *Journal of Japan Association for Earthquake Engineering* 16 (2016), pp. 1–14.
[204] S. Ahmed et al. “Sloshing Assessment of Oil Tanks in Keiyo Petrochemical Industrial Complex under Long-Period Seismic Ground Motion”. In: *Agriculture* 12 (2022), p. 379.
[205] F. Cheli et al. “Simulation of sloshing in tank trucks”. In: *International Journal of Heavy Vehicle Systems* 20 (2012), pp. 1–18.
[206] A. Romero-Calvo et al. “Novel propellant settling strategies for liquid rocket engine restart in microgravity”. In: *Acta Astronautica* 202 (2023), pp. 214–228.
[207] A. Romero-Calvo, G. Cano-Gomez, and H. Schaub. “Diamagnetically Enhanced Electrolysis and Phase Separation in Low Gravity”. In: *Journal of Spacecraft and Rockets* 59 (2022), pp. 59–72.
[208] S. Z. Shuja, B. S. Yilbas, and O. Momin. “Laser repetitive pulse heating and melt pool formation at the surface”. In: *Journal of Mechanical Science and Technology* 25 (2011), pp. 479–487.

[209] S. Madruga and C. Mendoza. “Heat transfer performance and melting dynamic of a phase change material subjected to thermocapillary effects”. In: *International Journal of Heat and Mass Transfer* 109 (2017), pp. 501–510.
[210] N. Garcia-Acosta et al. “Thermocapillary-enhanced Melting of Different Phase-change Materials in Microgravity”. In: *Microgravity Science and Technology* 34 (2022), p. 92.
[211] R. Varas et al. “Effects of thermocapillary and natural convection during the melting of PCMs with a liquid bridge geometry”. In: *Microgravity Science and Technology* 35.17 (Mar. 2023).
[212] S. Madruga and C. Mendoza. “Introducing a new concept for enhanced micro-energy harvesting of thermal fluctuations through the Marangoni effect”. In: *Applied Energy* 306 (2022), p. 117966.
[213] A. Laverón. *Experiment Scientific Requirement (ESR) document: Effect of Marangoni Convection on Heat Transfer in Phase Change Materials. Ref: ESA-HRE-ESR-Marangoni in PCM, Iss. 1, Rev 2.* 2021.
[214] P. Salgado Sanchez et al. “The “Effect of Marangoni convection on heat transfer in Phase Change Materials" experiment, from a student project to the International Space Station”. In: *Proccedings of the 4th Symposium on Space Education Activities* (2022), pp. 1–6.
[215] J. Miles and D. Henderson. “Parametrically forced surface waves”. In: *Annual Review of Fluid Mechanics* 22 (1990), pp. 143–165.
[216] D. Beysens. “Vibrations in space as an artificial gravity?” In: *Europhysics News* 37 (2006), pp. 22–25.
[217] V. Garcia Bennet et al. “Drifting frozen waves”. In: *Physical Review E* 104 (2021), p. 045107.
[218] C. Renaud et al. “The Yeoh model applied to the modeling of large deformation contact/impact problems”. In: *International Journal of Impact Engineering* 36 (2009), pp. 659–666.
[219] *https://gipoc.grc.nasa.gov/wp/pims/home/*. Last visited: December 2022.
[220] P. Salgado Sanchez et al. “The “Thermocapillary-based control of a free surface in microgravity" experiment”. In: *Acta Astronautica* 205 (2023), pp. 57–67.
[221] S. N. C. Govindan and M. E. Dreyer. “Experimental Investigation of Liquid Interface Stability During the Filling of a Tank in Microgravity”. In: *Microgravity Science and Technology* 35.3 (2023), p. 23.
[222] B. Vukasinovic, M. K. Smith, and A. Glezer. “Dynamics of a sessile drop in forced vibration”. In: *Journal of Fluid Mechanics* 587 (2007), pp. 395–423.
[223] Andrey Ivantsov et al. “The Shape of a Compressible Drop on a Vibrating Solid Plate”. In: *Mathematics* 11.21 (2023), p. 4527.
[224] C. Peromingo et al. “Sloshing reduction in microgravity with passive baffles: design, performance, and supplemental thermocapillary control”. In: *Physics of Fluids* 35 (2023), p. 112108.
[225] C. Peromingo et al. “Sloshing reduction in microgravity: thermocapillary-based control and passive baffles”. In: *Physics of Fluids* 35 (2023), p. 102114.
[226] R. V. Birikh et al. “Control of thermocapillary convection in a liquid bridge by high frequency vibrations”. In: *Microgravity Q.* 3 (1993), pp. 23–28.

[227] R. V. Birikh et al. “Interaction of the thermovibrational and thermocapillary convection mechanisms”. In: *Fluid Dynamics* 29.5 (1994), pp. 681–692.
[228] O. H. Yeoh. “Some Forms of the Strain Energy Function for Rubber”. In: *Rubber Chemistry and Technology* 66.5 (Nov. 1993), pp. 754–771.
[229] S. F. Kistler. *Wettability*. Ed. by J. Berg. CRC Press, 1993, p. 311.
[230] T. P. Lyubimova. “The interaction of thermocapillary and vibrational instabilities in a two-layer system subjected to the tangential vibrations”. In: *The European Physical Journal Special Topics* 226.6 (2017), pp. 1263–1272.
[231] B. Apffel et al. “Liquid walls and interfaces in arbitrary directions stabilized by vibrations”. In: *Proceedings of the National Academy of Sciences* 118.48 (2021), e2111214118.
[232] B.J. Huang and C.L. Duang. “System dynamic model and temperature control of a thermoelectric cooler”. In: *International Journal of Refrigeration* 23.3 (2000), pp. 197–207.
[233] J. Plaza et al. “Controlling a Free Surface With Thermocapillary Flows and Vibrations in Microgravity”. In: *Microgravity Science and Technology* 36.2 (2024), p. 13.
[234] M. Stange, M. Dreyer, and H. Rath. “Capillary driven flow in circular cylindrical tubes”. In: *Physics of Fluids* 15 (2003), pp. 2587–2601.
[235] B. Figliuzzi and C. R. Buie. “Rise in optimized capillary channels”. In: *Hournal of Fluid Mechanics* 731 (2013), pp. 142–161.
[236] S. T. Chen et al. “Capillary-driven flows in eccentric annuli under microgravity”. In: *Archives of Applied Mechanics* 93 (2023), pp. 731–743.
[237] M. M. Weislogel and S. Lichter. “Capillary flow in an interior corner”. In: *Journal of Fluid Mechanics* 373 (1998), pp. 349–378.
[238] M. M. Weislogel and C. L. Nardin. “Capillary driven flow along interior corners formed by planar walls of varying wettability”. In: *Micogravity Science and Technology* 17 (2005), pp. 45–55.
[239] Y. Chen, M. Weislogel, and C. Nardin. “Capillary driven flows along rounded interior corners”. In: *Journal of Fluids Mechanics* 556 (2006), pp. 235–271.
[240] Y. Q. Li et al. “Study of capillary driven flow in an interior corner of rounded wall under microgravity”. In: *Microgravity Science and Technology* 27 (2015), pp. 193–205.
[241] Z. Y. Wu et al. “Capillary driven flows along curved interior corners”. In: *International Journal of Multiphase Flow* 109 (2018), pp. 14–25.
[242] M. Dreyer, A. Delgado, and H. J. Rath. “Capillary rise of liquid between parallel plates under microgravity”. In: *Journal of Colloidal Interface Science* 163 (1994), pp. 158–168.
[243] S. L. Chen et al. “Capillary phenomena between plates from statics to dynamics under microgravity”. In: *Microgravity Science and Technology* 34 (2022), p. 70.
[244] S. Dominick and S. Driscoll. *Fluid acquisition and resupply experiment (FARE l) flight results*. American Institute of Aeronautics, Astronautics 29th Joint Propulsion Conference, and Exhibit, Monterey, 1993.
[245] S. Dominick and J. Tegart. *Orbital test results of a vaned liquid acquisition device*. American Institute of Aeronautics, Astronautics 30th Joint Propulsion Conference, and Exhibit, Indianapolis, 1994.
[246] D. Jaekle. *ropellant management device conceptual design and analysis-Vanes*. 27th Joint Propulsion Conference, 1991.

[247] D. Jaekle. *Propellant management device conceptual design and analysis-Sponges*. 29th Joint Propulsion Conference and Exhibit, 1993.

[248] D. Jaekle. *Propellant management device conceptual design and analysis-Galleries*. 33rd Joint Propulsion Conference and Exhibit, 1997.

[249] D. Chato and T. A. Martin. "Vented Tank Resupply Experiment: Flight Test Results". In: *Journal of Spacecraft and Rockets* 43 (2006), pp. 1124–1130.

[250] W. Tam, I. Ballinger, and D. Jaekle. *Propellant Tank with Surface tension PMD for Tight Center-of-Mass Propellant Control*. 44th AIAA/ASME/SAE/ASEE Joint Propulsion Conference and Exhibit, 2008.

[251] L. Wang et al. "Numerical simulation of the reorientation process under different conditions in a vane-type surface tension propellant tank". In: *MIcrogravity Science and Technology* 34 (2022), p. 37.

[252] S. T. Chen et al. "Study on the shape and motion of bubbles in the tank model with a central column aboard the Chinese Space Station". In: *Physics of Fluids* 36 (2024), p. 012124.

[253] A. Borshchak Kachalov et al. "Thermocapillary effects during the melting of phase change materials subjected to lateral heat flux in microgravity". In: *International Journal of Heat and Mass Transfer* 218 (2024), p. 124806.

[254] A. Borshchak Kachalov et al. "Preliminary Design of a Space Habitat Thermally Controlled using Phase Change Materials". In: *Thermo* 3 (2023), pp. 232–247.

[255] U. Martínez et al. "Effect of surface heat exchange on phase change materials melting with thermocapillary flow in microgravity". In: *Submitted to Physics of Fluids* (2023), accepted.

[256] A. Borshchak Kachalov et al. "Optimizing the thermocapillary-driven melting of phase change materials in microgravity". In: *Proceedings of the 10th EUCASS* (2023).

[257] B. Seta et al. "Effect of Marangoni induced instabilities on a melting bridge under microgravity conditions". In: *International Journal of Heat and Mass Transfer* 179 (2021), p. 121665.

[258] B. Seta et al. "Transitions between nonlinear regimes in melting and liquid bridges in microgravity". In: *International Journal of Heat and Mass Transfer* 193 (2022), p. 122984.

[259] B. Seta et al. "Effect of heat transfer through an interface on convective melting dynamics of phase change materials". In: *Journal of Fluid Mechanics* 966 (2023), A46.

[260] P. Salgado Sánchez et al. "Simulating vibrated fluids and vibroequilibria in the CFVib microgravity experiment". In: *Proccedings of the 8th European Conference for Aeronautics and Aerospace Science* (2019), p. 0224.

[261] N. Martínez Figueira et al. "Effect of surface heat exchange on phase change materials melting with thermocapillary flow in microgravity". In: *Physics of Fluids* 35 (2023), p. 084115.

[262] M. Lappa. "Coalescence and Non-coalescence Phenomena in Multi-material Problems and Dispersed Multiphase Flows: Part 2, A Critical Review of CFD Approaches". In: *FDMP-Fluid Dynamics and Materials Processing* 1 (2005), pp. 213–234.

[263] G. R. Fowles and G. L. Cassiday. *Analytic Mechanics*. Saunders College Publishing, 1986.

[264] Nafees Ahmad, Mehul Varshney, and Mohammad Farooqi. “Design and CFD analysis of baffles of fuel tanker trucks for normal and grade highway conditions”. In: *International Journal of Forensic Engineering and Management* 1 (Jan. 2020), p. 76.

[265] Xue-lian Zheng et al. “Effects of Transverse Baffle Design on Reducing Liquid Sloshing in Partially Filled Tank Vehicles”. In: *Mathematical Problems in Engineering* 2013 (2013), pp. 1–13.

[266] M. A. Goudarzi, S. R. Sabbagh-Yazdi, and W. Marx. “Investigation of sloshing damping in baffled rectangular tanks subjected to the dynamic excitation”. In: *Bulletin of Earthquake Engineering* 8.4 (Aug. 2010), pp. 1055–1072.

[267] S. V. Jalikop and A. Juel. “Steep capillary-gravity waves in oscillatory shear-driven flows”. In: *Journal of Fluid Mechanics* 640 (2009), pp. 131–150.

[268] R. Garcia-Roco et al. “Dynamics of PCM melting driven by radiative flux at the free surface in microgravity”. In: *Thermal Science and Engineering Progress* (2024), under review.

[269] Domenico Fiorini et al. “Effect of inertia on the dynamic contact angle in oscillating menisci”. In: *Physics of Fluids* 34.10 (Oct. 2022), p. 102116.

[270] O. M. Faltinsen et al. “Multidimensional modal analysis of nonlinear sloshing in a rectangular tank with finite water depth”. In: *Journal of Fluid Mechanics* 407 (2000), pp. 201–234.

[271] S.M. Gardarsson, H. Yeh, and M. Asce. “Hysteresis in Shallow Water Sloshing”. In: *Journal of Engineering Mechanics* 113 (2007).

[272] S-C. Jiang, W. Bai, and L. Liu. “Hysteresis phenomenon of the sloshing-mode resonance in a moonpool induced by rolling motion excitations”. In: *Physics of Fluids* 36 (2024), p. 012112.

[273] Man Liu and D.G. Gorman. “Formulation of Rayleigh damping and its extensions”. In: *Computers & Structures* 57.2 (1995), pp. 277–285.

[274] M. A. Mendez, M. Balabane, and J.-M. Buchlin. “Multi-scale proper orthogonal decomposition of complex fluid flows”. In: *Journal of Fluid Mechanics* 870 (2019), pp. 988–1036.

[275] J.-J. Park et al. “Study on tank shape for sloshing assessment of LNG vessels under unrestricted filling operation”. In: *Journal of Marine Science and Technology* 20 (4 2015), pp. 640–651.

[276] Baozeng Yue and Zhaolin Wang. “Numerical study of three-dimensional free surface dynamics”. In: *Acta Mecanica Sinica* 2 (2006), pp. 120–125.

[277] Bole Ma et al. “Study on the dynamical characteristics and experimental validation for liquid sloshing in a common bulkhead tank”. In: *Acta Mecanica Sinica* 39 (2023), p. 523127.

[278] N. N. Moiseyev and V. V. Rumyantsev. *Dynamic Stability of Bodies Containing Fluid*. Springer, New York, 1968.

[279] Osborne Reynolds. “XXIX. An experimental investigation of the circumstances which determine whether the motion of water shall be direct or sinuous, and of the law of resistance in parallel channels”. In: *Philosophical Transactions of the Royal Society of London* 174 (1883), pp. 935–982.

[280] Clayton T. Crowe et al. *Engineering Fluid Mechanics*. Wiley, 2009.

[281] Anupam Das, Damodar Maity, and Sriman Kumar Bhattacharyya. “Characterization of liquid sloshing in U-shaped containers as dampers in high-rise buildings”. In: *Ocean Engineering* 210 (2020), p. 107462.

[282] Martin Konopka et al. “Active slosh control and damping - Simulation and experiment”. In: *Acta Astronautica* 158 (2019), pp. 89–102.

[283] D. Gligor et al. “Sloshing reduction with passive spring–mass baffles in partially filled containers”. In: *Ocean Engineering* 310 (2024), p. 118675.

[284] Y. Tsoumpas et al. “Effect of Marangoni Flows on the Shape of Thin Sessile Droplets Evaporating into Air”. In: *Langmuir* 31.49 (2015), pp. 13334–13340.

[285] A. Baldygin et al. “Effect of gravity on the spreading of a droplet deposited by liquid needle deposition technique”. In: *npj Microgravity* 9 (2023), p. 49.

[286] Álvaro Romero-Calvo et al. “Free and Forced Oscillations of Magnetic Liquids Under Low-Gravity Conditions”. In: *Journal of Applied Mechanics* 87.2 (Dec. 2019), p. 021010.

[287] D. Fiorini et al. “An Experimental Characterization of Capillary Driven Flows in Microgravity”. In: *Microgravity Science and Technology* 36.6 (2024), p. 61.

[288] S. Karpitschka et al. “Droplets move over viscoelastic substrates by surfing a ridge”. In: *Nature Communications* 6.1 (2015), p. 7891.

[289] Hans-Jürgen Butt et al. “Contact angle hysteresis”. In: *Current Opinion in Colloid & Interface Science* 59 (2022), p. 101574.

[290] A. F. A. Gawad et al. “Roll stabilization by anti-roll passive tanks”. In: *Ocean Engineering* 28.5 (2001), pp. 457–469.

[291] I. Jiménez Blanco et al. “Microgravity Control of a Free Surface in Elliptical Containers Via Thermocapillary Flows”. In: *Microgravity Science and Technology* 37 (2025), p. 10.

[292] Johann Radon. “On the determination of functions from their integral values along certain manifolds”. In: *IEEE Transactions on Medical Imaging* 5.4 (1986), pp. 170–176.

[293] A. Sanchis and A. Jensen. “Dynamic masking of PIV images using the Radon transform in free surface flows”. In: *Experiments in Fluids* 51 (2011), pp. 871–880.

[294] A. Simonini, L. Peveroni, and M.R. Vetrano. “Simultaneous interface position and bulk velocity measurements in cryogenic sloshing”. In: *Aerospace Science and Technology* 90 (2019), pp. 452–462.

List of publications

V. García Bennet, P. Salgado Sánchez, **Dan Gligor** and J. Porter. Drifting frozen waves. *Physical Review E* **104**, 045107 (2021) https://doi.org/10.1103/PhysRevE.104.045107 (not included in the Thesis).

D. Gligor, P. Salgado Sánchez, J. Porter, and I. Tinao. Thermocapillary-driven dynamics of a free surface in microgravity: response to steady and oscillatory thermal excitation. *Physics of Fluids* **34**, 042116 (2022). https://doi.org/10.1063/5.0087975.

D. Gligor, P. Salgado Sánchez, J. Porter, and J. M. Ezquerro Navarro. Thermocapillary-driven dynamics of a free surface in microgravity: control of sloshing. *Physics of Fluids* **34**, 072109 (2022) https://doi.org/10.1063/5.0097954.

P. Salgado Sánchez, U. Martínez, **D. Gligor**, I. Torres, J. Plaza and J. M. Ezquerro. The "Thermocapillary-based control of a free surface in microgravity" experiment. *Acta Astronautica* **205**, 57-67 (2023). https://doi.org/10.1016/j.actaastro.2023.01.032.

J. Porter, A. Laverón-Simavilla, M.M. Bou-Ali, X. Ruiz, F. Gavalda, J.M. Ezquerro, P. Salgado Sánchez, U. Martínez, **D. Gligor**, I. Tinao, J. Gómez, J. Fernández, J. Rodríguez, A. Borshchak Kachalov, V. Lapuerta, B. Seta, J. Massons, D. Dubert, A. Sanjuan, V. Shevtsova and L. García-Fernández. The "Effect of Marangoni Convection on Heat Transfer in Phase Change Materials" experiment. *Acta Astronautica* **210**, 212-223 (2023). https://doi.org/10.1016/j.actaastro.2023.05.026 (not included in the Thesis).

U. Martínez, **D. Gligor**, P. Salgado Sánchez, J. M. Ezquerro and J. Porter. Ray-tracing images for melting PCM bridges in microgravity. *Advances in Space Research* **72**, 5, 1915-1928 (2023). https://doi.org/10.1016/j.asr.2023.06.013 (not included in the Thesis).

C. Peromingo, **D. Gligor**, P. Salgado Sánchez, A. Bello and K. Olfe. Sloshing reduction in microgravity: Thermocapillary-based control and passive baffles. *Physics of Fluids* **35**, 102114 (2023). https://doi.org/10.1063/5.0170304.

C. Peromingo, P. Salgado Sánchez, **D. Gligor**, A. Bello and J. Rodríguez. Sloshing reduction in microgravity with passive baffles: design, performance, and supplemental thermocapillary control. *Physics of Fluids* **35**, 112108 (2023). https://doi.org/10.1063/5.0174635.

J. Plaza, **D. Gligor**, P. Salgado Sánchez, J. Rodríguez and K. Olfe. Controlling a free surface with thermocapillary flows and vibrations in microgravity. *Microgravity Science and Technology* **36**, 13 (2024) https://doi.org/10.1007/s12217-024-10099-8.

D. Gligor, C. Peromingo, P. Salgado Sánchez, J. Porter, J. Fernández and M. A. Méndez. Sloshing mitigation in microgravity with moving baffles. *Acta Astronautica* **219**, 639-652 (2024). https://doi.org/10.1016/j.actaastro.2024.03.047.

D. Gligor, P. Salgado Sánchez, J. Rodríguez and U. Martínez. Sloshing reduction with passive spring-mass baffles in partially filled containers. *Ocean Engineering* **310**, 118675 (2024). https://doi.org/10.1016/j.oceaneng.2024.118675.

D. Gligor, P. A. Marques, P. Salgado Sánchez, J. Porter, M. A. Méndez and J. M. Ezquerro. Experiments on sloshing mitigation using tuned oscillating baffles. *Physics of Fluids* **36**, 092122 (2024). https://doi.org/10.1063/5.0225917.

I. Jiménez Blanco, P. Salgado Sánchez, **D. Gligor**, A. Borshchak Kachalov and A. Arshadi. Microgravity control of a free surface in elliptical containers via thermocapillary flows. *Microgravity Science and Technology* **37**, 10 (2025) https://doi.org/10.1007/s12217-025-10165-9.

P. Salgado Sánchez, F. Varas, J. Porter and **Dan Gligor**. Optical Processing of Melting PCM Bridges in Microgravity Using SVD and ANNs. *Microgravity Science and Technology* **37**, 12 (2025) https://doi.org/10.1007/s12217-025-10166-8 (not included in the Thesis).